Integration and optimisation of a novel industrial Fused Composite Manufacturing process for prepreg filament

Master Thesis Report

J.Driezen

Technische Universiteit Delft

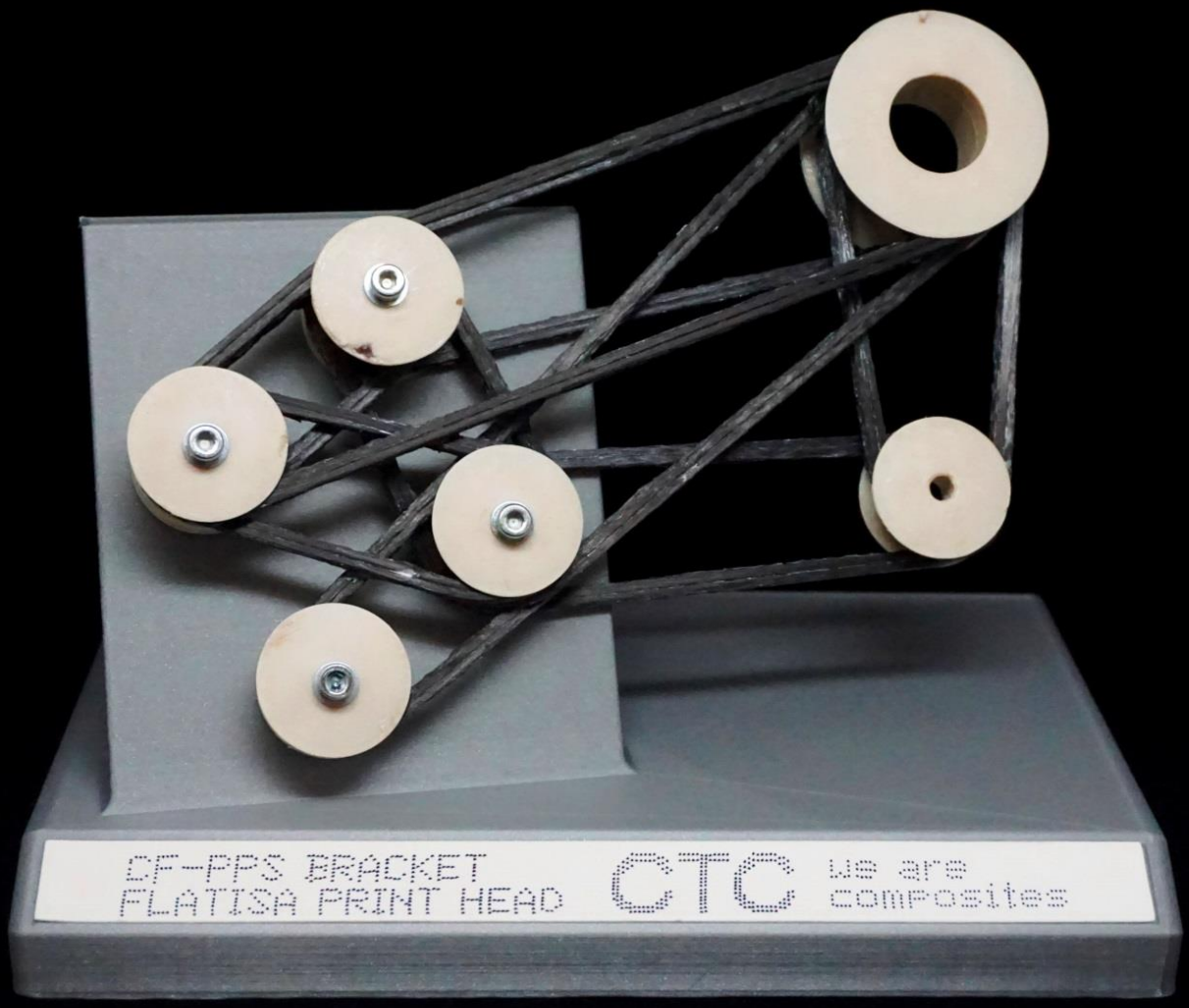

TU Delft Delft University of Technology

CTC we are composites

[This page intentionally left blank]

Integration and optimisation of a novel industrial Fused Composite Manufacturing process for prepreg filament

Master Thesis Report

by

J.Driezen

to obtain the degree of Master of Science

at the Delft University of Technology,

to be defended publicly on Friday October 18, 2019 at 11:00 AM.

Student number:	4285395	
Project duration:	November 1, 2018 – September 30, 2019	
Thesis committee:	Dr. I. Fernandez Villegas	TU Delft
	Dr. C. D. Rans	TU Delft
	Dr. ir. O.K Bergsma	TU Delft, supervisor
	Dipl.-Ing. J. Born	CTC GmbH, supervisor

This thesis is confidential and cannot be made public until December 31, 2024.

TU Delft

CTC we are composites

[This page intentionally left blank]

Confidentiality Clause

AIRBUS

Non-Disclosure Agreement

1. The entire / the marked part of the final thesis of:

   Mr. Jorne Driezen

   contains confidential data of Airbus Operations GmbH which may only be used for the issue of the final thesis and the conjoint examination procedures.

   The contents of the thesis may only be made accessible to the supervisors and the members of the examination office.

   The use of the thesis particularly as part of lectures is not allowed without written consent of the Airbus Operations GmbH.

2. Confidential information shall not, either as a whole or in part, be published, reproduced or disclosed to a third party unless the express written consent of Airbus Operations GmbH has been obtained.

3. Secrecy shall be observed in regard to all corporate matters and operations of Airbus Operations GmbH and its affiliated companies which are not publicly known and of which knowledge is obtained by tutoring the student – in written or oral form – either from the student or from Airbus Operations GmbH itself.

4. The declaration of secrecy shall enter into force once this agreement has been signed and shall remain valid for 5 years.

Delft University of Technology

Place, date Delft, 30 August 2018

Signature

(On behalf of Delft University of Technology)

[This page intentionally left blank]

Preface

This master thesis report is submitted as final step towards the completion of the degree Master of Science at the faculty of Aerospace Engineering at the Delft University of Technology.

CTC GmbH, located in Stade Germany, has given me the opportunity to perform this work within a professional and industrial environment. After short discussions on my personal interest and the possibilities at CTC GmbH, I got the opportunity to design, implement, optimise and test a novel manufacturing technique for continuous fiber reinforced additive manufacturing. During this period I did not only gain theoretical knowledge about the topic, but learned a lot about the practical insights going along with the industrialisation of such process. I therefore would like to thank all the collegues, in particular Johannes Born and Claus Fastert, for the support and feedback during my period as a thesis student at CTC GmbH. Furthermore I would like to thank my supervisor, Otto Bergsma, for the guidance throughout the past months.

Last I would like to thank Prof. Dr. Axel Herrmann for giving me the opportunity to start my professional career as a PhD at Faserinstitut Bremen e.V. continuing research on Fused Composite Manufacturing.

J.Driezen
Delft
October 4, 2019

[This page intentionally left blank]

Summary

The research presented in this report covers a feasibility study on a novel industrial Fused Composite Manufacturing process for high performance prepreg filament and is split into the design, integration and optimisation of the process.

Based on a pre-research on Polyphenylene Sulphide (PPS) filament with 50 % carbon Fiber Volume Content (FVC) on an Utimaker S5 printer, it is identified that the thermal stability of the hardware is a must for printing high performance polymers. Therefore an experimental set-up including heated build plate and build environment is designed.
The implementation of a novel set-up requires a new approach for print path generation. Because the current status of print path planning exists of manually creating print path in CAD-sofware, a combination between Mathcad Prime and Python is being used to provide an intermediate solution in an automated way. Predefined closed loop geometries are selected and have input data which consists of a number of nodes, the minimum radius around each node, the number of layers with their layer height and the number of lines with their line width. The tool calculates a number of points in chronological order which represents the print path. The output data consists of three columns containing x-, y- and z-coordinates and are being transferred into a SRC-code, able to be recognized by the KUKA system.

Several pre-trial prints are being performed from which the main observation is that a limited amount of layers can be printed without failure. Analysis on the samples shows a buckling and twisting behaviour to occur in the radius areas. The reason for this behaviour is due to the concave inner shape of the nozzle which allows the filament to be placed away from its centreline. Because the feeding unit is synchronised with the velocity of the Tool Centre Point (TCP) and defined at the nozzle centre point, the offset causes over-extrusion in curvatures. This issue is being solved by the introduction of an Extrusion Overwrite function which decreases the amount of filament being extruded in curvatures. Together with an additional Active Cooling unit, which cools the extrudate after being placed, the robustness of the print process is increased.

A Design of Experiments (DoE), more specifically a face centered Central Composites Design (CCD) is being used to generate samples and test their quality based on the void content and inter-laminar shear strength (ILSS). The key influencing parameters are identified as the layer height (0.15 - 0.25 mm), print speed (2 - 6 mm) and nozzle temperature (340 - 380 $^{\circ}C$).
Results from the inter-laminar shear strength test according to the DIN EN 2563 standards indicate inter-layer shear and plastic deformation to be the main failure modes with a median for the stress at break equal to 29.95 MPa and 32.8 MPa respectively.
Microscopic inspection of the cross-section shows voids due to inaccurate print bed levelling at the bottom of the specimen, voids due to inefficient fusion between the layers and gaps in between printed lines due to the tolerance of the filament. The averaged void content of the complete cross-section results in 12.4 % and for a single tower of print lines 5.2 %.
Minitab 2018 is being used to generate and analyse the Surface Response Design (RSD). Using the backward elimination procedure the models predicting the relation between the terms and responses are being optimised. The main finding is that a higher layer thickness increases the void content and reduces the stress at break. A low print speed results in many failures due to overheating of the nozzle, where higher print speeds result in bad quality of the outer surface and inefficient fusion between the layers. An increase in the nozzle temperature causes the stress at break to increase and a reduction of the voids in between the layers. The final parameter settings are set at 0.21 mm for the layer height, 4.1 mm/s for the print speed and 380 $^{\circ}C$ for the nozzle temperature. The corresponding response results in a stress at break of 39.2 MPa and 5 % void content in a tower section.

In order to show the feasibility of the integrated and optimised FCM process for the aerospace industry, several use cases are being identified from which a demonstrator part is being selected and printed using the optimum parameter settings. Manually implementing support structure in the process allows the bracket to be printed in a single go. The resulting bracket has shown the capabilities of the overall process and proven the possibility to use such process within the manufacturing of strong and lightweight components. In future research, the Print Path Planning tool needs to be improved to allow for more complex geometries and the void content in the specimen needs to be reduced.

[This page intentionally left blank]

Contents

[This page intentionally left blank]

List of Figures

[This page intentionally left blank]

List of Tables

[This page intentionally left blank]

List of Abbreviations

TCP	Tool Centre Point
FCM	Fused Composite Manufacturing
DoE	Design of Experiments
ILSS	Inter-laminar shear strength
RSD	Response Surface Design
FVC	Fiber Volume Content
PPS	Polyphenylene Sulphide
CCD	Central Composites Design
ACCOOL	Active Cooling
EXOV	Extrusion Overwrite
IR	Infrared
CAD	Computer-aided design
FLM	Filament Layer Manufacturing
CF	Carbon fiber
SEM	Scanning Electron Microscope
STL	Standard Triangle Language
SRC	Source
UD	Uni-directional
OEM	Original Equipment Manufacturer

[This page intentionally left blank]

List of Symbols

Symbol	Description	Unit
$V_{abs_{TCP}}$	Absolute velocity of the Tool Centre Point	mm/s
I_{bit}	Input bit-signal of the Controllino	–
$V_{set_{max}}$	Maximum velocity setting in the KRC unit	mm/s
RPM	Rotation per minute	rpm
r, R	Radius	mm
n_{micro}	Number of micro-steps per full rotation of the stepper motor	–
f	Pulse rate of the micro-stepping	$1/s$
L_{12}	Distance between nozzle centre point and ironing surface	mm
$EXOV$	Extrusion overwrite	–
A	Area	mm^2
D_{fil}	Filament diameter	mm
L_{ww}	Hatch spacing or line width	mm
t_{lay}	Layer thickness	mm
L	Length	mm
dx	Sub-elements along the length	mm
$\dot{m}$	Mass flow rate	kg/s
C_p	Heat capacity	J/K
T_m	Melt temperature	K
T_s	Surface temperature	K
h	Heat transfer coefficient	W/m^2K
$\bar{h_p}$	Averaged heat transfer coefficient	W/m^2K
P	Perimeter	mm
k_{fl}	Thermal conductivity of the fluid	W/mK
N_{UD}	Nusselt Number	–
U_z	Print speed	mm/s
P_{break}	Maximum load at the moment of first failure	N
τ	Inter-laminar shear strength	MPa

[This page intentionally left blank]

1

Introduction

Fused Composite Manufacturing (FCM) is a relatively new manufacturing technique which describes the process of material extrusion through a nozzle in order to build a part by thermal fusion of subsequent placement of continuously fiber reinforced thermoplastic material strands. The placement process has to allow for an in- and out-of-plane reinforcement, whereas a plane is defined as a non-curved or curved layer [7]. Additive manufacturing using neat thermoplastic materials, also referred to as Filament Layer Manufacturing (FLM), has been used for many years and is widely known by the public. The freedom of design makes this technique ideal for rapid prototyping, but limits its use cases as weak load bearing capabilities are present. The inclusion of a continuous reinforcement in such manufacturing process however increases the mechanical properties [8].

As the steady aim of the aerospace industry is to identify and bring to use new lightweight solutions, Fused Composite Manufacturing is a technique with much potential [19]. Compared to conventional manufacturing techniques, FCM includes the benefits of manufacturing without the need for expensive moulds and restrictions from tooling and allows parts to be manufactured without the removal of material. The ability of tailoring the print path direction in three dimensional space allows the reinforcement to be placed along the load path of the structure. This enables parts to be produced with a low buy-to-fly ratio, which is a lightweight solution to current manufacturing methods.

A detailed study on the State-of-the-Art of FCM concluded the maturity of the technology to be of low order [8]. The temperature range and print capabilities of the printers used are limiting the material to low grade thermoplastics with low Fiber Volume Content. The slicing capabilities for these desktop printers are based on neat filament printing and use a layer-by-layer approach. This results in retractions and travel movement which are not possible with a continuous reinforcement.

Based on these weaknesses, the research in this thesis focusses on the integration of such FCM process within an industrial set-up, incorporating a 6-axis industrial robot and print head capable of printing a high performance prepreg filament. The research is divided into three main steps. The first step consists of the integration of a novel print head within an industrial 6-axis robot. The second step is the generation of a print path for continuous fiber reinforced filament, which can be used within a KUKA KR30 HA robot. The last step is the optimisation of the process and is done by optimising the experimental set-up until a robust process is obtained, whereafter the print results are optimised on microscopic level using a DoE approach.

The layout of the report starts by providing a background on FCM in Chapter 2. The experimental set-up is being designed in Chapter 3 and is based on a pre-research to identify the needed implementations. In Chapter 4, the working principle of the experimental set-up is used to develop a Print Path Planning tool, based on predefined geometries. The problems encountered with their corresponding solutions are explained in Chapter 5. In order to optimise the results on microscopic level, a Design of Experiments approach is used and explained in Chapter 6. Chapter 7 shows how the samples are printed and prepared. The optimisation is performed in Minitab 2018 and the main results are given in Chapter 8. To conclude the feasibility of the overall process, several use cases are identified and a demonstrator part is printed in Chapter 9.

2

Fused Composite Manufacturing

As motivated in the introduction, this thesis research aims to integrate and optimize an industrial Fused Composite Manufacturing (FCM) process. During the preparation of this research, a Literature Study has been performed [8]. During this phase the different Fused Composite Manufacturing techniques were analysed and the weaknesses of the current state were identified. This Chapter provides these main findings, after which the outline of the report is given.

2.1. FCM Techniques

Fused Composite Manufacturing describes the process of material extrusion through a nozzle in order to build a part by thermal fusion of subsequent placement of continuously fiber reinforced thermoplastic material strands. The placement process has to allow for an in- and out-of-plane reinforcement, whereas a plane is defined as a non-curved or curved layer [7]. There exist different FCM techniques, which are distinguished based on the stage of impregnation of the reinforcement. The three main categories are identified as pre-, in-situ- and post-impregnation. Figure 2.1.1 provides an overview of the different stages of impregnation.

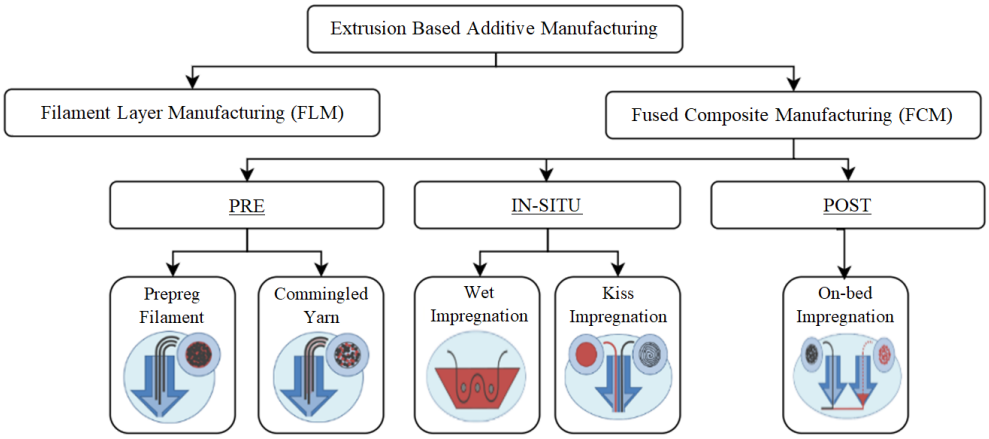

Figure 2.1.1: Extrusion based AM categories, FLM and FCM exclude and include a continuous reinforcement respectively

Impregnation of the reinforcement before the extrusion process can take place in different combinations. Firstly by means of a prepreg material, which consists of thermoplastic pre-impregnated fibers as a semi-finished product. This material is fed into the extrusion head by means of a filament strand and is remolten in the heated print head during extrusion [17]. Secondly by means of a commingled yarn, consisting of thermoplastic and reinforcing fibers spun together. The thermoplastic fibers will melt in the heated print head, impregnating the reinforcing fibers during extrusion.

In-situ impregnation of the reinforcement allows the fibers to be impregnated within the process. Likewise to the pre-impregnation, different combinations are possible. One is to draw the reinforcement through a chamber of molten thermoplast. The fiber is then conveyed onto the print bed using a roller system. This process is called "Wet Impregnation". Another is where reinforcement and thermoplastic material are fed into the nozzle separately, after which they are molten, mixed and extruded, referred to as "Kiss-impregnation" [29].

The embedment of the reinforcement on the print bed, or post-impregnation, is achieved by the use of separate mechanism. One for printing the neat polymer structure, the other for reinforcing the structure by extruding a fiber on top. This technique requires additional means of post-treatment like autoclaving or oven compaction to create a composite material [18].

2.2. State-of-the-Art

The main stages within FCM are identified as the generation of a print path, referred to as "Print Path Planning" and the printing process itself. The state-of-the-Art of the Print Path Planning capabilities and the quality of the overall printing results are critically analysed and their main results are provided below.

2.2.1. Print Path Planning

In the early stages of design, topology optimisation is often used to determine the optimum shape of a loaded and constrained structure [26]. The inclusion of a continuous reinforcement introduces anisotropic material properties, which implies the need for a simultaneous approach of density and orientation optimization. Density optimization is done using the modelling of the density as parameter, 0 and 1 being the absence and presence of material respectively. The optimization function is then reduced to find the optimum of the density, meaning the minimum density [24]. The result of such geometry can quickly result in complex structures like the bone structure of the human body. In addition the orientation of the fiber should be taken into account. The fiber should be oriented along the principal stress direction, as in the fiber steering technique [11]. The simultaneous optimization of material distribution and fiber orientation have been performed for 2D geometries successfully, but in a limited amount [20].

FCM printing of highly complex geometries will introduce difficulties related to the capabilities of the printer. At first a print path is needed and should be retrieved out of the optimized structure. Based on the printer capabilities, several manufacturing effects will imply. Examples include a minimum printable radius, a set value for layer height and line width, the problem of overlapping regions were fibers run into each other, a minimum cutting length of the filament and other criteria. The current solution exist of manually drawing the print path using computer-aided design (CAD) and creating a robotic code with the use of digital manufacturing software, for example DELMIA. This print path generation does not connect to the optimization and therefore the need for an automated approach, capable of introducing manufacturing effects is needed.

2.2.2. Printing

From the Literature Study, it is concluded that besides research being done within institutions, several companies have established themselves on the market and sell parts or even complete desktop printers [8].

Out of the different stages of impregnation, pre-impregnated filament shows the best results regarding material properties. In addition, it is the least complex printing process as only a single axis nozzle system is of use and up until now the highest Fiber Volume Content is obtained [8]. This can be explained by the fibers which are already completely impregnated before extrusion, in contradiction to Kiss-impregnation where the fibers are completely dry before extrusion. However, the major concern is still a low quality part, which is the direct result from the relatively high void content and low inter-laminar properties.

Another observation is the materials being used in current research are of low performance with regard to aerospace requirements [8]. Low grade thermoplastics are commonly used as matrix materials in the know approaches, mainly because of their low melt temperatures. They do not have the need for a heated build plate and controlled environment and therefore thermal stresses will be less critical compared to high performance thermoplastics. Several companies on the market claim to be able to print high performance thermoplastics including continuous reinforcement, without publishing justifiable data.

Most of the revised parts are being manufactured using off-the-shelf desktop printers, like the MarkForged Mark2 or modified FCM printers, which use 3-axis kinematics. For Filament Layer Manufacturing (FLM)

processes, which stack up layers of neat thermoplastic material, the orientation of the print head is of minor importance. The inclusion of a continuous reinforcement in such process would solely result in an in-plane reinforcement. To fully take advantage of the FCM technology, different kinematics are needed which allow reinforcement being placed in all arbitrary directions.

2.3. Research Objective

The observations made from the State-of-the-Art of FCM conclude that the maturity of this technology is still of low order. At the moment the parts are limited to low grade thermoplastics with limited complexity. In order to introduce high performance thermoplastics within a print head capable of orienting the reinforcement in all arbitrary directions, a novel industrial set-up, including a 6-axis robot, heated environment and print head capable of reaching high temperatures is needed.

In addition this novel set-up requires an automated approach of generating print path. An intermediate solution is proposed which is based on the stacking two dimensional geometries in a three dimensional structure. The Print Path Planning tool needs to generate a print path in an automated way and be able to incorporate manufacturing effects.

As the parameter settings of the new print head need be optimised and validated for each different material of use, the optimisation process can be time consuming. It is therefore proposed to automate the optimisation process as much as possible.

By the design and implementation of the above discussed features within a novel industrial set-up, the end-to-end process of Fused Composite Manufacturing is analysed and the feasibility of such process for aerospace applications can be identified. Therefore the research objective of this thesis is defined as:

"The objective of this research is to evaluate the feasibility of a novel robotic Fused Composite Manufacturing process for aerospace applications by introducing a novel experimental set-up, optimizing the key process parameters and by setting up a Print Path Planning tool based on the printer capabilities."

2.4. Methodology

The methodology used in order to answer the stated research objective, is shown in the flowchart of Figure 2.4.1 and discussed below.

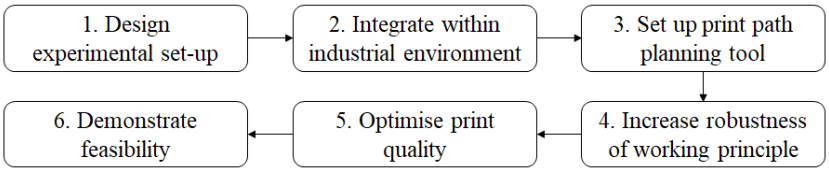

Figure 2.4.1: Methodology of the performed research

In this research, Polyphenylene Sulphide (PPS) is used as matrix material with the inclusion of continuous carbon fiber (CF). The filament is not being sold as finished product on the market, but is part of an ongoing research project. Therefore no print settings exist and the question raises if this filament is printable at all. Due to this reason, pre-trail prints are being performed on an Ultimaker S5. The results from this pre-trail printing are requirements and needed implementations which need to be taken into consideration when designing and integrating the experimental set-up, because the importance of a well-functioning experimental set-up is key to obtaining accurate results.
In order to identify the flaws within the working principle of the experimental set-up, a problem solving approach is used by trial and error printing until a robust print process is obtained.

In addition a Print Path Planning tool is being developed. The reason for the integration of such tool is that currently, manually creating a print path within CAD-software is done. This however is time consuming and does not link to the design of optimised structures. The ideal case would be to directly obtain a print path from a topology optimized structure [24]. Because currently manufacturing effects limit the complexity to generate such parts, an intermediate solution is proposed. This solution consists of designing predefined geometries which are based on the capabilities of the printer. These geometries are then used to form a three dimensional structure by printing them sequentially and fusing them together within a single print process.

The tool is being developed using a combination of Mathcad Prime 5.0 and Python. Based on the dimensions of the predefined geometry, a chronological order of points is created in x-, y- and z-coordinates. These points represent the print path which the nozzle will follow during printing. A python script is then used to transfer these coordinates into the correct format for the KUKA robot.
The outcome of this tool is not to be integrated within industry, but is rather used to generate different geometries in an fast and efficient manner. Because the uncertainty exist that such approach is not feasible for industrial robots, this tool will provide more information on the additional needs towards the ideal Print Path Planning.

One of the important parts of this research is the optimisation of the resulting print quality on microscopic level. Randomly changing the key influencing parameters will result in many experiments and inaccurate data and therefore a different approach is being used. A strategy for the planning and analysis of a parameter study is a Design of Experiments. This method uses the minimum required experiments needed to obtain the best process conditions resulting in efficient and low cost experimentation [2]. Because this optimisation is a first iteration, careful selection of the parameter boundaries is being done. These boundaries depend on the material type of use, Fiber Volume Content (FVC), diameter of the filament and other criteria. It is therefore chosen to automate the optimisation procedure, which allows future optimisations to be performed on different material in a more efficient manner. The selection of the parameter boundaries is automated by the analysis of a steady-state thermal model on the nozzle geometry and simulating the melt flow of the filament. With respect to the material properties, the print speed, nozzle temperature and layer height are varied to check a molten condition is obtained at the end of the nozzle.

layer-to-layer bonding is an important parameter in Additive Manufacturing, as it greatly influences the mechanical properties of printed parts [15]. Therefore one of the responses to be optimised is the inter-laminar shear strength (ILSS) and is obtained by performing ILSS tests according to the DIN EN 2563 standards. The second response is the analysis of the cross-sectional area to determine the amount of defects and voids for each parameter setting. The responses obtained from the printed specimen are optimised in Minitab 2018, because it provides the collection of statistical and mathematical methods in a single program. The purpose of the optimisation is to check the effect of the parameter settings on the selected responses and find the optimum conditions. These optimum conditions are then used to draw conclusions on the quality of the overall process and to identify the criteria which need to be improved in future research.

Because the feasibility of a new manufacturing method does not only depend on the resulting material properties, several use cases are identified which can potentially have a positive business case. A demonstrator part, resulting from an aerospace application, is chosen and printed to indicate the capabilities of the current state, but also to identify the points for improvement in order to draw an accurate conclusion on the feasibility of this technology for aerospace applications.

3

Experimental Set-up

As identified during the Literature Study, printing of high performance polymers requires a controlled build environment and high temperature capabilities [8]. A different approach is needed in the design of such system and each of the functions need to be critically evaluated. This chapter contains the design of the experimental set-up and explains its working principle.

3.1. Design Experimental Set-up

The design of the experimental set-up is based reviewed literature and on the findings from the pre-research using the Ultimaker S5, explained in Appendix A [8]. A KUKA KR30 HA 6-axis robot and print head manufactured by an external company are available and can be modified according to the research. The main task consists of implementing the print head into the KUKA system, generating code and optimize the print result. The importance of a functioning experimental set-up is therefore key to a good quality system. The result of the design is shown in Figure 3.1.1.

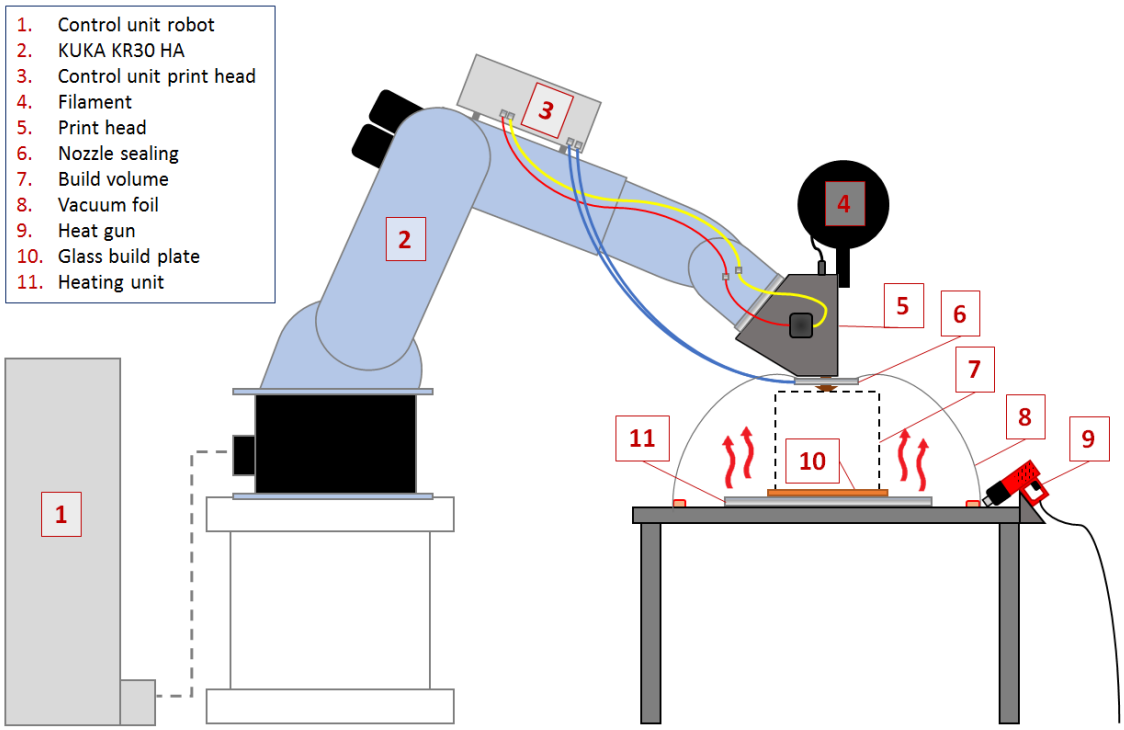

Figure 3.1.1: Experimental set-up

The main parts of the experimental set-up are the KUKA KR30 HA robot (2) with control unit (1). The KUKA KR30 HA is a 6-axis industrial robot, capable of handling a payload of $30kg$. The HA stands for "High Accuracy" and uses compared to the normal variant, different mechanical gears with an absolute calibration [12]. The operating system at use is the KRC2 which implicates that the code generated needs to have the correct format.

The print head (5) is mounted on the robot at an angle of approximately 30 degrees around the x-axis and 15 degrees around the z-axis with respect to the KUKA flange coordinate system. The reason for this orientation is to avoid singularities during movement of the robot axes. Based on the type of singularity, the robot can instantaneously turn an axis 180 degrees or lock in position, which will lead to reduced quality and uneven movement or even failure of the print. Making sure each of the axis is rotated with a slight angle, the probability of singularities is reduced.

The control unit of the print head (3) is mounted onto the robot for easy access of the wiring. A filament spool (4) is designed and is mounted on the print head to feed the filament directly into the inlet. The table (10) includes a heated build plate (11) and heat gun (9) to control the temperature of the build volume. The nozzle and table are equipped with sealing disks (6) which contain Velcro to connect with the insulation (8) and close the controlled build volume (7).

3.1.1. Controlled Build Volume

During the design of the controlled build volume, the decision is made to keep its size as small as possible. In this way the energy consumption is kept low, but also the electronics from the KUKA robot and print head are protected from the heated environment. The final design of the controlled build volume can be seen in Figure 3.1.2 and is based on the following criteria:

- The insulation should be transparent to have a clear view on the printing process
- The insulation should be heat resistant above $150°C$
- The insulation should close the area between the nozzle and build plate and allow for easy removal
- The insulation should be flexible to allow movement of the print head during printing
- The insulation should be lightweight, in order to be inflated using air pressure

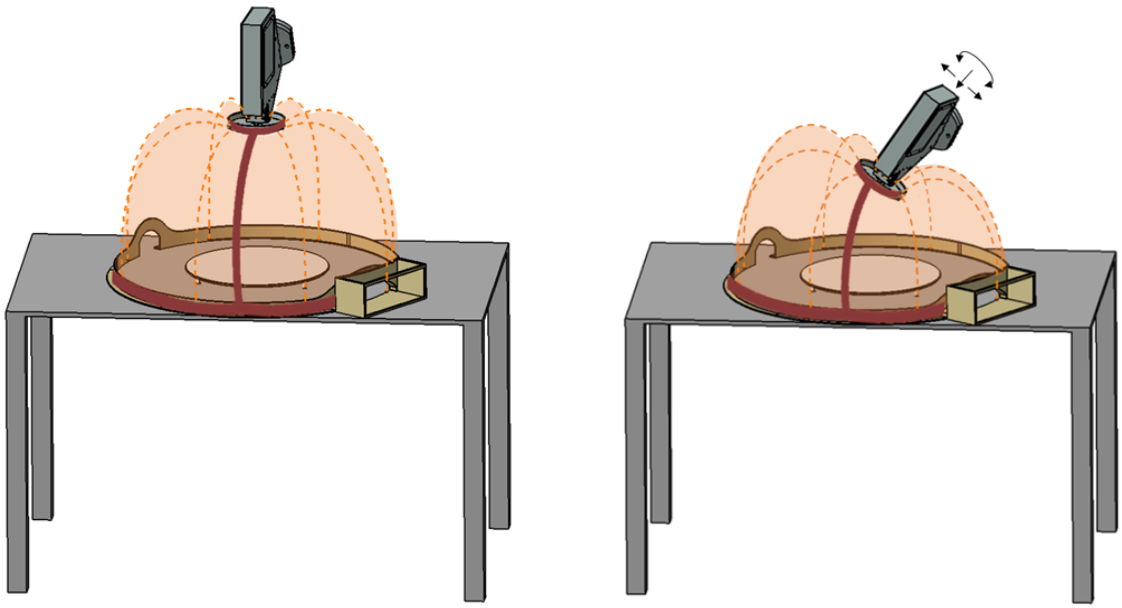

(a) Steady position of the print head

(b) Allowable freedom of motion

Figure 3.1.2: Design of the controlled build volume. Orange being pieces of vacuum foil adhered together in the shape of a sphere, red being the velcro which allows removal of the insulation

Appendix B shows the heat tests performed on a number of different foils, including Nylon sheets and vacuum foil. By heating the foil to 150°C using a heat gun, the behaviour of the foil is being analysed from which silicone- and Airtech IPPLON foil show to be thermally stable and so are feasible materials. For both materials a controlled build volume is manufactured and the proof of concept is demonstrated. In the end, Airtech IPPLON foil is chosen to be used for the reason that it is more robust compared to silicone foil.

3.1.2. Filament Spool

The used filament is manufactured by an external company and is coiled up in small batches. Because the filament coil does not have a fixed diameter, a filament spool is being designed and manufactured. The design consists of two water-jet Aluminium sides which contain 4 notches at which 3D-printed inserts are entered. The inserts can move up and down, depending on the diameter of the filament coil. The spool is being attached onto an Item-profile, straight above the inlet. Both parts are shown in Figure B.3.1 and B.3.2 and can be seen in Appendix B.

3.2. Identification Print Head

A closer look on the components of the print head can be seen in Figure 3.2.1. The main components exist of the nozzle (1) which is screwed into a heating block, the feeding unit (2), cutting unit (3), stepper motor (4) and inlet (5) for the filament.

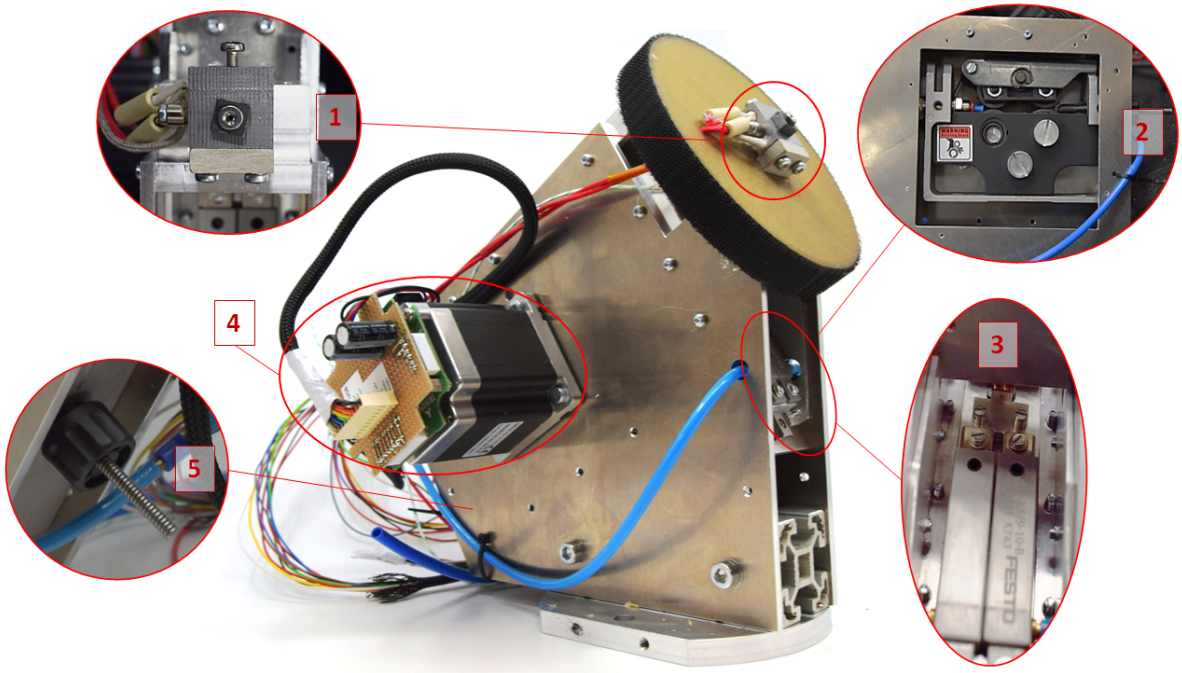

Figure 3.2.1: Print head FLATISA

As already mentioned in Chapter 2, the print head has been designed for using pre-impregnated filament. The functions of the print head are therefore simplified to re-melt and place the filament according to the predefined print path.

The sequence at which the filament travels through the print head starts with entering at the inlet, which directly connects the filament to the feeding unit. The feeding unit consist of two pairs of clamping wheels which are driven by an electric stepper motor. The stepper motor rotates synchronously to the absolute velocity of the Tool Centre Point (TCP), which is measured at the tip of the nozzle. This ensures the same filament is extruded as there is movement of the print head. A cutting unit is attached in between the feeding unit and the heating block and is able to cut the filament at a predefined size. The heating block is kept at a constant temperature using a 24 V, 30 W heating element and is directly connected to the nozzle. When printing, the feeding unit pushes the filament through the nozzle, where the ironing surface is used to squeeze and place the filament at the build plate, based on the movement of the print head.

3.3. Control Experimental Set-up

Each of the functions, discussed in previous section, require some sort of input data or activator. These inputs are generated by additional steps and can be seen in the flowchart of Figure 3.3.1.

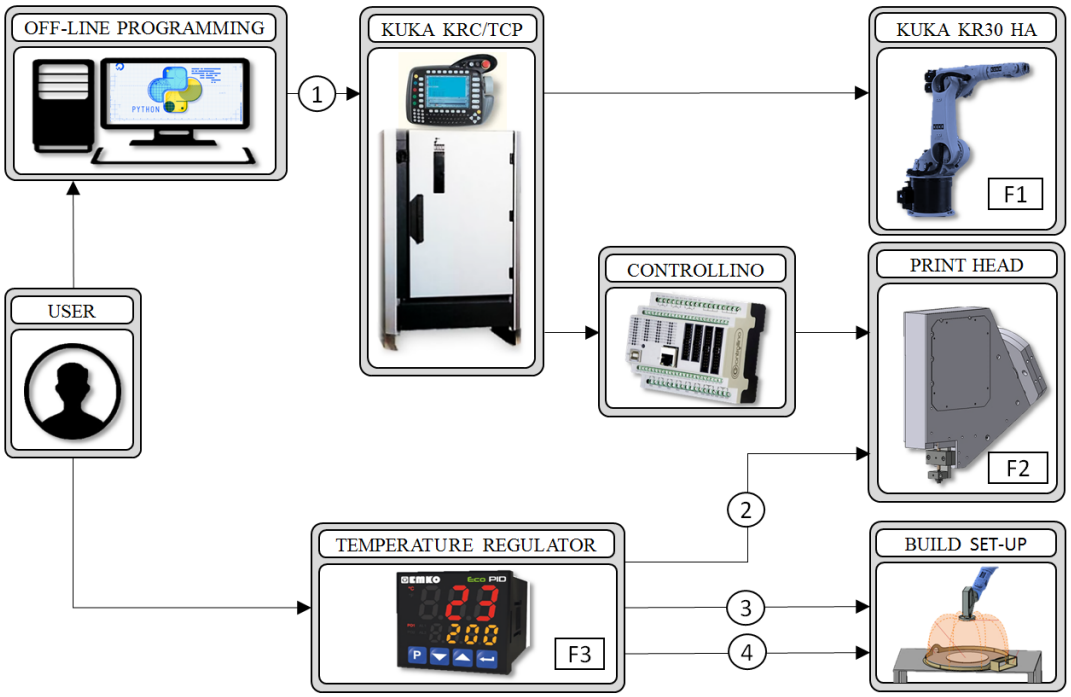

Figure 3.3.1: Work flow diagram of main printing functions

Programming KUKA robot

The first manual input (1) consist of the off-line programming in order to generate a print path. This step is referred to as "Print Path Planning" and creates a chronological order of points which the TCP should follow. Chapter 4 explains in detail how this is being done, where in Appendix C and D example scripts can be seen. The output of these scripts is a single SRC-file, which stands for Source Code File. This file needs to be transferred into the internal computer of the KUKA KRC unit, from where the program is run.

Feeding filament

A second function of the print head is feeding the material towards the nozzle. Due to the inclusion of a continuous reinforcement, over- and under-extrusion will be fatal to the process as they introduce defects. This means that the feeding rate needs to be synchronized with the movement of the TCP, or in other words the amount of filament extruded needs to be the same as the distance travelled of the TCP.

The KUKA KRC unit provides the absolute velocity of the TCP and is stored within the KRC unit as an output value. In order to transfer this signal to the stepper motor, 8 Beckhoff BK5100 bus couplers are used to transfer the absolute velocity into an 8-bit signal. This is done by first dividing the absolute velocity with the maximum set velocity of the KUKA robot and multiplying with 255 steps. This means that a maximum absolute velocity corresponds to 255 steps, where every fraction of this maximum velocity results in the same fraction of 255 steps. The bus couplers internally convert the received amount of steps over their 8 outputs. These outputs directly connect to the inputs of a Controllino MEGA, which is a Programmable Logic Controller (PLC). Such device consists of a digital computer which continuously monitors the state of input values received from sensors and controls the outputs for the operation of actuators [25]. These devices typically consist of an embedded computer, inputs, outputs and a power supply. By programming the Controllino in the Arduino development environment according to Figure 3.3.2, the input signal is being transferred into a step pulse for the stepper motor.

The input signal (I_{bit}) consists of 2^0, 2^1, 2^2, 2^3, 2^4, 2^5, 2^6 and 2^7 number of steps for each of the 8 inputs respectively. The maximum velocity of the robot ($V_{set_{max}}$) is set at a certain value within the KRC unit. Inside the Controllino, this step signal is converted back to an absolute velocity, according Equation 3.1.

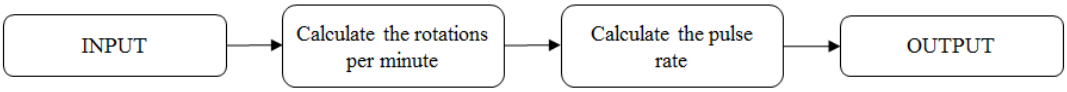

Figure 3.3.2: Work flow of the Arduino code

$$V_{abs_{TCP}} = \frac{I_{bit} \cdot V_{set_{max}}}{255} \tag{3.1}$$

In order to synchronise the movement between TCP and feeding unit, the velocity of the TCP needs to be exactly similar to the rotational velocity of the feeding unit. Because the radius (r) of the feeding gear is known, the rotations per minute (RPM) of the stepper motor can be calculated according to Equation 3.2.

$$V_{abs_{TCP}} = \frac{2\pi r \cdot RPM}{60} \quad \Rightarrow \quad RPM = \frac{2 \cdot I_{bit} \cdot V_{set_{max}}}{17 \cdot \pi \cdot r} \tag{3.2}$$

The stepper motor is a Trinamic PD60-1060, which has a step angle of 1.8 degrees, meaning 200 steps are needed for one complete rotation of 360 degrees. The micro-stepping, which divides a full step into multiple micro-steps, is set at 16, so the micro-step angle equals 0.1125 degrees. In the same manner, 3200 micro-steps are needed for one complete rotation. The number of rotations per minute can therefore be written in terms of the pulse rate (f) and the number of micro-steps per full rotation (n_{micro}) according to Equation 3.3.

$$RPM = \frac{1}{n_{micro}} \cdot f \cdot 60 \tag{3.3}$$

Substituting Equation 3.3 into 3.2 and solving for the pulse rate gives:

$$f = \frac{I_{bit} \cdot V_{set_{max}} \cdot n_{micro}}{255 \cdot 2\pi r} \tag{3.4}$$

This pulse rate is programmed within the Arduino development environment and loaded onto the Controllino MEGA. During operation, the output signal of the Controllino adapts its pulse rate according to the received input signal and in this manner synchronizing movement of the TCP and feeding unit.

Heating set-up

A last function besides movement of the KUKA robot and feeding material, is the heating of the nozzle (2), print bed (3) and environment (4). These temperature settings are done manually at the beginning of the printing process using a temperature regulator for each of the heating elements.

The missing link in the control of the experimental set-up is the off-line programming part. This part is discussed in detail in the next chapter. With the inclusion of this Print Path Planning tool, the overall set-up is being tested and is discussed in the next chapters.

4

Print Path Generation

This chapter explains the development of the offline programming. The intermediate solution to the ideal Print Path Planning tool, as discussed in Chapter 2, starts with identifying the limitations of the experimental set-up and the inclusion of a continuous reinforcement in print process. Based on these limitations, several predefined geometries are being selected to be used within the generation of print path. A combination of PTC Mathcad Prime 5.0 and Python is used to generate the SRC-code. Lastly, teaching of the KUKA robot is explained, which is done as a last phase before the actual printing.

4.1. Limitations of a Continuous Reinforcement

Conventional additive manufacturing techniques, for example Filament Layer Manufacturing, do not include a continuous fiber reinforcement in the printing process. Because these techniques are mainly used for rapid prototyping or creating parts which do not have a load bearing function, the direction of printing is not of concern [4]. In these techniques, print path generation is referred to as "Slicing" and is usually done by a layer-by-layer approach, determined by filling a certain layer in the most optimum condition.

The inclusion of a continuous reinforcement however, introduces several limitations and are given below:

1. **Machinery limitations:**
    - LIM-1.1 Minimum cutting length of the filament
    - LIM-1.2 Printer hardware influencing the capabilities and complexity of motion
2. **Material limitations:**
    - LIM-2.1 Layer height and line width
    - LIM-2.2 Minimum printable radius
    - LIM-2.3 Maximum overhang
    - LIM-2.4 Filament squeezing
    - LIM-2.5 Angle of change in between layers and lines
3. **Process limitations:**
    - LIM-3.1 Thermal expansion of the heated machinery and thermal shrinkage of the printed part (spring-in)
    - LIM-3.2 Anchoring the filament at the start of the print or after each cut

From the structural point of view, the orientation, start- and end position of the continuous reinforcement will affect the mechanical performance of the printed part. To make optimal use of the reinforcement, the following design requirements are being introduced:

- REQ-1 The filament should be cut as less as possible to decrease the number of possible defects resulting from the start of a new line. This will make more efficient use of the continuous reinforcement and increase the robustness of the process.
- REQ-2 To make optimal use of the reinforcement, the filament should be placed in the direction of the load path. As the loads can act in all directions, it should be possible to place the filament in all arbitrary directions.

Taking into account these limitations and requirements within the Print Path Planning tool, generating print path for three dimensional geometries will be out of the scope of this research objective. The number of variables and possibilities make the approach too complex and therefore the choice is being made to simplify the approach.

As an intermediate step towards the ideal tool, a solution is being proposed which consists of predefined geometries, stacked in three dimensional space to form the complete part. The advantage of this method is that these predefined geometries can be designed according to the printer capabilities. The stacking in three dimensional space allows to orient and locate the fiber at the locations where it is needed the most and lastly, these predefined geometries will keep their shape, allowing simplified automatization. In the next section these predefined shapes are discussed.

4.2. Selection Predefined Geometries

Based on REQ-1 and LIM-2.1, the print path should consist of a continuous path, where the geometry needs to be filled using the same line width and layer height along the print. This quickly results in sections with a constant width. A continuous motion, without cutting, requires the geometry to consist of a closed section loop, for example a circle. The print path however needs to change in between lines and layers and cannot be achieved if the same fill sequence is used every layer. The solution to this problem is explained in Figure 4.2.1. The print path starts at point "S", from which a designed loop shape is followed (1). This loop can be any preferred shape, as long as it will reach back to the starting point. After the first complete contour, the line changes to a next line, keeping a constant line width (2) and continue with the same sequence until the complete width is filled. The transition to the next layer is done by a smooth movement in a straight line (3). Then the same sequence is performed as in the first layer, only now the lines will go from inward to outward (4,5), opposite to the direction of the previous layer. This leads to a complete geometry fill and provides a symmetric design of the transition area as can be seen in Figure 4.2.1.

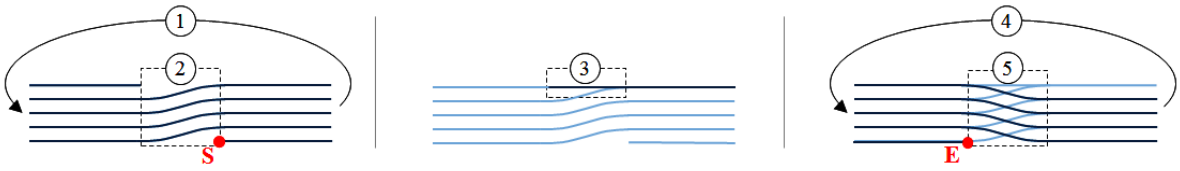

Figure 4.2.1: Sequence of the loop

This sequence can be used for any geometry which is closed and has a constant width. Therefore depending on the number of nodes, any geometry can be formed.

4.3. Source-code Generation

The script which generates the source-code is based on the flowchart in Figure 4.3.1. The input data consist of the number of nodes with their corresponding location, minimum radius around each node, number of lines with their line width and number of layers with their layer height. The script generates a number of points in x-, y- and z-coordinates, which are in a chronological order as the TCP will follow them during printing. Additional functions are added in the code which are discussed in a later stage. These points and functions are then transferred into the correct format for the KUKA system using a Python script.

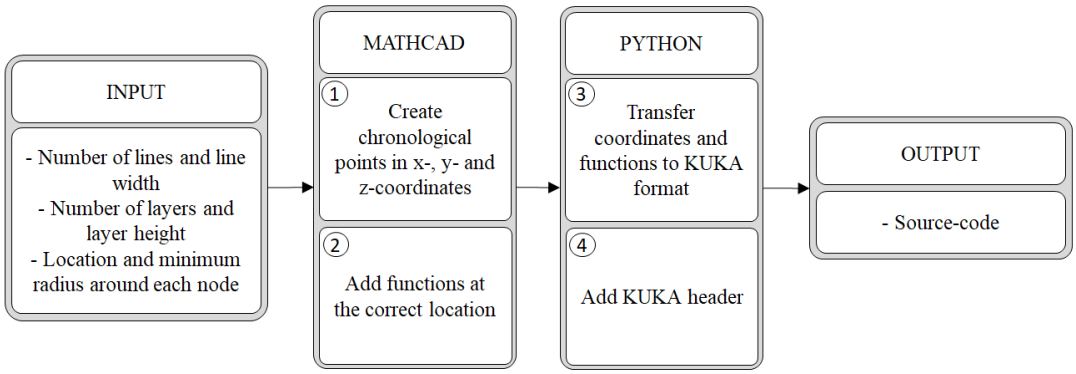

Figure 4.3.1: Flowchart of the source-code generation

4.3.1. Mathcad Point Generator

The script which transfers the input data into coordinates and functions is being implemented within PTC Mathcad Prime 5.0 as it provides a clear overview of the script and works as a living document.

The working principle of this script can be explained by modelling coordinates in a chronological order, based on the geometrical input data. Firstly, a distinction is being made between two regions, namely straight- and radius sections. The radius sections are determined by the location of the input nodes and the corresponding minimum radius and half line width. The straight sections connect the radius sections.

Each of these sections is put into a separate array. One of the straight sections is chosen as starting point and will act as the transition area, as seen in Figure 4.2.1. The start point is chosen in the middle of a straight section, from which several points are generated along the line until it reaches the radius area. Here, a new array is created which contains points based on the formula of a circle. The start- and endpoint on this radius are determined by the tangential point between radius and straight section of the previous and following node respectively. Once the radius is covered, the script will create a new array containing the straight section to the following node. This sequence is used until a complete contour is created. The next contour will be performed according to the same manner, but with one line width less. This sequence is done for the number of lines, which is one of the input variables. If the first layer is completed, the next layer will perform the same sequence in the same direction of movement, but from the inside towards the outside of the loop. In this manner, it is made sure that the complete area is filled without the need for retractions and travel movement.

Each change of line-to-line and layer-to-layer is done in a smooth motion. The distance between the end- and start point of the next round or layer can be modified by setting the array of the straight section with an offset, not starting from the first element and not ending with the last element. By changing this variable, the angle of change can be modified according to the desired specifications. In this research this value is being set at a constant level which results in a robust interchange.

The output of the Mathcad Point Generator contains 3 different arrays, including the x-, y- and z-coordinates. The code for this 2 node loop is shown and explained in Appendix C and its visual result can be seen in Figure 4.3.2.

4.3.2. Python Source-code Generator

The output from Mathcad is transferred into a Python script, where it is changed into the desired format for the KUKA system, as shown in Appendix D. Firstly the header for the KUKA robot is loaded, which contains all the necessary information for starting up and orienting the print head. The next part transfers each line of the x, y and z-columns into the correct format according to the existing function in that line. Finally, the transferred code is written in a single SRC-file, which needs to be loaded into the KUKA KRC unit.

4.4. Start-up and Teaching KUKA System

In order to start a print using the obtained SRC-code, the KUKA system needs to be prepared for this type of code. Preparation starts by teaching the KUKA robot the location and orientation of the print head and build plate.

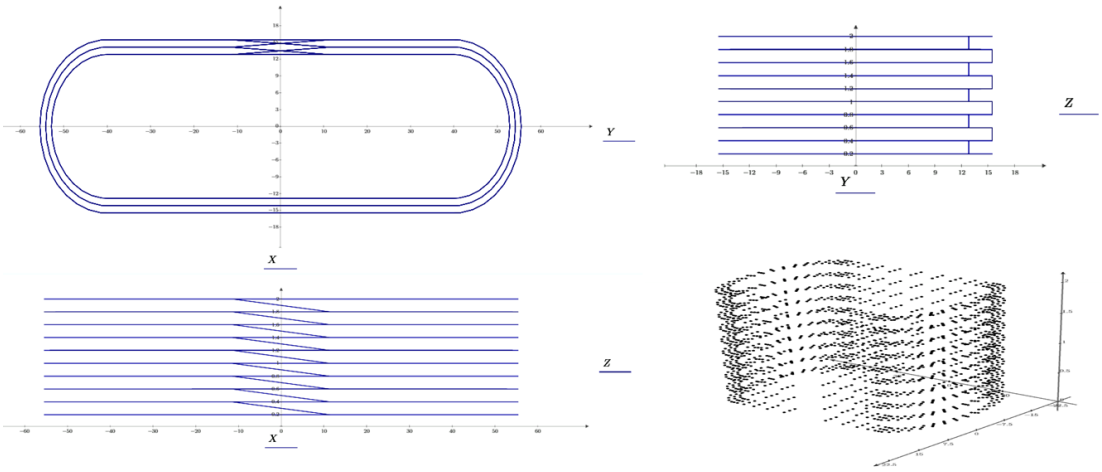

Figure 4.3.2: Example chronological point visualisation for a two node loop

Tool calibration is being performed in two steps. Firstly, the origin of the tool coordinate system needs to be determined by the use of a XYZ 4-point method. By approaching a pointy object, like a needle, from 4 different directions, the different flange positions allow the robot controller to calculate the location of the origin. Secondly, the orientation of the tool coordinate system is being determined. Because CAD-drawings of the print head are available, the orientation of the tool coordinate system is being taught by numeric input.

The location and orientation of the build plate, or base coordinate system is being defined by the 3-point method. Before defining the points, it has to be made sure that the orientation of the nozzle aligns with the build plate in order to guarantee the printed lines will be parallel to the build plate. This is done by heating the nozzle and touching a piece of paper on top of the build plate. An aligned nozzle is supposed to leave a complete circular mark on the paper. If not, the orientation of the print head needs to be adapted until build plate and nozzle are completely aligned. The first point of the 3-point method defines the origin of the base coordinate system. This point is chosen to be in the middle of the build plate. The second and third point define the positive x- and y-direction respectively. The KRC unit is able to identify the location and orientation of the base coordinate system by these three points.

With the purpose to increase the dimensional quality and neglect thermal effects, teaching of the KUKA robot is being done in heated state of the nozzle and build plate.

5

Pre-Trial Printing

After setting up a tool which generates a print path for the KUKA robot, several geometries are being printed. This chapter contains the main findings and problems encountered during the pre-trial printing. Based on these results, changes and implementations may apply to the experimental set-up which in the end are supposed to result in a robust print process.

5.1. Results of Pre-printing Trials

Different samples consisting of multiple node geometries, as shown in Figure 5.1.1, are printed. It is observed that not more than three to four layers can be printed without failure, which is about 0.6 to 0.8mm in total thickness.

(a) Pre-trial sample examples

(b) Closer look at a radius section

Figure 5.1.1: Results from the pre-trial prints

By analysing the failed samples and nozzle, it is being observed that buckling and warpage in the radius areas, an overall rough outer surface with pultruding fibers and a non-continuous movement of the KUKA robot are taking place. This behaviour becomes worse over time and eventually cause failure.

5.1.1. Twist and Warping

A closer look onto the samples can be seen in Figure 5.1.2. In part (b), which represents a radius area, the filament tends to twist and warp. The light reflection indicates that there exists a local thickness increase. Because the current state of the print head does not have a damping system, meaning there is no margin for an increase in thickness, this local twisting and warping results in the nozzle to run into previously deposited material. Potential effects that may occur are a fiber shear off, followed by a clogged nozzle or a complete

dragging of the build plate. These effects do not only fail the print, but can also damage the set-up.

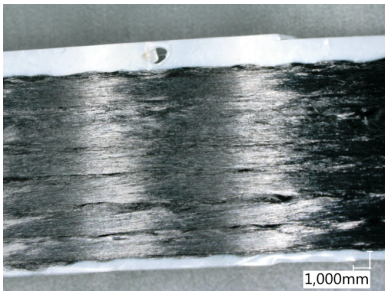

(a) Straight section, without twist or warpage

(b) Radius area with local thickness increase due to twisting and warpage of the filament

(c) Example of the top section where the nozzle runs into previously deposited material

Figure 5.1.2: Example geometry with typical failure behaviour

Such behaviour is not applicable to a robust process. Therefore these critical areas are being analysed thoroughly from which an explanation is found based on two elements. The first being the behaviour of the filament itself and the second by the shape and design of the nozzle.

Filament behaviour

The CF-PPS prepreg filament has a circular cross-section when entering the print head. During printing, the filament is pressed into a quasi-rectangular shape and placed on the build plate or fused to the previous layer. When the print head follows a curved pattern, the inner area of this quasi-rectangular shape will travel less distance than its counterpart on the outer area. The thermoplastic material is above its melt temperature, so mobility of the polymer chains will not be restricted. The problem arises with the inclusion of a continuous reinforcement, which keeps its solid state during printing. When printing a curvature, the reinforcement will endure a stress level, in compression and tension for inner and outer area respectively. This has as a consequence that the inner area tends to buckle and the outer area tends to move inward. When printing multiple lines next to each other, this behaviour results in a stepwise change of local thickness increase and empty spots.

As a remark, the CF-PPS filament is not being dried before printing, but is stored in a closed environment including Silica gel bags. Attempts on drying result in kinking of the filament which makes it not printable. The inclusion of small percentages of moisture in the filament causes defects as bubbles, voids and a more rough outer surface after printing [27]. This can potentially be another explanation for the unwanted behaviour. Therefore more tests need to be performed on the effect of drying the filament before printing, which is recommended for future research.

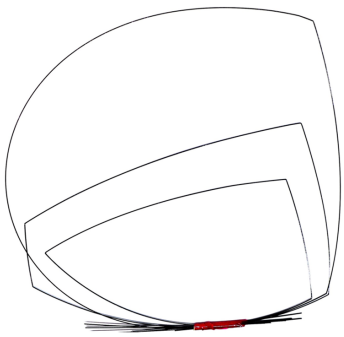

(a) Result of filament twisting

(b) Microscopic image of a twisting area

Figure 5.1.3: Result of dried filament at $80^{\circ}C$ for two hours

The last limitation on the filament is that not all batches are within the tolerance needed for extruding without problems. Several spots along the filament contain a thickness increase, which cause failure in the filament tube, as shown in Figure 5.1.4.(d).

Figure 5.1.4: Failure withing the Nickel-Silver tubes

Figure 5.1.5: Result of a clogged nozzle on the filament

Nozzle geometry

The second reason for twist and warping is due to the geometry of the nozzle. The design of the nozzle is based on providing a smooth transition of the filament from a vertical position at the inlet, to a horizontal position on the build plate. Figure 5.1.6.(b) shows that this is achieved by introducing a concave shape on the exit of the nozzle. The consequence is that a hollow section is formed in which the filament can freely move. Because the print head keeps its orientation during printing and does not rotate along with the print, the filament tends to go inward when printing a radius or curvature. Therefore the path on which the filament will be placed is less than the intended one, see Figure 5.1.6.(c). In addition the feeding unit is programmed in such way that it will feed material based on the travelled distance with respect to the centreline of the nozzle, which means it will over-extrude material when printing a radius area.

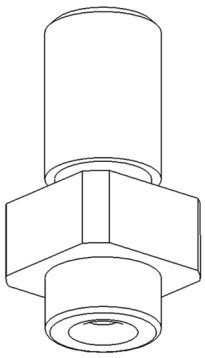

(a) Nozzle 3D geometry

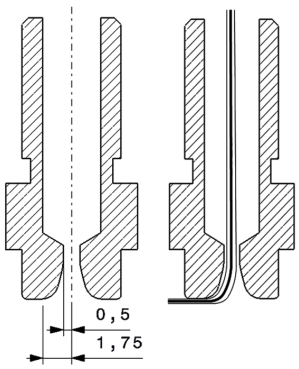

(b) Section view of the nozzle and filament

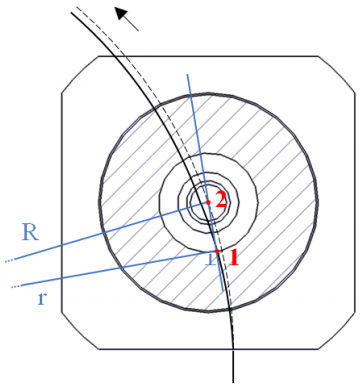

(c) Top view of the intended print path (dashed line) and actual print path (solid line)

Figure 5.1.6: Filament behaviour in curvatures

5.1.2. Surface Roughness

Besides twisting and warping in the curvatures, fiber pultrusions and a fuzzy top surface are identified. Microscopic inspection shows this is due to sheared fibers which are not impregnated and stick out of the specimen. It can be concluded that the reason for this fuzzy outer surface is due to the relative large ironing surface of the nozzle. Once the fiber is printed, the ironing surface presses onto the filament and induces heat to fuse the placed fiber onto the previous layer. Because the print head is not rotating with the motion of the print, the ironing surface will act as a shearing surface on top of the filament, with fiber rupture as a consequence.

5.1.3. Non-continuous Movement

Visual inspection of the motion of the KUKA robot during printing, indicates a non-continuous movement in between the points. The SRC-code resulting from the Print Path Planning tool is programmed using a linear motion with a continuous distance approach between each point. This linear motion allows the print head to keep its orientation with respect to the base coordinate system, as discussed in Chapter 4. The continuous distance approach is set at a level of 0.1, which means that the TCP cannot deviate more than $0.1mm$ from the points. A drawback of this approach is that the KUKA robot tends to slow down or even stop at the points to keep its continuous distance level valid. One possibility to obtain a smooth motion from point-to-point is to increase this continuous distance level. Because the motion of the KUKA robot becomes less accurate using this approach, a different solution is being implemented.

5.2. Changes and Implementations

The above discussed findings and problems encountered are being analysed, for which their corresponding solutions are discussed below.

5.2.1. Extrusion Overwrite

To solve the issue of over-extruding filament in radius areas, Figure 5.1.6 is used to derive the actual print path from the intended print path. By calculating the ratio between both, based on a set print radius, the stepper motor of the feeding unit is programmed to adjust its feeding rate. Figure 5.2.1, which is derived from Figure 5.1.6 (c), contains the geometrical distance between the centre point of the radius area (+), the location at which the filament will be placed (1) and the centre point of the nozzle (2). The ratio between the actual- and intended print path is calculated in Equation 5.1.

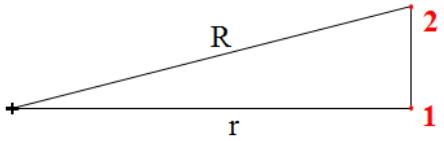

Figure 5.2.1: Validation points on the print head

$$EXOV = \frac{r}{R} = \frac{\sqrt{R^2 - L_{12}^2}}{R} \tag{5.1}$$

Where R is the radius of the intended print path, r the radius of the actual print path and L_{12} the distance between the nozzle centre point and ironing surface, in this case $1.75mm$.

This ratio is implemented as a function in the Mathcad Point Generator and as a command in the KUKA KRC unit, where it is multiplied with the absolute output velocity of the TCP. Before and after each radius, the extrusion overwrite function (EXOV) is set at its intended ratio. An EXOV equal to 1 means a straight section is printed. An example of the integration of this function in a SRC-code can be seen in Figure D.2.1 in Appendix D. In addition, the radius in the Mathcad Point Generator is multiplied with the inverse of the EXOV. This ensures the dimension of the printed radius to be the same as the set radius.
The validation of this function is being done by printing two samples consisting of concentric circles with a smooth change between each line. The samples are printed from outer to inner direction. Visual inspection using Figure 5.2.2 shows the positive effect of including the EXOV-function.

5.2.2. Active Cooling

The Fiber Volume Content (50%) in the filament makes it stiff compared to neat filament, which is not favourable for printing small geometries incorporating sharp radius. During trial printing, it is being noticed that blowing air onto the extrudate decreases the formation of buckling behaviour and allows to print smaller radius. This can be explained by the mobility of the polymer chains, when the thermoplastic material is above its glass transition temperature, the polymer chains are still able to move. When a radius section is printed, the compressive and tensile stress on the inner and outer area of the filament tend to release their stress state and try to go back to their original position, which causes the buckling behaviour. When cooling the thermoplastic material to restrict motion of the polymer chains, the filament is "frozen" and will keep its position. This principle is used as an intermediate solution and is shown in Figure 5.2.3.
Similar to the EXOV-function, the Active Cooling (ACCOOL) only needs to be activated in the radius areas. Therefore the same approach is used as for the EXOV-function, only here not a numeric value is needed, but a string in the form of "TRUE" or "FALSE".

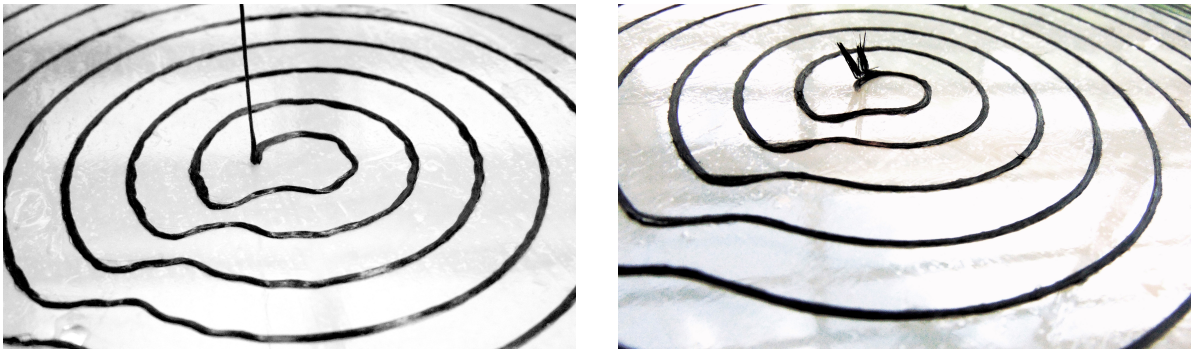

(a) Sample excluding EXOV

(b) Sample including EXOV

Figure 5.2.2: Concentric circular pattern geometry for validation of the EXOV-function

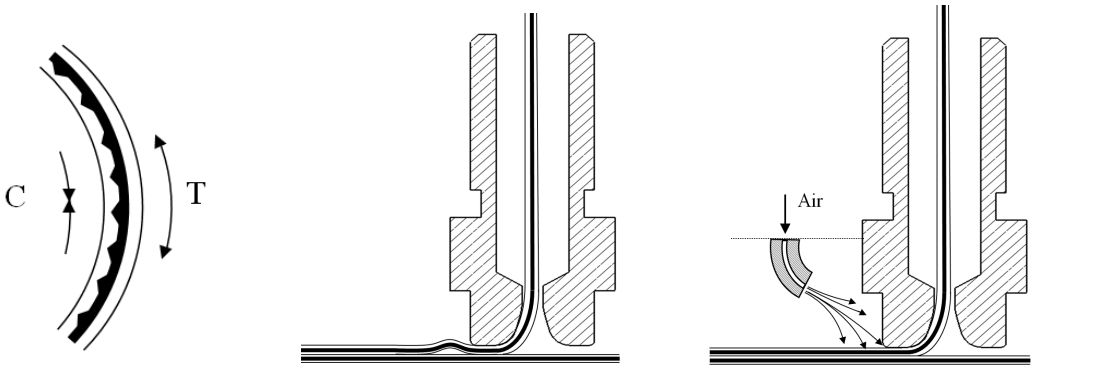

(a) Buckling behaviour due to compression (C) and tension (T) side

(b) Buckling behaviour visible without cooling unit

(c) Sample including ACCOOL, no buckling visible

Figure 5.2.3: Improved quality by inclusion of Active Cooling unit

To integrate the ACCOOL-function in the KUKA KRC unit, the command is programmed on one of the available output ports. Each time the ACCOOL function is called, the port sends an output signal to an electro-pneumatic pressure valve. This valve opens and closes depending on its received signal. To control the amount of air cooling the extrudate, a proportioning valve is used. Figure B.4.1 in Appendix B shows the design of the ACCOOL-device and an example of the integration of this function in a SRC-code can be seen in Figure D.2.1 in Appendix D.

5.2.3. Advance Function

To account for the non-continuous movement between each of the points in the print path, an ADVANCE function is introduced. Within the KUKA software, the ADVANCE variable can be used to define the maximum number of motion instructions that can be calculated and planned in advance [**?**].

The problem that arises is that now all the lines in the SRC-code are being read in advance, meaning the Extrusion Overwrite and Active Cooling function as well. An example code in Figure D.2.1 in Appendix D shows how this is solved. By introducing multiple variable Advance Functions within the SRC-code, a variable equal to 1 will keep the original point, whether a higher level will check the points in advance. By switching in between these advance variables, the points can be chosen to be in advance and the functions at the exact location.

5.2.4. Trade-off Nozzle Geometry

The main cause of the previous discussed problems was identified due to the nozzle geometry. Therefore a trade-off is being performed on four different nozzle geometries. Besides the original, three extra nozzles have been manufactured which differ on the size of their ironing surface and shape of the nozzle exit. Figure 5.2.4 to 5.2.7 show these different geometries with their corresponding print results. The prints consist of a 2-node loop with an inner radius of $10mm$.

Nozzle geometry 1

As a reference, the first loop is printed using the original nozzle. It can be seen that straight sections consist of a smooth outer surface without defects. The radius areas however show twisting and warping as discussed earlier.

(a) Nozzle geometry 1

(b) Print result nozzle 1

Figure 5.2.4: Nozzle trade-off geometry 1

Nozzle geometry 2

The second nozzle geometry consists of a large ironing surface, ensuring more heat will be conducted into the material compared to the original nozzle. This allows the layers to be fused together more efficiently and print speed can be increased. The inner area of the nozzle consists of a straight section, making sure the filament is placed at the centreline of the nozzle. In this manner, the Extrusion Overwrite function does not apply. Print trials show that this nozzle geometry is not capable of producing prints without defects. The filament is sheared off at the first lines due to the non-concave nozzle exit. This direct change in filament orientation from vertical to horizontal position causes the print to fail early.

(a) Nozzle geometry 2

(b) Print result nozzle 2

Figure 5.2.5: Nozzle trade-off geometry 2

Nozzle geometry 3
Nozzle geometry 3 consists of half the ironing surface of nozzle geometry 2 and its exit diameter is slightly increased. This has as a consequence that the heat input into the filament will be less compared to nozzle geometry 2, but the filament has more freedom of movement within the exit to account for the direct change in orientation. The result of this geometry shows good printing capabilities with low aesthetic results. The outer surface of the print shows the same behaviour as for nozzle geometry 1, meaning a fuzzy surface with lots of un-impregnated fibers.

(a) Nozzle geometry 3

(b) Print result nozzle 3

Figure 5.2.6: Nozzle trade-off geometry 3

Nozzle geometry 4
The last nozzle geometry is similar to nozzle geometry 1, with a smaller ironing surface and a less concave inner section. Printing using this nozzle shows no defects, fuzziness and warpage.

(a) Nozzle geometry 4

(b) Print result nozzle 4

Figure 5.2.7: Nozzle trade-off geometry 4

From these results, it can be concluded that a large ironing surface enhances the fusion between the layers as more heat is conducted into the material. On the other hand, the current set-up is based on a statically oriented print head, which does not rotate around the nozzle centreline. This set-up introduces shearing between the ironing surface and previously deposited lines and layers which results in a fuzzy outer surface. Keeping the ironing surface small will mitigate this behaviour.

The inner area of the nozzle determines the dimensional accuracy of the print path as a bigger concave shape allows the filament to be placed within an offset from the centreline. The ideal case is a nozzle inner diameter a little bigger than the filament diameter, to allow for smooth passage. The concave shape needs to be kept small in order to decrease the size of the hollow section and restrict the filament from freely moving within the nozzle. However, it needs to be large enough to not shear the fiber. The optimum geometry is not yet

found, but out of the tested geometries, nozzle geometry 4 has a nozzle inner diameter closest to the filament diameter, the smallest ironing surface and a concave shaped nozzle exit. Therefore this nozzle is used in next print trials. Several print results using nozzle geometry 4 can be seen in Figure 5.2.8.

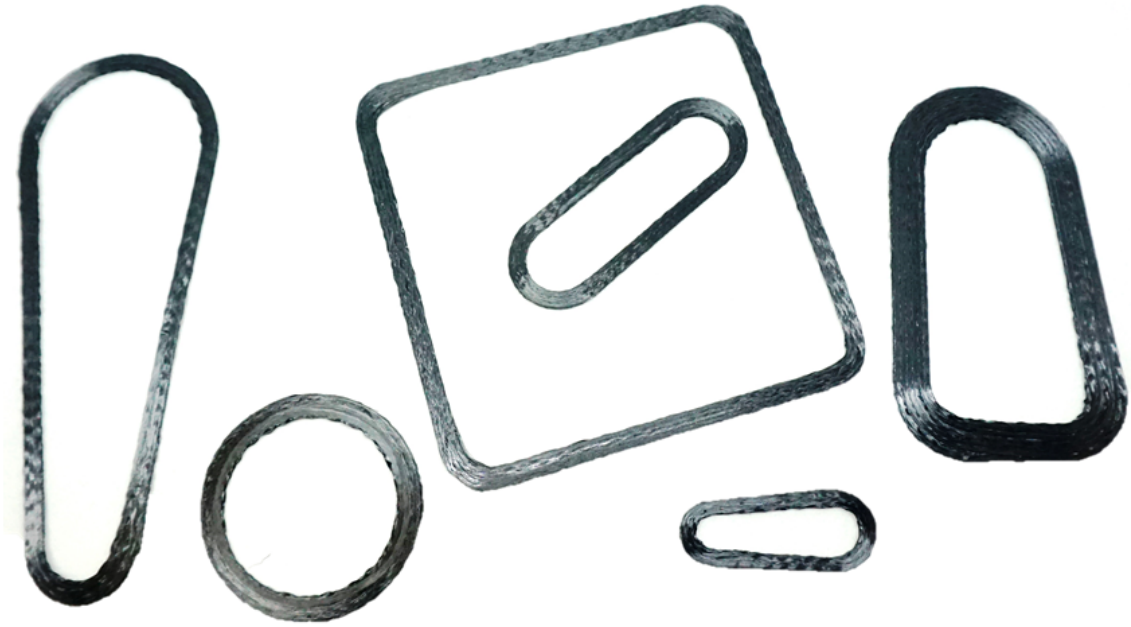

Figure 5.2.8: Examples of the final result of the pre-trial samples

At this point it is decided that the robustness of the printing process is optimized in such amount that the next step in the optimisation process can be performed. This next step consists of the optimisation of the material on microscopic level and is being done by performing an optimisation on the printer parameter settings, which is discussed in the next chapter.

6

Design of Experiments

In previous chapters it is explained how the functionality of the print head is optimized until a robust print process. In addition, there are several factors which do have an influence on the material properties on microscopic level. Because testing and analysing these factors in a random manner will be time consuming, first the set of parameters is being reduced to only the key influencing parameters. Using these parameters, a Design of Experiments (DoE) approach is being selected, for which the boundary levels are determined by simultaneously testing and modelling their behaviour.

6.1. Reduction of Parameters

During previous pre-trial printing, the parameters which have an influence on the quality of the resulting print are assumed to be:

- Temperature build volume
- Temperature build plate
- Temperature nozzle
- Print speed nozzle
- Rotational speed feed unit
- Layer height
- Hatch spacing or line width

The number of experimental tests needed increases rapidly with an increase of parameters in the Design of Experiments [2]. Therefore the choice is being made to make the DoE more efficient in terms of costs and time, by considering only the key influencing parameters. As already discussed in Chapter 3, the print speed and rotational speed of the feeding unit are synchronized, so the rotational speed can be neglected. Another assumption that can be made is the mass flow on the inlet of the nozzle equals the mass flow on the outlet. The effect of this assumption is that layer height and line width can be coupled to the input value of the filament diameter. It is assumed that the filament is pressed from a circular cross-section into a rectangular shape, assuming zero void content in between the layers and lines. This results in a line width in function of the layer height as shown in Figure 6.1.1 and Equation 6.1.

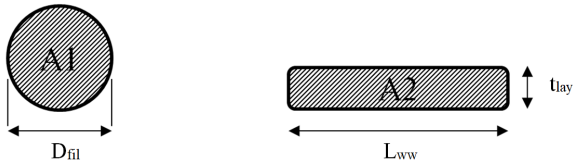

Figure 6.1.1: Cross-sectional area of the filament and extrudate respectively

$$A_1 = A_2 \Leftrightarrow \frac{\pi D_{fil}^2}{4} = L_{ww} t_{lay} \tag{6.1}$$

$$L_{ww}(t_{lay}) = \frac{\pi D_{fil}^2}{4 t_{lay}} \tag{6.2}$$

Where L_{ww} equals the hatch spacing or line width, D_{fil} is the diameter of the filament and t_{lay} is the layer thickness. As the layer thickness can be controlled more accurately than the line width, layer thickness is chosen as process parameter.

In such manner a reduction of two process parameters is obtained and the key influencing process parameters can be defined as:

1. Temperature of the build volume
2. Temperature of the build plate
3. Temperature of the nozzle
4. Print speed of the nozzle
5. Layer height

Because the function of the controlled build volume and build plate is to decrease thermal stresses in the printed material, these are chosen to be kept constant. Therefore the DoE is being performed using three variables, which are the temperature of the nozzle, print speed and layer height. Based on these three variables, a DoE technique is being chosen and explained below.

6.2. Trade-off DoE Technique

Based on the three parameters and taking into account the efficiency of performing the experiments, it is decided to use a three level DoE technique, meaning each parameters has three different parameter settings. Resulting from the Literature study, the DoE techniques shown in Table 6.2.1 are considered feasible [8]:

Table 6.2.1: Sample size DoE techniques [8]

	Full Factorial	**Box-Behnken**	**Central Composites**
Sample Size	27	13	15

In order to improve the efficiency of a test program, for example reduce time for experimenting, the Full Factorial approach, seen in Figure 6.2.1 is neglected as its sample size is too large. The Box-Behnken and Central Composites Design (CCD) have a smaller sample size and their coverage of the design space differ. The Box-Behnken design does not include the corners of the design space, as can be seen in Figure 6.2.2 and therefore does not explore the full capabilities of the parameter boundaries. Because this optimization is a first iteration, it is of interest to investigate the extreme conditions as well. Therefore the decision is made to use the face centered Central Composites Design, shown in Figure 6.2.3.

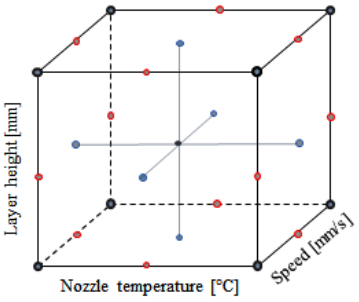

Figure 6.2.1: Full factorial design

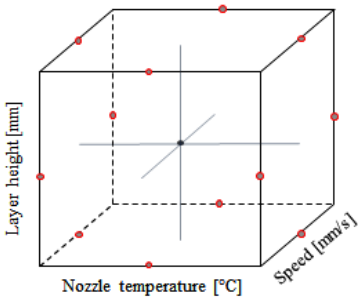

Figure 6.2.2: Box-Behnken design

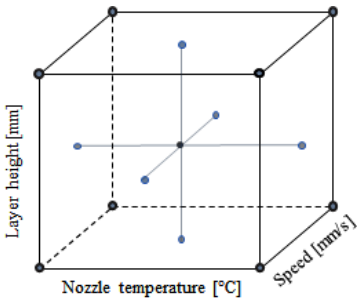

Figure 6.2.3: Central Composites Design

6.3. Determining DoE Boundaries

One approach of selecting the boundaries for the DoE is by experimentally testing the parameter range until their limit is reached. This approach is however time consuming and is only valid for that specific material of use. Therefore, a different method is proposed which makes use of simulating the concrete parameters. By performing a steady-state thermal analysis using ANSYS Mechanical, the temperature distribution of the nozzle is obtained. This temperature distribution is then used to simulate the melt flow of the filament trough the filament tube and obtain the resulting temperature at the end of the nozzle. By selecting a minimum temperature needed, the print speed can be adapted and the optimum conditions selected. The steps taken are shown in the flowchart in Figure 6.3.1 and discussed in detail below.

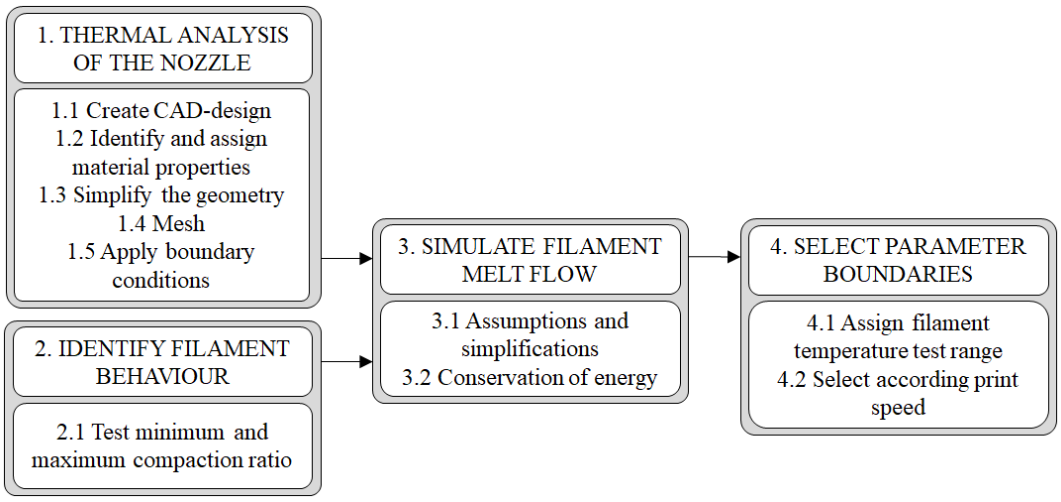

Figure 6.3.1: Steps to determine the parameter boundaries

6.3.1. Thermal Analysis of the Nozzle

Create CAD-design

Firstly, a three dimensional model of the print head needs to be created. This can be done within ANSYS Mechanical or another default program. In this case CATIA V5 is used. Because the print head consists of a geometry in which several elements are not of interest and will only increase the computational effort required, only the sections close to the nozzle are chosen to be used in the analysis. The components of the print unit are shown in Figure 6.3.3.

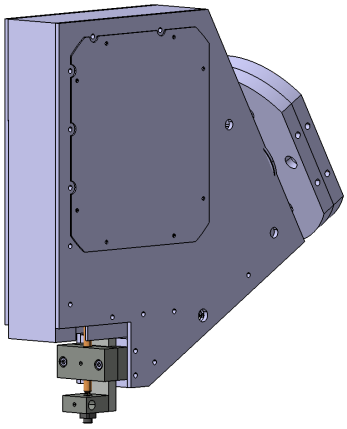

Figure 6.3.2: CAD-model of the print head

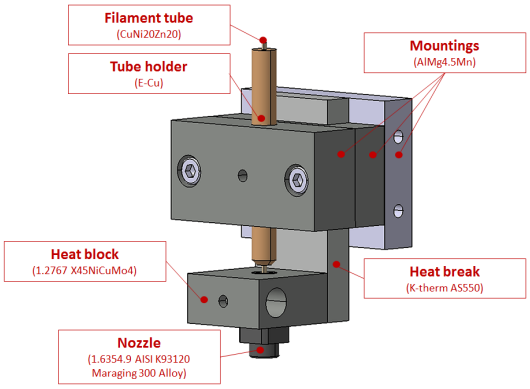

Figure 6.3.3: CAD-model of the print unit

Identify and assign material properties

The next step is to identify the material properties for the filament and print head components. Both are received from their manufacturer. Figure 6.3.3 provides the material of each component of the print head. The material properties for both are given in Table A.1.1 and A.1.2 in Appendix A.

Simplify the geometry

The print head consists of small geometric features which are not important for the overall analysis. The removal of these small features, for example fillets and holes, allows for a simpler geometry which will reduce the computational effort needed. This step is shown in Figure 6.3.4.(a).
This first hypothesis can be extended by supposing planar symmetry of the print head with regard to a central plane which runs trough the centreline of the nozzle. This is shown in Figure 6.3.4.(b).
Next the print head is enclosed by air. This allows heat to be transferred by conduction trough the material and convection trough the air. Figure 6.3.4.(c) shows two enclosures, one for the conditioned manufacturing hall, the other for the controlled build volume.

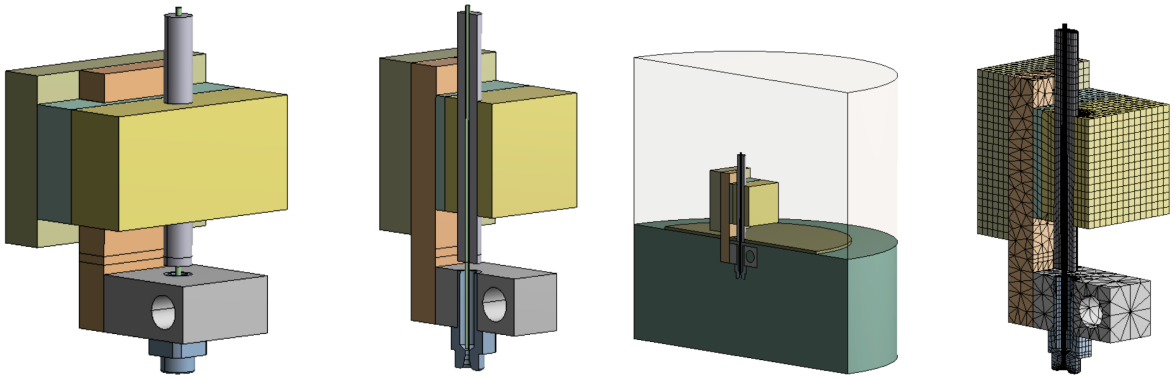

(a) Removed geometric features (b) Model symmetry (c) Air enclosure (d) Mesh

Figure 6.3.4: Ansys model set-up

Mesh

After the geometry is simplified, a meshing strategy is performed. Firstly coincident faces and edges are being detected and imprinted to allow for mesh connections. Afterwards, different meshing strategies as sweeping and edge sizing are being performed onto the clean geometries. Hexahedral elements are preferred over tetrahedral elements as they result in a reduced run time and better accuracy [21].

Apply boundary conditions

The thermal boundary conditions acting on the print unit consist of the heat input due to the heating element and the heat convection of the enclosure. The temperature of the heating element is applied inside the cylindrical cavity as a constant surface temperature. The enclosure is split up in a hot- and cold section and both are assumed to have a film coefficient of 5 W/m^2K. In addition, a conductive boundary condition has been applied on the top enclosure, to simulate the cold enclosure is of infinite size. These boundary conditions with their corresponding location on the print unit are shown in Figure 6.3.5.

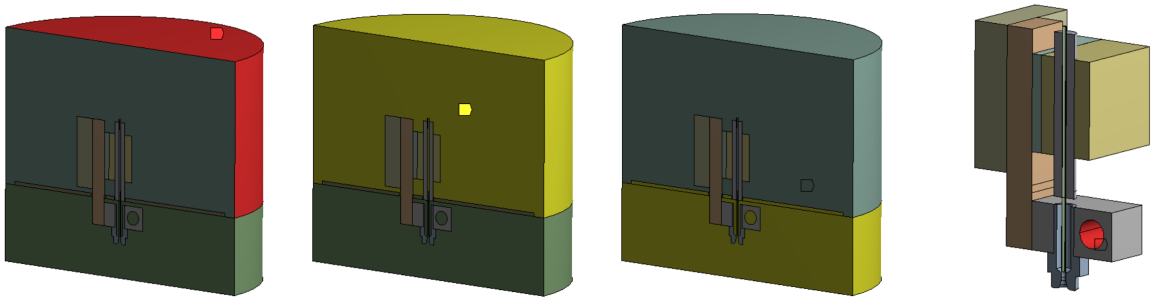

(a) Conduction cold (b) Convection cold (c) Convection hot (d) Heat unit

Figure 6.3.5: Thermal boundary conditions

Obtain filament tube temperature distribution

By performing the steady-state thermal analysis, the temperature distribution along the print unit is being obtained as shown in Figure 6.3.6. The overall data of the print unit is not of importance. Because the filament only runs trough the filament tube and nozzle, the inner surface of the filament tube is being selected as output parameter, which can be seen in Figure 6.3.7.

The output of this thermal analysis consists of a csv-file containing the temperature at each element along the length of the filament tube with its corresponding location.

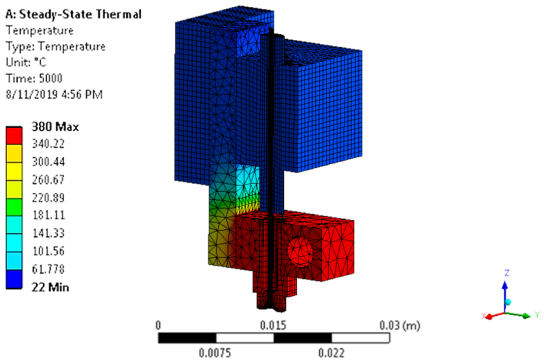

Figure 6.3.6: Temperature distribution of the print head, nozzle temperature of 380°C

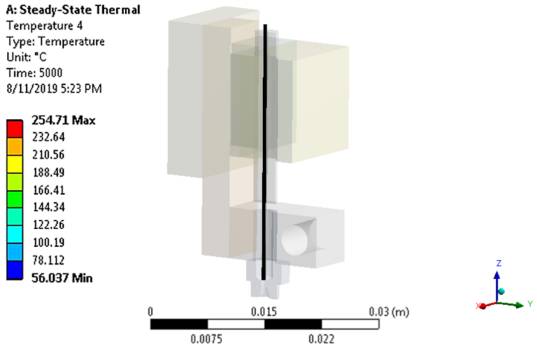

Figure 6.3.7: Temperature distribution of the tube inner surface, nozzle temperature of 380°C

6.3.2. Identify Filament Behaviour

When simulating the filament melt flow, it can be assumed that the layer thickness will have a big influence on the amount of heat being conducted trough its thickness. Since the limitations of the layer height cannot be modelled easily, the choice is made to test this parameter experimentally.

With the fact that the filament consists of 50% FVC, the adhesion between the printed line and previous layers or build plate will not be as efficient as for neat polymer filament. The main reason is that a reinforcement increases the viscosity and therefore changes the surface characteristics [15]. In addition, the continuous reinforcement can break with the application of too much pressure. In order to determine the two outer boundaries, which are filament shear-off and the point of adhesion, the print unit is moved towards the build plate in a stepwise sequence during printing. After several tests, the compaction ratio, defined as the ratio between the filament diameter and layer thickness, resulted in 4.33 and 2.6 and correspond to a layer thickness of 0.15 mm and 0.25 mm respectively.

6.3.3. Simulate Filament Melt Flow

The approach to calculate the temperature increase of the filament running trough the filament tube is based on heat transfer in pipes [32]. Because a composite filament is of use, additional assumptions are made which simplify the calculations.

1. Due to the inclusion of a continuous reinforcement, the flow is assumed to be laminar and fully developed
2. The filament is considered as a solid in which phase-change is neglected
3. The fluid is considered incompressible
4. Heat transfer in axial direction is neglected
5. The tube is of finite length

The next step is to calculate the heat input into the filament which causes a temperature increase. Because the temperature of the filament tube changes along its length L, the tube is being divided into multiple smaller elements of length dx in which the temperature is assumed to be constant. Within each sub-element, the conservation of energy needs to be satisfied. This means that the amount of energy going into the system equals the amount of energy going out, or:

$$\dot{m}\, C_p\, T_m + h\, A(T_s - T_m) = \dot{m}\, C_p (T_m + dT_m) \tag{6.3}$$

Where C_p is the heat capacity of the fluid, T_m is the the temperature of the filament melt flow, h represents the heat transfer coefficient of the fluid, $\dot{m}$ the mass flow rate, A equals the area of the interface between tube and filament flow, in this case the inner surface of the tube and lastly T_s equals the temperature of the tube.

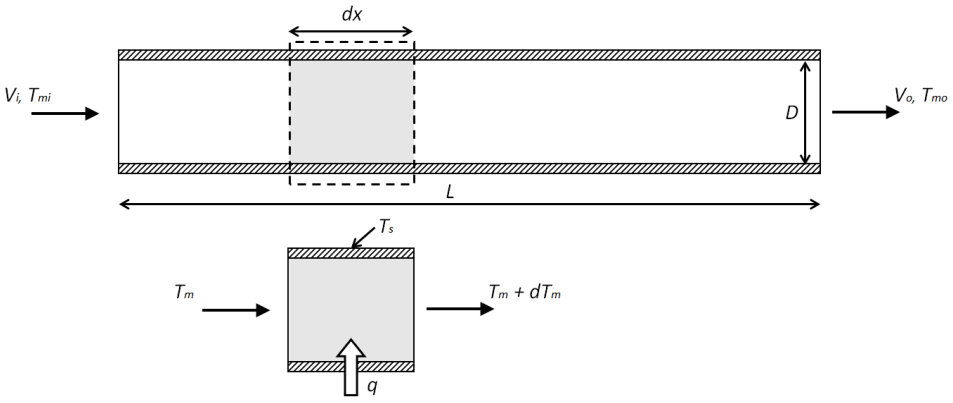

Figure 6.3.8: Representation filament tube with sub-element

Rearranging and simplifying leads to:

$$h\,A(T_s - T_m) = \dot{m}\,C_p\,dT_m \tag{6.4}$$

Note that $(T_s - T_m)$ is only valid locally as T_m is not a constant.

$$-\frac{h\,A}{\dot{m}\,C_p} = \frac{dT_m}{(T_m - T_s)} \tag{6.5}$$

The area of the inner tube can be written in function of the perimeter P and distance dx. Therefore Equation 6.5 can be integrated over its length:

$$-\int_0^x \frac{h\,P}{\dot{m}\,C_p}dx = \int_{T_{m,i}}^{T_m(x)} \frac{1}{(T_m - T_s)}dT_m \tag{6.6}$$

Where A is the area of the inside tube which equals the perimeter times dx.

$$ln\left(\frac{T_m(x) - T_s}{T_{m,i} - T_s}\right) = -\frac{P\,\bar{h_p}}{\dot{m}\,C_p}\,x \qquad \Rightarrow \qquad \frac{T_m(x) - T_s}{T_{m,i} - T_s} = exp\left(-\frac{P\,\bar{h_p}}{\dot{m}\,C_p}\,x\right) \tag{6.7}$$

$\bar{h_p}$ is the averaged heat transfer coefficient of the pipe between 0 and x and can be written in function of the hydraulic diameter of the fluid (D_{hyd}), the thermal conductivity of the fluid (k_{fl}) and the Nusselt Number (N_{UD}):

$$\bar{h_p} = \frac{k_{fl}\,N_{UD}}{D_{hyd}} \tag{6.8}$$

Setting $x = L$ in Equation 6.7, the mean temperature of the fluid at the output can be estimated as:

$$T_{mo} = \left[(T_{mi} - T_s)\,exp\left(-\frac{4\,k_{fl}\,N_{UD}\,L}{\rho\,U_z\,C_p\,D_{hyd}^2}\right)\right] + T_s \tag{6.9}$$

Equation 6.9 is valid for a pipe with constant wall temperature, constant print speed (U_z) and length L. As the tube used in the print head has an increasing wall temperature towards the end, the tube is being discretised along its length into smaller tubes. It is assumed that these smaller tubes have a constant wall temperature equal to the average between 2 following nodes.

In addition, the ironing surface of the nozzle adds a certain amount of heat to the filament. This is being modelled by two flat plates, one representing the compressed filament, the other the ironing surface. Because

the nozzle has a constant ironing surface temperature, the same approach as for the filament tube is being used.
By defining the nozzle temperature T_N, layer thickness t_{lay} and line width L_{ww} of the printed line, Equation 6.7 is changed with respect to an ironing surface of length L_{iron}.

$$\frac{T_{mf} - T_N}{T_{mo} - T_N} = exp\left(- \frac{L_{ww}\, h\, L_{iron}}{\dot{m}\, C_p} \right) \tag{6.10}$$

Where h represents the heat transfer coefficient, defined as the CF-PPS filament conductivity divided by the layer thickness. The final output temperature after the ironing surface can therefore be written as:

$$T_{mf} = \left[(T_{mo} - T_N)\, exp\left(- \frac{L_{ww}\, h\, L_{iron}}{\dot{m}\, C_p} \right) \right] + T_N \tag{6.11}$$

6.3.4. Select Parameter Boundaries

Assign filament temperature test range

In the above simulation, the nozzle temperature and layer height are both variables. In order to select the print speed at which the filament exits the nozzle in molten state, the boundaries of the nozzle temperature need to be selected. These are being based on reference data and the capabilities of the current set-up. For the lower boundary, suggested print temperatures from commercially available PPS filament are being used and result in $340°C$ [14]. The maximum boundary is determined by testing the maximum capable temperature of the current set-up. This value is set at $380°C$. This temperature setting is still below the decomposition temperature of PPS, which occurs above $400°C$ [14].

Select according print speed

Using these boundary levels, the steady-state thermal analysis and melt flow simulation are being performed. From the filament manufacturer it is known that neat PPS has a melt temperature of $285°C$. By considering the extreme condition, which is the result of highest layer thickness, lowest nozzle temperature and highest print speed, the upper boundary for print speed is determined. Figure 6.3.9 shows this temperature distribution, from which it can be concluded that a print speed of $6mm/s$ corresponds to the maximum print speed at which the filament is still above its melt temperature.

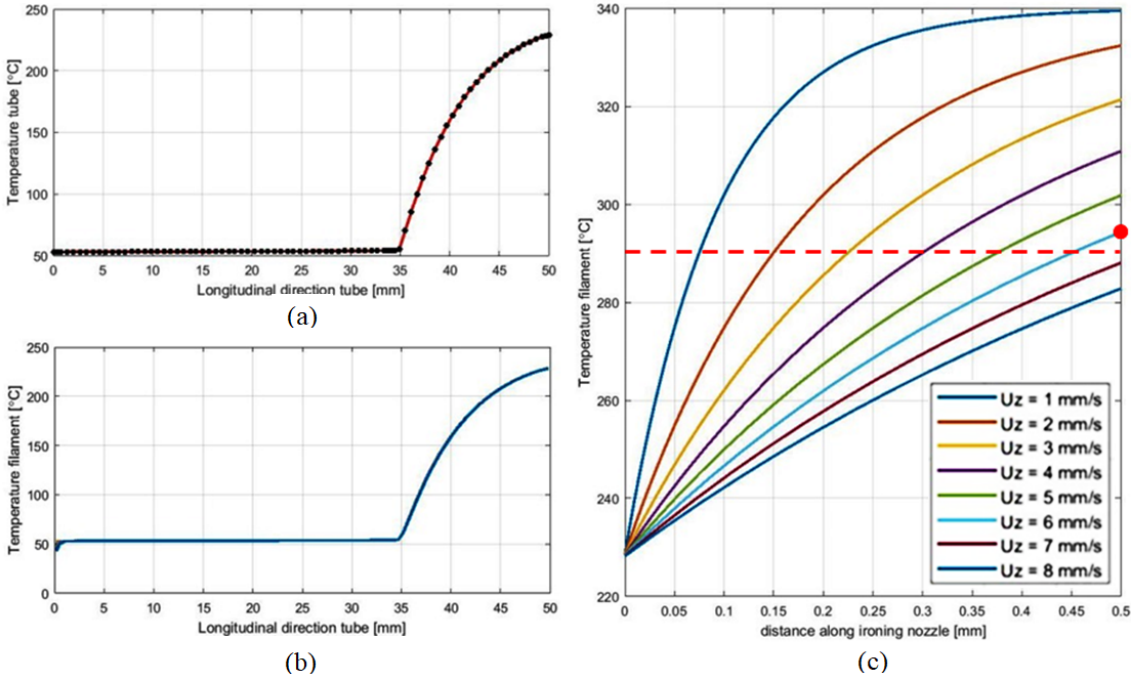

Figure 6.3.9: Filament melt flow, (a) temperature distribution along the tube, output from Ansys, (b) temperature of the filament along the tube, (c) temperature of the filament along the ironing surface, the red dashed line represents the minimum extrusion temperature and the red dot represents the maximum print speed setting

To have redundant temperature settings and be sure the filament is in molten state when leaving the ironing surface, the limit for the print speed is taken at $6mm/s$. In addition, the choice is made to investigate the behaviour of the print and its corresponding quality when the fusing time is elongated. Therefore $2mm/s$ is chosen as lower boundary.

Since a three-level DoE is of use, the middle parameter settings is taken as the average of minimum and maximum values. The final parameter settings used within the DoE are therefore:

Table 6.3.1: Final parameter settings

	Layer Height $[mm]$	**Nozzle Temperature** $[^\circ C]$	**Print Speed** $[mm/s]$
Min	0.15	340	2
Mid	0.20	360	4
Max	0.25	380	6

6.3.5. Validation Thermal Analysis

The validation of the steady-state thermal model is done by measuring the temperature distribution of the nozzle unit using an infrared (IR) camera, an Optris PI 640. The set-up can be seen in Figure E.1.1 in Appendix E.1.

Before the measurement, the components of interest are being covered with Tooltec® CS5 tape. The reason for this is that metallic components tend to have highly reflective surfaces which have a low absorptivity. During an infrared measurement, the camera uses the amount of radiation emitted by a body to determine the temperature of the object. As metal surfaces emit energy inefficiently, the infrared camera cannot measure its temperature accurately. In addition, these surfaces are influenced by their surrounding bodies by parasitic reflection, which is neglected when the surface is dimmed using a non-reflective material [16].

Because Tooltec® CS5 tape is not designed to be used as material within infrared measurements, the error in the measurement is measured by checking the temperature difference on a metal and ceramic surface, before and after removing the tape. Appendix E.1 shows the result of this validation, from which it can be concluded

that the effect of Tooltec® CS5 tape on the temperature measurement is negligible.

Figure 6.3.10 and 6.3.11 show an example of a temperature setting resulting from simulation and IR measurement respectively. The corresponding locations 1 to 6 are being compared for which their differences are shown in Figure 6.3.13.

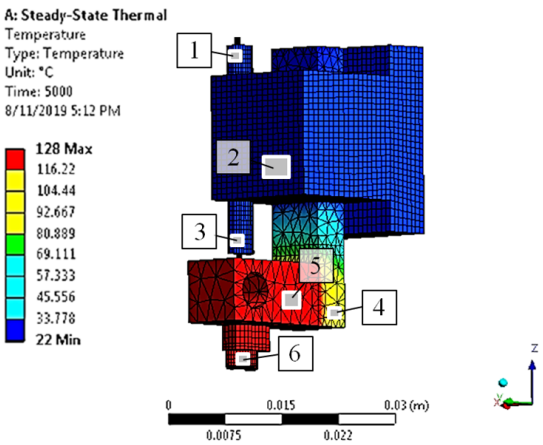

Figure 6.3.10: Simulated temperature distribution of the print head, nozzle temperature of 130 °C

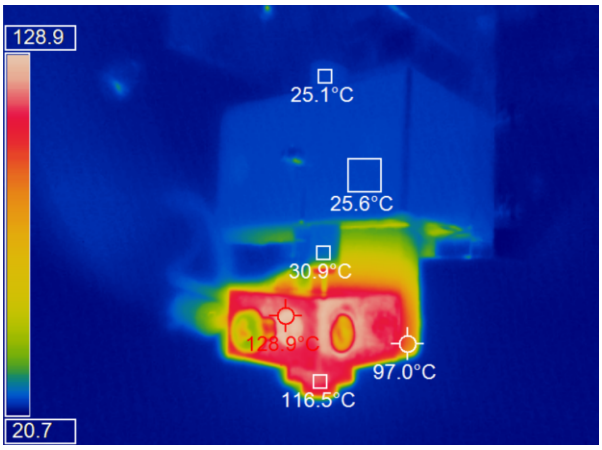

Figure 6.3.11: Measured temperature distribution of the print head, nozzle temperature of 130 °C

The slope of the graph in Figure 6.3.12 suggests the difference between temperature setting at the thermostat and actual temperature of the nozzle, increases with increasing temperature. An explanation for this effect is assumed to be inaccurate elongation of the thermocouple wiring. However, this interaction provides an accurate relation between both setting and result and is therefore used in further research as a guideline between temperature setting and actual temperature at the nozzle.

The nozzle temperature is varied between 50°C and 300°C in steps of 50°C. Based on the interaction curve of Figure 6.3.12, the corresponding temperature settings are chosen.

The results of both simulation and IR measurement are shown in Table E.2.1, E.2.2 and E.2.3 in Appendix E. When comparing both results, the relative error between measurement and simulation reduces when getting closer to the end of the nozzle, which is shown in Figure 6.3.13. The reason for this behaviour can be explained by the location closer to the heat source and therefore less chances on influences from inaccurate data and assumptions on material properties exist. Another explanation is due to the steady-state condition which is not reached for the top part of the print head. As the heat travels trough convection and conduction, but rather slowly, the test need to be performed for longer periods of time to obtain more accurate results.

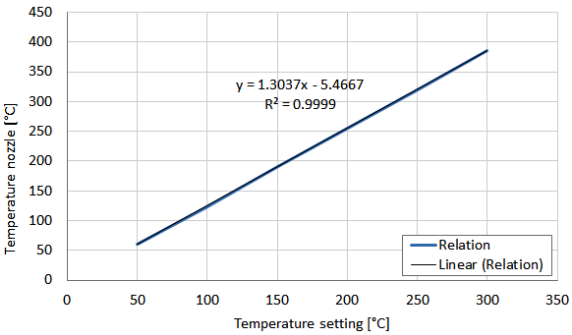

Figure 6.3.12: Relation between temperature of the nozzle and temperature setting

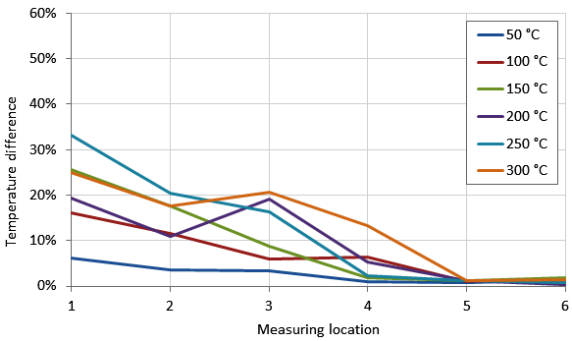

Figure 6.3.13: Temperature difference in percentage between the outcome from the thermal analysis and actual measured temperature at each measuring point from Figure 6.3.10

The estimation of the temperature distribution becomes more critical closer to the nozzle, as the end of the filament tube and ironing surface of the nozzle mainly determine the temperature of the filament exiting the nozzle. For the purpose of this simulation, which is determining the boundary values for the parameter settings, the results are determined to be valid to be used. Appendix E.1 provides the measured and simulated data.

The strategy to validate the filament melt flow consist of overprinting of a thermocouple to measure the temperature of the extrudate. Because the thermocouple has a delay in its response, this measurement will not result in an accurate validation. For this reason, several verification strategies are being performed to inspect and test the validity of the model.

- Filament temperature should reach the nozzle temperature towards infinity
- The filament temperature at zero print speed should equal the nozzle temperature at the beginning of the tube
- The filament temperature at infinite print speed should equal room temperature at the end of the tube

7

Specimen Preparation and Testing

The obtained parameter settings from previous chapter are added to the DoE, randomized and printed. Resulting from the Literature Study Report, the response criteria which determine the quality of the print are chosen to be the inter-laminar shear strength and void content [8]. After printing, a third criteria is being added, which is the robustness of the parameter settings. For these three criteria, the printed samples are cut, prepared and tested.

7.1. Fabrication of Specimen

The specimen used for analysing the print quality are created by first printing them according to different parameter settings, cutting with respect to the desired dimensions and post-treatment depending on their planned test method.

7.1.1. Printing

Table 7.1.1 shows the run order of the experiments with the corresponding parameter settings in codified and absolute values and are the result of the face centered Central Composites Design. It can be seen that the standard order is randomized, which is done to decrease the effect of uncontrollable conditions or user mistakes.

Table 7.1.1: DoE order with corresponding parameter settings

StdOrder	**RunOrder**	**X1**	**X2**	**X3**	**Layer height [*mm*]**	**Print speed [*mm/s*]**	**Nozzle temperature [°*C*]**
6	1	1	0	1	0.25	2	380
13	2	0	1	-1	0.20	4	340
4	3	1	-1	-1	0.25	6	340
10	4	1	1	0	0.25	4	360
7	5	-1	-1	1	0.15	6	380
14	6	0	-1	1	0.20	4	380
12	7	0	-1	0	0.20	6	360
9	8	-1	0	0	0.15	4	360
8	9	1	0	1	0.25	6	380
15	10	0	1	0	0.20	4	360
1	11	-1	0	-1	0.15	2	340
11	12	0	-1	0	0.20	2	360
5	13	-1	0	1	0.15	2	380
3	14	-1	1	-1	0.15	6	340
2	15	1	1	-1	0.25	2	340

According to the above parameter settings, the samples are printed. The geometry used for these prints is shown in Figure 7.1.1 and is being determined by the need for a transition area (1) at a straight section, straight sections to cut out the specimen (2, 3), keeping print radius large to increase the robustness and an check for the optimum combination which produces the least amount of waste material and with the largest number of specimen. Four specimen are obtained from one single sample. It is however suggested to use at least 5 specimen, but considering the available material and efficiency to print all the samples, it is chosen not to enlarge the size. All the printed samples are shown in Appendix E.

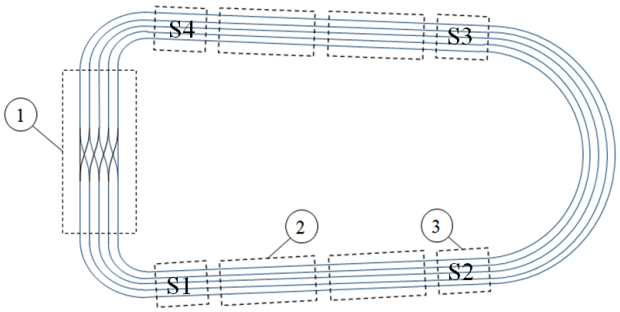

(1) Transition area
(2) ILSS specimen:
$Lxbxh = 20 \pm 0.25x10 \pm 0.2x2 \pm 0.2mm$
(3) Void content specimen:
$Lxbxh = 10x10x2mm$

Figure 7.1.1: Geometry of the DoE samples

7.1.2. Preparation and Test Methods

Depending on the test method, the samples are being cut to the correct size. Cutting is done using a water-cooled high-precision saw. This allows the specimen to be cut within the tolerances set by the DIN EN 2563 standards. The water cooling makes sure the polymer does not melt, so that the results are not influenced by this process. Each specimen is marked in such way that its location and orientation in the original sample can be easily retrieved during analysis.

ILSS specimen

After cutting, the specimen for the inter-laminar shear strength test are being conditioned for 24 hours. Before testing, the dimensions are measured and stored for post-analysis, in order to determine the stress from the obtained loads at break according to Equation 7.1 [10].

Figure 7.1.2: Example of ILSS specimen, bottom and top view respectively

$$\tau = \frac{3}{4}\frac{P_{break}}{wt} \tag{7.1}$$

In Equation 7.1, P_{break} represents the maximum load at the moment of first failure, w is the width and t is the thickness of the specimen.

Out of the mechanical properties applied in the structural design, a critical property for additive manufactured structures is the inter-laminar shear strength of the material [9]. Because unidirectional prints do not contain a reinforcement along the thickness direction of the sample, the inter-laminar shear properties are not supported and mainly depend on the behaviour of the matrix and matrix-fiber interaction. As for FCM, the importance lies within the strength of the interface between each printed layer, the ILSS test will provide information on how the fusion between the printed layers is changing with different parameter settings.

The ILSS tests are being performed according to the DIN EN 2563 standards. A Zwick 1464 testing machine is being used with a load cell of 2.5 kN. The test conditions are under room temperature ($21°C$) and the distance between the support rollers is set at 11 mm. By carefully placing the specimen on the supports and applying a speed of testing of 1 mm/min until failure, the test results are obtained.

Void Content Specimen
The preparation for the void content specimen is done by sorting and placing the specimen in cylindrical moulds surrounded by a fast curing resin. The outer surface of the cured moulds are sanded using increasingly finer sand disks. To obtain a clear surface, polishing using diamond paste is performed as a last step. This result is shown in Figure 7.1.3.

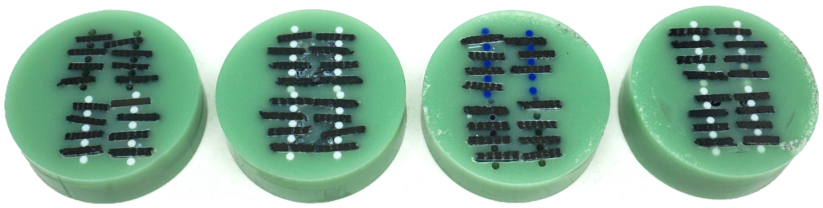

Figure 7.1.3: Embedded specimen for microscopic inspection

Using a Keyence vhx-6000 microscope with VH-Z100UR lens at 100 and 300 times zoom, these embedded specimen are inspected on their cross-sectional area. Analysis on the location and quantity of voids will provide information on the efficiency of the resulting parameter setting.

7.2. Test Results

After preparing the specimen and defining the corresponding test methods, the specimen are being tested. This section provides the results for the additional robustness response, inter-laminar shear strength and void content.

7.2.1. Robustness Parameter Setting

The response of the first criteria is identified during printing. The number of failures are counted for each parameter setting and are shown in Figure 7.2.1. It can be seen that two of the outer parameter settings (Sample 11 and 13) are not feasible to print as they result in failed prints. These results are therefore taken out of the DoE.

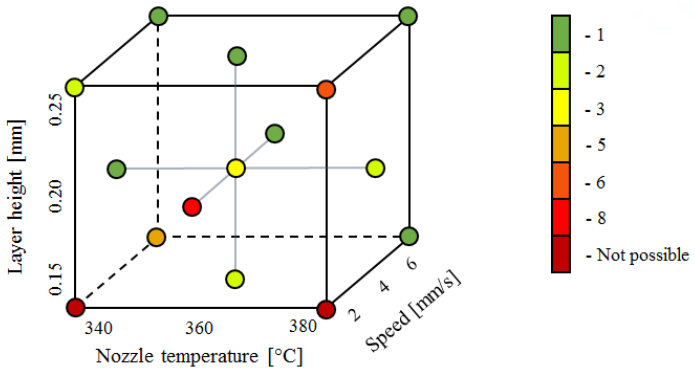

Figure 7.2.1: Visual representation of the number of failures for each parameter setting

The robustness response is loaded in Minitab 2018 based on the number of failures. A failure is being counted when the print process needs to be aborted or the process stops out of itself. The observed failures consist of clogging of the nozzle or filament tube and a detached print line.

7.2.2. Inter-laminar Shear Strength

The results from the ILSS tests are shown in Table G.1.1 and G.1.2 in Appendix G. According to the DIN EN 2563 standards, typical failure modes are single- or multiple shear failure, plastic deformation and flexure failure. With respect to Figure 7.2.2, the failure mode of each specimen is being determined. For plastic deformation, the yield point is taken as stress at break, for shear failure, the point of fracture. An example of the result on their cross-section can be seen in Figure 7.2.3 and 7.2.4.

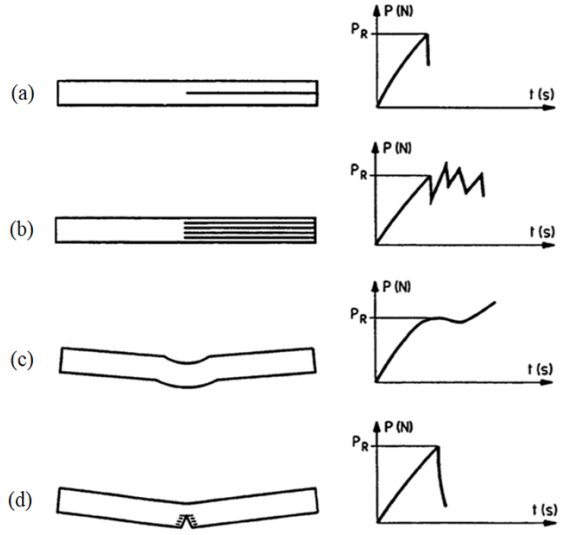

Figure 7.2.2: Possible failure modes resulting from the ILSS test, (a) single shear, (b) multiple shear, (c) plastic deformation and (d) Flexure failure [10]

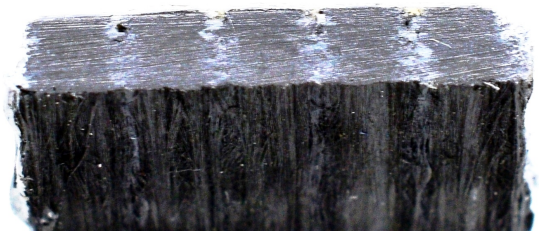

Figure 7.2.3: Cross-sectional view of a plastic deformed specimen

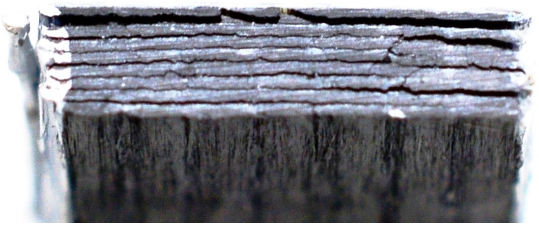

Figure 7.2.4: Cross-sectional view of a specimen in shear failure

From the results of the ILSS test, it can be concluded that not all specimen failed due to shear failure. By analysing the cross-section of the tested specimen, the failure mode which resulted from the load displacement graph as inter-laminar shear failure is in point of fact the result of delamination between the printed layers, or an inter-layer failure. This indicates the specimen have a weak bonding at the interface. In contradiction to the validity of the DIN EN 2563 standards, the preferred failure mode is not shear failure, but plastic deformation as this indicates an strong interface and so a an efficient fusion between the printed layers.
This finding is supported by the data obtained in Figure 7.2.5 and 7.2.6. It is observed that the difference in the obtained stress at break between the shear failure modes and plastic deformation modes is significant. The shear failure modes show a median stress at break of 29.95 MPa, compared to 32.8 MPa for the plastic deformation failure modes. This concludes that indeed the shear failure in the ILSS tests is purely a delamination failure due to inefficient bonding within the interface.

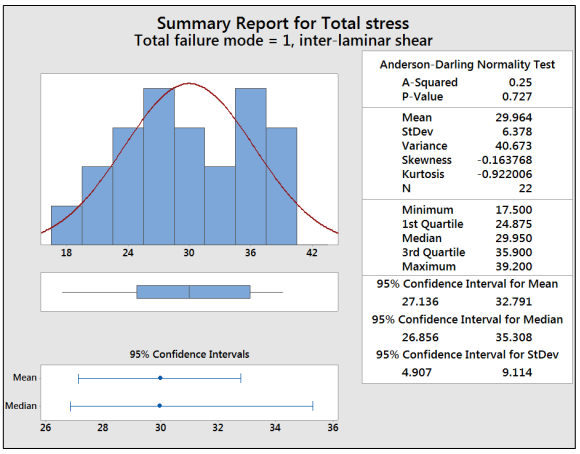

Figure 7.2.5: Stress at break results for the shear- and multiple shear failure mode

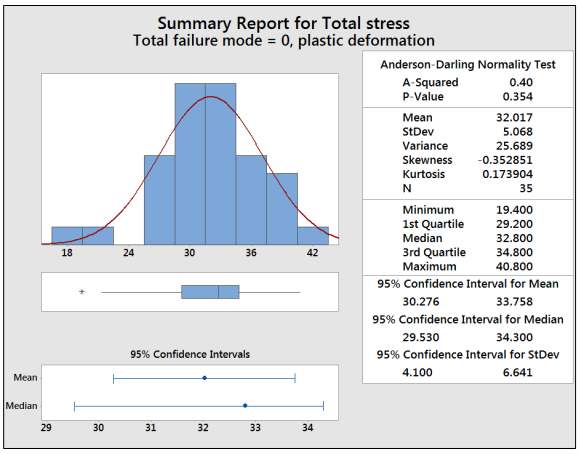

Figure 7.2.6: Stress at break results for the plastic deformation failure mode

Because for thermoplastic composites, a single failure mode during an ILSS test is not common, often multiple failure modes are the result [9]. Therefore additional microscopic inspection needs to be performed on the failed areas to make a solid conclusion about the failure mode. This step is not being performed at the moment, but is presented as recommendation for future work.

7.2.3. Void Content

Microscopic inspection of the cross-sectional areas shows different types of voids. The first, most occurring, is the formation of gaps in between the lines, as can be seen in Figure 7.2.7.(a). This defect is the result of inaccurate line width settings. In the Print Path Planning tool, the line width is calculated from the diameter of the filament and the layer thickness. Because the diameter of the filament varies roughly between 0.60 mm and 0.70 mm. This has as a consequence that the programmed line width from Equation 6.2 varies as well. Because a unidirectional loop with constant width must be filled using parallel lines and layers, the line width and layer height cannot be varied during printing. A first solution proposed, is to take the average between minimum and maximum diameter. This quickly results in a decrease of the robustness as several lines run into each other during printing. Therefore it is chosen to increase the robustness, as this is the most important criteria at the moment and take the maximum diameter as input for the calculation of the corresponding line width.
The same behaviour is observed at prints with poor build plate levelling. The slightest deviation between nozzle and build plate during the 3-point method, results in a difference between setting and actual value of the layer height. This leads to the formation of gaps which disappear along the height of the specimen, as can be seen in Figure 7.2.7.(b).

The second type is identified as voids in between the printed layers. These defects are the result of inefficient bonding and are caused by an extreme combination of parameter settings, moisture in the filament and a rough outer surface of the previous printed layer. An example of such defect can be seen in Figure 7.2.7.(c).

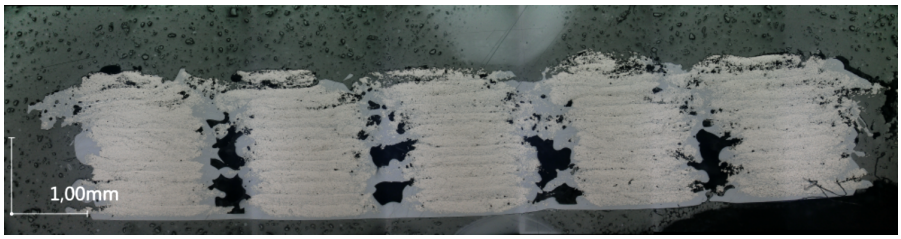

(a) Gap formation in between the printed lines

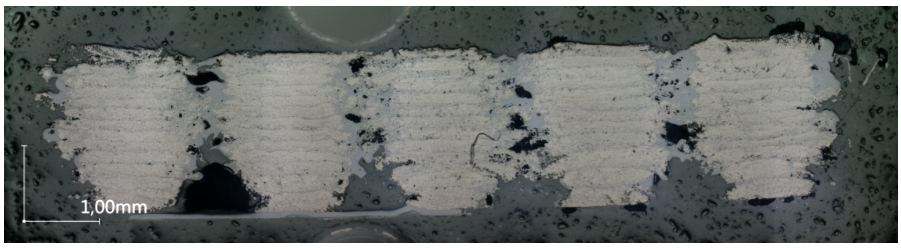

(b) Gap formation on the bottom of the specimen due to poor bed levelling

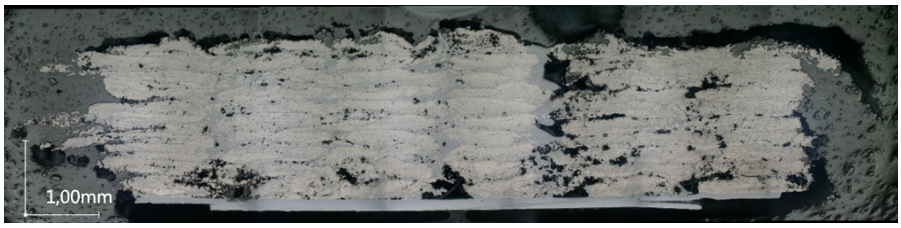

(c) Void formation due to inefficient bonding

Figure 7.2.7: Identified voids in the specimen

In addition, voids are identified within the core of the filament. Microscopic inspection of the filament before printing shows small microvoids to be present, as seen in Figure A.1.2 in Appendix A, which is one explanation. The other explanation is that microvoids are created due to the thermal stresses in the material after printing. However for concluding these findings, more elaborate inspections are needed using a Scanning Electron Microscope (SEM). Due to the multiple identified voids, the measurement is being split up in the void content of a tower (1) and the complete cross-section (2), as shown in Figure7.2.8

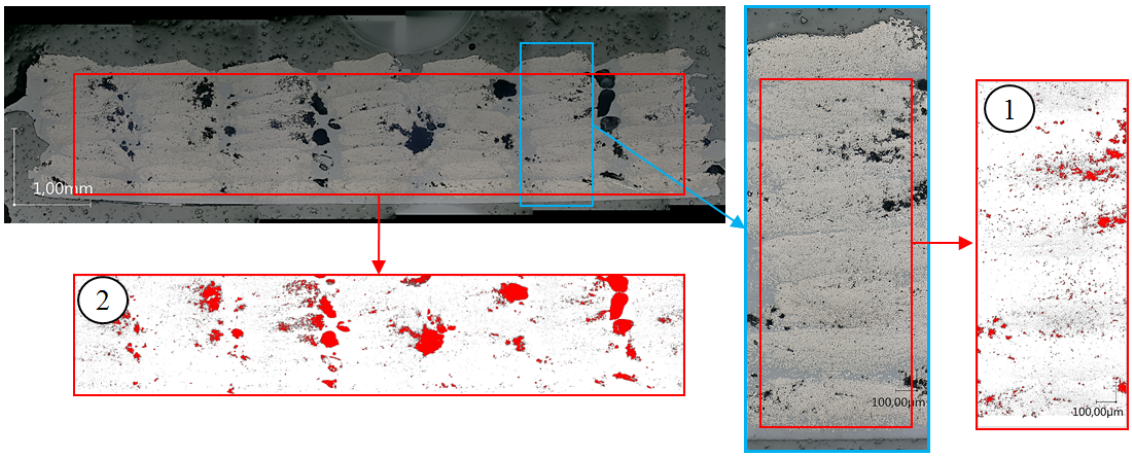

Figure 7.2.8: Used approach for measuring the void content in a tower using a Keyence vhx-6000 microscope. 1: tower void content, 2: complete void content

Another observation is related to the location of the specimen in the printed loops. The specimen for the void content are located at the edges of the straight section, as shown in Figure 7.1.1. With clockwise printing direction, Specimen S1 and S3 are printed directly after a radius area. It can be seen in Sample 7, 8, 9, 11 and 12 in Appendix G, that the layers and lines are not completely aligned. This indicates that there is a visible effect in the void content specimen due to the radius area. Because a certain amount of the specimen are cut too close towards the radius areas, the overall void content measurement will not result in an accurate response. Therefore the decision is made only to focus on the void content in between printed layers by the use of a tower section. The results from this measurement are given in Table 7.2.1.

Table 7.2.1: Results of the void content in percentage, outliers are crossed out and replaced Sample 11 and 13 and the additional Sample 16 are in italic

Sample	**Specimen 1 tower**	**Specimen 2 tower**	**Specimen 3 tower**	**Specimen 4 tower**	**Average tower**	**Average complete**
S1	6.88	5.61	6.18	6.14	6.20	9.87
S2	4.36	5.89	3.97	5.57	4.95	9.68
S3	4.68	6.22	2.64	1.94	3.87	4.20
S4	6.26	7.22	~~18.38~~	5.38	6.29	13.28
S5	5.64	5.31	5.21	3.96	5.03	13.51
S6	9.27	3.02	2.75	4.44	4.87	9.44
S7	9.65	3.78	4.51	5.14	5.77	11.54
S8	5.79	3.26	4.42	3.4	4.22	16.13
S9	9.55	8.55	9.52	5.52	8.29	16.09
S10	7.14	5.02	4.48	2.63	4.82	10.78
S11	*12*	*3.63*	*8.53*	*(-)*	*8.05*	*20.09*
S12	~~20.31~~	13.73	7.7	4.07	8.50	17.22
S13	*4.77*	*3.91*	*2.63*	*7.75*	*4.77*	*12.67*
S14	6.41	2.97	3.33	3.1	3.95	12.15
S15	10.21	10.66	9.02	7.69	9.40	15.19
S16	*3.7*	*2.85*	*3.9*	*4.16*	*3.65*	*8.19*

8

Response Optimisation

One of the last steps in the optimisation of the print process, is selecting the ideal parameter settings which result in the optimum print conditions. These conditions are characterised by the most robust process, the highest stress at break and lowest void content. The choice is made to perform the optimisation on each of the criteria separately to draw accurate conclusions on the effect of each parameter. In the end the combined optimisation is being performed, which is used as the final result. The main steps in generating the Response Surface Design (RSD) and optimisation thereof are presented in the flow-chart in Figure 8.0.1.

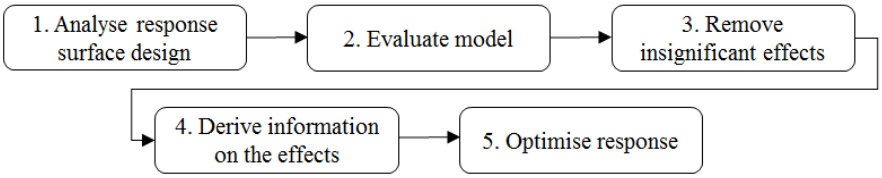

Figure 8.0.1: Flow chart of the steps to be taken to optimise the response

In the next sections, the response optimisation is explained using the robustness criteria. The additional response criteria use the same approach and are provided in Appendix H.

8.1. Generation Response Surface Design

The first phase in optimising the response consists of the generation of the Response Surface Design and is represented by step 1 to 3 in Figure 8.0.1.

Step 1:
The first step consists of setting up the face centered Central Composites Design including obtained response values within Minitab 2018. When analysing the RSD, the terms taken into consideration for the model need to be selected. The choice is made to start the model by incorporating all terms, which means linear, quadratic and interaction terms. Secondly, the confidence level needs to be selected, which is set at the default of 95 %. This means that 95 % of samples from the same population will be expected to contain the true parameter [13].

After performing the analysis, Minitab provides the results of the obtained model in the model summary and coded coefficients table [28]. For the robustness, this result can be seen in Figure 8.1.1.

Step 2
In the model summary, the fit of the model to the obtained response is shown [28]. S indicates the standard deviation of the distance between the data values and fitted values, measured in the unit of the response. $R-sq$ determines how well the model fits the data, the higher this value, the better. Similar, $R-sq(adj)$ is the percentage of the variation in the response, adjusted for the number of predictors in the model. Compared to $R-sq$, this term is more important as it does not contains the effects of the insignificant terms. Lastly, $R-sq(pred)$ provides information on how well the model predicts the response for new observations, outside

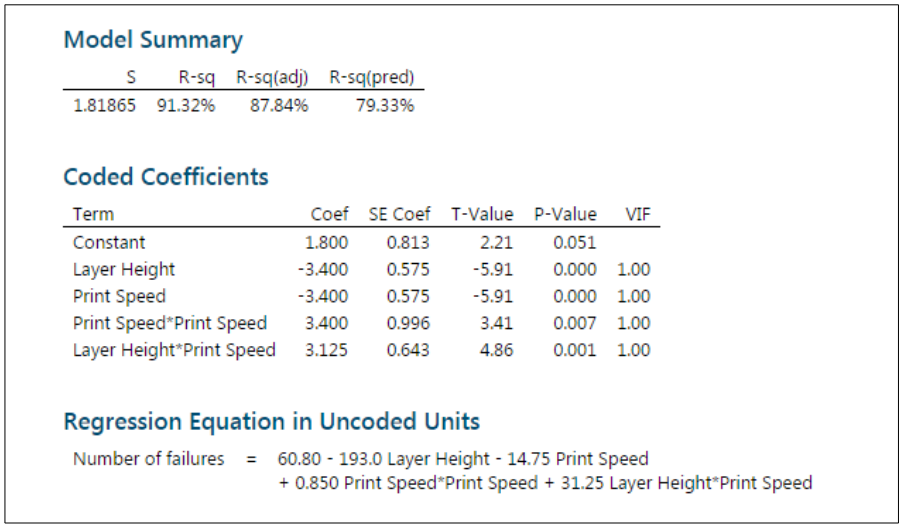

Model Summary

S	R-sq	R-sq(adj)	R-sq(pred)
1.81865	91.32%	87.84%	79.33%

Coded Coefficients

Term	Coef	SE Coef	T-Value	P-Value	VIF
Constant	1.800	0.813	2.21	0.051	
Layer Height	-3.400	0.575	-5.91	0.000	1.00
Print Speed	-3.400	0.575	-5.91	0.000	1.00
Print Speed*Print Speed	3.400	0.996	3.41	0.007	1.00
Layer Height*Print Speed	3.125	0.643	4.86	0.001	1.00

Regression Equation in Uncoded Units

Number of failures = 60.80 - 193.0 Layer Height - 14.75 Print Speed
+ 0.850 Print Speed*Print Speed + 31.25 Layer Height*Print Speed

Figure 8.1.1: Optimised parameter settings for robustness

the current model population. This last value is for this DoE less of concern as the outer boundaries of the parameter settings were determined thoroughly, so the focus needs to be on the $R-sq(adj)$ value.

The coded coefficients table provides more detailed information about the model fit [28]. The first column $Coef$ describes the size and direction of the relationship between term and response variable. For example, a negative coefficient will cause a decrease in response when this selected term is increased. The precision of this coefficient can be estimated by the standard error of the coefficient estimates ($SECoef$). The smaller this standard error, the more precise the estimate is. The ratio between the coefficient and standard error is displayed as the $T-value$. Next, the $P-value$ is used to determine whether the null hypothesis can be neglected. A P-value larger than the significance level, which equals 1 minus the confidence level, means that the association of that term is not statistically significant, or no conclusion can be made that there exists a statistically significant relation between the response and the term.

Step 3:
The next step is to evaluate the obtained model and improve its fit. Because all terms are incorporated at the start of the analysis, most likely there exist several terms which do not have a statistically significant influence on the response. These terms need to be removed from the model one by one, starting with the most insignificant term. Then at each removal of a single insignificant term, the model summary of the new model is compared to the old model. If the fit becomes better, more insignificant terms can be removed. On the other hand, if the fit of the model becomes worse, the last removed term is added again and the model is taken as the optimum. This method is called the Backward Elimination procedure [3].

8.2. Interpretation and Selection Optimum Conditions

The second phase of the response optimisation consists of critically analysing the obtained model and their interactions. Several graphs and tools are used which provide information on how each of the significant terms effect the response. The final model is then used to obtain the optimum parameter settings using the integrated response optimiser.

Pareto Chart
The Pareto chart of the standardized effects, as seen in Figure 8.2.1, provides a visual indication on the significance level of the selected terms. Each term which value is above the red line, indicates their effect is statistically significant on the set significance level. The larger the value of the standardized effect, the more influence the factor has on the response. This graph is being used to verify the importance of each of the effects.

Normal Plot of the Standardized Effects
Since the Pareto chart only provides information on the size of the effects, a normal plot of the standardized effects is being used to determine the direction of the effects. In Figure 8.2.2, a term located on the left side

of the red diagonal, representing the line at which the effects are zero, will decrease the response if its value is increased. In the same manner an effect on the right side will decrease the response.

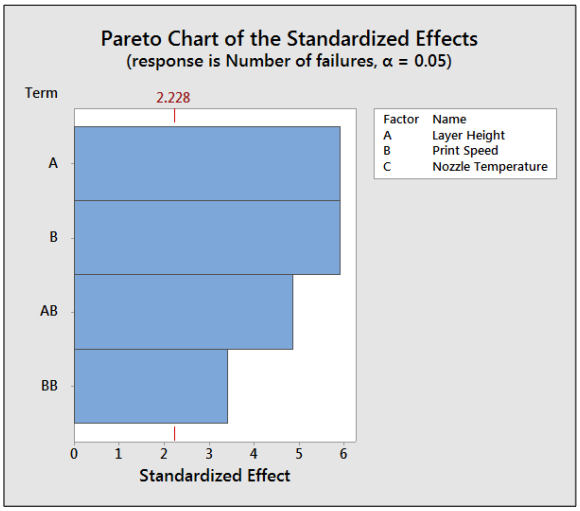

Figure 8.2.1: Pareto chart of the standardized effects for the robustness response

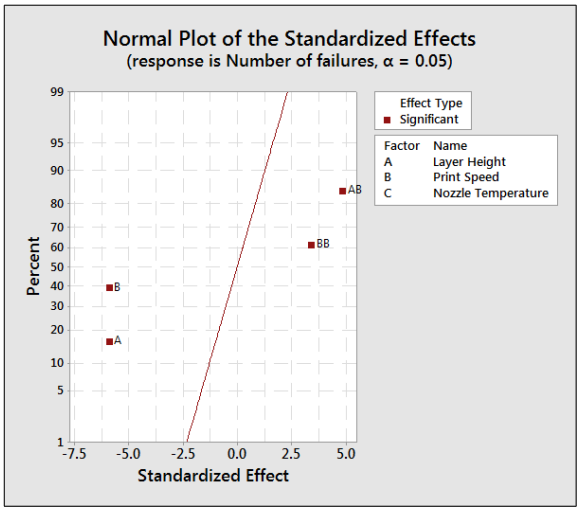

Figure 8.2.2: Normal plot of the standardized effects for the robustness response

Residual Plots

Removing insignificant terms using the backward elimination procedure does not always results in an accurate model. Therefore it is necessary to check the quality and make sure no outliers exist in the obtained model. This is done by using the Residual plots in Figure 8.2.3 and check for unexpected behaviour. The first plot on the top left, represents the normal probability plot of the residuals. This plot is being used to verify the residuals follow a normal distribution. This can be done visually or by using the Anderson-Darling statistic displayed next to the plot. The Anderson-Darling statistic is a measure for the goodness-of-fit of the data to a particular distribution. In this case, a normal distribution is of order. If the corresponding P-value is less than the chosen significance level (0.05), the null hypothesis can be rejected, which means the data does not follow a normal distribution. For the robustness, the Anderson-Darling test has a P-value larger than the significance level, so the residuals follow a normal distribution.

The second plot on the top right shows the residuals versus fits. This plot is being used to validate that the residuals have a constant variance. Visually this means that the points fall randomly above and below the dashed line at 0 with no outliers in x-direction.

On the bottom left, the histogram of the residuals is shown. This plot is being used to determine the skewness of the data. It should be noted that small sample sizes might show similar behaviour to the presence of a skewed distribution. This is because inadequate data points are used within each bar of the histogram and therefore do not show a reliable result.

The last plot on the bottom right shows the residuals versus order. This plot should not show any trend or pattern along its x-axis, which is the time order. No trend or pattern verifies that the residuals are independent from one another.

By analysis of the previously discussed plots, the effect of the factors on the responses are being analysed and the quality of the model is being checked. The last step consist of the optimisation of the response, which is done by the incorporated response optimiser and is provided in next section.

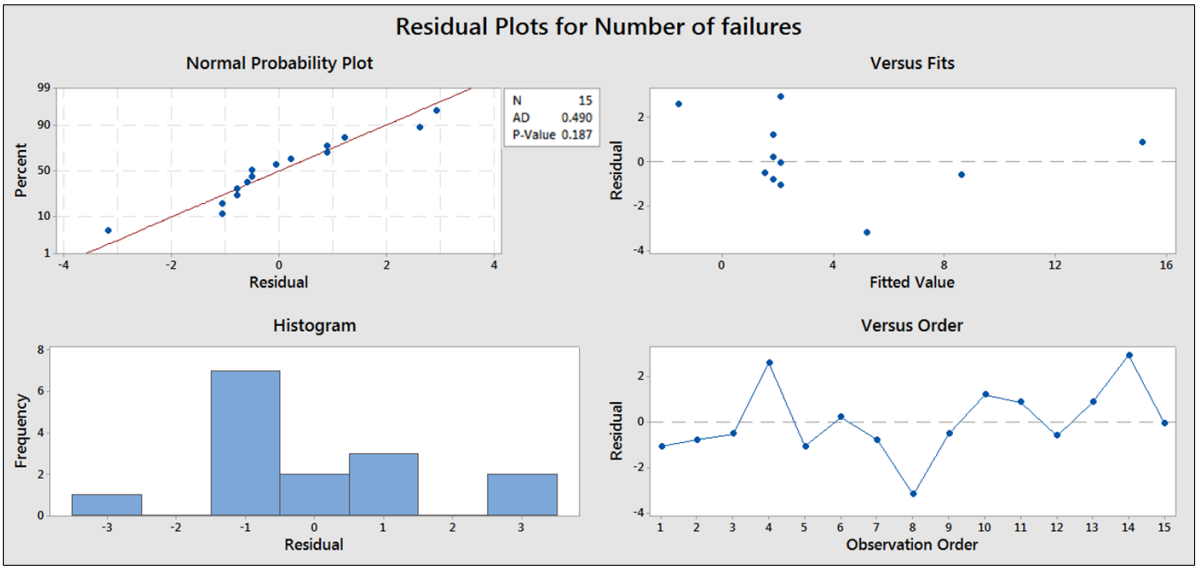

Figure 8.2.3: Residual plots for robustness response

8.3. Results of Parameter Optimisation

In this section, the results from the response optimisation are discussed for each response separately, where in the end the optimum parameters are selected from the combined optimisation.

8.3.1. Robustness

The Response Surface Design for the robustness is being analysed, but does not show any statistically significant factors. The explanation is the exclusion of two parameter settings, which are not feasible to print. Instead of excluding these results, their response is included by assigning a number of failures which overtake all other observations. Two models are being analysed, one by setting a value of 50 failures during printing, the other by two times the highest number of failures occurring in the other observations, which equals 16. The result of both models shows the same behaviour of the optimised response, but the second model is being chosen to be used in further analysis as this regression's model summary indicates a better fit.

The significant factors for the robustness are the layer height, print speed, interaction between layer height and print speed and print speed squared as can be seen in Figure 8.2.1. The normal plot of the standardized effects shows that both one way interactions have a negative effect on the response, which means an increase in layer height or print speed results in a decrease in the number of failures. The interaction term between layer height and print speed shows a positive significant behaviour. In Figure 8.3.1 it can be clearly seen that the 2 mm/s print speed setting does result in more failures, where both other settings show a constant failure behaviour.

The optimum condition for a minimum amount of failures, or most robust process results in a layer height of 0.25 mm and print speed of 4.10 mm/s. The nozzle temperature is not statistically significant and therefore not shown in Figure 8.3.2.

The working principle of the print head has a substantial influence on these optimum parameters. An increase in layer height will cause the pressure on the filament to be decreased, causing less friction between ironing surface and filament and therefore allows for a smooth exit. This results in a lower probability of clogging up the filament tube and nozzle, which explains the downward slope of the layer height on the response in Figure 8.3.2.

For the print speed, the optimum condition is obtained in between its boundary conditions, which is the result of the statistical significant influence of the print speed squared term. The explanation for a high amount of failures at low print speeds is due to clogging up the filament tubes. A certain amount of mass flow is needed to overcome the static friction between the nozzle inner wall and filament. In addition, the heat will conduct trough the axial direction of the filament, upward towards the filament tube. The consequence of printing at low print speeds is that the relative velocity of the heat travelling upward in axial direction is faster

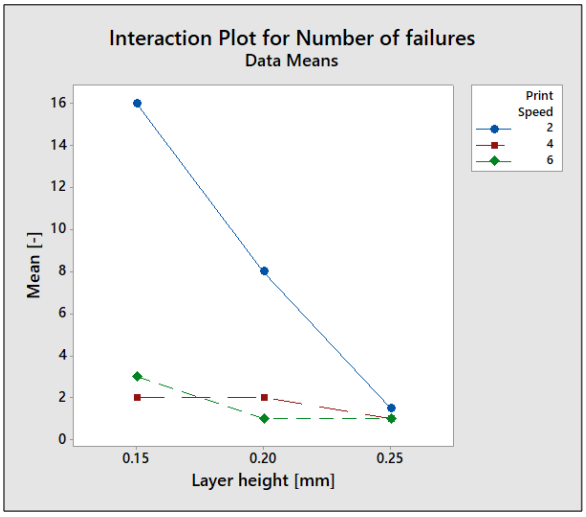

Figure 8.3.1: Interaction plot between the layer height and print speed, based on the robustness criteria

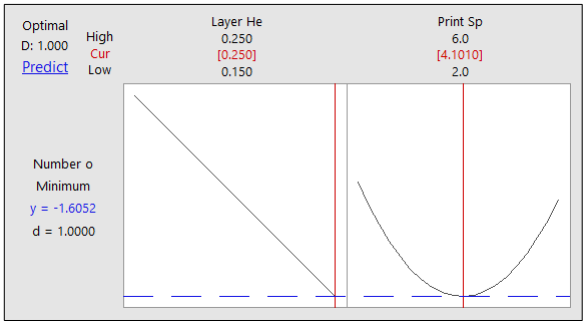

Figure 8.3.2: Optimised parameter settings for robustness

than the print speed itself. Therefore the filament in the filament tube will eventually heat up above its glass transition temperature and start to clog against the inner walls. This event will over time result in failure of the print.
More failures are also observed at higher print speeds. The failure mode here is not related to clogging of the filament tube and nozzle, but is based on detached print lines. At high print speeds, the fusion time between the layers is decreased. At the critical locations as the radius or transition area, there exists a change in direction of the filament, which results in a small tensional force on the filament. This combination leads to several detached print lines, which result in the need to abort the print process.

8.3.2. Stress at Break

The final model obtained for the stress at break criteria consists of four terms, namely the nozzle temperature, interaction between layer height and nozzle temperature, print speed and print speed squared. Their magnitude and direction can be seen in Figure 8.3.3 and 8.3.4.

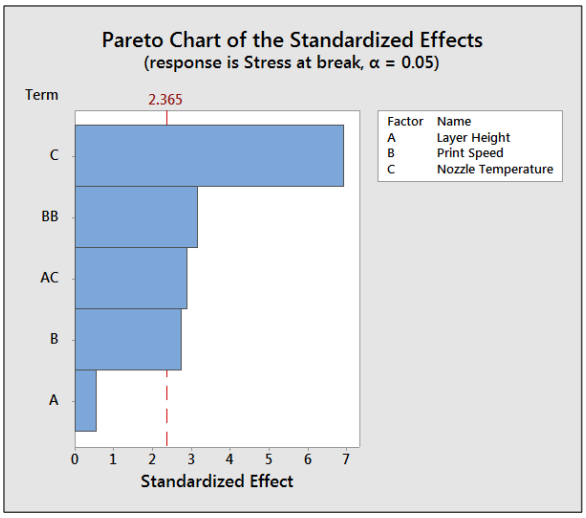

Figure 8.3.3: Pareto chart of the standardized effects for the stress at break response

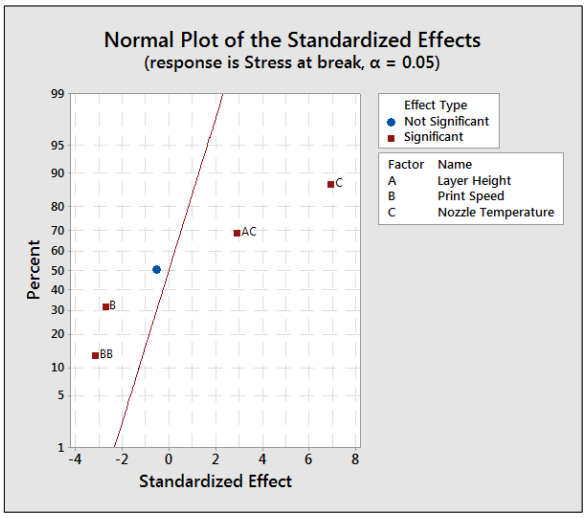

Figure 8.3.4: Normal plot of the standardized effects for the stress at break response

The most significant term in the model is the nozzle temperature and has a direct positive effect on the response.

Figure 8.3.5 shows the interaction plot between layer height and nozzle temperature. It can be seen that the interaction term does not result a clear behaviour. At 0.15 mm thickness, the response values lie closer together than for 0.25 mm thickness. The interaction suggests an increase in stress at break with increasing layer height as general behaviour, but is not observed for the 340°C temperature setting. The scatterplot between the stress at break and layer height is shown in Figure 8.3.6. It can be seen that the number of observations is not the same for every layer height setting, which is explained by the absence of Sample 11 and 13. Compared to the already existing observations at 0.15 mm layer thickness, the expected location of Sample 11 and 13 will be the indicated red areas. This is based on a lower print speed setting compared to the already existing data points and therefore is assumed to increase the fusion and so stress at break. Therefore the trend of the optimum response in Figure 8.3.5 will change according to the indicated 'X'. It can be concluded that a significant behaviour is out of order and therefore the interaction term is removed from the model.

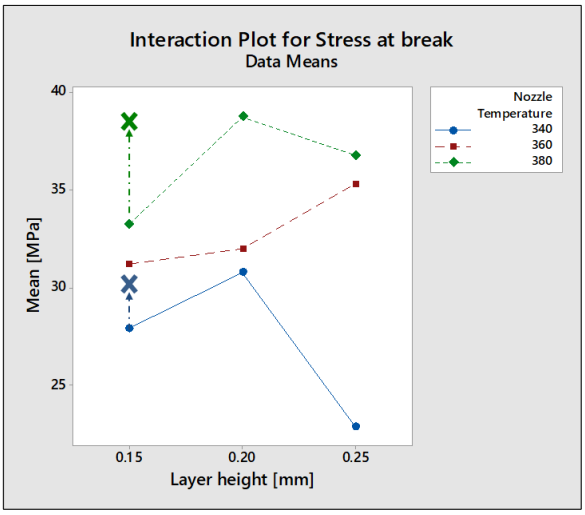

Figure 8.3.5: Interaction plot between the layer height and nozzle temperature, X indicates the expected behaviour with the inclusion of Sample 11 and 13

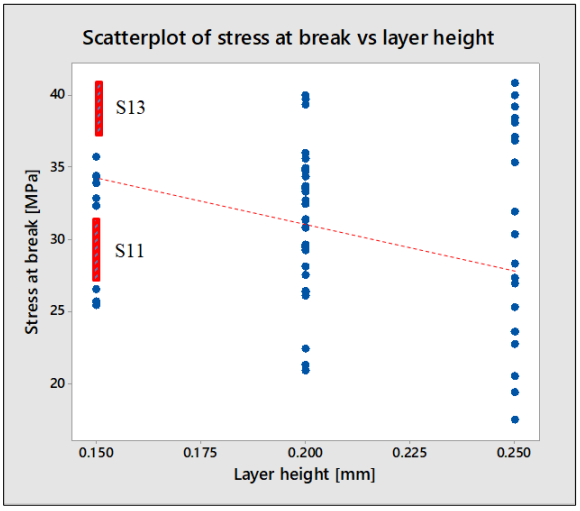

Figure 8.3.6: Scatterplot between stress at break and layer height, red areas indicate the expected stress at break of Sample 11 and 13, blue dots are the original data

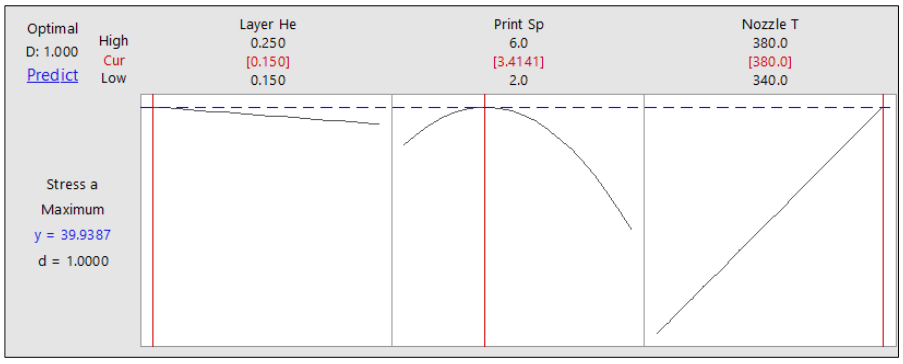

Figure 8.3.7: Optimised parameter settings for stress at break

By maximizing the stress at break, the result from the response optimisation tends towards an optimum condition with a layer height of 0.15 mm, print speed of 3.41 mm/s and nozzle temperature of 380°C.

After removal of the interaction term between layer height and nozzle temperature, the layer height term is kept in the model and causes a slight decrease in the slope of the layer height.

The plot for the print speed shows to have reached its optimum condition in between the boundaries, which is due to the influence of the print speed squared term. An increase in print speed will decrease the fusion time between the layers, introduce more defects and so decrease the stress at break. At the lower boundary, one possible explanation for a decrease in response is due to the increase of defects which are the related to

the static friction between filament end ironing surface. However, missing Sample 11 and 13 were printed in the lower print speed regime and therefore it is concluded that more tests at lower print speeds are needed in order to make valid conclusions about this behaviour.

Finally, the nozzle temperature shows a clear increase in response. A higher temperature will increase the heat conduction trough the thickness of the filament, in this way decrease the viscosity of the previous layers, which ensures a better wettability of the fibers and result in a better bond at the interface.

8.3.3. Void Content

As already explained in Chapter 7, the void content used is the result from the tower sections. The outcome of the Response Surface Design shows that the significant factors are identified as the layer height, print speed, interaction between print speed and nozzle temperature, interaction between layer height and nozzle temperature and the print speed squared as can be seen in Figure 8.3.8.

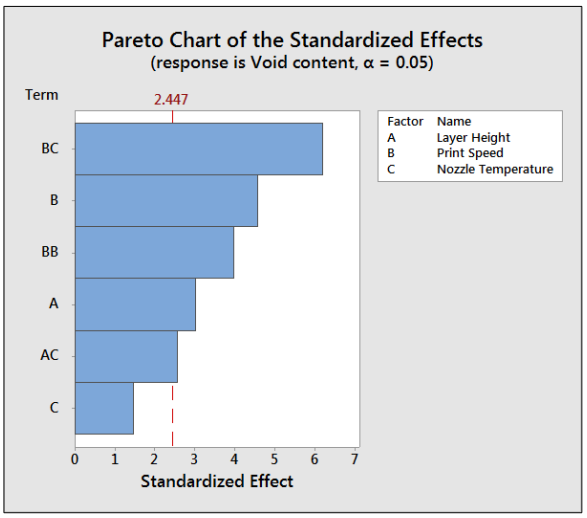

Figure 8.3.8: Pareto chart of the standardized effects for the void content response

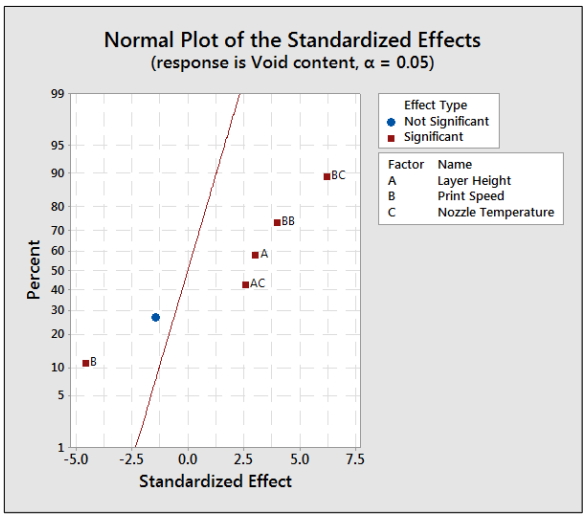

Figure 8.3.9: Normal plot of the standardized effects for the void content response

From the Normal plot in Figure 8.3.9, it can be seen that there exist two one-way effects. The first is the print speed and is the only term with a negative coefficient. This term indicates that out of the obtained data, there exists a statistically significant effect that an increase in print speed results in less voids within the tower sections. The second term is the layer height, which has a direct positive influence on the void content, which corresponds to results obtained in literature, e.g. higher void content with increasing layer height [1].

Figure 8.3.10 and 8.3.11 show the behaviour of the interaction terms. It is observed that the general trend of the different temperature settings are aligned with one another, but small deviations exist in both graphs. The explanation for this behaviour is assumed to be the effect of the radius area on the samples with in addition a small sample size that provides inadequate data points.

The optimum condition for a minimum void content results in a layer height of 0.15 mm, print speed of 3.50 mm/s and nozzle temperature of 380°C.

The layer height and nozzle temperature show a distinct behaviour which corresponds to earlier explained findings, namely a decrease in void content is the result of a higher pressure on the filament, obtained by decreasing the layer height and a better fusion between the layers, obtained by increasing the temperature of the nozzle. Similar to the stress at break, the print speed shows its optimum condition in between the boundary conditions, due to the significance of the print speed squared term.

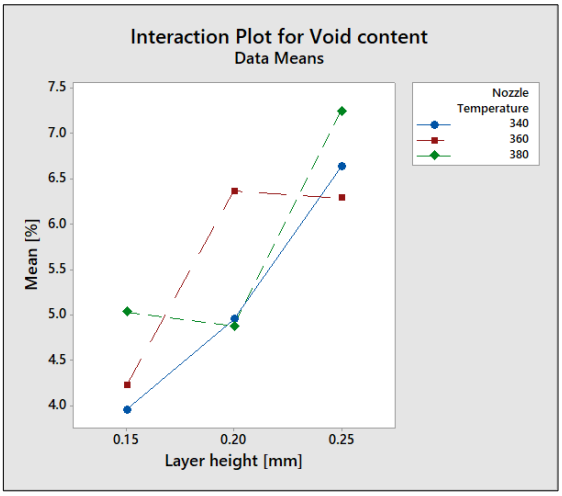

Figure 8.3.10: Interaction plot for the void content between nozzle temperature and layer height

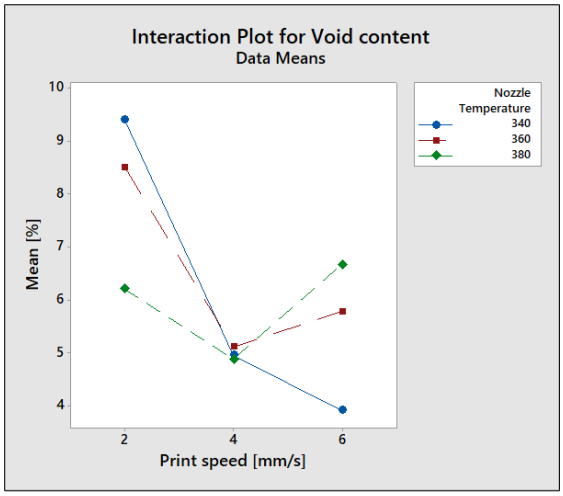

Figure 8.3.11: Interaction plot for the void content between nozzle temperature and print speed

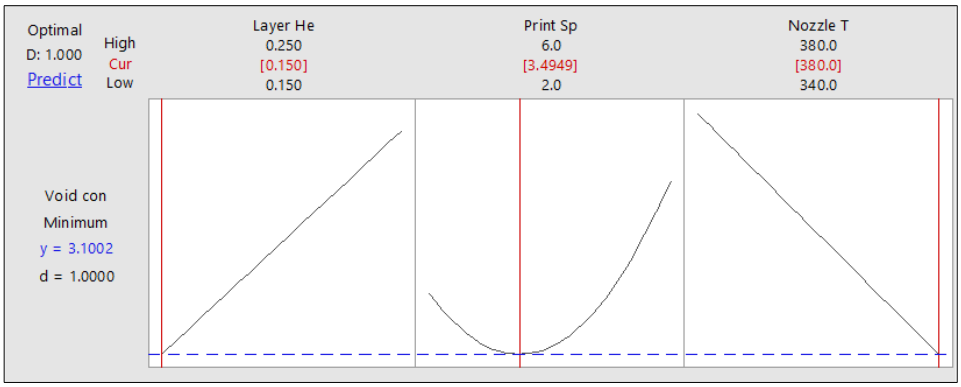

Figure 8.3.12: Optimised parameter settings for void content at break

8.3.4. Combined Case

It is concluded that the optimum results obtained for each of the responses correspond to the observations made during printing and analysis. Therefore the results are confirmed to be valid and its main conclusions are summed up as:

1. Two main failure modes are identified as inter-layer failure and plastic deformation, where the inter-layer failed samples endure a lower stress level
2. Specimen with higher layer thickness tend to fail in inter-layer failure
3. Specimen with higher layer thickness show an increase in void content in between the layers, which explains the reason for inter-layer failure
4. An averaged print speed results in the best condition for all the responses
5. Robustness is improved with increasing layer height
6. Stress at break is improved with decreasing layer height
7. Stress at break and void content are improved with increasing nozzle temperature

Not all the main conclusions align with each other. For example conclusion (5) and (6) clash as they both try to shift the optimum layer height in two different directions. Therefore as a final optimisation, all previous responses are combined and different weights are given to the responses, based on their importance.

Because an experimental set-up is unable to provide accurate results if it is not working properly, the robustness criteria is identified as the most important. The stress at break and void content go hand in hand and

therefore have equal weights. The weights are given 2, 1 and 1 for robustness, stress at break and void content respectively. This final result is shown in Figure 8.3.13.

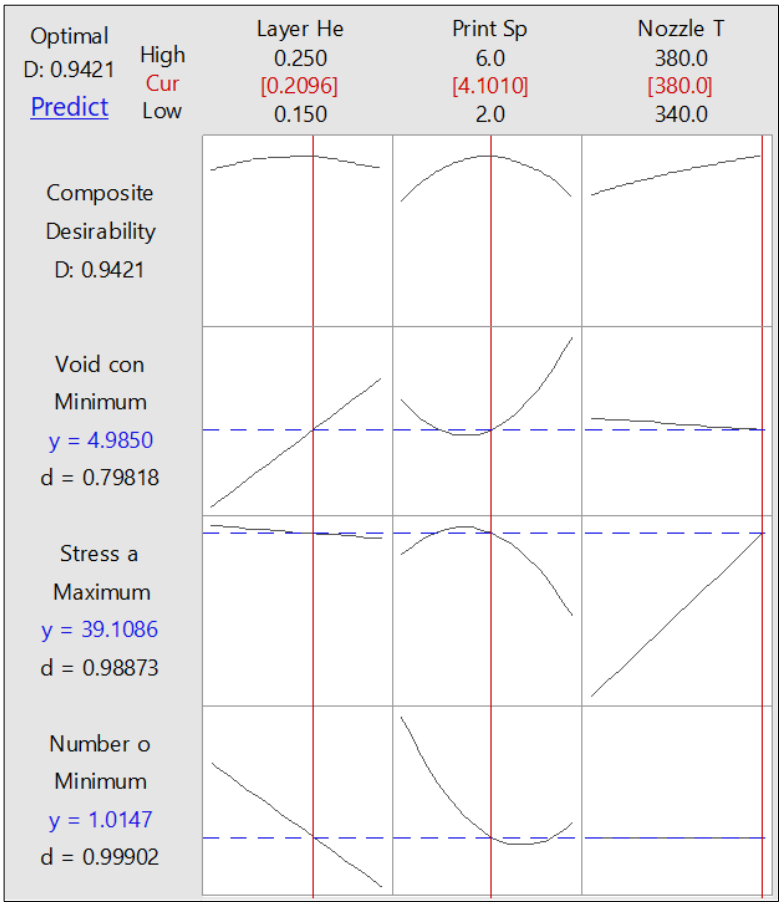

Figure 8.3.13: Final optimised parameter settings

The final optimum parameter settings result in a layer height of 0.21 mm, print speed of 4.10 mm/s and nozzle temperature of 380°C.
The response of these parameter settings results in a void content of 5 % with a stress at break of 39.1 MPa. Approximately one failure is expected when printing the same sample with same size.

The obtained results need to be validated by printing the same sample according to the optimum parameter settings and afterwards testing their responses. This step is not being performed at the moment and is therefore recommanded for future work.

9

Potential and Future Perspective

The feasibility of a new manufacturing technique is not only determined by the quality of its parts. A crucial point in the feasibility analysis is the selection of part families which potentially could have a positive business case. This chapter provides the description of such use cases and envisions the future perspective of the technology to make a solid conclusion towards the research objective.

9.1. Use Cases

The advantages of FCM compared to other manufacturing technologies, as discussed in Chapter 2, do not apply to all geometries or parts. To provide a lightweight and cost efficient solution to existing aircraft parts, the production rate, material, complexity and other criteria need to be taken into account. Several use cases are being identified which could potentially be a more efficient solution to their current manufacturing methods and are listed below.

High buy-to-fly parts
The first use case consist of the family of parts which have simple load cases, with a high buy-to-fly ratio (15-20 for many flying parts), meaning the weight of raw material used for the part is considerably higher than the weight of the finished part [6]. These parts are manufactured by removing lots of material mechanically and have restrictions from the machining capabilities. The reason why FCM has a potential positive business case, is not because of a cost saving on the manufacturing method, but rather a weight saving compared to the original part. In order to select proper applications, the load requirements need to be reviewed as these drive the part weight and design. Aluminium parts are difficult because of their cheap manufacturing methods. However due to the challenging machining and costs of Titanium parts, this can potentially be a feasible application.

Reinforcing function
One of the advantages of FCM is the ability to fuse material to an existing structure without the need for additional bonding or fasteners. A potential use case is therefore the use of FCM as reinforcement to existing structures by overprinting a continuous fiber reinforcement. As traditional reinforcement using stiffeners is limited in complexity, FCM allows to add the reinforcement at the locations needed in all arbitrary directions on both curved and double curved panels. This allows conventional manufacturing methods to be used to produce sub-elements, but make the use of FCM for the optimum reinforcing strategy which results in a more lightweight design.

Custom Parts
Another application is the manufacturing of custom or tailor-made parts. Conventional manufacturing for this part family results quickly in high costs as tooling and machining need to be changed for every single part. Mould-less manufacturing in this case is an ideal solution. A typical example for such use case is the manufacturing of reinforced shims, used to adjust the structure for a better fit. Because Aluminium shims result in galvanic corrosion with the carbon fiber reinforced structure, these are not usable. Currently, the use of Titanium is a solution to this problem but results in more weight and costs. Therefore FCM is a potential substitute for this use case.

A second use case is by retrofitting parts which are not available due to retired aircraft. Because the aircraft Original Equipment Manufacturer (OEM) has to secure spares until the end of life of aircraft and companies and manufacturing plants close, a potential solution is the use of FCM for these spare parts.

Repair Function
The competitive market environment in which airlines operate nowadays does not allow for a margin in costs. Unforeseen circumstances can happen which drive up the maintenance costs of aircraft [31]. A typical example is an impact defect on a wing cover. Currently, manual labour is used to repair such defect using bonding of patches. As the use of thermoplastic polymers in aircraft are on the rise, this repair could be replaced by printing the patch on site [22]. Orientation of the fibers can be changed and depending on the stiffness needed, additional layers of neat polymer can be inserted.

9.2. Demonstrator

Out of these potential use cases, one category is being selected to be used as demonstrator for development and showcase. In addition, several concepts are being made which allow the manufacturing of the demonstrator.

9.2.1. Part Selection

To show the capabilities of the overall FCM process, a metal bracket which corresponds to the high buy-to-fly ratio parts is selected for demonstration. The bracket as seen in Figure 9.2.1.(a). consists of a relatively flat geometry and is loaded with in-plane loads during operation. It is manufactured by removing roughly 60 % of material by milling. The bracket is connected with 4 rivets to the aircraft frame and consists of a floating nut and main lug. This simple load case allows the bracket to be redesigned using the stacking of closed loop structures, as explained in Chapter 4. Several loops are being created to connect the frame of the bracket together. The design optimisation of the chosen demonstrator part has not been performed in the course of this study, but its result is shown in step (c) of Figure 9.2.1. The maximum weight potential to an Aluminium bracket is in the range of 55 %.

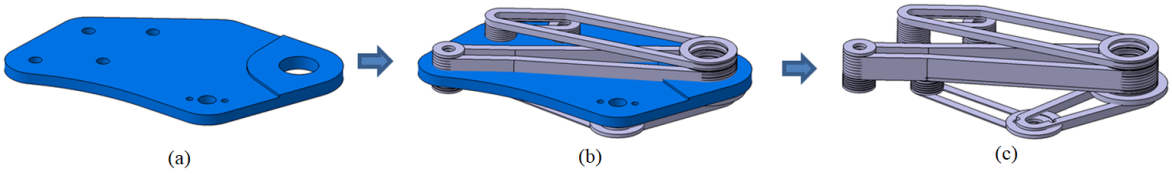

Figure 9.2.1: Composite design of the Aluminium bracket

9.2.2. Manufacturing Concepts

The overall structure of the demonstrator is connected using the fusion of separate closed loops. The problem occurring with this design is that the single loops have a certain overhang. Because the printer is not capable of printing an overhanging structure, a different manufacturing strategy needs to be implemented. In Additive Manufacturing, a common technique to solve these issues is by the use of support structure. The current set-up does not contain a second nozzle capable of printing support structure, so a different concept needs to be implemented. In the following list, four concepts are mentioned which introduce the usage of support structure.

1. Over-moulding of a printed loop
2. Replacing the complete build plate onto a second printer capable of printing support structure
3. Manually placing pre-manufactured support structure
4. Collaboration between multiple robots or print heads

The first possibility is to use a combination of printing followed by over-moulding, to create a smooth plane on which the next loop can be printed. The issue of this concept is the relatively long waiting time needed for the resin to be cured. The glass build plate needs to be sealed off to ensure no resin leaks out and needs to be exactly levelled to avoid misalignment between the printed loop and resin due to gravitational forces.

The second strategy is to remove the complete build plate, including printed loop and place it within a second

printer, capable of printing support material. The issues in this case is the uncontrollable temperature of the environment and build plate as it is sequentially heated and cooled down. The rapid cooling will create thermal stresses in the printed material and cause warpage. Since the build plate is installed by hand, any minuscule deviation will cause misalignment of the print result.

Another option is the placement of pre-manufactured support structure within the print process. This strategy avoids the misalignment and temperature issues from the second strategy, but needs additional tooling to clamp the support within place.

A last strategy is the collaboration between multiple robots. One robot prints the part, where the other prints support structure only at the location where it is needed. For this strategy to work, multiple robots need to be programmed at the same time without causing collisions.

9.2.3. Manufacturing Sequence

Out of the four manufacturing concepts, manually printing pre-manufactured support structure is being chosen. Over-moulding support will take too much time, replacing the build plate will introduce misalignment in the print path and lastly the collaboration between two robots will be possible in the future, but at this moment this approach still needs to be investigated, which is out of the scope of the research objective.

The main steps in the process chain for manufacturing the demonstrator part consist of Print Path Planning, printing of additional support material, preparing the set-up, printing, post-processing, assembly and inspection. These steps are shown in Figure 9.2.2.

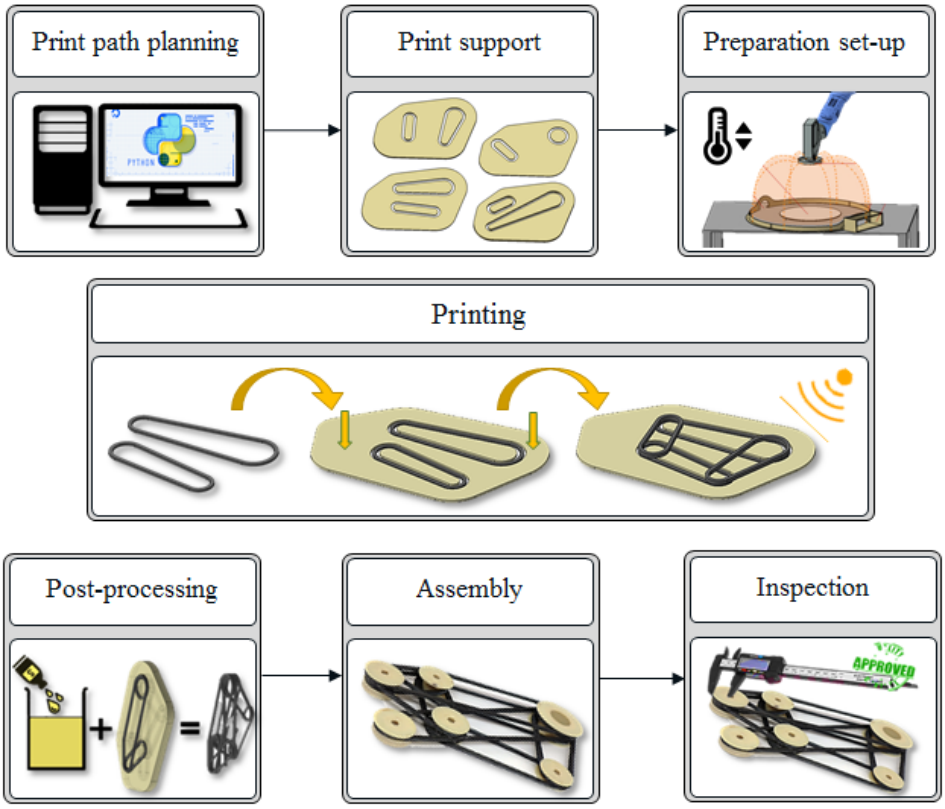

Figure 9.2.2: Demonstrator manufacturing strategy

Print Path Planning is performed using the Print Path Planning tool, as discussed in Chapter 4. Additional support structures are printed beforehand. Different support materials are available to be used, which consist of breakaway or soluble materials. The last is preferred as the post-processing step would require less effort and no mechanical harm can be done to the demonstrator part. It is important that the support material does not warp and is thermally stable within the print process. In addition, it needs to provide adhesion with the printed material so that it does not loosen during printing.

To test these requirements and choose the best option, a trade-off is being performed based on small experimental tests on the different materials. This support study is explained in Appendix I, from which the result is that Antero SUP8000B provides the best behaviour.

The preparation of the set-up consists of manual steps which include loading the filament, levelling the build plate, inserting the SRC-code and heating the nozzle, build plate and controlled build volume.
After preparing the set-up, printing is performed by sequentially printing layers of CF-PPS and adding manually the support structure. When all the layers are printed, the support material is being removed from the bracket and additional features as bushings are inserted. The last step consists of inspection of the dimensions and possible defects.

The resulting bracket is shown in Figure 9.2.3 and each of the steps explained above are provided in Appendix I.

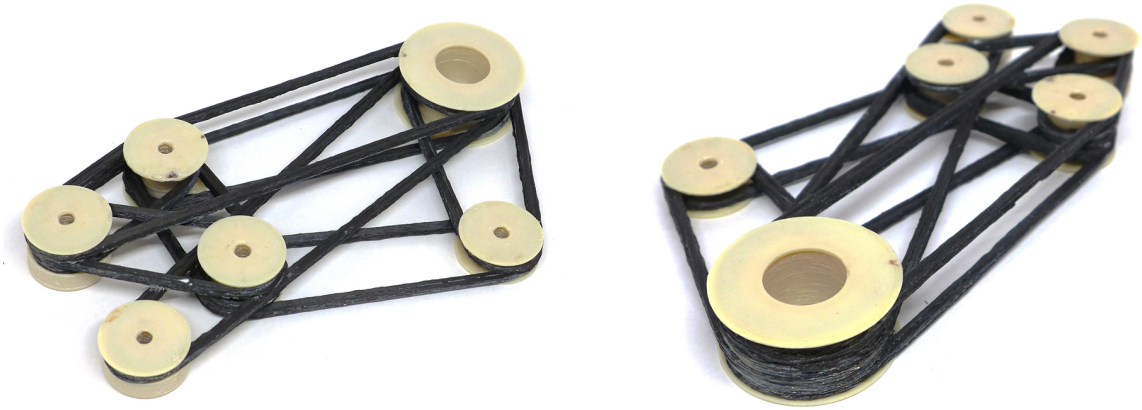

(a) View 1 (b) View 2

Figure 9.2.3: Demonstrator CF-PPS including PPS bushings

9.3. Future Perspective

The previous use cases and demonstrator are based on the capabilities of FCM and the design of aircraft parts at this moment. Because FCM is still in its early stages of development, improvements will be made. To identify which process related steps do have the largest margin and need for improvement, the assessment on the maturity of the technology, as performed in the Literature Study Report, is performed for the current state [8]. The result of this assessment can be seen in Figure 9.3.1 under 'FLATISA'.

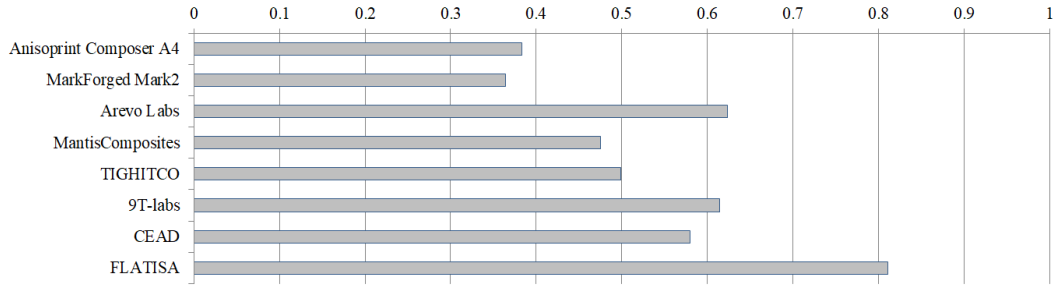

Figure 9.3.1: Maturity plot of the technologies analysed in the Literature Study Report, including the result from this research [8]

The grading is shown in Table I.3.1 and I.3.2 in Appendix I. and each criteria is discussed below.

Part complexity and size
The introduction of the print head within an industrial environment and 6 degrees of freedom has increased the part complexity and size with a tremendous amount. At this moment, the capabilities of the set-up do meet the needs for future applications. There exist however process related limitations as the minimum printable radius, which need to be addressed in future research.

Polymer Performance
The capability of the experimental set-up provide a thermally stable environment which allows to print high performance polymers. It is however observed from the robustness criteria that the nozzle set-up including the filament tube is not the best solution to print for extensive periods of time. Since the nozzle set-up can be adapted, the polymer performance category can still be increased towards the use of materials with higher strength and thermal properties, for example PEEK.

End-to-end software capability
The demonstrator part has proven the end-to-end software capability to work, but is limited in generating closed loop geometries. The automated solution to obtaining print path from topology optimized structures is still far-off and needs to be investigated in future research.

Control of the build chamber
A controlled build chamber is designed and implemented within the experimental set-up. In addition, a patent application has been filed, which is defined as "Flexible conditioned print volume for 3D Printing processes". This leads to a fully conditioned print environment including heated print bed and build volume.

Material cost potential
Because the print head is designed by an external company and does not have the restrictions towards the use of a predefined material, the material cost potential is low. The cost potential is also influenced by the quality of the base material, as there is the opportunity to reach out for every filament on the market, this criteria does not need to be improved.

Layup rate
The current flow rate of the used filament with nominal diameter 0.65 mm and optimised print speed setting of 4.1 mm/s is 1.36 mm^3/s. This value is still on the low side and does need to be improved. In comparison with existing 3D printers on the market, Table 9.3.1 provides typical reference values.

Table 9.3.1: 3D printer volume flow references

Material	**Printer**	**Volume flow** [mm^3/s]
Ultimaker S2+ [30]	PLA, ABS	<23
Stratasys Fortus 450mc [7]	Antero 800NA	6

Quality
The quality of the base material is within the high performance category. Resulting from the ILSS tests and microscopic inspection, the quality of the specimen are not without defects, but the issues are being identified and improved. One of the key tasks to perform in order to increase the quality is limiting the gaps in between the lines during printing. However the printed results provide an efficient bond at the interface.
Because the material supplier does not provide ILSS properties of the used filament, as a reference to the obtained ILSS values in this research, Table 9.3.2 provides ILSS results from materials typically used in aerospace applications. Because their manufacturing method, material and Fiber Volume Content differ, comparisons cannot be made.

Table 9.3.2: ILSS value references

Material	**Manufacturing Method**	**FVC** [%]	**ILSS** [MPa]
CF - PEEK UD [5]	Tape placement + autoclave processing	(-)	76
CF - PEEK UD [5]	Tape placement	(-)	94
CF - PLA UD [1]	Filament Layer Manufacturing	(-)	31.94

10

Conclusion and Recommendations

Conclusion

The research presented in this thesis covers the analysis on the feasibility of introducing a novel Fused Composite Manufacturing process with regards to aerospace applications. A novel print head capable of extruding prepreg filament consisting of CF-PPS with 50% FVC has been implemented within an industrial environment. A KUKA KR30 HA 6-axis robot is used to drive the print head, making it possible to place the fiber in all arbitrary directions. Resulting from a pre-research on the filament, it was observed that a heated build plate and build volume are a must to print high performance polymers without creating thermal stresses in the part.

Careful design went into the experimental set-up. A missing link in the working principle consisted of a Print Path Planning tool, able to generate print path for the KUKA robot. To identify the needed specifications of such tool, an intermediate solution has been developed which creates print path for closed loop geometries in an automated way. It was concluded that a KUKA robot needs a SRC-code, containing Cartesian axis systems with origin x, y, z and orientation a, b, c in chronological order as the Tool Center Point should follow them during printing. Each of these axis systems correspond to the nozzle location and orientation and so define the print path. The current tool has been developed using a combination of Mathcad Prime 5.0 and Python, but needs more development to allow for more complex geometries and the inclusion of manufacturing effects.

The main results from pre-trial prints, was a buckling and twisting behaviour in the radius areas, which led to premature failure of the process. The analysis of the failed specimen and nozzle geometry showed that an over-extrusion of the filament caused a buckling and warping behaviour. Based on the inner concave shape of the nozzle, it was identified that the filament was not being placed at the centerline, but tended inward in curvatures. This had as a consequence that the feeding unit was over-extruding material. The Print Path Planning tool and feeding unit have been modified using an Extrusion Overwrite function, which adapts the path and feeding rate. In addition an Active Cooling unit has been implemented to improve the dimensional accuracy of the print, which resulted in a smooth and robust print process.

A first iteration on the optimisation of the key influencing parameters has been done using the face centered Central Composites Design, because it contains the extreme outer boundaries.
The parameter boundaries of the Design of Experiments were determined using a combination of simulating the filament melt flow and performing experimental tests on the capabilities of the filament. The simulation felt within a margin of 5 % compared to the corresponding IR measurement. Additional print trails have shown the new approach to be valid, which concludes it can be used to efficiently select parameter boundaries for filament with different material properties or size.

The parameter combinations have been printed and samples were prepared for inter-laminar shear strength tests according to the DIN EN 2563 standards and microscopic inspection.
Two occurring failure modes resulted from the inter-laminar shear strength tests, namely inter-layer failure and plastic deformation. Inter-layer failure happened at the specimen which did have a weak interface be-

tween the layers. This was the result of a low nozzle temperature and high layer thickness. The void content specimen showed high percentages of voids. The main reason is that the current experimental set-up does not allow for margins in material and processing conditions. Inaccurate bed levelling and tolerances of the filament caused gaps in between the printed lines and therefore need to be improved.

The optimum value for the layer height in the combined response optimisation resulted in 0.21 mm. This value is influenced by the robustness which tends towards maximum layer height and ILSS and void content tending towards minimum layer height. The optimum condition for the print speed resulted in 4.1 mm/s. High print speeds will cause inefficient fusion in between the layers and therefore are not preferred. Since two samples with 2 mms/s print speed setting were not feasible to be printed, conclusions about the low print speed regime are not considered and more tests need to be performed to make valid conclusions. The optimum condition of the nozzle temperature resulted in 380°C, which is the outer boundary. A higher temperature resulted in a better bond in the interface with higher ILSS and less voids as a result.
These optimum conditions will result in a void content of 5 % with a stress at break of 39.1 MPa. Validation of the obtained optimum condition has not been performed, but is recommanded for future research.

In order to answer the research objective of this thesis, which is to evaluate the feasibility of a novel robotic Fused Composite Manufacturing process for aerospace applications, not only the working principle and proof of concept of the manufacturing method have been investigated, but also the potential use cases for future applications. It is concluded that within the aerospace sector, the design and manufacturing of strong and lightweight parts have a crucial influence on the performance of aircraft and therefore the industrialisation of this FCM technology has a great potential in the future. It is therefore concluded that the integration of this novel FCM process has succeeded. Continuous reinforced high performance parts have been printed using the incorporation of the complete end-to-end manufacturing process. The proof of concept has been made, but does still have margin for improvement. Considering the technology on the short- and long term, several improvements and recommendations have been listed, which are discussed below.

Recommendations

The current set-up used in this research has proven to comply with the requirements needed to obtain results usable for aerospace applications. Due to limitations which are out of the scope of this thesis assignment, several points of interest have not been investigated and are written down as recommendations for future research on the short- and long term.

short term

The obtained optimum parameter settings for nozzle temperature, print speed and layer height should be validated using experimentally testing for their response.
Another possibility, is to run a second DoE which is centered around the optimum parameter settings from the first iteration, but using smaller boundaries. This follow-up research can be performed in the same manner with the inclusion of additional test methods such as tensile- and lap-shear tests. These methods have to be defined in detail.

The previously performed research focusses on the optimisation of the material properties on microscopic scale. After a second DoE is performed and optimised, the optimum parameter settings obtained by testing at coupon level can be used to print parts for element level testing. A perfect use case is the demonstrator from Chapter 9. A test set-up needs to be designed to test the printed loops on their tensional properties. The end-to-end process can then be closed by implementing the mechanical properties, resulting from coupon and element level testing, back into the simulation. In addition, the loop-like structures used in this use case, can be analysed as well. The weakest spot of a single loop in tension exists in the lug area or the straight section at which layers and lines are changed. Additional research needs to focus on the optimisation of such loop by selecting the angle of change between each line and layer, resulting in the highest tensional stress at failure. The lug area of the loop needs to be optimized and changed according to the desired failure mode of the lug. Different strategies need to be designed to change the fiber path in such way that the desired failure mode of the lug is obtained and optimized. Examples which could be investigated are the ability of squeezing fibers to obtain different dimensions for the width and height of the lug area, compared to the straight sections.

Within the current experimental set-up, the possibility exists to add a second robot. Because the demonstrator has been printed using manually inserting support structure, it is of interest to implement a multiple

robot interaction which allows the complete process to be automated, without the need for manual input. The second robotic print head is in this manner programmed to print support structure in a synchronous way. The challenge in implementing this approach lies within the automation and synchronisation of two KUKA robots without causing collisions and malfunctions.

As the tolerances on the diameter of the filament cannot be changed within the process, different stacking techniques could solve the relatively large voids in between the lines. One of the techniques is retrieved from the housing industry, called "Running Bond" [23]. This stacking sequence does not place each line aligned on top of each other, also referred to as "Stack Bond", but starts each next layer with an offset of half a line width. This could potentially improve the issue related to the formation of gaps, as explained in Chapter 7 and is therefore interesting to investigate.

long term

On the long term, a point of interest is to improve the hardware of the print head. The current set-up is the result of a first iteration, build to validate the working principle. An important additional feature is the inclusion of a damping system. This ensures the same pressure on the filament during printing, which introduces more steady processing conditions and so a better quality. Together with the inclusion of a damping system, a simple contact sensor and coding at start-up are able to automate the process for bed levelling. This approach is similar to the bed levelling in FLM desktop printers. By touching the build plate with the tip of the nozzle at several points, the damping system will contract and activate a contact sensor. At this time, a signal is send to the KRC unit, which then stores the location of the point. If these steps are performed in a certain sequence along the build plate, the KRC unit can determine the location and orientation of the build plate. In addition, minor defects as little height increase will not cause the process to fail as the damping mechanism will contract. This introduces the capabilities of crossing fiber path until a certain amount, which opens a new range of possibilities for fiber path planning.
Furthermore, the orientation of the print head has been kept in a single orientation during printing. The wiring towards the control unit make it impossible to have a rotating print head. It is however beneficial for the torsional stresses in the filament to have a print head which rotates along with the print direction. For this issue a solution needs to be found in further research.

The presented research showed lots of difficulties in printing curvatures, which resulted in warpage, buckling and twisting of the printed lines. These issues have been solved consequently by introducing an Extrusion Overwrite function and Active Cooling unit. However the capabilities are still limited to a set radius of roughly 10 mm which is mainly determine by the high stiffness of the filament. This minimum radius has a negative effect on the Print Path Planning tool as no sharp corners can be printed and therefore it is proposed to test the capabilities of filament with less Fiber Volume Content with different filament diameters and analyse their effect on these critical areas. In addition the parameter settings for this different filament need to be optimised and therefore the used approach in this thesis can be consulted and validated.

A last recommendation for the long term is the introduction of real three dimensional printing. In the current set-up, the generated code uses a set orientation of the print head during the complete print. For double curved surfaces, the orientation of the print head should be kept perpendicular to the print surface, which should allow for rotation and therefore new manufacturing effects need to be introduced.

Bibliography

[1] M.A. Caminero, J.M. Chacón, I. García-Moreno, and J.M. Reverte. Interlaminar bonding performance of 3d printed continuous fibre reinforced thermoplastic composites using fused deposition modelling. *Polymer Testing*, 68:415 – 423, 2018. ISSN 0142-9418. doi: https://doi.org/10.1016/j.polymertesting.2018.04.038. URL http://www.sciencedirect.com/science/article/pii/S0142941818304264.

[2] M. Cavazzuti. *Optimization methods: from theory to design*. 01 2013. ISBN 9783642311864.

[3] S. Chatterjee and A. Hadi. *Regression Analysis by Example. Fourth edition*. 2012.

[4] C.K. Chua, K.F. Leong, and J. An. Introduction to rapid prototyping of biomaterials. In *Rapid Prototyping of Biomaterials*, pages 1 – 15. Woodhead Publishing, 2014. ISBN 978-0-85709-599-2. doi: https://doi.org/10.1533/9780857097217.1. URL http://www.sciencedirect.com/science/article/pii/B9780857095992500015.

[5] A.J. Comer, D. Ray, W.O. Obande, D. Jones, J. Lyons, I. Rosca, R.M. O' Higgins, and M.A. McCarthy. Mechanical characterisation of carbon fibre–peek manufactured by laser-assisted automated-tape-placement and autoclave. *Composites Part A: Applied Science and Manufacturing*, 69:10 – 20, 2015. ISSN 1359-835X. doi: https://doi.org/10.1016/j.compositesa.2014.10.003. URL http://www.sciencedirect.com/science/article/pii/S1359835X14003133.

[6] C. Cozmei and F. Caloian. Additive manufacturing flickering at the beginning of existence. *Procedia Economics and Finance*, 3:457–462, 2012. doi: 0.1016/S2212-5671(12)00180-3.

[7] CTC GmbH. Document x, 2019. Retrieved from: internal and confidential documentation at CTC GmbH.

[8] J. Driezen. Evaluation of robotic fused composite manufacturing, 2019. Literature Report.

[9] T. Dutra, R. Ferreira, and H. Resende. Interlaminar shear strength of continuous carbon fiber reinforced thermoplastic composites manufactured by 3d printing. 01 2017. doi: 10.26678/ABCM.COBEM2017.COB17-0282.

[10] Galdabini S.P.A. Application note EN 2563 | ASTM D 2344 interlaminar shearing test, 2017. Retrieved from https://www.schuetz-licht.de/anwendungen/biegeversuch/3-punkt-biegeversuch/din-en-2563-astm-d-2344-ils/.

[11] H. Ghiasi, K. Fayazbakhsh, D. Pasini, and L. Lessard. Optimum stacking sequence design of composite materials part ii: Variable stiffness design. *Composite Structures*, 93(1):1 – 13, 2010. ISSN 0263-8223. doi: https://doi.org/10.1016/j.compstruct.2010.06.001. URL http://www.sciencedirect.com/science/article/pii/S0263822310001947.

[12] KUKA Roboter GmbH. Kr30, 60 ha with c variants specification, 2017. Manual: Spez KR 30, 60 HA V1.

[13] A. Hazra. Using the confidence interval confidently. *Journal of thoracic disease*, 9(10):4125–4130, 2017. doi: 10.21037/jtd.2017.09.14.

[14] V. Kishore, X. Chen, C. Ajinjeru, A.A. Hassen, J. Lindahl, J. Failla, V. Kunc, and C. Duty. Additive manufacturing of high performance semicrystalline thermoplastics and their composites. 08 2016. Proceedings of the 26th Annual International Solid Freeform Fabrication Symposium.

[15] Q. Li, W. Zhao, Y. Li, W. Yang, and G. Wang. Flexural properties and fracture behavior of cf/peek in orthogonal building orientation by fdm: Microstructure and mechanism. *Polymers*, 11, 04 2019. doi: 10.3390/polym11040656.

[16] X.P.V. Maldague. *Nondestructive Evaluation of Materials by Infrared Thermography*. 1993. ISBN 13:978-1-4471-1997-5.

[17] G.T. Mark and A. Gozdz. Three dimensional printer with composite filament fabrication, 03 2013. URL https://patents.google.com/patent/US20150108677. US Patent 20150108677.

[18] K. Mori, T. Maeno, and Y. Nakagawa. Dieless forming of carbon fibre reinforced plastic parts using 3d printer. *Procedia Engineering*, 81, 2014. doi: 10.1016/j.proeng.2014.10.196.

[19] J. Moxon. From air transport system 2050 vision to planning for research and innovation. The Association of European Research Establishments in Aeronautics, 2012. Retrieved from www.erea.org.

[20] T. Nomura, D. M.Ercan, J. Lee, S. Yamasaki, T. Matsumori, A. Kawamoto, and N. Kikuchi. General topology optimization method with continuous and discrete orientation design using isoparametric projection. *International Journal for Numerical Methods in Engineering*, 101(8):571–605, 2015. doi: 10.1002/nme.4799. URL https://onlinelibrary.wiley.com/doi/abs/10.1002/nme.4799.

[21] Phoenix Analysis and Design Technologies. Ansys meshing advanced techniques. PADT Lunch and Learn Series: PDF Slideshow, 2017. URL http://www.padtinc.com/blog/wp-content/uploads/2017/04/Advanced-Techniques-in-ANSYS-Meshing_Blog.pdf.

[22] C. Red. The outlook for thermoplastics in aerospace composites. *High-Performance Composites*, 10(3): 54–63, 2014.

[23] D.A. Reid. Teaching mathematics through brick patterns. *Nexus Network Journal*, 6(2):113–123, Oct 2004. ISSN 1522-4600. doi: 10.1007/s00004-004-0022-7. URL https://doi.org/10.1007/s00004-004-0022-7.

[24] Alexander A. Safonov. 3d topology optimization of continuous fiber-reinforced structures via natural evolution method. *Composite Structures*, 215:289 – 297, 2019. ISSN 0263-8223. doi: https://doi.org/10.1016/j.compstruct.2019.02.063. URL http://www.sciencedirect.com/science/article/pii/S0263822318305609.

[25] P. Seneviratne. *Building arduino plcs : the essential techniques you need to develop arduino-based plcs*. 2017. doi: 10.1007/978-1-4842-2632-2.

[26] O. Siegmund and K. Maute. Topology optimization approaches. *Structural and Multidisciplinary Optimization*, 48(6):1031–1055, Dec 2013. ISSN 1615-1488. doi: 10.1007/s00158-013-0978-6.

[27] Solvay. Additive manufacturing filaments processing guide, 2018. Retrieved from: https://www.solvay.com/en.

[28] Minitab 18 Support. Overview for create response surface design (central composite), 2019. URL https://support.minitab.com/en-us/minitab/18/help-and-how-to/modeling-statistics/doe/how-to/response-surface/create-response-surface-design/create-central-composite-design/before-you-start/overview/.

[29] X. Tian, T. Liu, C. Yang, Q. Wang, and D. Li. Interface and performance of 3d printed continuous carbon fiber reinforced pla composites. *Composites Part A: Applied Science and Manufacturing*, 88:198 – 205, 2016. ISSN 1359-835X. doi: https://doi.org/10.1016/j.compositesa.2016.05.032. URL http://www.sciencedirect.com/science/article/pii/S1359835X16301695.

[30] Ultimaker. Ultimaker2 extended+ our most advanced 3d printer just got even better: Installation and user manual, 2015. URL https://ultimaker.com/.

[31] D.J.G. Vega, D.A. Pamplona, and A.V.M. Oliveira. Assessing the influence of the scale of operations on maintenance costs in the airline industry. *Advances in Operations Research*, 10(3):10–14, 2016. doi: https://dx.doi.org/10.1590/2238-1031.jtl.v10n3a2.

[32] V. Vuorinen. Internal Flow: Heat Transfer in Pipes, 2016. Heat and Mass Transfer Course, URL: https://mycourses.aalto.fi/ Last visited on 2019/06/03.

A

Pre-research Printing

Before designing the experimental set-up, the needed implementations are identified by performing pre-trial prints using the CF-PPS filament on an off-the-shelf desktop 3D printer, the Ultimaker S5.

A.1. Material

The material used consists of Carbon fiber reinforced PPS in the form of a pre-impregnated filament as shown in Figure A.1.1. The filament has a nominal diameter ranging from $0.60mm$ to $0.70mm$ and consist of T800H-6K Carbon Fibers with a volume fraction of 50%. The quality of the base material is excellent as only tiny microvoids are visible.

Figure A.1.1: CF-PPS filament

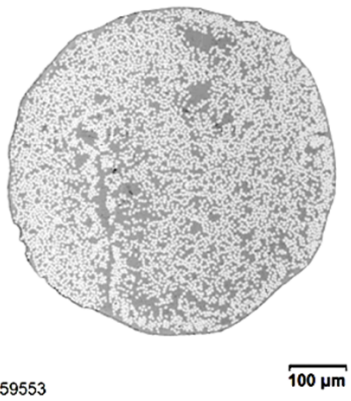

Figure A.1.2: cross-sectional view of CF-PPS prepreg filament

The material properties of the filament were measured by the manufacturer and are listed below in Table A.1.1. The thermal conductivity of the nozzle components are given in Table A.1.2 and were given by the print head manufacturer.

Table A.1.1: Material properties CF-PPS

	Neat PPS	**Carbon fiber**	**CF-PPS**
Glass transition temperature $[^\circ C]$	95	-	95
Melt temperature $[^\circ C]$	285	-	285
Specific heat $[J/kgK]$	950	750	950
Thermal conductivity $[W/mK]$	0.2	10	1
Viscosity $[Pas]$	100000 - 200	-	-

Table A.1.2: Thermal conductivity of nozzle components

Material	**Thermal conductivity** [W/mK]
Air	0.026
AlMg4.5Mn	117
CuNi20Zn20	25.94
E-Cu	394
K-therm AS550	0.37
Maraging-K93120	25.3
X45NiCrMo4	28

A.2. Print Trials

Before printing, the nozzle for neat filament is being changed with an adapted nozzle. This nozzle has a bigger inner diameter to allow the filament to fit and the end section is slightly chamfered in order to not shear the continuous fibers.

Generation of a print path is done by creating a 3D-model, transferring it into an Standard Triangle Language (STL) file and loading it in Ultimaker Cura, the slicing software used by Ultimaker. The problem which occurred is that the printer set-up is not designed to print a continuous reinforcement. Ultimaker Cura slices the 3D geometries, based on neat polymer printing. After some modifications into the software, it was possible to generate a simple continuous motion.

A.3. Findings

By printing the prepreg filament, it is found that the results become better with increasing nozzle temperature. The maximum temperature is limited to 340 $^{\circ}C$, which is on the lower side for high performance polymers. Therefore a higher extrusion temperature is needed to investigate the complete range of temperature settings.

Another finding is that the filament does not adhere to the build plate. The build plate consists of borosilicate glass, which can be heated to a maximum temperature of 105 $^{\circ}C$. Tests are being performed by using glue and foils on the build plate, from which a neat PPS foil results in the best adhesion. Due to the heating of the build plate above the glass transition temperature of PPS, the foil adheres onto the glass build plate and allows fusion between the foil and extruded filament, which provides the ideal conditions for printing the first layer.

Besides heating the build plate, the environment needs to be controlled to both have a better control on the fusion between the layers, but also to decrease the effect of thermal stresses on the part which cause warpage.

Based on these findings, the needed implementations for the experimental set-up are a heated print bed with similar heating capabilities to the Ultimaker S5, a nozzle which can be heated over 380 $^{\circ}C$ and a controlled build volume.

B

Experimental Set-up

This appendix provides all relevant data concerning the experimental set-up and the integration thereof.

B.1. Main Components

The main components of the experimental set-up are shown below.

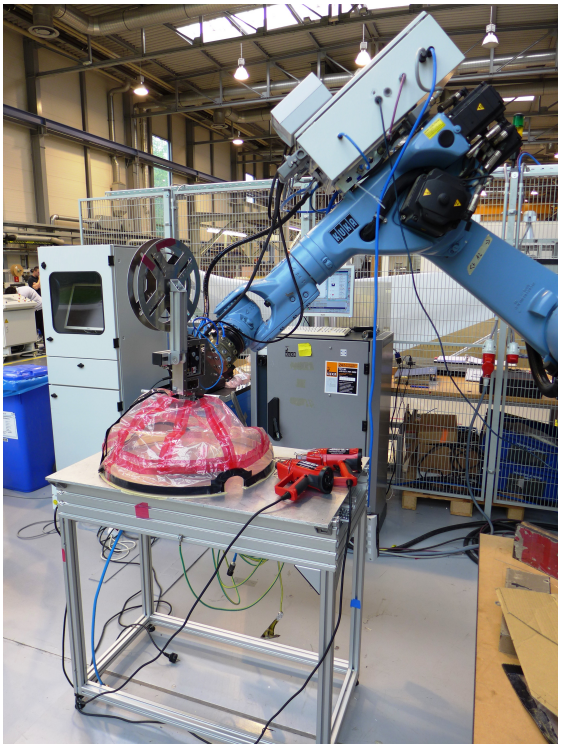

Figure B.1.1: Experimental set-up

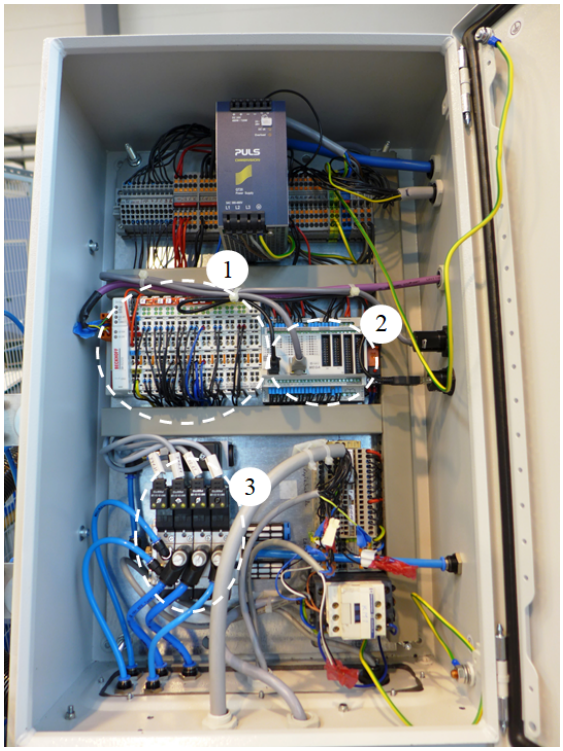

Figure B.1.2: Control Unit of the print head, 1: Bus couplers, 2: Controllino, 3: Electro-pneumatic pressure valve

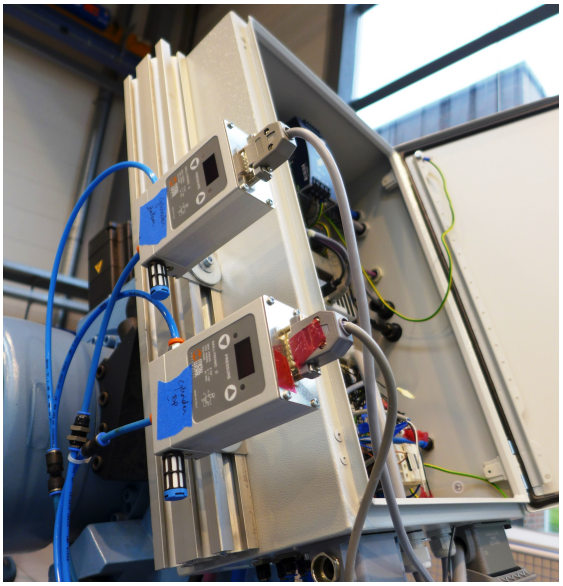

Figure B.1.3: Pressure regulators

Figure B.1.4: PID controller for the nozzle temperature setting

B.2. Foil Heat Test

Different foils are tested with respect to their temperature resistance. By using a heat gun, hot air is blown on the foils. By increasing the temperature and checking the behaviour around 150 $°C$, silicone and Airtech IPPLON foil result in the best behaviour. Examples of foils which did not work are given in Figure B.2.1 and B.2.2.

Figure B.2.1: Heat test on transparent vacuum foil

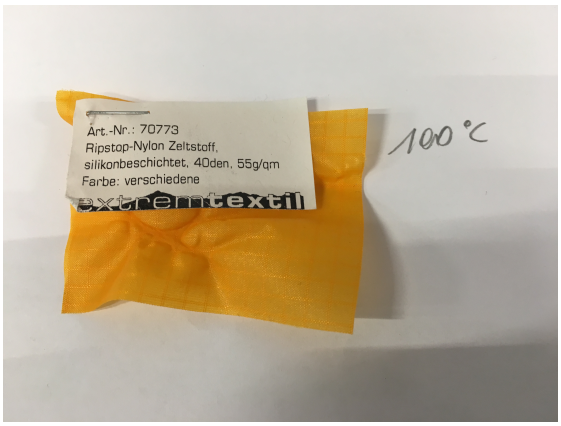

Figure B.2.2: Heat test on Ripstop-Nylon

For the proof of concept, two different tents are build. One out of silicone, glued together, the other of vacuum foil taped together.

Figure B.2.3: Airtech IPPLON foil tent

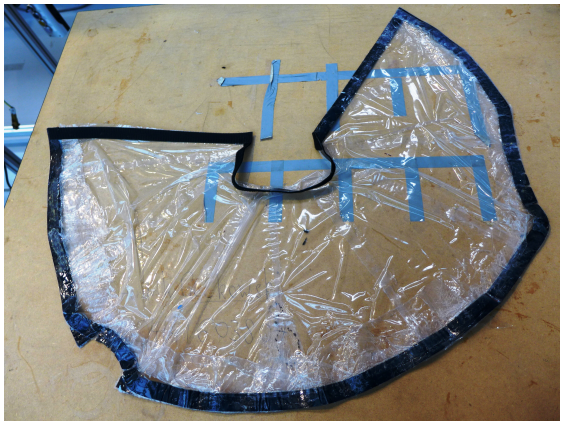

Figure B.2.4: silicone foil tent

B.3. Filament Spool

For the desing of the filament spool, Aluminium sheets of 2 mm thickness are water-jetted into spool holders. Black PLA inserts are printed using an Ultimaker S5 which can slide along the metal sides and adapt its diameter based on the received filament winding diameter. The result can be seen in Figure B.3.1 and B.3.2.

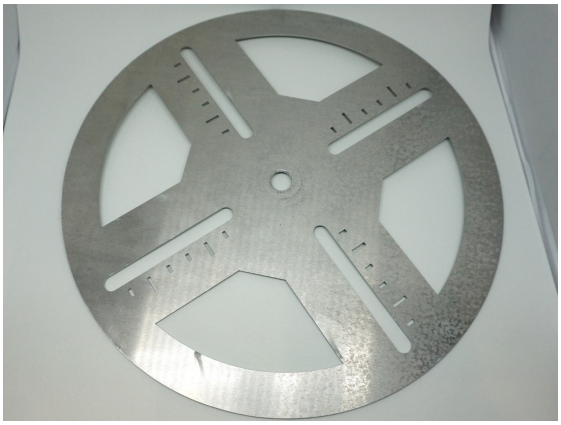

Figure B.3.1: Aluminium spool holders

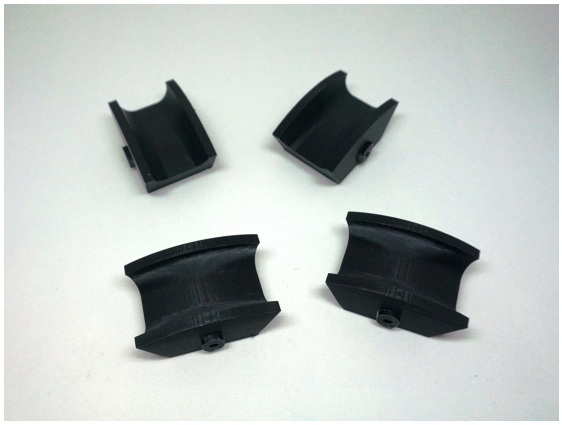

Figure B.3.2: PLA 3D-printed inserts

B.4. Active Cooling Unit

The cooling unit is made out of two copper tubes, folded around the nozzle. Small holes are drilled into the inner part of the tubes, directing the air stream to the nozzle. The tubes are soldered together and connected using pneumatic tubing to the electro pneumatic valve.

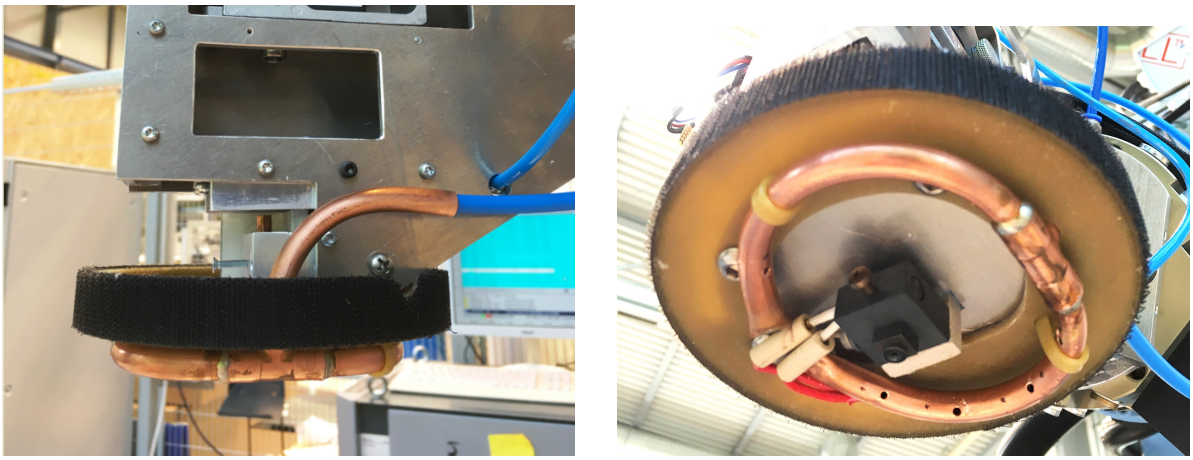

(a) Side view

(b) Bottom view

Figure B.4.1: Active Cooling unit

B.5. Exploded View of the Nozzle Geometry

To provide a clear view on the layout of the nozzle components, Figure B.5.1 shows an exploded view of the nozzle unit.

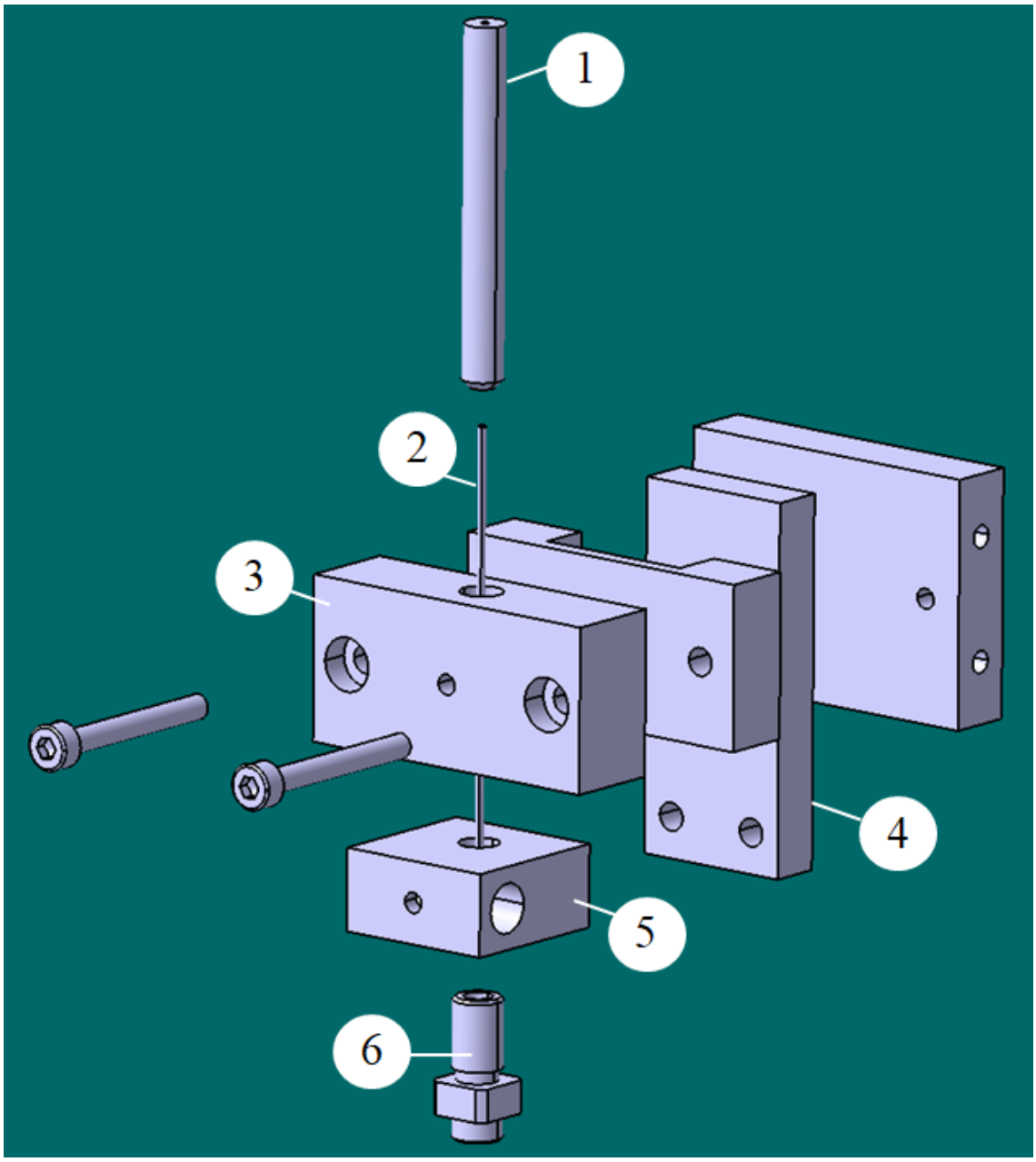

Figure B.5.1: Exploded view of the print head, 1: guiding tube, 2: filament tube, 3: filament tube fixation , 4: Insulation, 5: heat block, 6: nozzle

C

Mathcad Script

This appendix provides the script from the Matchad point generator which creates the chronological order of points. The code in this script is based on the DoE samples.

```
**********************************************************************
Company: CTC GmbH, Stade, Germany www.ctc-gmbh.com
***
Author: Jorne Driezen  jorne.driezen@airbus.com
***
Initial Date: 01.07.2019
***
Version: V1.0
**********************************************************************
```

FLATISA print head - DoE sample code

1. Input Data

The input data consist of geometrical dimensions, Fin representing the x- y coordinates of each node with the third input the minimum diameter around the node. Input data which should be changed manully is indicated with gray infill.

$$F_{in} := \begin{bmatrix} 20\ m & 0\ m & 20\ m \\ 0\ m & 20\ m & 20\ m \\ -35\ m & -35\ m & 40\ m \end{bmatrix}$$

Manual input:
Data representation: [x y Min.Diameter]

$$F := \text{stack}\left(F_{in}, \overbrace{F_{in}^{0}}\right)$$

Adds the first entry again to the list, used for closing the loop

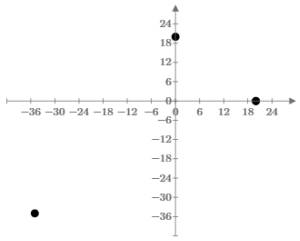

$$D_{fil} := 0.65\ m \qquad t_{lay} := 0.20\ m$$

$$n_{line} := 6 \qquad n_{lay} := 10$$

Manual input:
Diameter of the filament, layer thickness, number of lines and number of layers

$$L_w := \frac{\pi \cdot D_{fil}^{\ 2}}{4 \cdot t_{lay}} = 1.659\ m$$

Line width based on a complete fill of the volume

2. Connections between the nodes

The DoE samples consist of a 'triangular' shape, 3 nodes, which should be connected to each other. The following matrix (Cc) presents the connection between each node.

$$c_c := \begin{bmatrix} 1 & 0 \\ 2 & 1 \\ 2 & 0 \end{bmatrix}$$

Manual input:
Node number connections based on entries from [F]. First entry should have the smallest x-value

$$L_{tot} := \text{for } i \in 0 \,..\, \text{rows}(F_{in}) - 1 \;\; L_{tot}(i) \leftarrow \sqrt{\left(F_{\left(c_c^{\langle 2 \rangle}\right)_{0,1},0} - F_{\left(c_c^{\langle 2 \rangle}\right)_{0,0},0}\right)^2 + \left(F_{\left(c_c^{\langle 2 \rangle}\right)_{0,1},1} - F_{\left(c_c^{\langle 2 \rangle}\right)_{0,0},1}\right)^2}$$

L_{tot} equals the length of the straight sections between the nodes

$$\alpha_{tot} := \text{for } i \in 0 \,..\, \text{rows}(F_{in}) - 1 \;\; \alpha_{tot_i} \leftarrow \text{atan}\left(\frac{F_{\left(c_c^{\langle 2 \rangle}\right)_{0,1},1} - F_{\left(c_c^{\langle 2 \rangle}\right)_{0,0},1}}{F_{\left(c_c^{\langle 2 \rangle}\right)_{0,1},0} - F_{\left(c_c^{\langle 2 \rangle}\right)_{0,0},0}}\right) \;\; \alpha_{tot}$$

Angle with respect to the x-axis of each of the straight sections

These straight sections should be connected with the radius at each node in a tangential manner. As the starting point at the radius depends on the location of the node, an extra input (tb) is added which provides if the starting position of the radius is at the 'top' or 'bottom' of the loop. Each radius has one start and end point, so 6 entries in total.

$$tb := \begin{bmatrix} 1 \\ 1 \\ 1 \\ 3 \\ -1 \\ 1 \end{bmatrix}$$

Manual input:
1 - end point is at top of loop, start point at the top, 3 - end point is at bottom of loop, start point at the top, -1 - end point is at bottom of loop, start point at bottom

$$\alpha_{st} := \begin{bmatrix} \alpha_{tot_0} \\ \alpha_{tot_1} \\ \alpha_{tot_1} \\ \alpha_{tot_2} \\ \alpha_{tot_2} \\ \alpha_{tot_0} \end{bmatrix} \qquad \alpha_s := tb \cdot \frac{\pi}{2} + \alpha_{st} = \begin{bmatrix} 0.785 \\ 2.575 \\ 2.575 \\ 5.279 \\ -1.004 \\ 0.785 \end{bmatrix}$$

List containing start- and end point of the radius around node 1,2 and 3 respectively

The following command is used to present a visualization of the connections

$$L_{line} := \text{for } i \in 0 \,..\, \text{rows}\left(F_{in}\right) - 1 \;\; L_{line}(i) \leftarrow \begin{bmatrix} F_{\left(c_c^{\langle 2 \rangle}\right)_{0,0},0} & F_{\left(c_c^{\langle 2 \rangle}\right)_{0,0},1} \\ F_{\left(c_c^{\langle 2 \rangle}\right)_{0,1},0} & F_{\left(c_c^{\langle 2 \rangle}\right)_{0,1},1} \end{bmatrix}$$

Show the loops in a graph

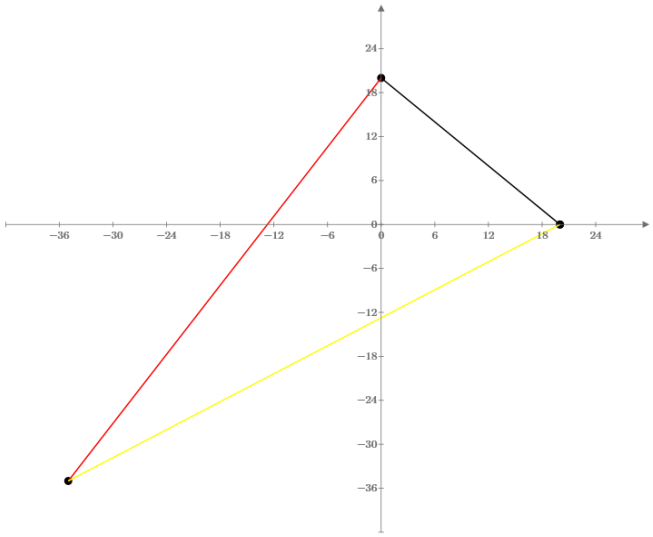

3. Extrusion overwrite

As identified during trial printing, an extrusion overwrite needs to be implemented to account for the difference in fiber and nozzle path. This is done using the RATIO-command, which calculates the percentage of underextrusion based on the radius.

$$RATIO(i) := \left\| \begin{array}{l} \text{for } k \in 0 .. n_{line} - 1 \\ \quad RATIO_k \leftarrow \dfrac{\sqrt{\left(\dfrac{F_{i,2}}{2} + k \cdot L_w\right)^2 - 0.9^2\ m^2}}{\left(\dfrac{F_{i,2}}{2} + k \cdot L_w\right)} \\ RATIO \end{array} \right.$$

Manual input:
RATIO indication the Extrusion overwrite ratio. Manual input of the distance between nozzle centerline and ironing surface (0.9mm for the current nozzle)

$$D := \left\| \begin{array}{l} \text{for } i \in 0 .. \text{rows}(c_c) - 1 \\ \quad D(i) \leftarrow \dfrac{F_{i,2}}{RATIO(i)_{\text{last}(RATIO(i))}} + \dfrac{1}{2} \cdot L_w \end{array} \right.$$

Inner diameter of at the nodes, taking into account the extrusion overwrite and half linewidth

$$Ds := \left\| \begin{array}{l} \text{for } i \in 0 .. \text{rows}(c_c) - 1 \\ \quad Ds(i) \leftarrow F_{i,2} + \dfrac{1}{2} \cdot L_w \end{array} \right.$$

Inner diameter without the extrusion overwrite, which is used as start and end diameter for the straight sections.

4. Point generation

As the start and end position of the straight sections and radius are determined, they need to be divided into multiple points which are used as a guidance for the KUKA robot. Both radius and straight sections use the same method, as inner diameter and starting points differ, it is split up.

$divarc := 16$

Manual input:
Number of divisions in the arc regions

$div(i) := \alpha_{s_{2 \cdot i+1}} - \alpha_{s_{2 \cdot i}} - 0.2$

Angle of the radius, -0.2 to make sure the end points of the straight sections do not coincide with the end points of the radius.

$divr(i) := \frac{div(i)}{divarc}$

The radius of each division

$\theta_r(i) := \left| \begin{array}{l} \text{for } f \in 1 .. divarc \\ \quad ff_f \leftarrow f \cdot divr(i) \\ ff \end{array} \right.$

List containing the angle of each point

A general definition used to transfer submatrixes into a single matrix is used in the next calculations.

$$nested2norm(NA) := \left| \begin{array}{l} \text{for } i \in 0 .. \text{last}(NA) \\ \quad M^{\overbrace{i \cdot \text{length}(NA_i)}} \leftarrow NA_i \\ M \end{array} \right.$$

The x- and y-coordinates for the radius areas can be calculated:

$$xnode(i) := \left| \begin{array}{l} \text{for } k \in 0 .. n_{line} - 1 \\ \quad N1_k \leftarrow \left(\frac{D(i+1)}{2} + k \cdot L_w \right) \cdot \cos\left(\alpha_{s_{i \cdot 2}} + 0.1 + \theta_r(i) \right) + F_{i+1,0} \\ N1 \end{array} \right.$$

x-coordinates of the arcs, based on the i-th loop and k-th line width starting from the inner diameter

$xn(i) := nested2norm(xnode(i))$

transfer to single column array

$$ynode(i) := \left| \begin{array}{l} \text{for } k \in 0 .. n_{line} - 1 \\ \quad N1_k \leftarrow \left(\frac{D(i+1)}{2} + k \cdot L_w \right) \cdot \sin\left(\alpha_{s_{i \cdot 2}} + 0.1 + \theta_r(i) \right) + F_{i+1,1} \\ N1 \end{array} \right.$$

Same for the y-coordinates

$yn(i) := nested2norm(ynode(i))$

For the straight sections, the -0.2 rad is not of use, so a second list is calculated without:

$$divs(i) := \alpha_{s_{2\cdot i+1}} - \alpha_{s_{2\cdot i}}$$

$$divrs(i) := \frac{divs(i)}{divarc}$$

$$\theta_{rs}(i) := \left\| \begin{array}{l} \text{for } f \in 1 \,..\, divarc \\ \quad ff_f \leftarrow f \cdot divrs(i) \\ ff \end{array} \right.$$

The x- and y-coordinates for the radius areas can be calculated:

$$xnodes(i) := \left\| \begin{array}{l} \text{for } k \in 0 \,..\, n_{line} - 1 \\ \quad N1_k \leftarrow \left(\frac{Ds(i+1)}{2} + k \cdot L_w \right) \cdot \cos\left(\alpha_{s_{i\cdot 2}} + \theta_{rs}(i) \right) + F_{i+1,0} \\ N1 \end{array} \right.$$

Node 1: x-coordinates of the arcs, based on the i-th loop and k-th line width starting from the inner diameter

$$xns(i) := nested2norm(xnodes(i))$$

transfer to single column array

$$ynodes(i) := \left\| \begin{array}{l} \text{for } k \in 0 \,..\, n_{line} - 1 \\ \quad N1_k \leftarrow \left(\frac{Ds(i+1)}{2} + k \cdot L_w \right) \cdot \sin\left(\alpha_{s_{i\cdot 2}} + \theta_{rs}(i) \right) + F_{i+1,1} \\ N1 \end{array} \right.$$

Same for the y-coordinates

$$yns(i) := nested2norm(ynodes(i))$$

The start and end point of the radius out of these x- and y-coordinates are obtained using:

$$x_f(i,k) := \left(xnodes(i)_k\right)_0 \qquad x_s(i,k) := \left(xnodes(i)_k\right)_{last\left(xnodes(i)_k\right)}$$

$$y_f(i,k) := \left(ynodes(i)_k\right)_0 \qquad y_s(i,k) := \left(ynodes(i)_k\right)_{last\left(ynodes(i)_k\right)}$$

f - start, s - end

$$xy_{element}(k) := \begin{bmatrix} x_s(2,k) & x_f(0,k) & y_s(2,k) & y_f(0,k) \\ x_s(0,k) & x_f(1,k) & y_s(0,k) & y_f(1,k) \\ x_f(2,k) & x_s(1,k) & y_f(2,k) & y_s(1,k) \end{bmatrix}$$

matrix incorporating the start and end points

$$\beta(i,k) := \operatorname{atan}\left(\frac{xy_{element}(k)_{i,2} - xy_{element}(k)_{i,3}}{xy_{element}(k)_{i,0} - xy_{element}(k)_{i,1}}\right)$$

Angle and length of the straight sections

$$l_{straight}(i,k) := \sqrt{\left(xy_{element}(k)_{i,2} - xy_{element}(k)_{i,3}\right)^2 + \left(xy_{element}(k)_{i,0} - xy_{element}(k)_{i,1}\right)^2}$$

The straight sections are divided into multiple points in a biased division. First a list containing biased lengths should be created:

$$divbias := 15$$

Manual input:
Number of divisions in straight section

$$list(i) := \left(\frac{L_{tot}(i)}{2}\right) \cdot \left(\frac{1}{\sum_{d=0}^{\left(\frac{divbias}{2}\right)-1} d}\right)$$

List containing dimensions which are biased

$$kk(i) := \left\| \begin{array}{l} \text{for } t \in 0 .. \dfrac{divbias}{2} - 1 \\ \quad kk_t \leftarrow list(i) \cdot t \\ kk \end{array} \right.$$

Biased lengths are stacked into a matrix

$$biass(i) := \operatorname{stack}\left(kk(i), \operatorname{reverse}(kk(i))\right)$$

This matrix is reversed and added to the original

$$bias(i) := \left\| \begin{array}{l} \text{for } bb \in 0 .. \operatorname{rows}(biass(0)) - 1 \\ \quad bias_{bb} \leftarrow \sum_{bb=0}^{bb} biass(i)_{bb} \\ bias \end{array} \right.$$

The summation of this matrix is the final result.

This matrix is then multiplied with the cosine of the corresponding angle of the straight section, which results in the points needed.

$$x_{st}(i,k) := \left\| \begin{array}{l} \text{for } s \in 0 .. \text{length}(bias(i)) - 2 \\ \quad xst_s \leftarrow xy_{element}(k)_{i,0} - \left(bias(i)_s + 0.01\ m\right) \cdot \cos(\beta(i,k)) \\ xst \end{array} \right.$$

$$y_{st}(i,k) := \left\| \begin{array}{l} \text{for } s \in 0 .. \text{length}(bias(i)) - 2 \\ \quad yst_s \leftarrow xy_{element}(k)_{i,2} - \left(bias(i)_s + 0.01\ m\right) \cdot \sin(\beta(i,k)) \\ yst \end{array} \right.$$

The startpoint of one loop is not yet defined. It is chosen to put the starting point in one of the straight sections. Therefore the previously derived matrix needs to be split at one location.

$$split := 2$$

Manual input:
The node at which the first line should go to the next line, 0 means first node, 1 means second node etc.

The following is used to split one of the straight sections in two.

$$Xfirst_{spec}(i,k) := \left\| \begin{array}{l} \text{for } b \in split .. \dfrac{\text{length}\left(x_{st}(i,k)\right) - 2}{2} \\ \quad Nsp_{b-split} \leftarrow \left(x_{st}(i,k)\right)_{\frac{\text{length}\left(x_{st}(i,k)\right)}{2} + 0.5 + b} \\ Nsp \end{array} \right.$$

$$Yfirst_{spec}(i,k) := \left\| \begin{array}{l} \text{for } b \in split .. \dfrac{\text{length}\left(y_{st}(i,k)\right) - 2}{2} \\ \quad Nsp_{b-split} \leftarrow \left(y_{st}(i,k)\right)_{\frac{\text{length}\left(y_{st}(i,k)\right)}{2} + 0.5 + b} \\ Nsp \end{array} \right.$$

$$Xsec_{spec}(i,k) := \left\| \begin{array}{l} \text{for } b \in 0 .. \dfrac{\text{length}\left(x_{st}(i,k)\right) - 2}{2} - split \\ \quad Nsp_b \leftarrow \left(x_{st}(i,k)\right)_{0+b} \\ Nsp \end{array} \right.$$

$$Ysec_{spec}(i,k) := \left\| \begin{array}{l} \text{for } b \in 0 .. \dfrac{\text{length}\left(y_{st}(i,k)\right) - 2}{2} - split \\ \quad Nsp_b \leftarrow \left(y_{st}(i,k)\right)_{0+b} \\ Nsp \end{array} \right.$$

Then the obtained matrixes for the radius and straight sections, containing the coordinates in x- and y, should be added in a chronological order as the print head should follow. This is done by stacking them into a single matrix.

$$c_{in} := \left\| \begin{array}{l} \text{for } c \in 0 .. n_{line} - 1 \\ \quad \left\| cc_c \leftarrow c \right\| \\ cc \end{array} \right\|$$

Used to generate loops from outer to inner and inner to outer

$$c_{inv} := \text{reverse}\left(c_{in}\right)$$

Additional features are included as ADV - advance function, EXOV - extrusion overwrite, ACCOOL - active cooling, etc.

First layer:

$$Nxx_f := \left\| \begin{array}{l} \text{for } c \in 0 .. n_{line} - 1 \\ \quad x1_c \leftarrow \text{stack}\left(\text{“ADV”}, \text{“EXOV”}, Xfirst_{spec}\left(0, c_{inv_c}\right)\right) \\ \quad x2_c \leftarrow \text{stack}\left(\text{“DIR”}, \text{“EXOV”}, \text{“ACCOOL”}, \text{“ADV”}, xnode\left(0\right)_{c_{inv_c}}\right) \\ \quad x3_c \leftarrow \text{stack}\left(\text{“DIR”}, \text{“ACCOOL”}, \text{“EXOV”}, \text{“ADV”}, x_{st}\left(1, c_{inv_c}\right)\right) \\ \quad x4_c \leftarrow \text{stack}\left(\text{“DIR”}, \text{“EXOV”}, \text{“ACCOOL”}, \text{“ADV”}, xnode\left(1\right)_{c_{inv_c}}\right) \\ \quad x5_c \leftarrow \text{stack}\left(\text{“DIR”}, \text{“ACCOOL”}, \text{“EXOV”}, \text{“ADV”}, \text{reverse}\left(x_{st}\left(2, c_{inv_c}\right)\right)\right) \\ \quad x6_c \leftarrow \text{stack}\left(\text{“DIR”}, \text{“EXOV”}, \text{“ACCOOL”}, \text{“ADV”}, xnode\left(2\right)_{c_{inv_c}}\right) \\ \quad x7_c \leftarrow \text{stack}\left(\text{“DIR”}, \text{“ACCOOL”}, \text{“EXOV”}, \text{“ADV”}, Xsec_{spec}\left(0, c_{inv_c}\right)\right) \\ \quad xx_c \leftarrow \text{stack}\left(x1_c, x2_c, x3_c, x4_c, x5_c, x6_c, x7_c\right) \\ xx \end{array} \right\|$$

$$Nxst_f := nested2norm\left(Nxx_f\right)$$

$$Nx_f := \text{stack}\left(Nxst_f\right)$$

$$Nyy_f := \left\| \begin{array}{l} \text{for } c \in 0 .. n_{line} - 1 \\ \quad y1_c \leftarrow \text{stack}\left(\text{“”}, 1, Yfirst_{spec}\left(0, c_{inv_c}\right), \text{“”}, RATIO\left(0\right)_{c_{inv_c}}, \text{“ON”}, \text{“”}, ynode\left(0\right)_{c_{inv_c}}\right) \\ \quad y2_c \leftarrow \text{stack}\left(\text{“”}, \text{“OFF”}, 1, \text{“”}, y_{st}\left(1, c_{inv_c}\right), \text{“”}, RATIO\left(1\right)_{c_{inv_c}}, \text{“ON”}, \text{“”}, ynode\left(1\right)_{c_{inv_c}}\right) \\ \quad y3_c \leftarrow \text{stack}\left(\text{“”}, \text{“OFF”}, 1, \text{“”}, \text{reverse}\left(y_{st}\left(2, c_{inv_c}\right)\right), \text{“”}, RATIO\left(2\right)_{c_{inv_c}}, \text{“ON”}, \text{“”}, ynode\left(2\right)_{c_{inv_c}}\right) \\ \quad y4_c \leftarrow \text{stack}\left(\text{“”}, \text{“OFF”}, 1, \text{“”}, Ysec_{spec}\left(0, c_{inv_c}\right)\right) \\ \quad yy_c \leftarrow \text{stack}\left(y1_c, y2_c, y3_c, y4_c\right) \\ yy \end{array} \right\|$$

$$Nyst_f := nested2norm\left(Nyy_f\right)$$

$$Ny_f := \text{stack}\left(Nyst_f\right)$$

The second layer is the same method, only using the reverse of c_{inv} , which results in a inner-outer, outer-inner path.

$$
\begin{aligned}
Nxx_{sec} := & \Big\| \text{for } c \in 0 \,..\, n_{line} - 1 \\
& \quad x1_c \leftarrow \text{stack}\left(\text{“ADV”}, \text{“EXOV”}, Xfirst_{spec}(0, c)\right) \\
& \quad x2_c \leftarrow \text{stack}\left(\text{“DIR”}, \text{“EXOV”}, \text{“ACCOOL”}, \text{“ADV”}, xnode(0)_c\right) \\
& \quad x3_c \leftarrow \text{stack}\left(\text{“DIR”}, \text{“ACCOOL”}, \text{“EXOV”}, \text{“ADV”}, x_{st}(1, c)\right) \\
& \quad x4_c \leftarrow \text{stack}\left(\text{“DIR”}, \text{“EXOV”}, \text{“ACCOOL”}, \text{“ADV”}, xnode(1)_c\right) \\
& \quad x5_c \leftarrow \text{stack}\left(\text{“DIR”}, \text{“ACCOOL”}, \text{“EXOV”}, \text{“ADV”}, \text{reverse}\left(x_{st}(2, c)\right)\right) \\
& \quad x6_c \leftarrow \text{stack}\left(\text{“DIR”}, \text{“EXOV”}, \text{“ACCOOL”}, \text{“ADV”}, xnode(2)_c\right) \\
& \quad x7_c \leftarrow \text{stack}\left(\text{“DIR”}, \text{“ACCOOL”}, \text{“EXOV”}, \text{“ADV”}, Xsec_{spec}(0, c)\right) \\
& \quad xx_c \leftarrow \text{stack}\left(x1_c, x2_c, x3_c, x4_c, x5_c, x6_c, x7_c\right) \\
& xx
\end{aligned}
$$

$$Nxst_{sec} := nested2norm\left(Nxx_{sec}\right)$$
$$Nx_{sec} := \text{stack}\left(Nxst_{sec}\right)$$

$$
\begin{aligned}
Nyy_{sec} := & \Big\| \text{for } c \in 0 \,..\, n_{line} - 1 \\
& \quad y1_c \leftarrow \text{stack}\left(\text{“”}, 1, Yfirst_{spec}(0, c), \text{“”}, RATIO(0)_c, \text{“ON”}, \text{“”}, ynode(0)_c\right) \\
& \quad y2_c \leftarrow \text{stack}\left(\text{“”}, \text{“OFF”}, 1, \text{“”}, y_{st}(1, c), \text{“”}, RATIO(1)_c, \text{“ON”}, \text{“”}, ynode(1)_c\right) \\
& \quad y3_c \leftarrow \text{stack}\left(\text{“”}, \text{“OFF”}, 1, \text{“”}, \text{reverse}\left(y_{st}(2, c)\right), \text{“”}, RATIO(2)_c, \text{“ON”}, \text{“”}, ynode(2)_c\right) \\
& \quad y4_c \leftarrow \text{stack}\left(\text{“”}, \text{“OFF”}, 1, \text{“”}, Ysec_{spec}(0, c)\right) \\
& \quad yy_c \leftarrow \text{stack}\left(y1_c, y2_c, y3_c, y4_c\right) \\
& yy
\end{aligned}
$$

$$Nyst_{sec} := nested2norm\left(Nyy_{sec}\right)$$
$$Ny_{sec} := \text{stack}\left(Nyst_{sec}\right)$$

Both obtained matrices are stacked and multiplied for a number of times

$$Nx := \text{stack}\left(Nx_f, Nx_{sec}\right)$$
$$Ny := \text{stack}\left(Ny_f, Ny_{sec}\right)$$

$$Xlayer := \left\| \begin{array}{l} \text{for } lay \in 0, 1..20 \\ \quad \left\| LAY_{lay} \leftarrow \text{stack}\left(Nx\right) \right\| \\ LAY \end{array} \right\|$$

$$Xlay := nested2norm\left(Xlayer\right)$$

$$Ylayer := \left\| \begin{array}{l} \text{for } lay \in 0, 1..20 \\ \quad \left\| LAY_{lay} \leftarrow \text{stack}\left(Ny\right) \right\| \\ LAY \end{array} \right\|$$

$$Ylay := nested2norm\left(Ylayer\right)$$

Depending on the number of layers needed, a submatrix is formed.

$$Xsub := \text{submatrix}\left(Xlay, 0, \left(\frac{n_{lay}}{2} \cdot \text{length}\left(Nx\right)\right) - 4, 0, 0\right)$$
$$Ysub := \text{submatrix}\left(Ylay, 0, \left(\frac{n_{lay}}{2} \cdot \text{length}\left(Ny\right)\right) - 4, 0, 0\right)$$

$$Begxl := \left[Xsub_0\right] \qquad Begyl := \left[Ysub_0\right]$$

$$X := \text{stack}\left(Begxl, Xsub\right)$$

$$Y := \text{stack}\left(Begyl, Ysub\right)$$

In addition the z-coordinate is added.

$$Zz := \text{logspace}\left(1, 1, \left(\frac{\text{length}\left(Ny\right)}{2}\right)\right)$$

$$Zlayer := \left\| \begin{array}{l} \text{for } c \in 0..n_{lay} - 1 \\ \quad \left\| Z_c \leftarrow \text{stack}\left(Zz\right) \cdot \left(c + 1\right) \cdot t_{lay} \right\| \\ Z \end{array} \right\|$$

$$Zz := nested2norm\left(Zlayer\right)$$
$$Z := \text{submatrix}\left(Zz, 0, \text{last}\left(Zz\right) - 3, 0, 0\right)$$

5. Results

The points are then transferred to Excel-format.

$$lloop := \left\| \begin{array}{l} \text{for } k \in 0 .. n_{line} - 1 \\ \quad N1_k \leftarrow \left(\left(\frac{\pi}{2} \cdot \langle D(0) + k \cdot L_w + D(1) + k \cdot L_w \rangle \right) + 2 \cdot l_{straight}(1,0) + l_{straight}(0,0) \right) \\ N1 \end{array} \right\|$$

$$length := \left(\sum lloop \right) \cdot n_{lay} = (1.432 \cdot 10^4)\ m \qquad mass := length \cdot \pi \cdot \left(\frac{D_{fil}}{2} \right)^2 \cdot 0.00157 \frac{gm}{m^3} = 7.463\ gm$$

$$printspeed := 6 \quad \text{[mm/s]}$$

$$startnote := \begin{bmatrix} \text{"\_"} & \text{"\_\_\_\_\_"} \\ \text{"[kg]"} & \text{"Mass: "} \\ \text{"[mm]"} & \text{"filament length: "} \\ \text{"[mm]"} & \text{"Layer thickness: "} \\ \text{"[mm]"} & \text{"Line width: "} \\ \text{"[mm/s]"} & \text{"Print speed: "} \\ \text{"[min]"} & \text{"Print time: "} \end{bmatrix}$$

X	Y	Z
-	----------	-
[kg]	Mass:	0.007462596
[mm]	filament length:	14324.30986
[mm]	Layer thickness:	0.2
[mm]	Line width:	1.65915362
[mm/s]	Print speed:	6
[min]	Print time:	39.7897496
-	----------	-
ADV		0.2
EXOV	1	0.2
16.08043	30.3802896	0.2
14.65186	31.80886102	0.2
13.69948	32.76124198	0.2
13.22329	33.23743245	0.2
DIR		0.2

D

Python Script

This appendix provides the code which is used to transfer the data resulting from the Mathcad point generator into a SRC-code for the KUKA robot. In addition a sample SRC-code is given and explained.

D.1. Python Code Generator

```
#-------------------------------------------------------------------------
# Author:      Jorne Driezen, TH737D
# Purpose:     transfer excel coordinates into KUKA src-code
#-------------------------------------------------------------------------
import pandas as pd

# Import the .xlsx-file
data = pd.read_excel(r'loop_1.xlsx')
data.as_matrix()

# Open the header of the KUKA
head = open("header.txt","r")

# Add printer settings to the header
txt = open("KUKA_info.txt","w+")
for i in range(0,8,1):
        txt.write((";" + str(data['Y'][i]) + " "+ str(data['Z'][i])
        + " "+ str(data['X'][i]) + "\n"))
txt.write("\n")
txt.close()

 # Transfer columns containing functions (EXOV, ACCOOL and ADVANCE) to KUKA
 # code otherwise add the coordinates in the correct format
txt = open("KUKA_src-code.txt","w+")
for i in range(8,len(data),1):
    if data['X'][i] == "EXOV":
        txt.write("Continue" + " \n")
        txt.write("EXOV = %f"  % data['Y'][i] +" \n")
    elif data['X'][i] == "ACCOOL":
        if data['Y'][i] == "ON":
            txt.write("Continue" + " \n")
            txt.write("ACCOOL = TRUE" +"\n")
        else:
            txt.write("Continue" + " \n")
            txt.write("ACCOOL = FALSE" +" \n")
    elif data['X'][i] == "DIR":
        txt.write("$ADVANCE = 1" + " \n")
    elif data['X'][i] == "ADV":
        txt.write("$ADVANCE = 5" + " \n")
    else:
        txt.write("LIN {X %f" % data['X'][i] + " ,Y %f" % data['Y'][i]
        + " ,Z %f" % data['Z'][i] + " } C_DIS \n")
txt.write("Printer_Start_Out = False \n")
txt.write("END")
txt.close()

# Combine the header and code into a single SRC-file
filenames = ['KUKA_info.txt', 'header.txt', 'KUKA_src-code.txt']
with open('loop_1.src', 'w+') as outfile:
    for fname in filenames:
        with open(fname) as infile:
            outfile.write(infile.read())
```

D.2. Example SRC-code

An example SRC-code has been made for a 2-node loop and is shown in Figure D.2.1. Note that the code has been adapted to fit on one page, "..." represents a cut-out in the code.

```
1
&ACCESS RVP
&REL 10
&PARAM EDITMASK = *
DEF FLATISA()
;FOLD BASISTECH INI
GLOBAL INTERRUPT DECL 3 WHEN $STOPMESS==TRUE DO IR_STOPM ( )
INTERRUPT ON 3
BAS (#INITMOV,0 )
;ENDFOLD (BASISTECH INI)
Printer_Start_Out = False

2
;FOLD PTP HOME  Vel= 30 % DEFAULT;%{PE}%R 5.4.33,%MKUKATPBASIS,%CMOVE,%VPTP,%P 1:PTP, 2:HOME, 3:, 5:20, 7:DEFAULT
$BWDSTART=FALSE
PDAT_ACT=PDEFAULT
FDAT_ACT=FHOME
BAS(#PTP_PARAMS,20)
$H_POS=XHOME
PTP XHOME
;ENDFOLD

3
$APO.CVEL = 100
$APO.CDIS = 1
BAS(#TOOL,6)
BAS(#BASE,1)
BAS(#VEL_CP,0.1);

4
PTP {A1 63.86, A2 -37.82, A3 93.50, A4 -164.02, A5 27.19, A6 -87.77,E1 0,E2 0,E3 0,E4 0,E5 0,E6 0}
Printer_Start_Out = True

$ADVANCE = 5
Continue
EXOV = 1.000000
5
LIN {X 3.681590 ,Y 15.110161 ,Z 0.200000 } C_DIS
LIN {X -1.080315 ,Y 19.872066 ,Z 0.200000 } C_DIS
...
LIN {X -9.651743 ,Y 28.443495 ,Z 0.200000 } C_DIS
LIN {X -10.604124 ,Y 29.395876 ,Z 0.200000 } C_DIS
6
$ADVANCE = 1
Continue
EXOV = 0.997572
Continue
ACCOOL = FALSE
$ADVANCE = 5
LIN {X -12.644639 ,Y 31.095545 ,Z 0.200000 } C_DIS
LIN {X -14.644281 ,Y 32.187236 ,Z 0.200000 } C_DIS
...
LIN {X -32.187236 ,Y 14.644281 ,Z 0.200000 } C_DIS
LIN {X -31.095545 ,Y 12.644639 ,Z 0.200000 } C_DIS
$ADVANCE = 1
Continue
ACCOOL = FALSE
Continue
EXOV = 1.000000
$ADVANCE = 5
LIN {X -29.395876 ,Y 10.604124 ,Z 0.200000 } C_DIS
LIN {X -28.443495 ,Y 9.651743 ,Z 0.200000 } C_DIS
...
LIN {X 9.651743 ,Y -28.443495 ,Z 0.200000 } C_DIS
LIN {X 10.604124 ,Y -29.395876 ,Z 0.200000 } C_DIS
$ADVANCE = 1
Continue
EXOV = 0.997572
Continue
ACCOOL = FALSE
$ADVANCE = 5
LIN {X 12.644639 ,Y -31.095545 ,Z 0.200000 } C_DIS
LIN {X 14.644281 ,Y -32.187236 ,Z 0.200000 } C_DIS
...
LIN {X 32.187236 ,Y -14.644281 ,Z 0.200000 } C_DIS
LIN {X 31.095545 ,Y -12.644639 ,Z 0.200000 } C_DIS

7
Printer_Start_Out = False
END
```

Figure D.2.1: Example Source-code

Each section is explained with the use of the KUKA KRC2 manual [**?**].

Section 1:
The first section represents the header of the code. This part is copied every time without changing. $Printer\_Start\_Out = False$ deactivates the feeding unit, which makes sure no filament is extruded before reaching its start position.

Section 2:
This section implements the commands needed to put the KUKA robot in its home position. PTP means Point-to-point movement, so it will move from its current position to the set home position.

Section 3:
Section 3 specifies the criteria for approximating the different points. APO_CVEL should contain a value from 0 to 100, which specifies the percentage of the programmed velocity at which the approximate positioning process of the points will start. In the same manner, APO_CDIS represents the distance from the points, in mm, at which the approximate positioning process will start. The next three lines select the tool frame, base frame and velocity setting in m/s respectively.

Section 4:
From the home position, the TCP will make a point-to-point movement to the position defined in between the curly brackets. The position of the TCP is now defined by each of the robot axis rotations, A1 to A6. This orientation of the TCP is kept with respect to the selected base frame. $Printer\_Start\_Out = True$ is a command which activates the feeding unit.

Section 5:
These comments define a linear (LIN) movement between each of the points, indicated between the brackets. The coordinates are with respect to the selected base frame. The C_DIS indicates that the points are approached by means of the Continuous Distance approach, set at the beginning of the source code.

Section 6:
This section switches in between the levels of the Advance function from 1 to 5. For the commands $EXOV$ and $ACCOOL$, the Advance function should be set at 1 in order to not be activated too early. Once these commands have been activated, the Advance function can be set to 5, meaning the KUKA robot starts looking 5 points in advance. Because the Advance function tends to stop at each command, $Continue$ is placed in front to not make it stop and keep the set level.

Section 7:
The last section stops the feeding unit by $Printer\_Start\_Out = False$. END indicates the end of the code.

E

Thermal Analysis

In this appendix, the validation of the thermal analysis including their results are provided. In addition, the Matlab code which simulates the filament melt flow is given with its corresponding output.

E.1. Validation IR Measurement

The test set-up of the IR measurement is shown in Figure E.1.1. Their results are shown in Section E.2 and a comparison with the simulation in Section E.2.

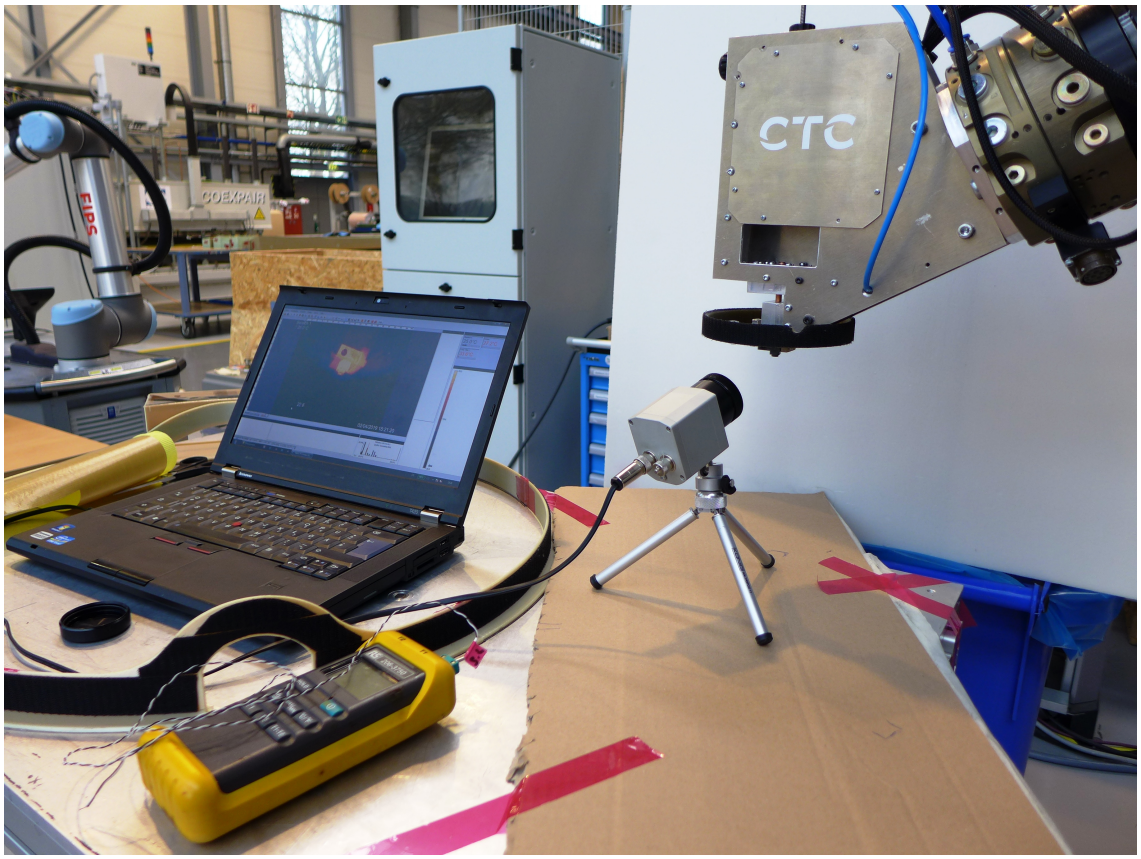

Figure E.1.1: Infrared measurement set-up

E.2. Results Temperature Comparison

Using an IR camera, the temperature distribution along the print head has been measured. As reference for the location of the measured points, Figure 6.3.10 can be used. $Tmax$ represents the maximum temperature measured in the heat block.

Table E.2.1: IR measurement results along the print head

Temperature Setting [$^{\circ}C$]	**T1** [$^{\circ}C$]	**T2** [$^{\circ}C$]	**T3** [$^{\circ}C$]	**T4** [$^{\circ}C$]	**T5** [$^{\circ}C$]	**T6** [$^{\circ}C$]	**Tmax** [$^{\circ}C$]
50	24.5	24.8	27	51.9	62.8	60.8	68.3
100	27.8	28.3	34.7	94.5	127.3	123.6	130.2
150	31.2	32.3	43.5	150	197.6	190.1	215.2
200	38.1	39.7	57	190.8	262	255.5	283.6
250	39.1	41.6	63.2	245.5	329.4	319.8	361.9
300	47.2	48.1	75.7	268	400.3	386.3	440.4

In the steady-state thermal analysis, the boundary condition for the temperature setting has been based on the maximum measured temperature resulting from the IR measurement. Running the simulation gave the following results at the same measurement points.

Table E.2.2: Thermal analysis results, final iteration

Temperature Setting [$^{\circ}C$]	**T1** [$^{\circ}C$]	**T2** [$^{\circ}C$]	**T3** [$^{\circ}C$]	**T4** [$^{\circ}C$]	**T5** [$^{\circ}C$]	**T6** [$^{\circ}C$]
62.8	26	25.7	26.1	52.4	62.3	61.7
127.3	32.3	31.6	32.6	100.5	126	124.9
197.6	39.2	38	39.7	152.9	195.4	193.6
262	45.5	44	46.1	200.8	259	256.6
329.4	52.1	50.1	52.9	251.1	325.5	322.5
400.3	59	56.6	60	303.9	395.5	391.8

A comparison between both obtained values for IR measurement and simulation are given in Table E.2.3 and present the absolute error and relative error in percentage.

Table E.2.3: Absolute- and relative error in percentage between simulation and IR measurement

Temperature Setting [$^{\circ}C$]	**T1** [$^{\circ}C$]	**T2** [$^{\circ}C$]	**T3** [$^{\circ}C$]	**T4** [$^{\circ}C$]	**T5** [$^{\circ}C$]	**T6** [$^{\circ}C$]
62.8	1.5 (6.1 %)	0.9 (3.6 %)	0.9 (3.3 %)	0.5 (1 %)	0.5 (0.8 %)	0.9 (1.5 %)
127.3	4.5 (16.2 %)	3.3 (11.7 %)	2.1 (6.1 %)	6 (6.3 %)	1.3 (1 %)	1.3 (1.1 %)
197.6	8 (25.6 %)	5.7 (17.6 %)	3.8 (8.7 %)	2.9 (1.9 %)	2.2 (1.1 %)	3.5 (1.8 %)
262	7.4 (19.4 %)	4.3 (10.8 %)	10.9 (19.1 %)	10 (5.2 %)	3 (1.1 %)	1.1 (0.4 %)
329.4	13 (33.2 %)	8.5 (20.4 %)	10.3 (16.3 %)	5.6 (2.3 %)	3.9 (1.2 %)	2.7 (0.8 %)
400.3	11.8 (25 %)	8.5 (17.7 %)	15.7 (20.7 %)	35.9 (13.4 %)	4.8(1.2 %)	5.5 (1.4 %)

E.3. IR Measurements

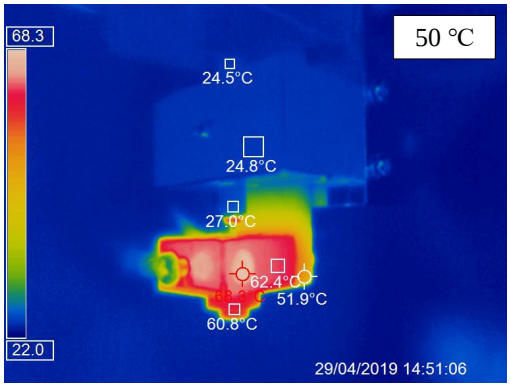

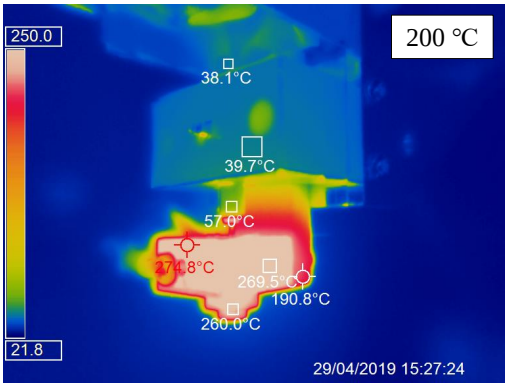

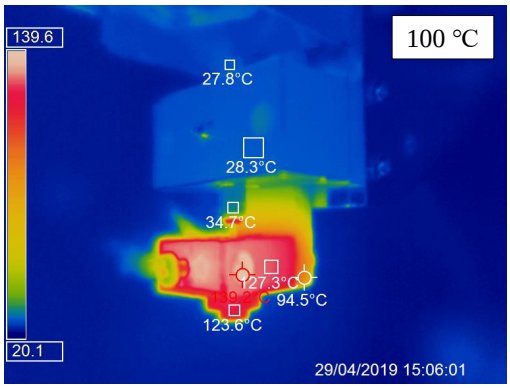

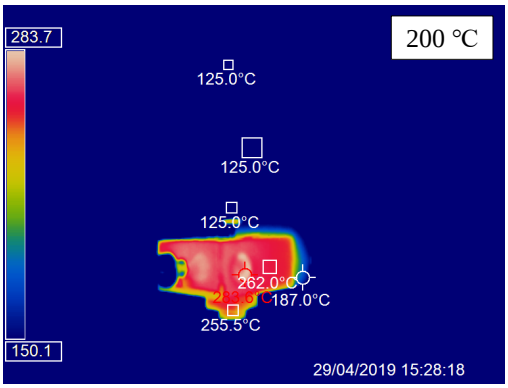

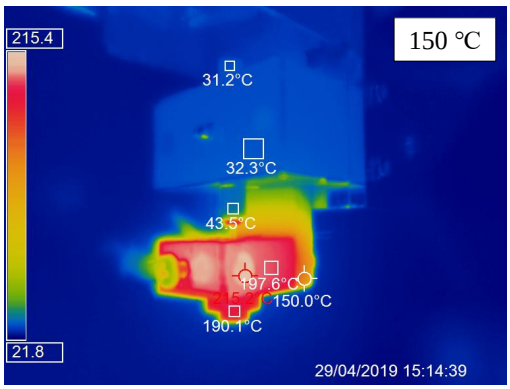

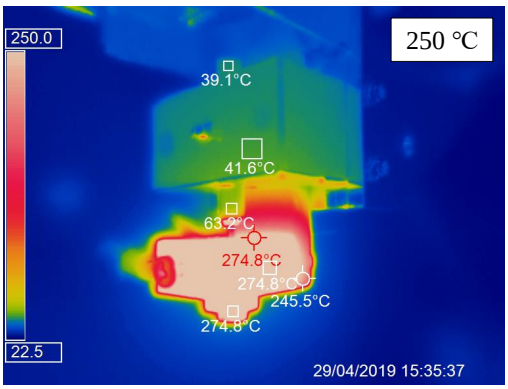

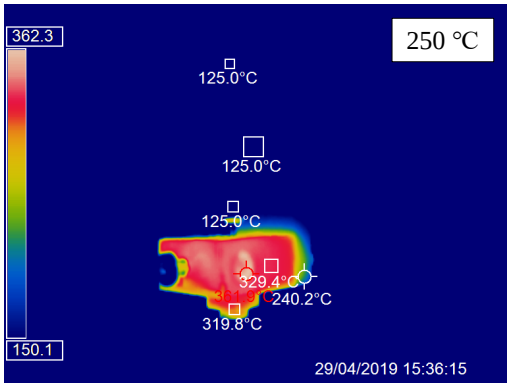
250 °C
362.3
125.0°C
125.0°C
125.0°C
329.4°C
240.2°C
319.8°C
150.1
29/04/2019 15:36:15

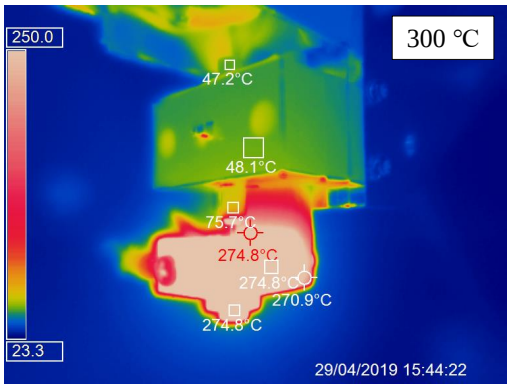
300 °C
250.0
47.2°C
48.1°C
75.7°C
274.8°C
274.8°C
270.9°C
274.8°C
23.3
29/04/2019 15:44:22

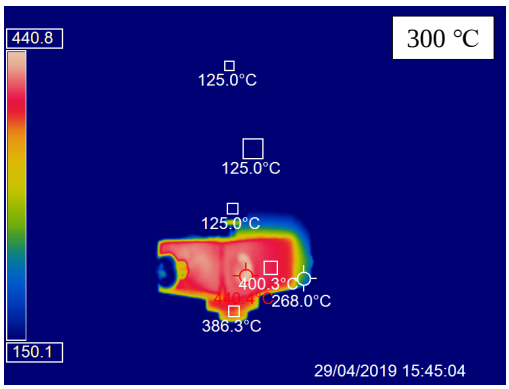
300 °C
440.8
125.0°C
125.0°C
125.0°C
400.3°C
268.0°C
386.3°C
150.1
29/04/2019 15:45:04

E.4. Filament Melt Flow Code

```
% ------------------------------------------------------------------------------------------
% Author:   Jorne Driezen, TH737D
% Purpose:  Simulate the filament melt flow in a AM process
% ------------------------------------------------------------------------------------------

%% 1. Import data
%% Initialize variables:
filename = 'C:\Users\Jorne\Documents\MATLAB\T_pipe-N380_final.txt';
delimiter = '\t';
startRow = 2;

%% Format for each line of text:
formatSpec = '%f%f%f%f%[^\n\r]';
%% Open the text file:
fileID = fopen(filename,'r');
%% Read columns of data according to the format:
dataArray = textscan(fileID, formatSpec, 'Delimiter', delimiter, 'TextType', 'string',
'HeaderLines' ,startRow-1, 'ReturnOnError', false, 'EndOfLine', '\r\n');
%% Close the text file:
fclose(fileID);
%% Create output variable:
DataTemp = table(dataArray{1:end-1}, 'VariableNames',
{'XLocationm','YLocationm','ZLocationm','TemperatureC'});
%% Clear temporary variables
clearvars filename delimiter startRow formatSpec fileID dataArray ans;

%% 2. Define constants and variables
%% Constants
T_in = 22+273.15;                   %[K] (filament temperature at inlet)
rho = 1570;                         %[kg/m3] (density of the filament)
Cp = 950;                           %[J/kgK] (specific heat of the filament)
R = 0.3*10^(-3);                    %[m] (Radius of filament)
k = 1;                              %[W/mK] (conductivity)
Nud = 3.66;                         %[-] (Nusselt number)
T_noz = 380+273.15;                 %[K] (temperature nozzle)

t_lay = 0.25*10^-3;                 %[m] (layer thickness)
L_iron = 0.5*10^-3;                 %[m] (ironing length nozzle)
dt = 0.005;                         %[-] (time steps, ironing)
%% Variables
Uz = [1 2 3 4 5 6 7 8]/1000;        %[m/s] (print speed)

%% 3. Plot temperature distribution of the tube
%% Read in Temperature distribution from Ansys
[len1,wid1] = size(DataTemp);
flip = flipud(DataTemp);                %flip columns from top to bottom
Result = table2array(flip);             %transfer data to array

Z = [];
T = [];
for i = 1:2:len1;
    Z = [Z,-Result(i,3)];
    T = [T,Result(i,4)+273.15];
end

%% Plot the data
subplot(2,2,1);
plot(Z*1000,T-273.15,'-ro',...
    'LineWidth',2,...'MarkerEdgeColor','k',...
    'MarkerFaceColor','k',...'MarkerSize',3, 'DisplayName', 'Temperature tube' )
xlabel('Longitudinal direction tube [mm]')
ylabel('Temperature tube [{\circ}C]')
grid on
hold on
```

```
%% 4. Simulate filament melt flow
%% Create sections along the tube with constant temperature:
%% Use Eq. 6.10 in Chapter 6 to calculate the temperature at each section:
Tm = [];
for i = 1:length(Uz);
    Tm_i = T_in;
    Tf_o = [];
    Zf_o = [];
    for j = 1:length(Z)-1;
         Ts = (T(1,j+1) + T(1,j))/2;
         Zs = Z(1,j+1) - Z(1,j);
        Tm_o = ((Tm_i - Ts)*exp(-((4*k*Nud*Zs)/(rho*Uz(i)*Cp*(2*R)^2))))+Ts;
        Zm_o = Z(1,j) + (Z(1,j+1) - Z(1,j))/2;
        Tf_o = [Tf_o,Tm_o];
        Zf_o = [Zf_o,Zm_o];
        Tm_i = Tm_o;
    end
    Tm = [Tm,Tm_o];

%% Produce data for the legend:
    txt = ['Uz = ',num2str(Uz(i)*1000), ' mm/s'];
    subplot(2,2,3);
    plot(Zf_o*1000, Tf_o - 273.15, 'DisplayName', txt,...'LineWidth',2)
    hold on
end
hold off
xlabel('Longitudinal direction tube [mm]')
ylabel('Temperature filament [{\circ}C]')
grid on

%% 5. Add the temperature increase due to the ironing surface
%% Calculate the time the filament conducts with the ironing surface:
time_iron = [];
for i = 1:length(Uz);
   t_i = L_iron/Uz(i);
   time_iron = [time_iron,t_i];
end

%% Add additional constants:
Lww = (pi*(2*R)^2)/(4*t_lay);       %[m] (Filament width in printed state)
h = k/(t_lay);                      %[W/m^2K] (heat transfer coefficient)
As = (L_iron*Lww);                  %[m^2] (ironing surface filament)
m = rho*(t_lay*As);                 %[kg] (mass ironing surface filament)

%% Divide the ironing surface into multiple sections and calculate the temperature
increase, based on a flat plate heat exchanger:
for j = 1:length(time_iron);
    simusteps = round(time_iron(j)/dt);
    alltime = linspace(0,time_iron(j), simusteps+1);
    txt = ['Uz = ',num2str(Uz(j)*1000), ' mm/s'];
    subplot(2,2,[2,4]);
    plot(alltime*Uz(j)*1000, (Tm(j)-T_noz)*(exp(-h*As*alltime/(m*Cp)))+
    T_noz-273.15, 'DisplayName', txt,... 'LineWidth',2)
    hold on
end
hold off
h=xlabel('distance along ironing nozzle [mm]');
h=ylabel('Temperature filament [{\circ}C]');
legend('Location','southeast')
legend show
grid on
```

Nozzle temperature: 340 °C Layer height: 0.15mm

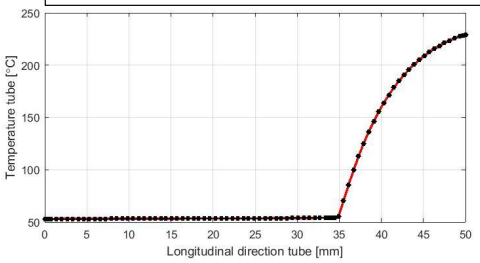

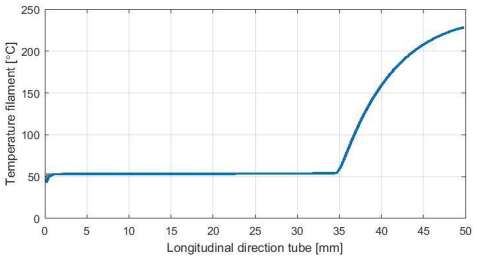

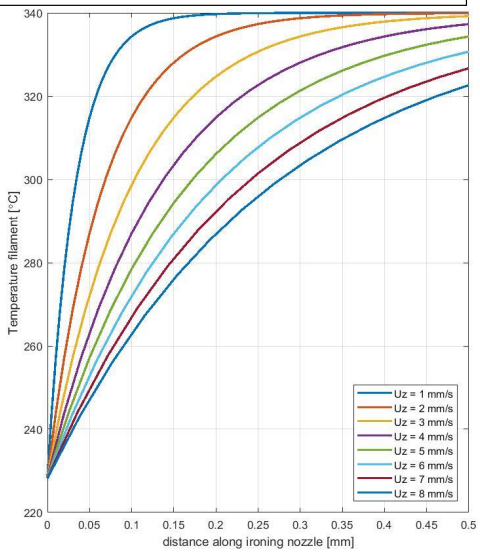

Nozzle temperature: 340 °C Layer height: 0.20mm

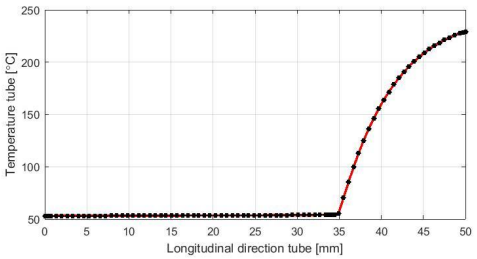

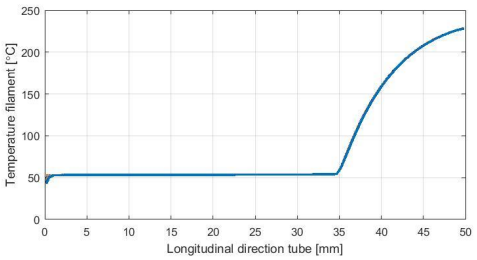

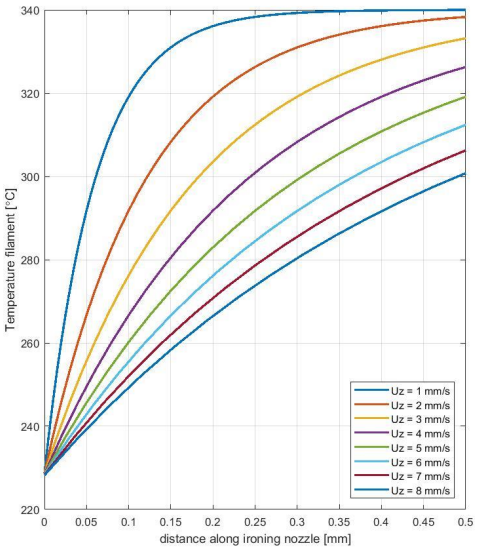

Nozzle temperature: 340 °C Layer height: 0.25mm

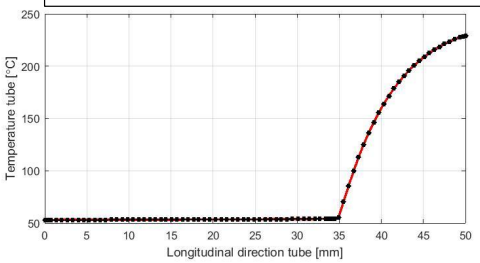

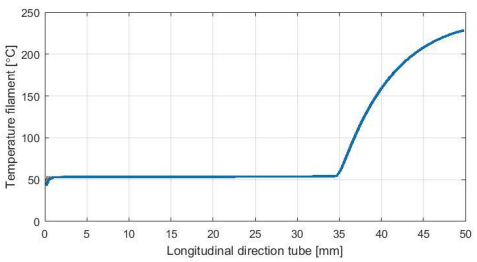

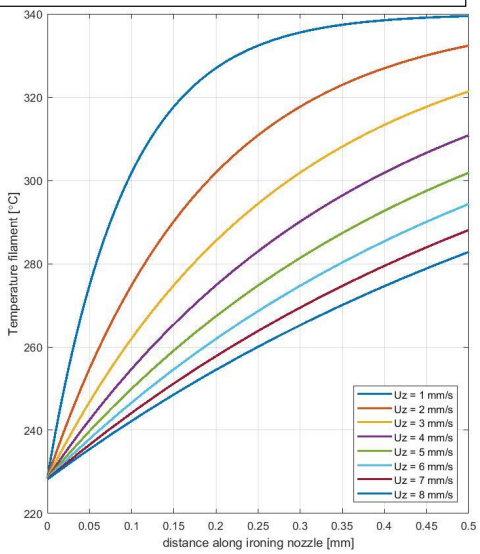

Nozzle temperature: 360 °C Layer height: 0.15mm

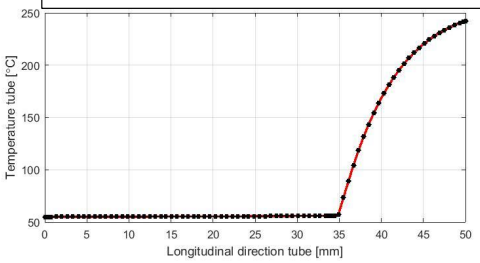

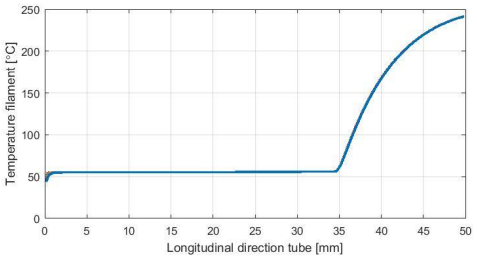

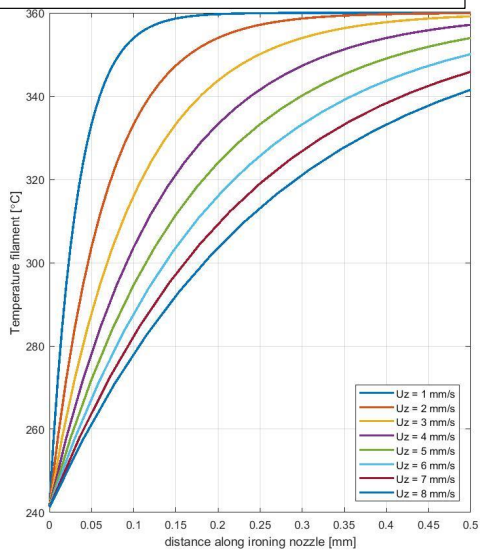

Nozzle temperature: 360 °C Layer height: 0.20mm

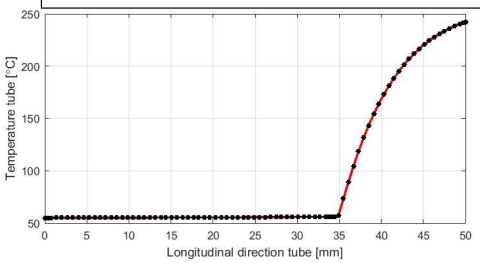

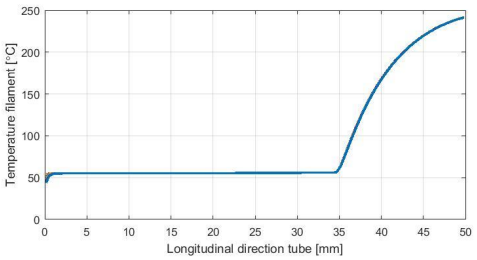

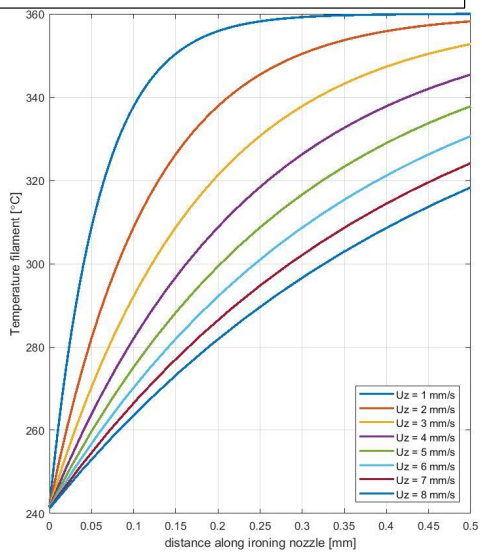

Nozzle temperature: 360 °C Layer height: 0.25mm

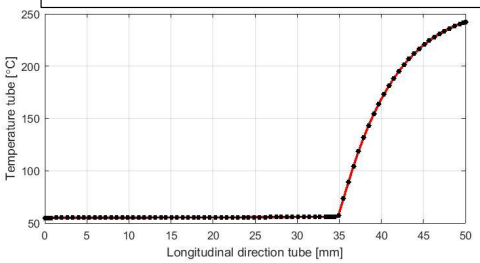

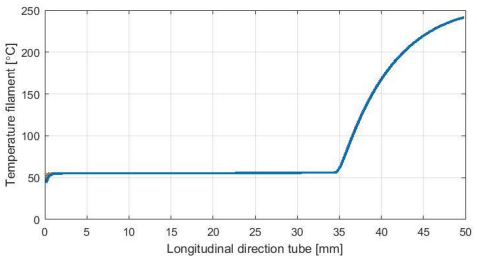

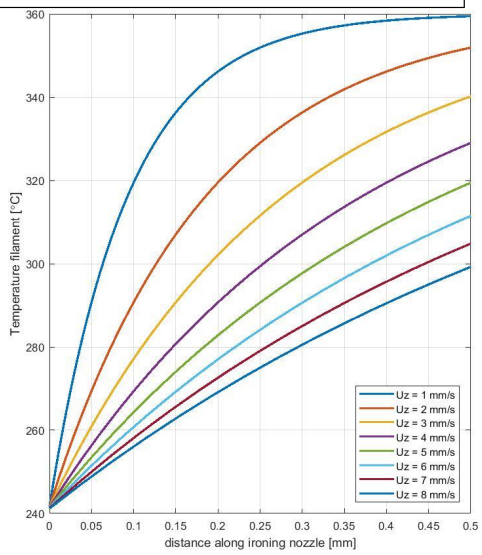

Nozzle temperature: 380 °C Layer height: 0.15mm

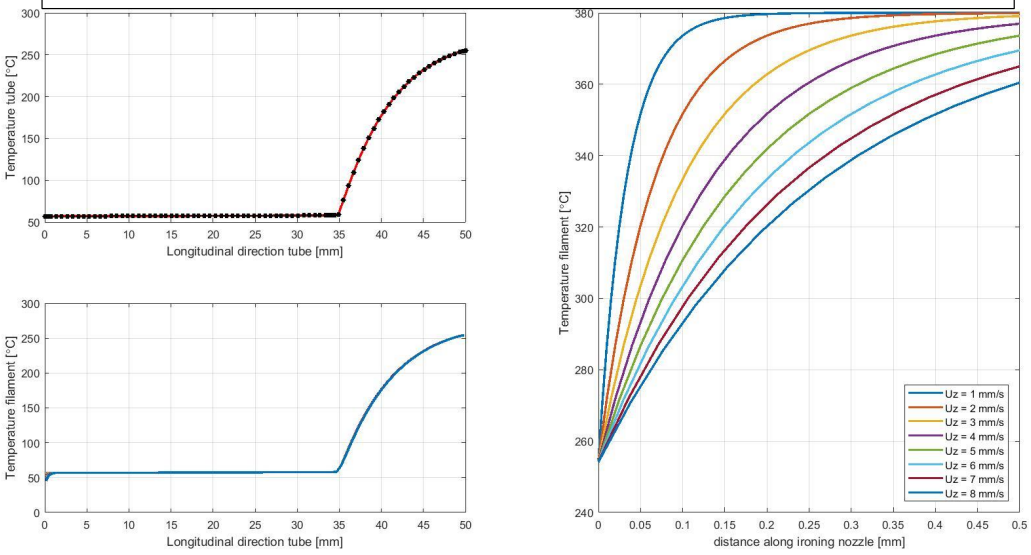

Nozzle temperature: 380 °C Layer height: 0.20mm

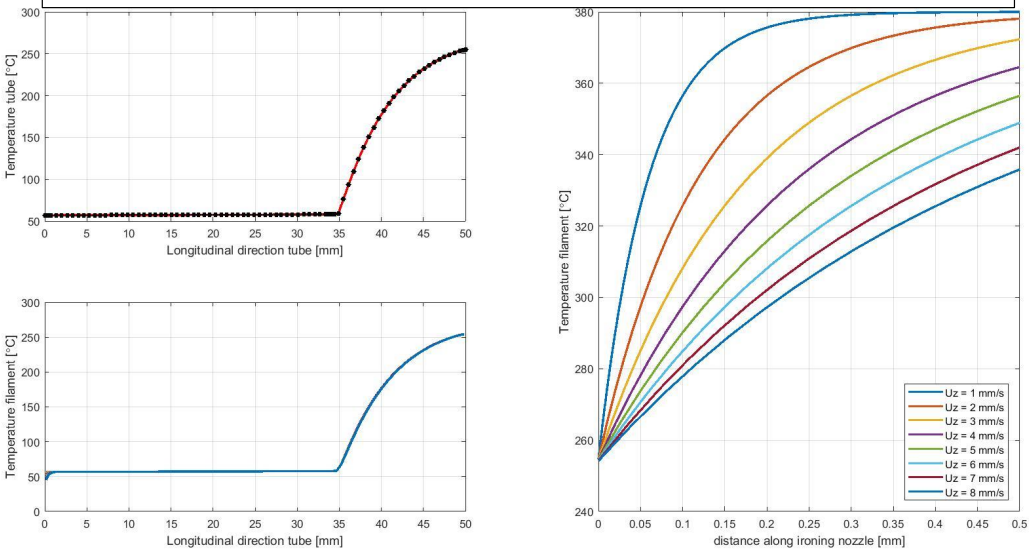

Nozzle temperature: 380 °C Layer height: 0.25mm

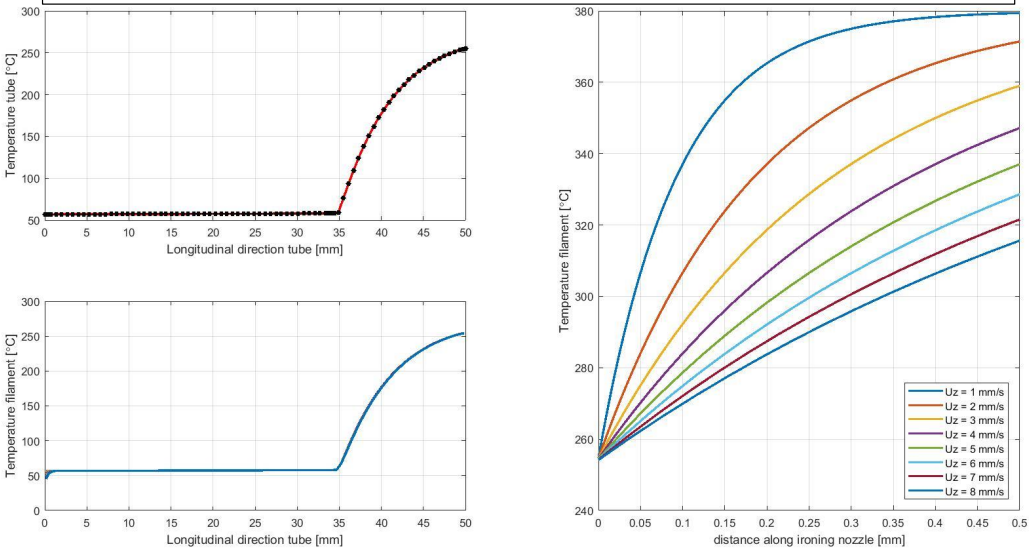

F

Specimen Preparation

The printed samples resulting from the DoE are provided in this Appendix.

F.1. Set-up Printing Samples

An example of a printed DoE sample within the experimental set-up is given in Figure F.1.1.

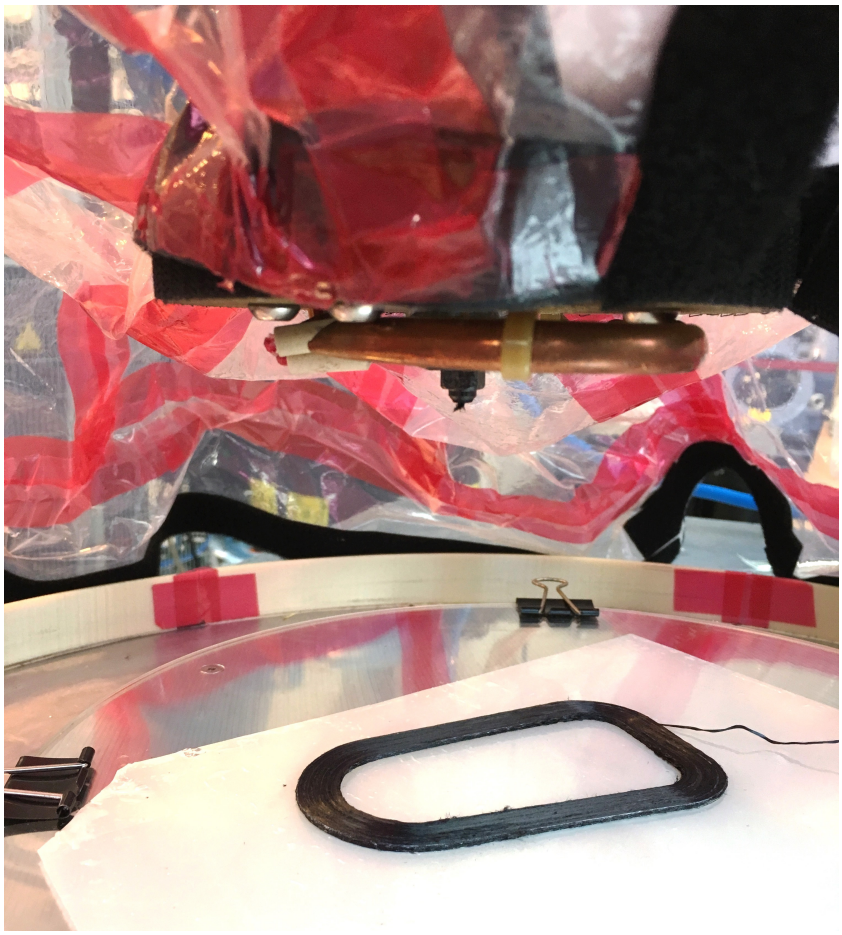

Figure F.1.1: Set-up of printing DoE samples

The additional samples are given in next section.

F.2. Printed Samples DoE

Sample 5

Sample 7

Sample 6

Sample 8

Sample 9

Sample 10

Sample 11

Sample 12

Sample 13

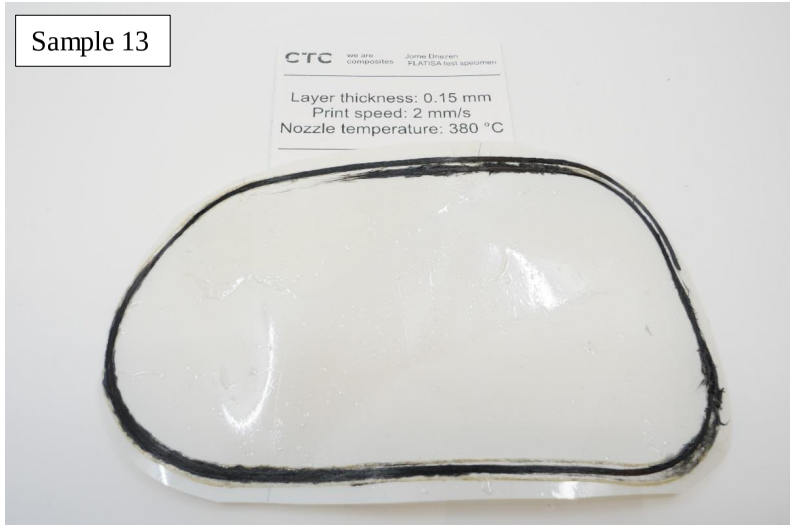

Sample 15

Sample 14

G

Test Results

This appendix provides the results from the ILSS tests and the microscopic inspection.

G.1. ILSS

In Table G.1.1 and G.1.2 the results from the ILSS test are shown. During printing of the samples, sample 11 and 13 were not feasible. These are being changed with previously printed samples from which the temperature settings were unknown. In addition sample 16 is being added which is a result from the same unknown temperature setting. Therefore the parameter settings for these samples do not match the ones shown in the Table G.1.1 and G.1.2.

Because the print temperature for sample 11, 13 and 16 is unknown, these are unable to be used in the DoE. To check the effect of the crystallinity on the void content and inter-laminar shear strength, specimen 11.1, 11.4, 13.1 an 13.4 are being annealed. It is however observed that no conclusions can be drawn on the effect of annealing, for which more analysis need to be performed.

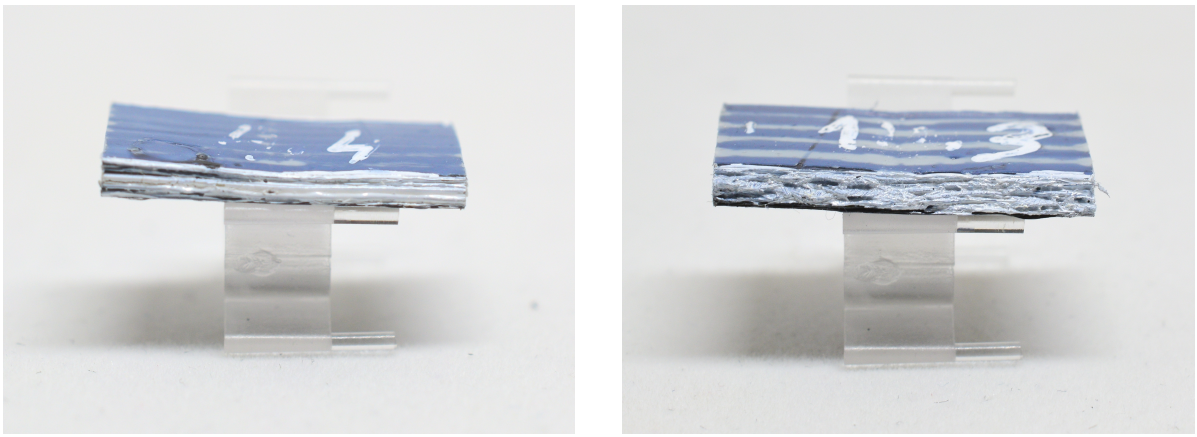

(a) Example shear failure

(b) Example plastic deformation

Figure G.1.1: Side view of the failed specimen

In addition, the load vs displacement graphs of each specimen are shown.

Table G.1.1: ILSS test results, part 1

Sample	Thickness [mm]	Width [mm]	Fmax [N]	Fbreak [N]	ILSS [Mpa]	Failure mode	Print speed [mm/s]	Layer height [mm]	Temperature [°C]	Valid
S1.1	2,09	9,75	1034	1034	38.1	Flexure	2	0.25	380	No
S1.2	2,05	9,76	991	991	37.1	Multiple shear	2	0.25	380	Yes
S1.3	1,87	10,65	1148	1061	40.0	Plastic deformation	2	0.25	380	No
S1.4	1,94	10,18	1081	1075	40.8	Plastic deformation	2	0.25	380	No
S2.1	2,37	10,35	1002	968	29.6	Multiple shear	4	0.2	340	Yes
S2.2	2,42	10,17	1310	1028	31.3	Plastic deformation	4	0.2	340	No
S2.3	2,18	10,92	1284	978	30.8	Plastic deformation	4	0.2	340	No
S2.4	2,16	10,92	1102	987	31.4	Multiple shear	4	0.2	340	Yes
S3.1	2,18	9,98	582	509	17.5	Multiple shear	6	0.25	340	Yes
S3.2	2,12	9,37	651	602	22.7	Multiple shear	6	0.25	340	Yes
S3.3	2,06	9,73	575	548	20.5	Multiple shear	6	0.25	340	Yes
S3.4	2,08	9,48	607	511	19.4	Plastic deformation	6	0.25	340	No
S4.1	2,20	10,71	1205	1205	38.4	Multiple shear	4	0.25	360	Yes
S4.2	2,15	9,87	1109	1109	39.2	Multiple shear	4	0.25	360	Yes
S4.3	2,08	10,62	1041	1041	35.3	Multiple shear	4	0.25	360	Yes
S4.4	2,04	10,48	1076	808	28.3	Multiple shear	4	0.25	360	Yes
S5.1	2,33	11,25	1184	1184	33.9	Plastic deformation	6	0.15	380	No
S5.2	2,17	11,11	1185	1149	35.7	Plastic deformation	6	0.15	380	No
S5.3	2,13	11,51	1195	1124	34.4	Plastic deformation	6	0.15	380	No
S5.4	2,14	12,11	1193	1003	29.0	Plastic deformation	6	0.15	380	No
S6.1	2,38	10,36	1183	1183	36.0	Plastic deformation	4	0.2	380	No
S6.2	2,36	10,50	1369	1300	39.3	Plastic deformation	4	0.2	380	No
S6.3	2,08	11,02	1231	1222	40.0	Plastic deformation	4	0.2	380	No
S6.4	2,03	11,08	1225	1190	39.7	Plastic deformation	4	0.2	380	No
S7.1	2,23	10,75	1038	879	27.5	Multiple shear	6	0.2	360	Yes
S7.2	2,20	10,27	1010	976	32.4	Multiple shear	6	0.2	360	Yes
S7.3	2,89	11,39	980	937	21.3	Plastic deformation	6	0.2	360	No
S7.4	1,93	11,43	1033	987	33.6	Plastic deformation	6	0.2	360	No
S8.1	2,35	11,35	1148	1148	32.3	Not detectable	4	0.15	360	(-)
S8.2	2,93	11,19	1137	1110	25.4	Not detectable	4	0.15	360	(-)
S8.3	2,13	11,26	1061	1050	32.8	Plastic deformation	4	0.15	360	No
S8.4	2,07	11,17	1069	1058	34.3	Plastic deformation	4	0.15	360	No
S9.1	2,38	9,99	968	961	30.3	Multiple shear	6	0.25	380	Yes
S9.2	2,25	9,72	931	931	31.9	Multiple shear	6	0.25	380	Yes
S9.3	2,09	9,60	984	984	36.8	Multiple shear	6	0.25	380	Yes
S9.4	2,10	9,31	1036	1021	39.2	Multiple shear	6	0.25	380	Yes
S10.1	2,30	10,94	1132	1132	33.7	Plastic deformation	4	0.2	360	No
S10.2	2,26	10,33	1156	1107	35.6	Multiple shear	4	0.2	360	Yes
S10.3	2,10	11,16	1250	1092	34.9	Plastic deformation	4	0.2	360	No
S10.4	2,05	11,29	1085	1072	34.7	Plastic deformation	4	0.2	360	No
S11.1	2,22	9,79	854	763	26.3	Plastic deformation	2	0.15	340	No
S11.2	2,17	9,88	896	745	26.1	Plastic deformation	2	0.15	340	No
S11.3	2,08	10,34	841	807	28.1	Plastic deformation	2	0.15	340	No
S11.4	2,14	10,26	936	864	29.5	Plastic deformation	2	0.15	340	No
S12.1	2,33	10,20	1087	1087	34.3	Plastic deformation	2	0.2	360	No
S12.2	2,42	10,30	1015	984	29.6	Plastic deformation	2	0.2	360	No
S12.3	2,20	10,39	1004	997	32.7	Plastic deformation	2	0.2	360	No
S12.4	2,16	10,31	995	995	33.5	Not detectable	2	0.2	360	(-)

Table G.1.2: ILSS test results, part 2

Sample	Thickness [mm]	Width [mm]	Fmax [N]	Fbreak [N]	ILSS [Mpa]	Failure mode	Print speed [mm/s]	Layer height [mm]	Temperature [°C]	Valid
S13.1	2,37	10,45	1089	1089	33.3	Plastic deformation	2	0.15	380	No
S13.2	2,18	10,28	1053	1041	34.8	Plastic deformation	2	0.15	380	No
S13.3	2,06	11,33	916	916	29.4	Plastic deformation	2	0.15	380	No
S13.4	2,04	10,61	842	842	29.2	Plastic deformation	2	0.15	380	No
S14.1	2,39	11,42	1064	1064	29.2	Plastic deformation	6	0.15	340	No
S14.2	2,34	11,36	1081	1075	30.3	Plastic deformation	6	0.15	340	No
S14.3	2,21	12,19	922	922	25.7	Plastic deformation	6	0.15	340	No
S14.4	2,15	11,73	891	891	26.5	Plastic deformation	6	0.15	340	No
S15.1	2,06	9,87	711	686	25.3	Multiple shear	2	0.25	340	Yes
S15.2	2,05	9,53	675	616	23.6	Multiple shear	2	0.25	340	Yes
S15.3	2,04	10,28	764	764	27.3	Multiple shear	2	0.25	340	Yes
S15.4	1,97	9,99	736	707	26.9	Multiple shear	2	0.25	340	Yes
S16.1	2,06	10,04	804	619	22.4	Multiple shear	4	0.2	360	Yes
S16.2	2,11	10,51	749	619	20.9	Not detectable	4	0.2	360	(-)
S16.3	1,85	10,85	707	707	26.4	Not detectable	4	0.2	360	(-)
S16.4	1,79	10,48	762	730	29.2	Not detectable	4	0.2	360	(-)

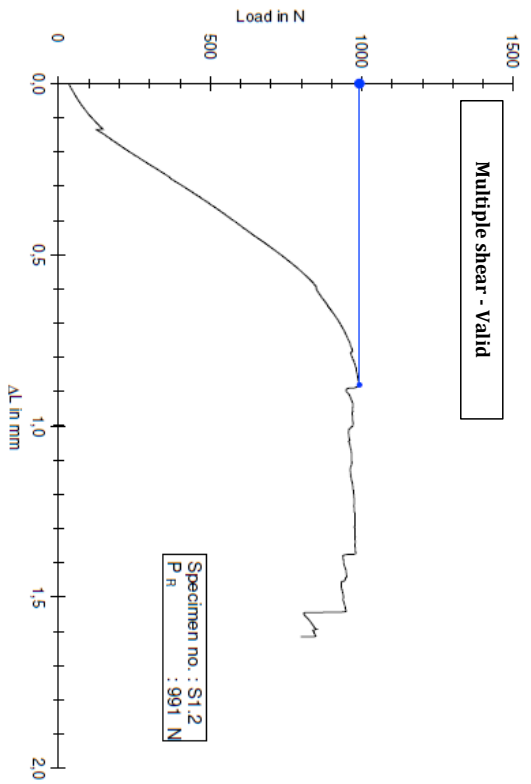
Flexure – Non valid
Load in N
ΔL in mm
Specimen no. : S1.1
P R : 1034 N

Multiple shear - Valid
Load in N
ΔL in mm
Specimen no. : S1.2
P R : 991 N

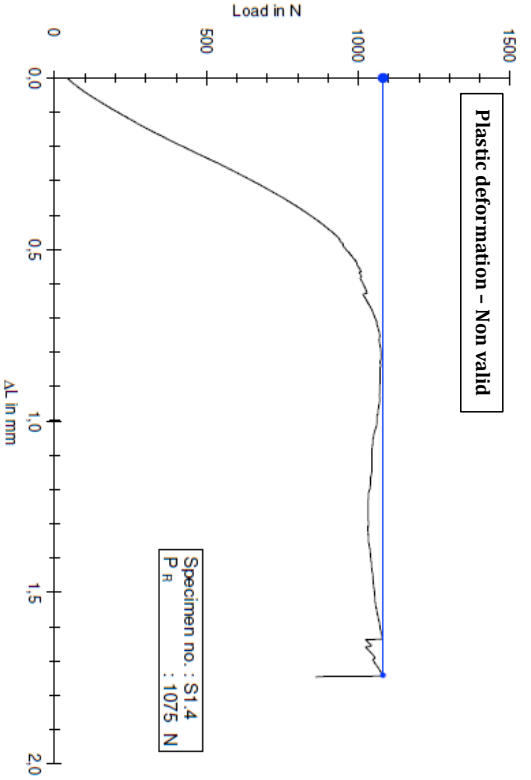
Plastic deformation – Non valid
Load in N
ΔL in mm
Specimen no. : S1.3
P R : 1061 N

Plastic deformation – Non valid
Load in N
ΔL in mm
Specimen no. : S1.4
P R : 1075 N

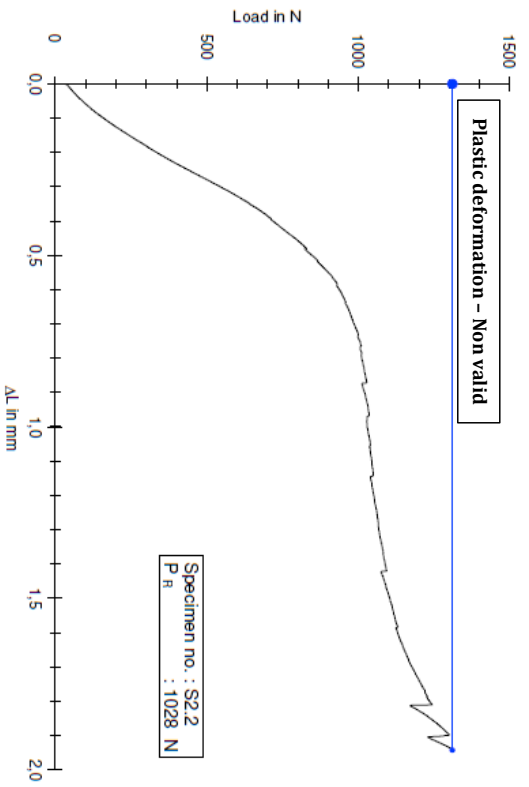
Plastic deformation – Non valid
Load in N
ΔL in mm
Specimen no. : S2.2
P R : 1028 N

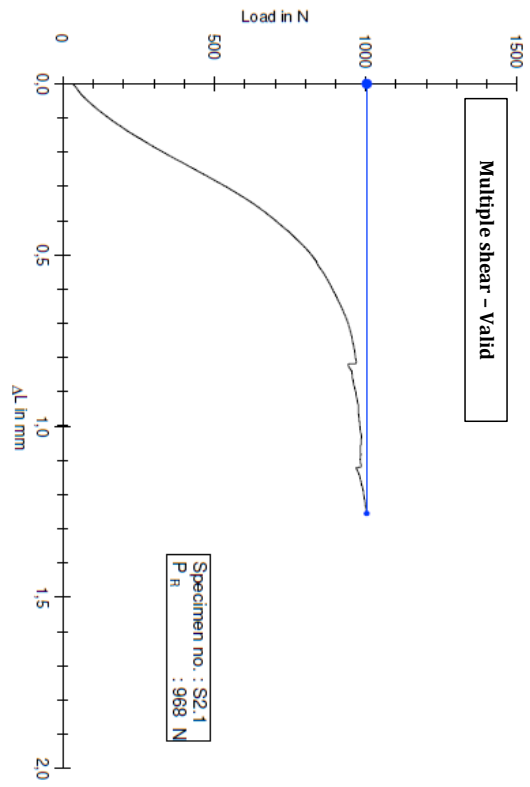
Multiple shear – Valid
Load in N
ΔL in mm
Specimen no. : S2.1
P R : 968 N

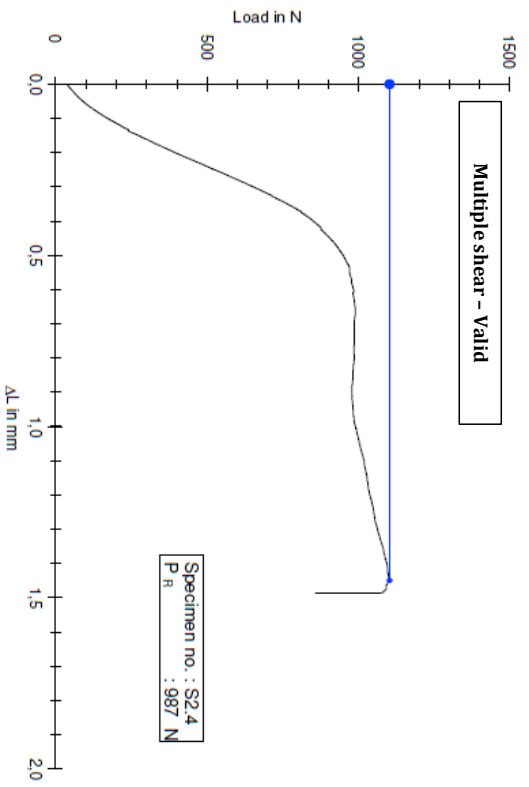
Multiple shear – Valid
Load in N
ΔL in mm
Specimen no. : S2.4
P R : 987 N

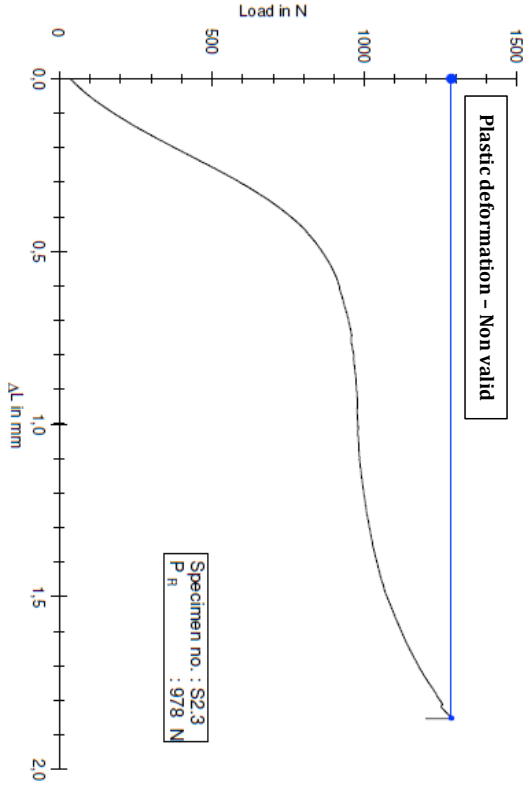
Plastic deformation – Non valid
Load in N
ΔL in mm
Specimen no. : S2.3
P R : 978 N

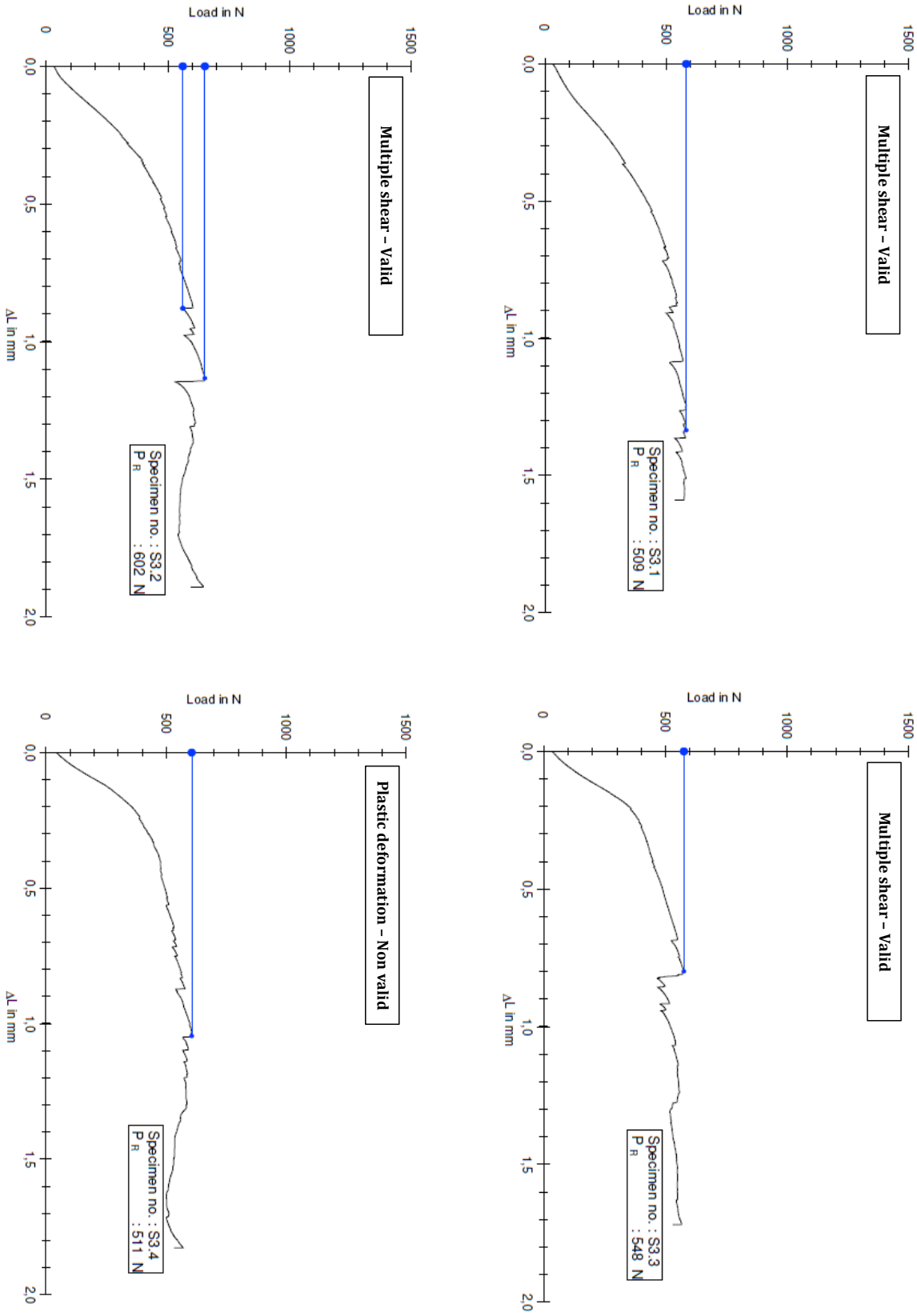
Multiple shear – Valid
Load in N
ΔL in mm
Specimen no. : S3.1
P R : 509 N
Multiple shear – Valid
Load in N
ΔL in mm
Specimen no. : S3.2
P R : 602 N
Multiple shear – Valid
Load in N
ΔL in mm
Specimen no. : S3.3
P R : 548 N
Plastic deformation – Non valid
Load in N
ΔL in mm
Specimen no. : S3.4
P R : 511 N

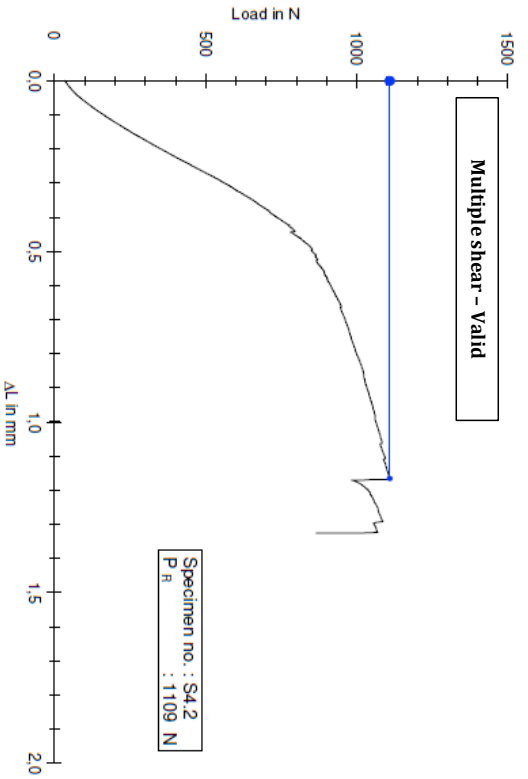
Multiple shear – Valid
Load in N
ΔL in mm
Specimen no. : S4.1
P R : 1205 N

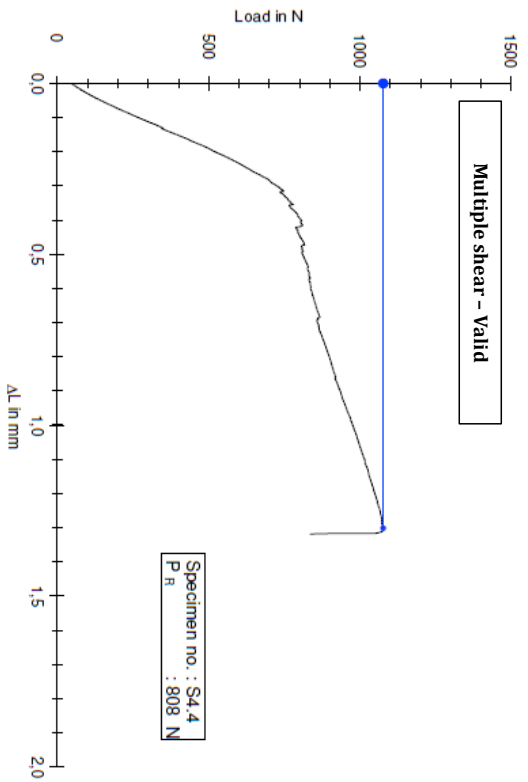
Multiple shear – Valid
Load in N
ΔL in mm
Specimen no. : S4.2
P R : 1109 N

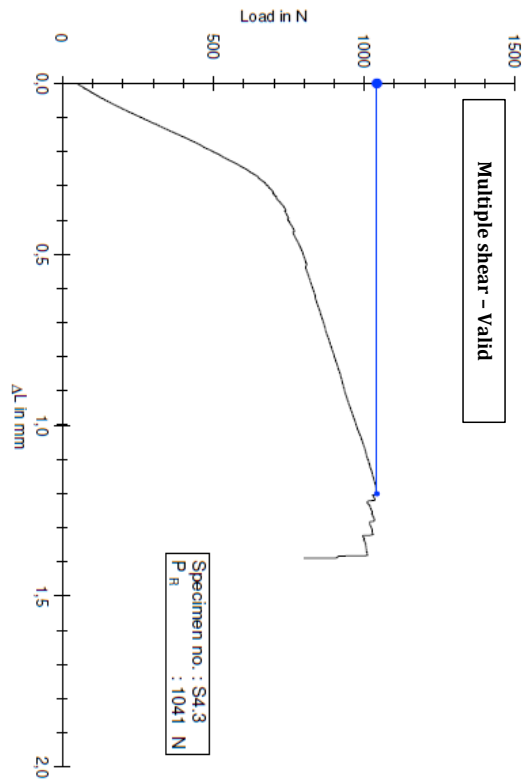
Multiple shear – Valid
Load in N
ΔL in mm
Specimen no. : S4.3
P R : 1041 N

Multiple shear – Valid
Load in N
ΔL in mm
Specimen no. : S4.4
P R : 808 N

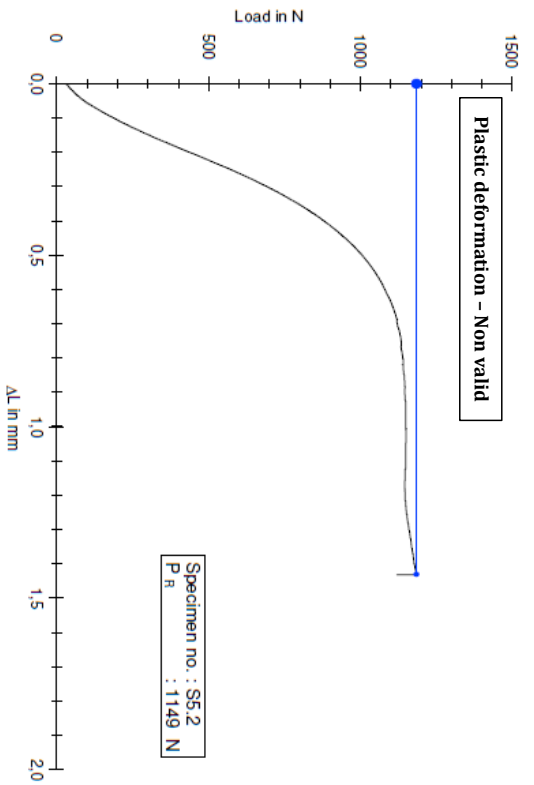
Load in N
ΔL in mm
Plastic deformation – Non valid
Specimen no. : S5.1
P R : 1184 N

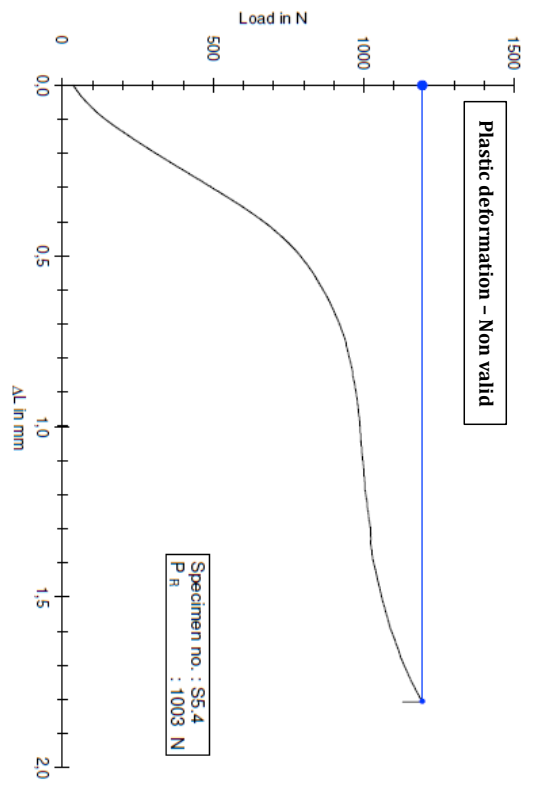
Load in N
ΔL in mm
Plastic deformation – Non valid
Specimen no. : S5.2
P R : 1149 N

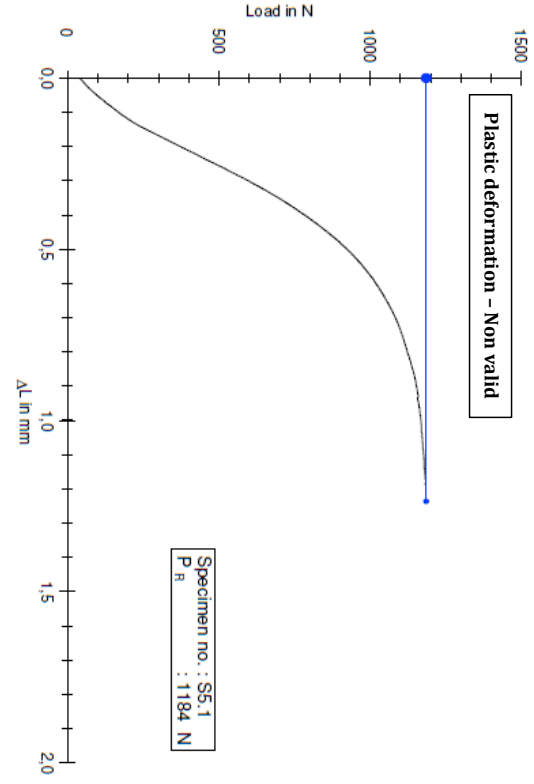
Load in N
ΔL in mm
Plastic deformation – Non valid
Specimen no. : S5.3
P R : 1124 N

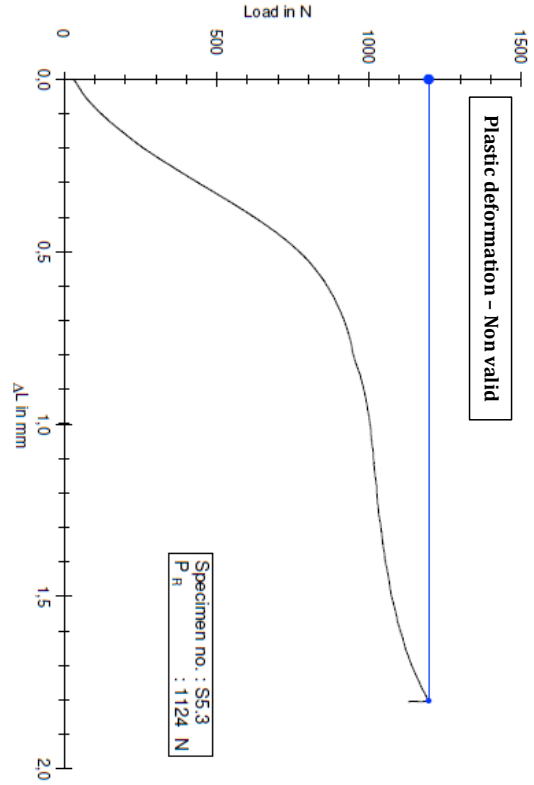
Load in N
ΔL in mm
Plastic deformation – Non valid
Specimen no. : S5.4
P R : 1003 N

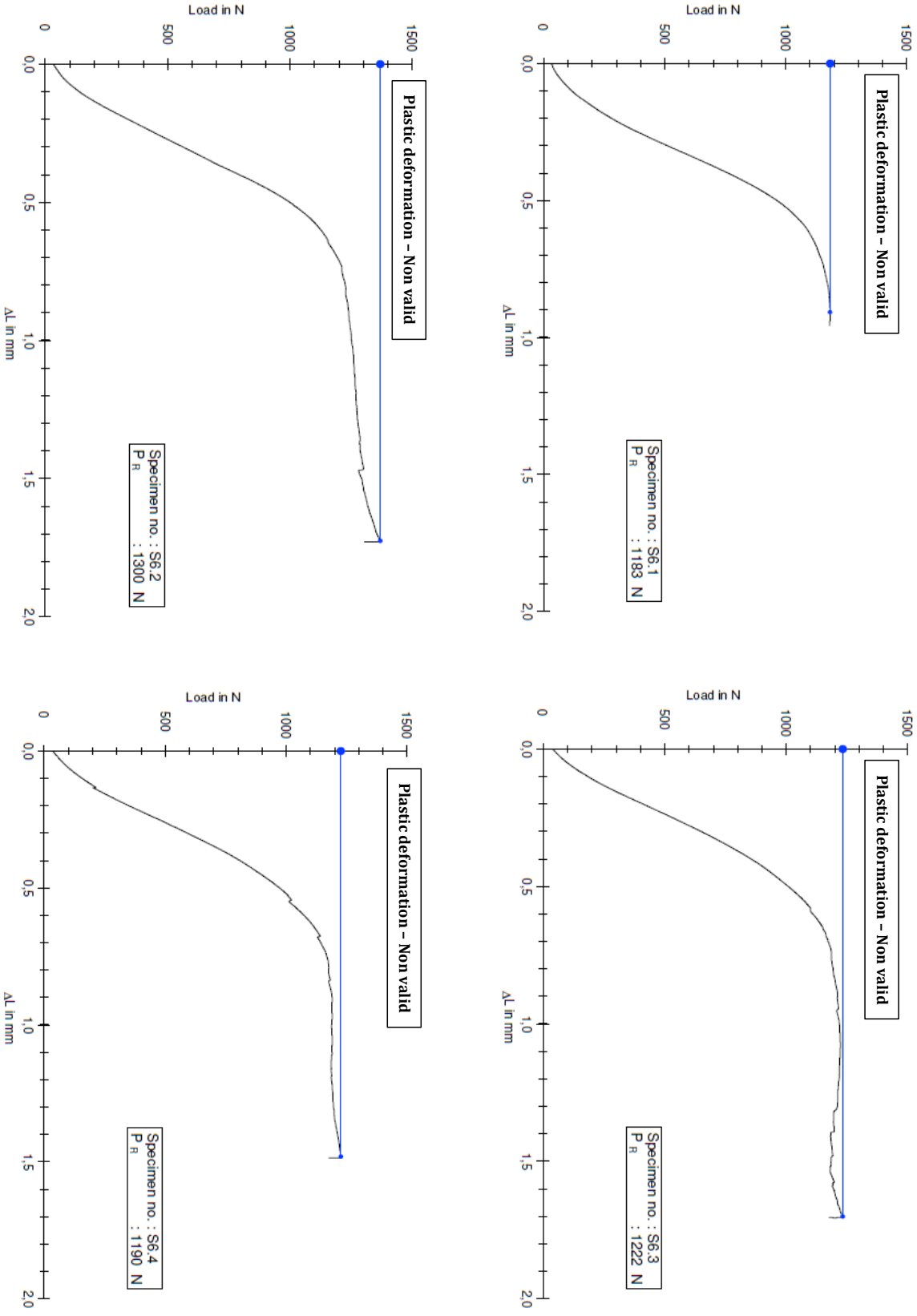
Plastic deformation – Non valid
Load in N
ΔL in mm
Specimen no. : S6.1
P R : 1183 N
Plastic deformation – Non valid
Load in N
ΔL in mm
Specimen no. : S6.2
P R : 1300 N
Plastic deformation – Non valid
Load in N
ΔL in mm
Specimen no. : S6.3
P R : 1222 N
Plastic deformation – Non valid
Load in N
ΔL in mm
Specimen no. : S6.4
P R : 1190 N

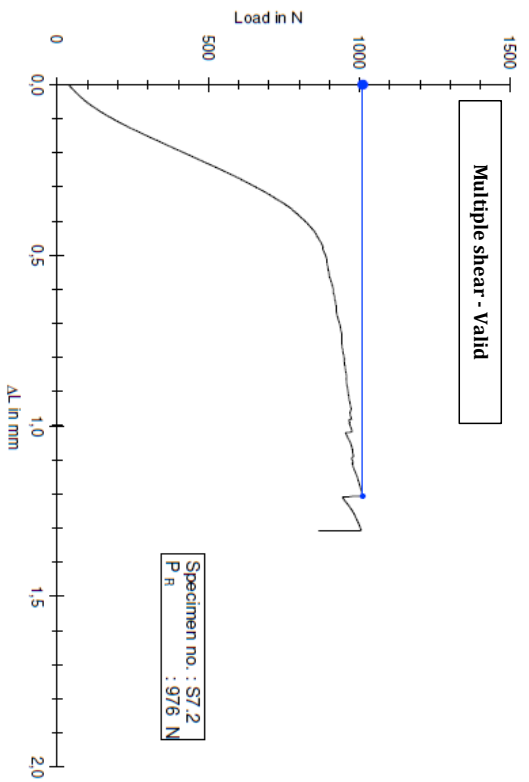
Multiple shear - Valid
Load in N
ΔL in mm
Specimen no. : S7.1
P_R : 879 N

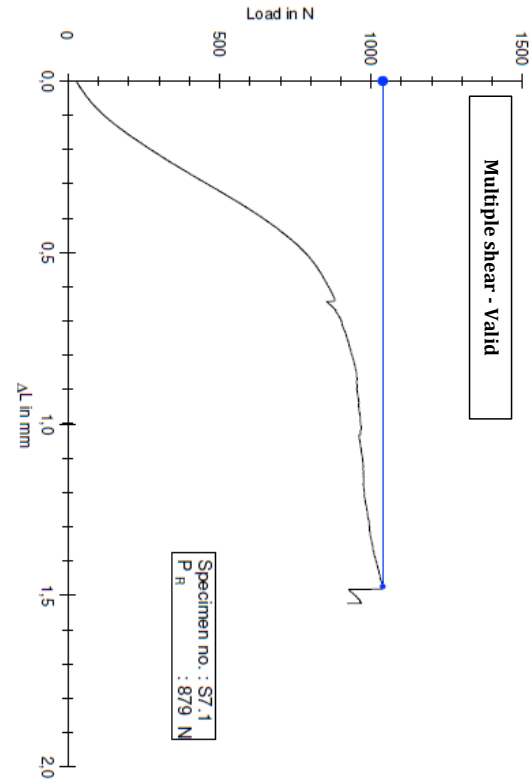
Multiple shear - Valid
Load in N
ΔL in mm
Specimen no. : S7.2
P_R : 976 N

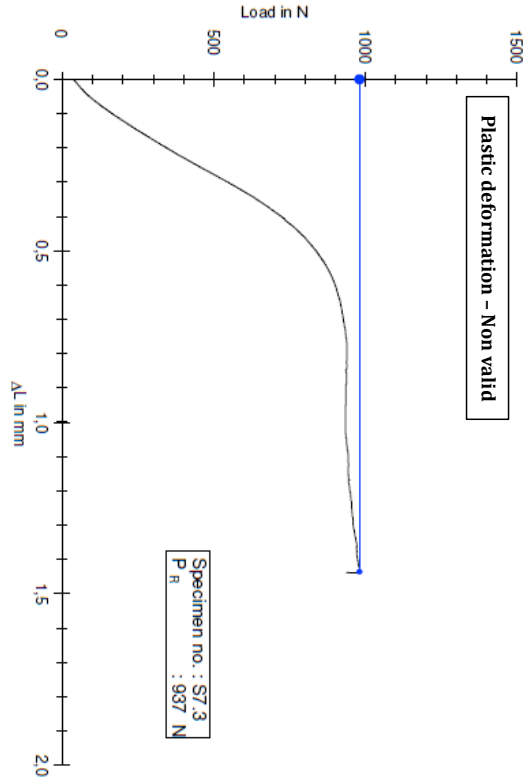
Plastic deformation – Non valid
Load in N
ΔL in mm
Specimen no. : S7.3
P_R : 937 N

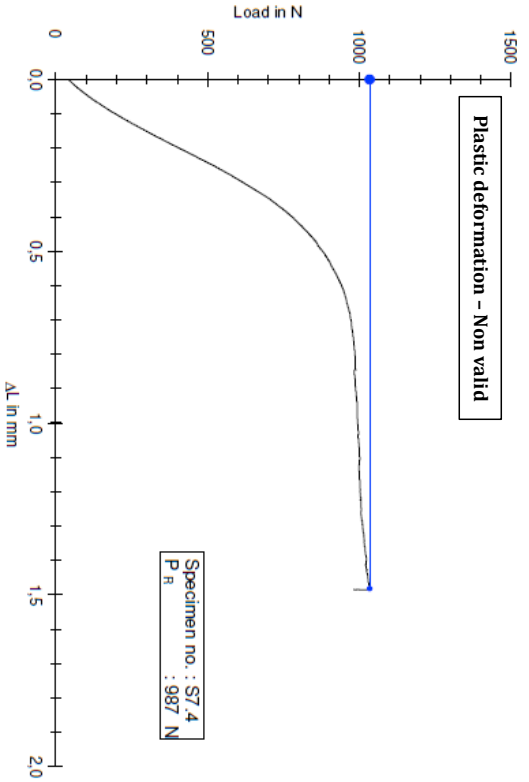
Plastic deformation – Non valid
Load in N
ΔL in mm
Specimen no. : S7.4
P_R : 987 N

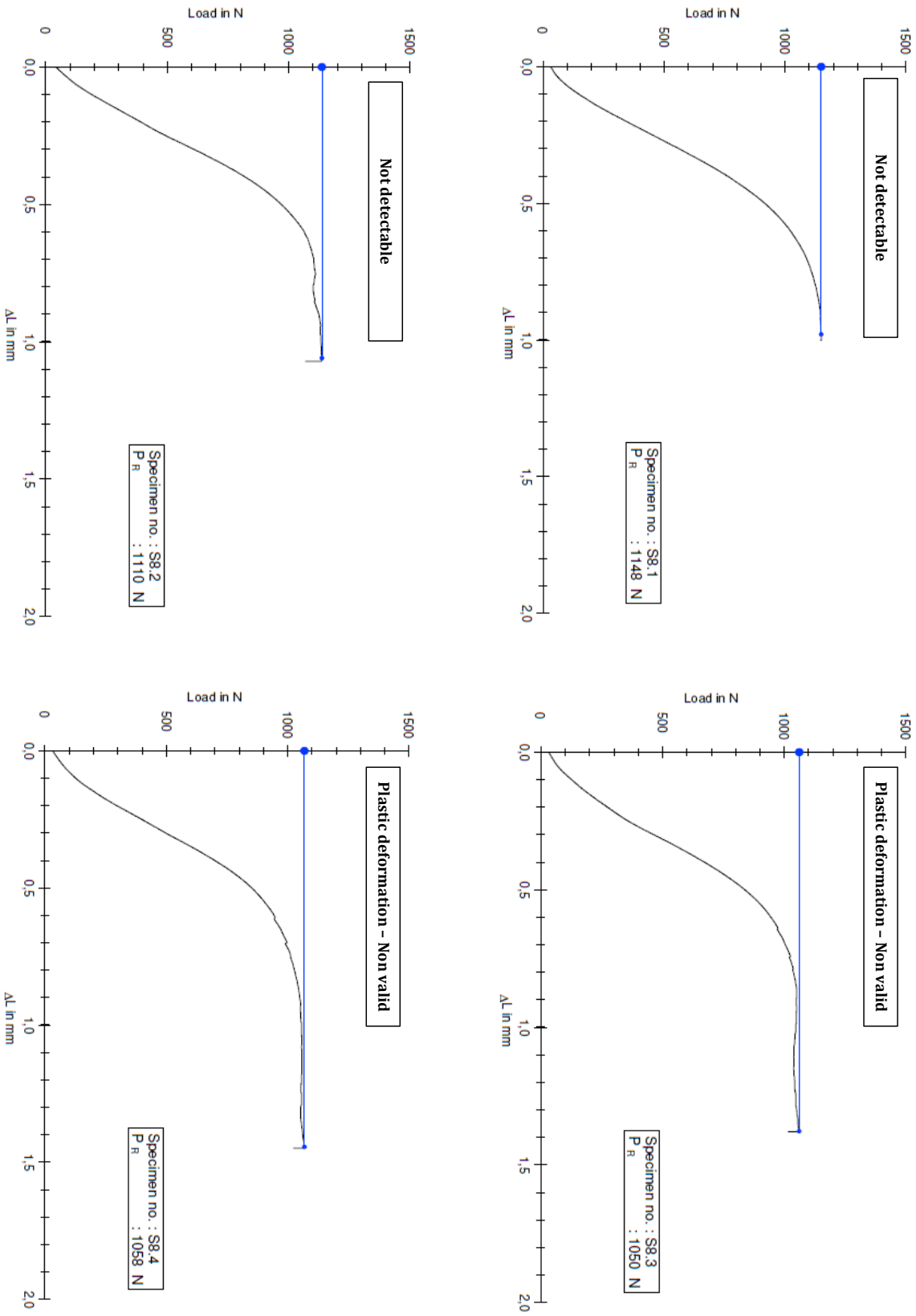
Not detectable
Load in N
ΔL in mm
Specimen no. : S8.1
P_R : 1148 N
Not detectable
Load in N
ΔL in mm
Specimen no. : S8.2
P_R : 1110 N
Plastic deformation – Non valid
Load in N
ΔL in mm
Specimen no. : S8.3
P_R : 1050 N
Plastic deformation – Non valid
Load in N
ΔL in mm
Specimen no. : S8.4
P_R : 1058 N

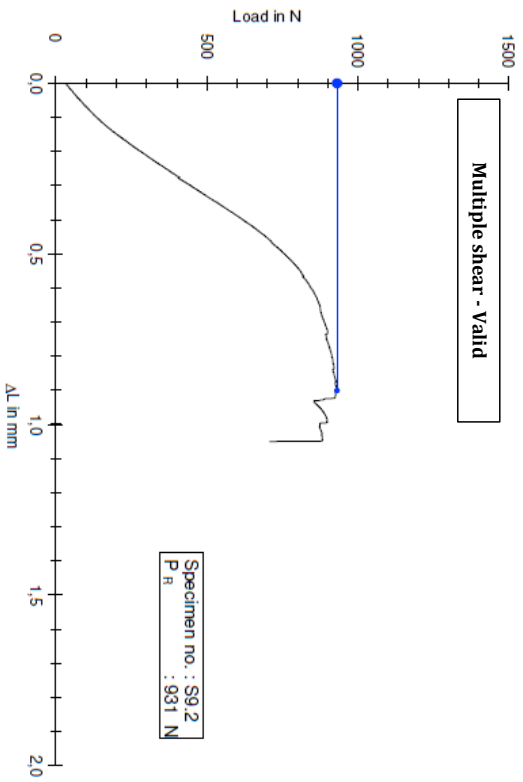
Multiple shear - Valid
Load in N
ΔL in mm
Specimen no. : S9.1
P R : 961 N

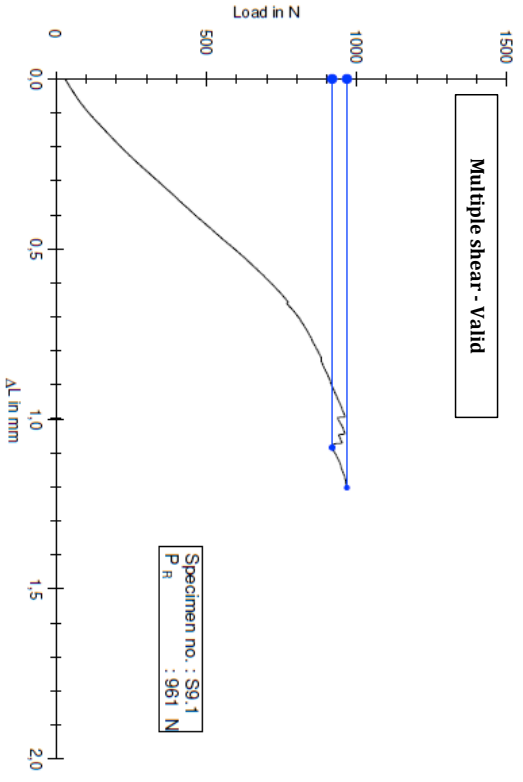
Multiple shear - Valid
Load in N
ΔL in mm
Specimen no. : S9.2
P R : 931 N

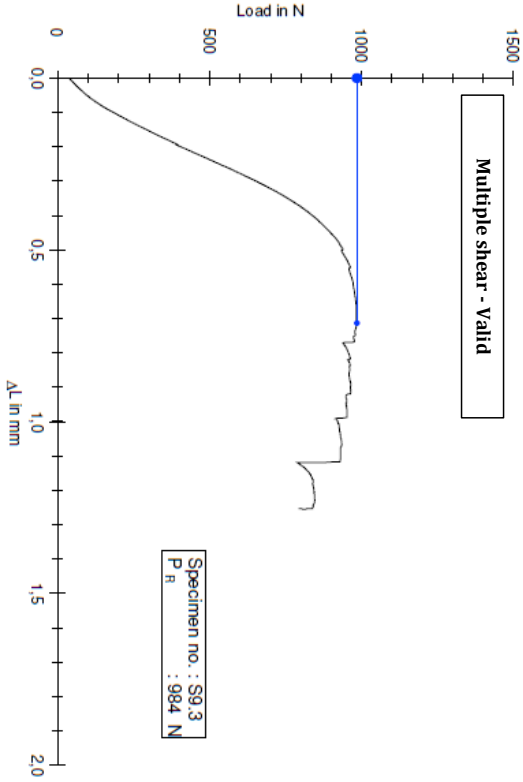
Multiple shear - Valid
Load in N
ΔL in mm
Specimen no. : S9.3
P R : 984 N

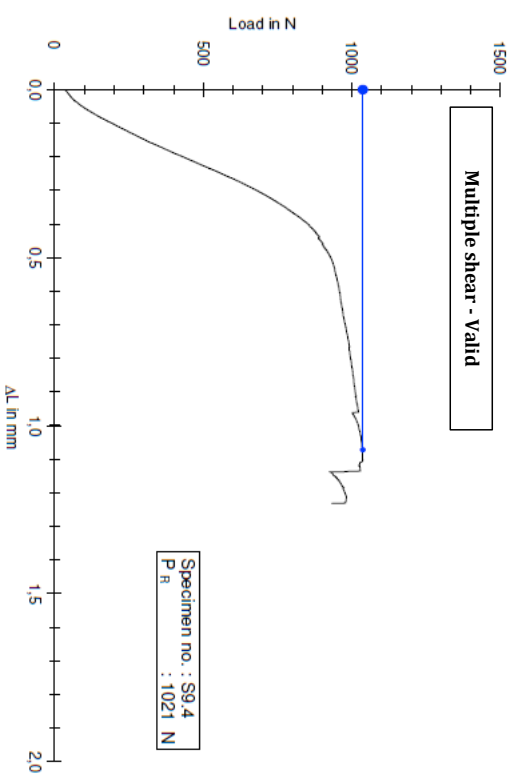
Multiple shear - Valid
Load in N
ΔL in mm
Specimen no. : S9.4
P R : 1021 N

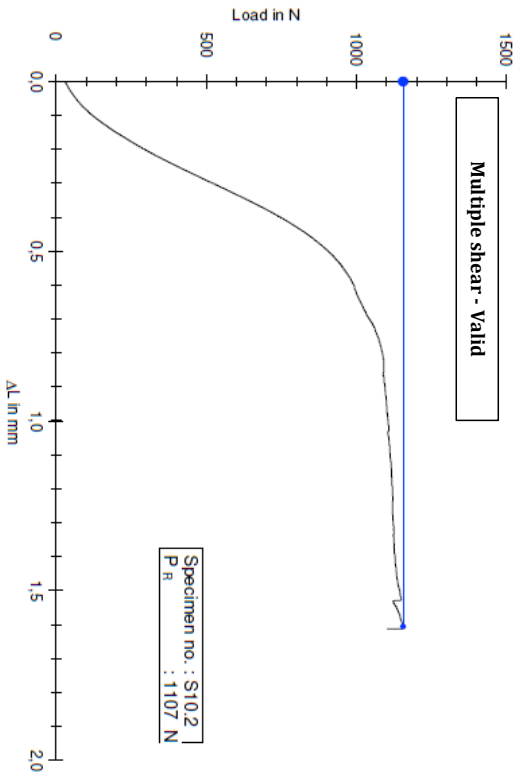
Plastic deformation – Non valid
Load in N
ΔL in mm
Specimen no. : S10.1
P R : 1132 N

Multiple shear - Valid
Load in N
ΔL in mm
Specimen no. : S10.2
P R : 1107 N

Plastic deformation – Non valid
Load in N
ΔL in mm
Specimen no. : S10.3
P R : 1092 N

Plastic deformation – Non valid
Load in N
ΔL in mm
Specimen no. : S10.4
P R : 1072 N

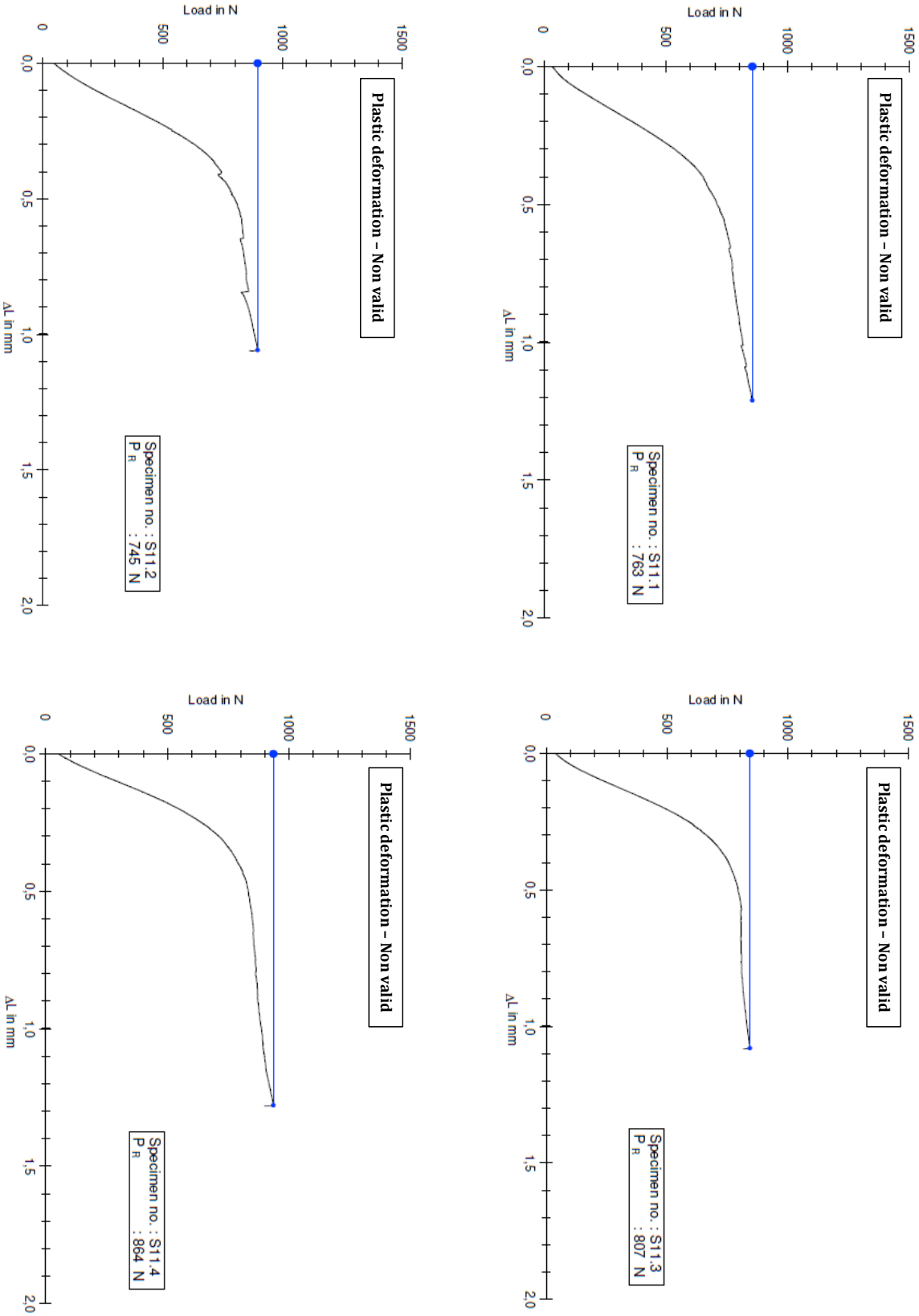
Plastic deformation – Non valid
Load in N
ΔL in mm
Specimen no. : S11.1
P R : 763 N
Plastic deformation – Non valid
Load in N
ΔL in mm
Specimen no. : S11.2
P R : 745 N
Plastic deformation – Non valid
Load in N
ΔL in mm
Specimen no. : S11.3
P R : 807 N
Plastic deformation – Non valid
Load in N
ΔL in mm
Specimen no. : S11.4
P R : 864 N

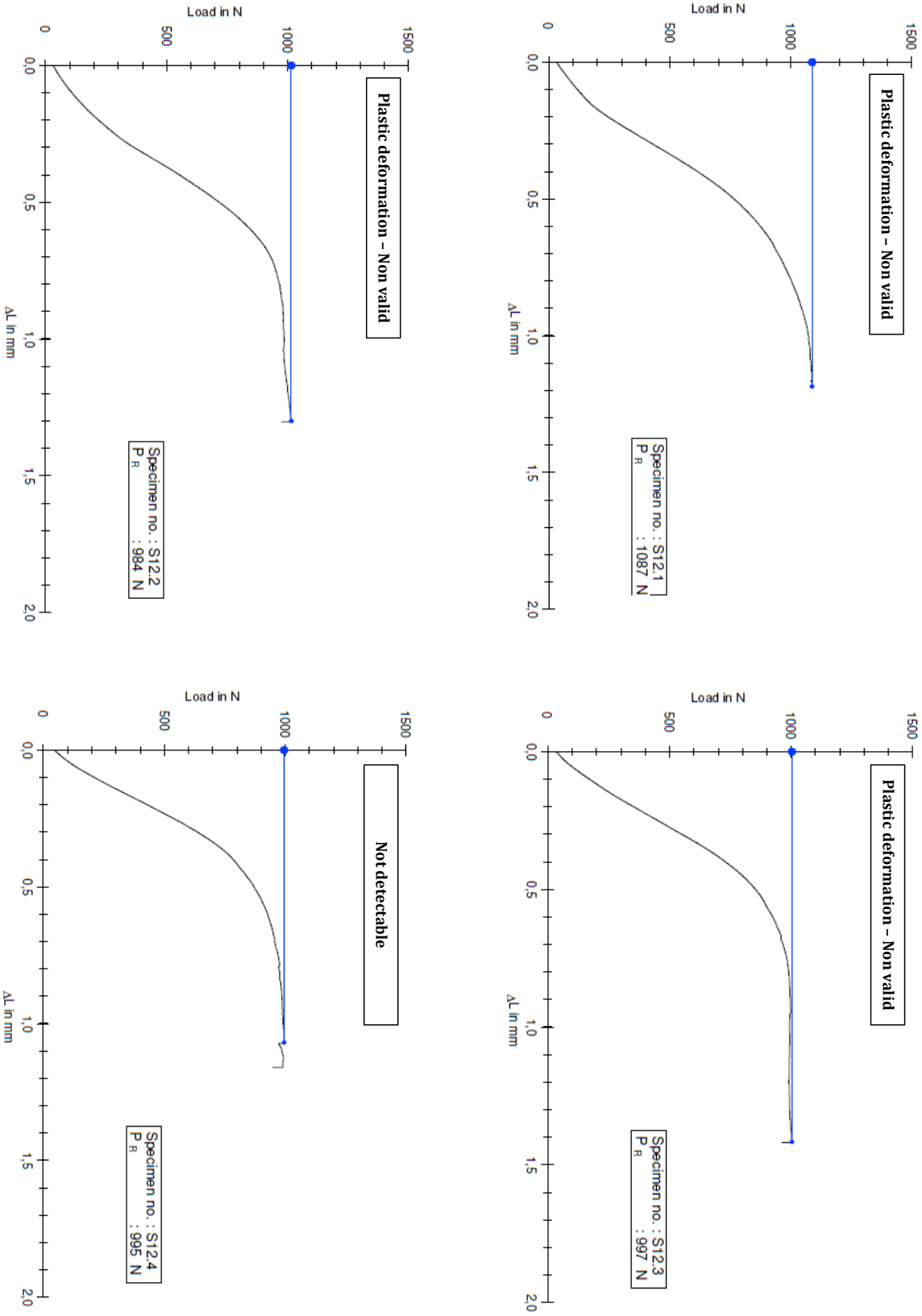
Plastic deformation – Non valid
Load in N
ΔL in mm
Specimen no. : S12.1
P R : 1087 N
Plastic deformation – Non valid
Load in N
ΔL in mm
Specimen no. : S12.2
P R : 984 N
Plastic deformation – Non valid
Load in N
ΔL in mm
Specimen no. : S12.3
P R : 997 N
Not detectable
Load in N
ΔL in mm
Specimen no. : S12.4
P R : 995 N

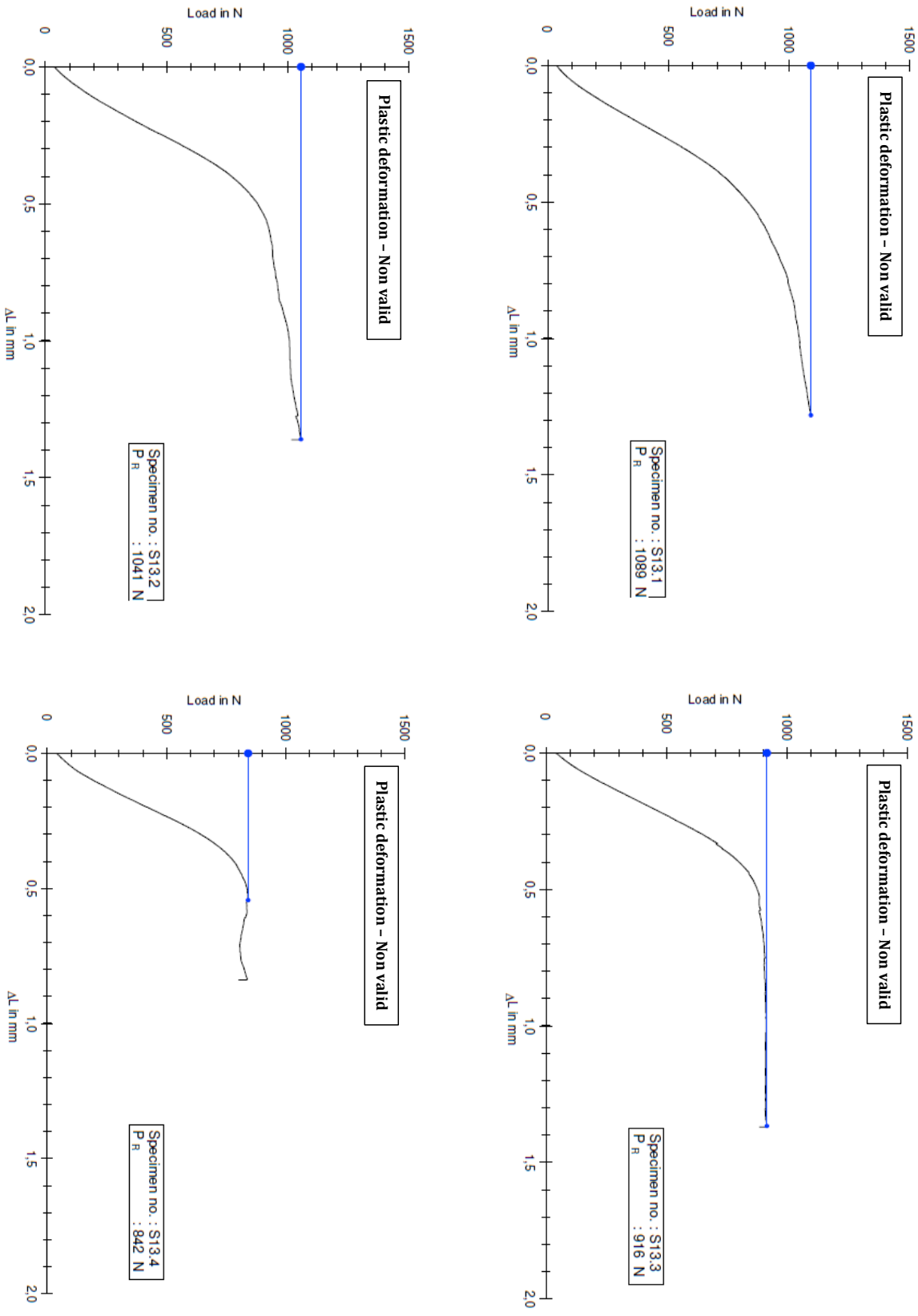
Plastic deformation – Non valid
Load in N
ΔL in mm
Specimen no. : S13.1
P R : 1089 N
Plastic deformation – Non valid
Load in N
ΔL in mm
Specimen no. : S13.2
P R : 1041 N
Plastic deformation – Non valid
Load in N
ΔL in mm
Specimen no. : S13.3
P R : 916 N
Plastic deformation – Non valid
Load in N
ΔL in mm
Specimen no. : S13.4
P R : 842 N

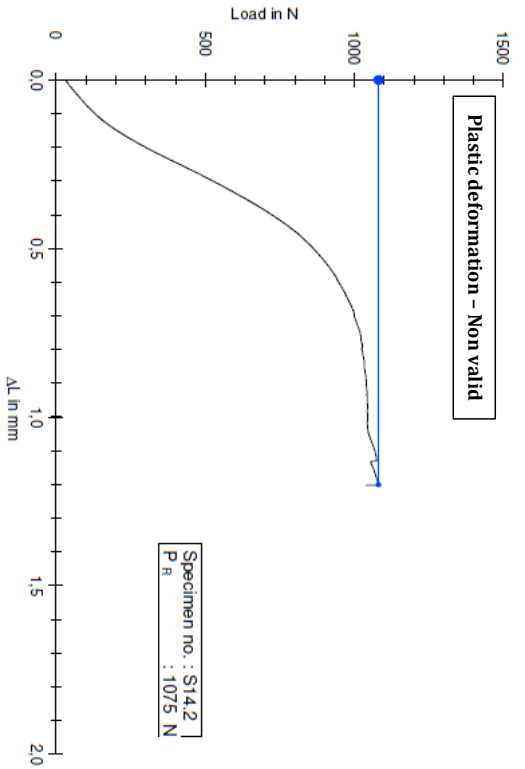
Plastic deformation – Non valid
Load in N
ΔL in mm
Specimen no. : S14.1
P R : 1064 N

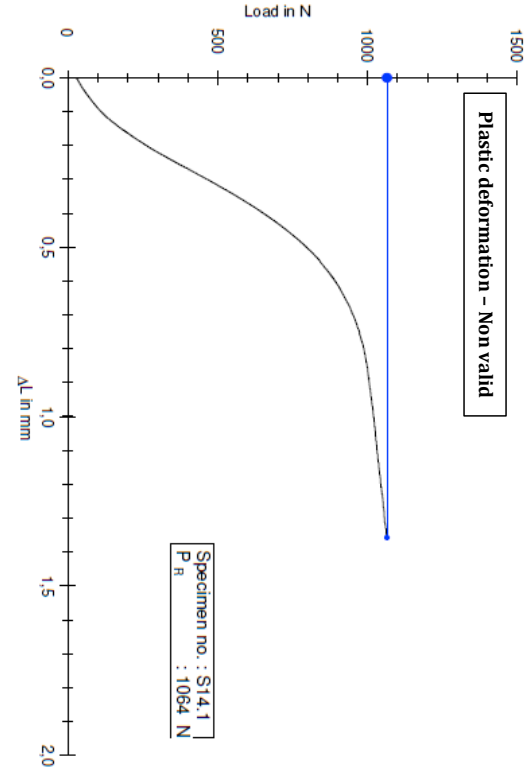
Plastic deformation – Non valid
Load in N
ΔL in mm
Specimen no. : S14.2
P R : 1075 N

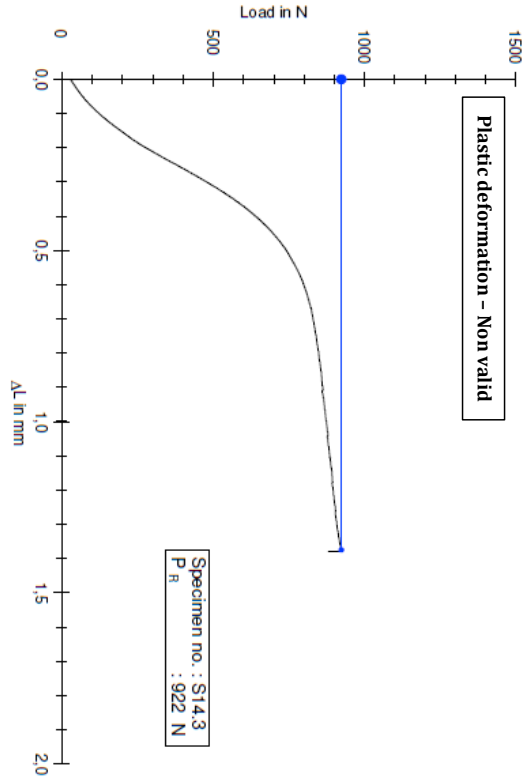
Plastic deformation – Non valid
Load in N
ΔL in mm
Specimen no. : S14.3
P R : 922 N

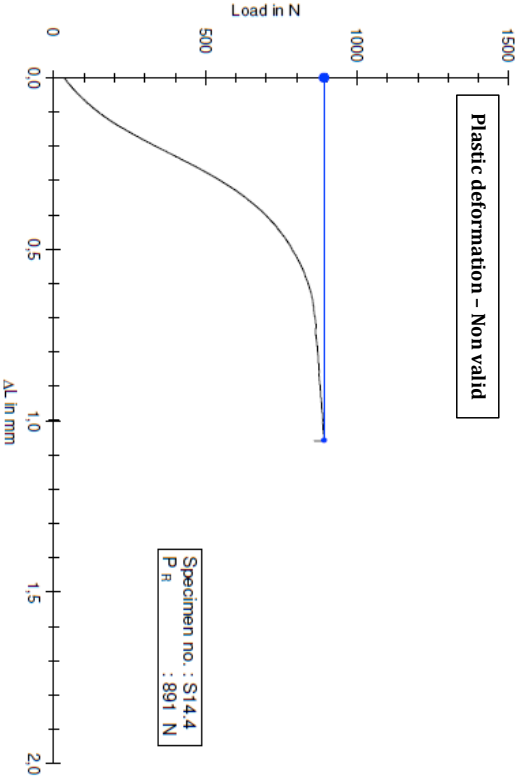
Plastic deformation – Non valid
Load in N
ΔL in mm
Specimen no. : S14.4
P R : 891 N

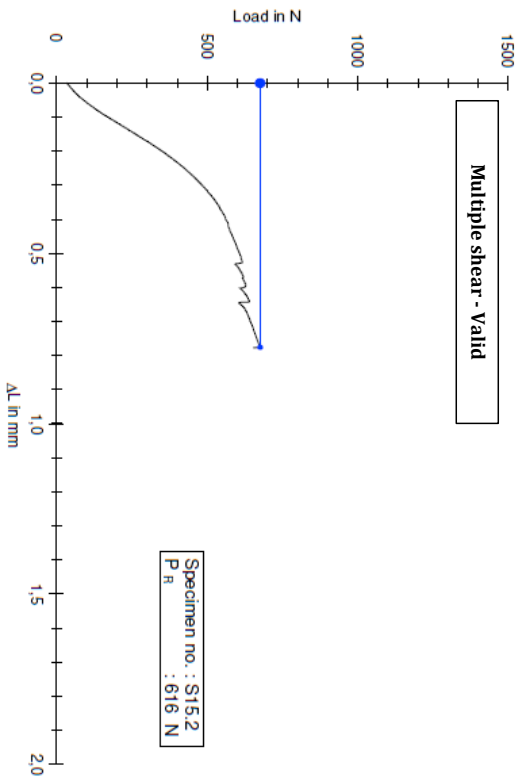
Multiple shear - Valid
Load in N
ΔL in mm
Specimen no. : S15.1
P R : 686 N

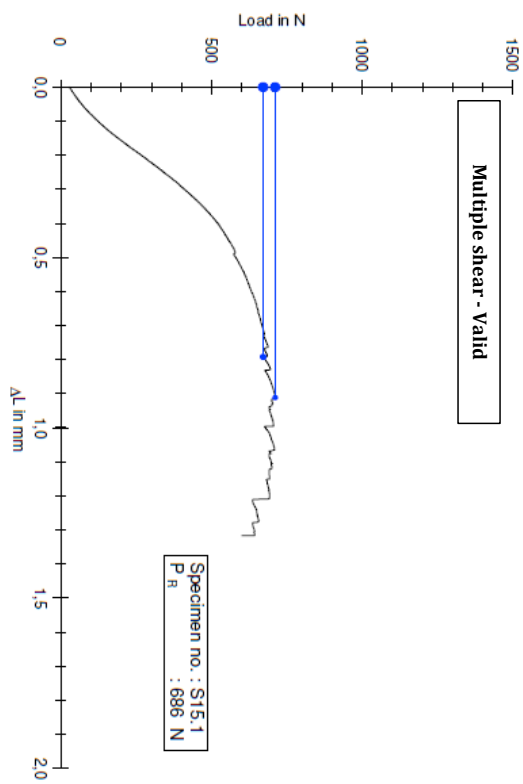
Multiple shear - Valid
Load in N
ΔL in mm
Specimen no. : S15.2
P R : 616 N

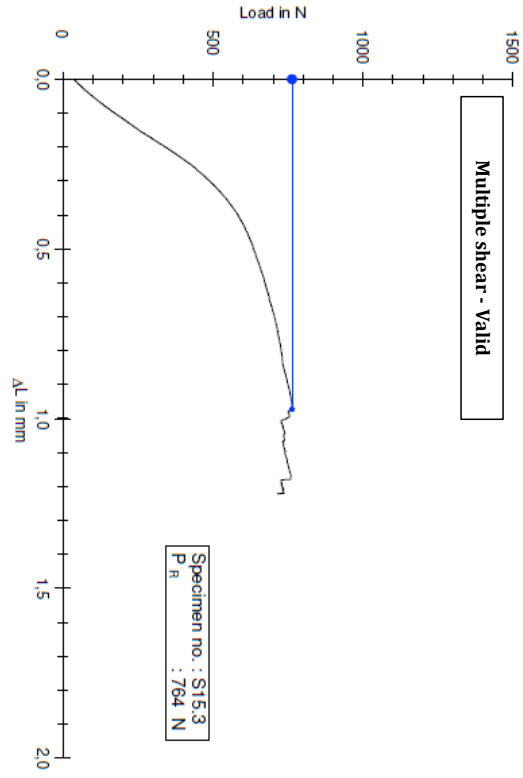
Multiple shear - Valid
Load in N
ΔL in mm
Specimen no. : S15.3
P R : 764 N

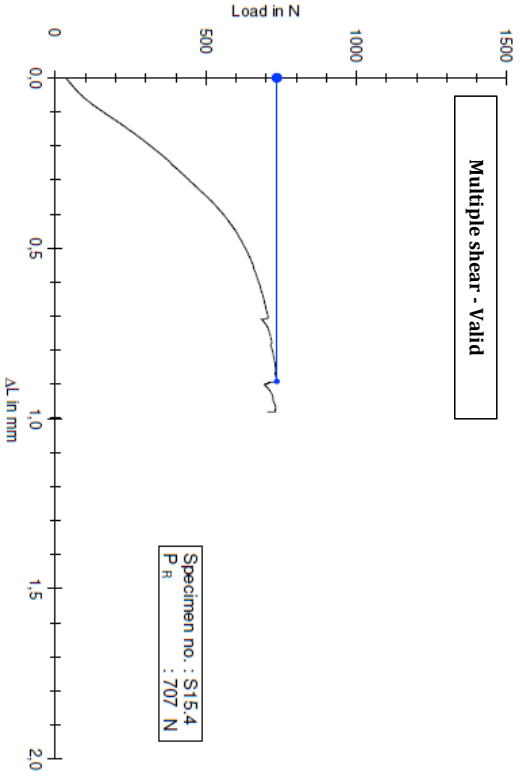
Multiple shear - Valid
Load in N
ΔL in mm
Specimen no. : S15.4
P R : 707 N

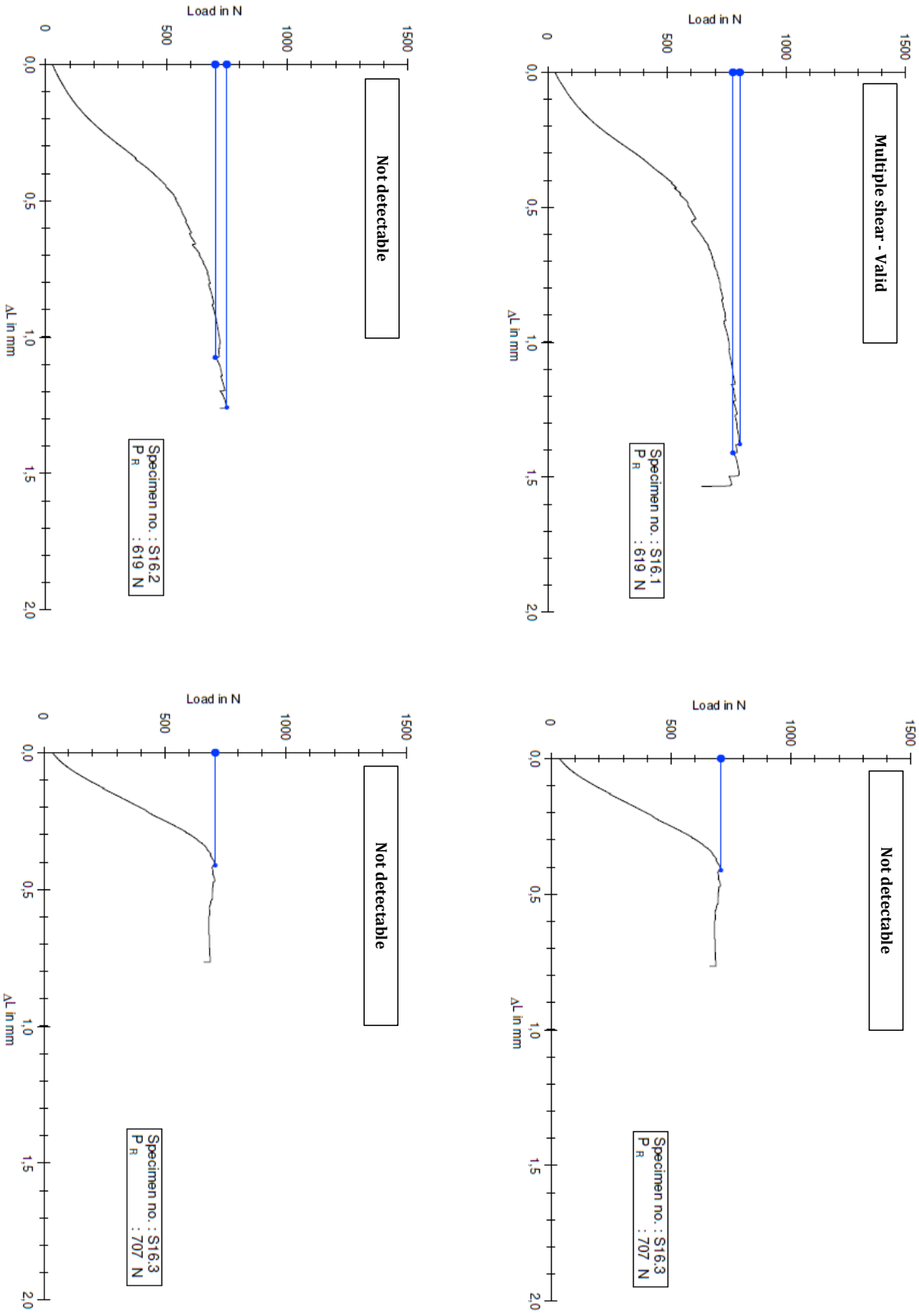
Multiple shear - Valid
Load in N
ΔL in mm
Specimen no. : S16.1
P_R : 619 N
Not detectable
Load in N
ΔL in mm
Specimen no. : S16.2
P_R : 619 N
Not detectable
Load in N
ΔL in mm
Specimen no. : S16.3
P_R : 707 N
Not detectable
Load in N
ΔL in mm
Specimen no. : S16.3
P_R : 707 N

G.2. Void Content

The cross-sectional areas of the void content specimen are shown below. Figure G.2.1 to G.2.4 show a measurement for the layer thickness, as validation of the printer settings. It can be seen that the layer thickness felt within margin as defined by the KUKA robot, a repeatability of 50 micron. However the width of the printed lines does not corresponds to the theoretical line width the lines need to have. For example Figure G.2.3 shows the cross-section of a sample with layer thickness equal to 0.25 mm. The corresponding line width, based on the diameter of filament of 0.65 mm should be 1.32 mm. This is however not reached. The line width obtained, corresponds to a filament diameter of 0.61 mm, which concludes the problems of the formation of gaps are due to the tolerance of the filament.

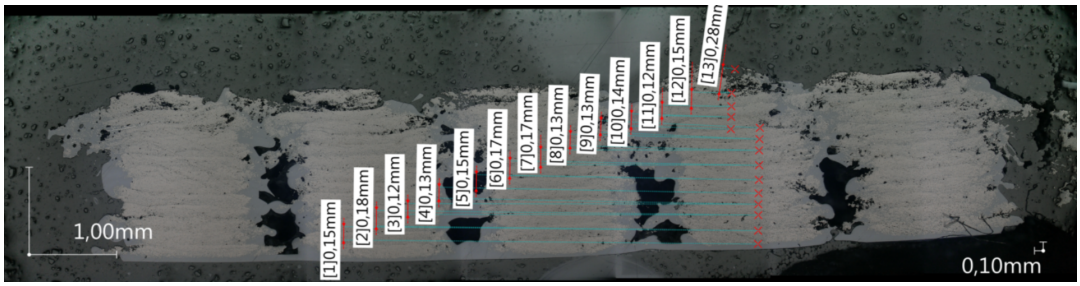

Figure G.2.1: Layer thickness measurement, t = 0.15 mm

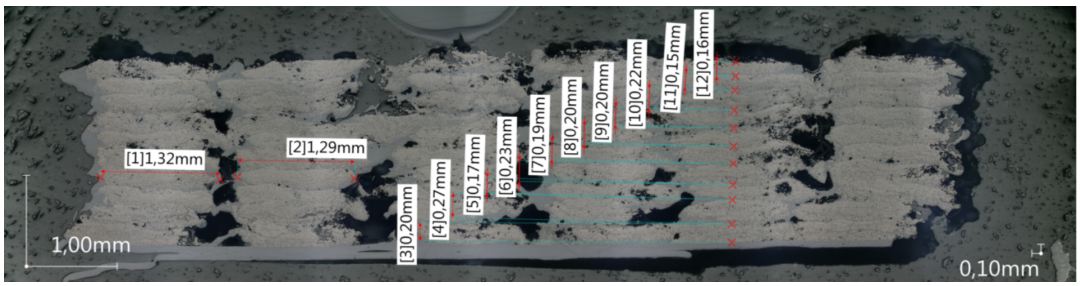

Figure G.2.2: Layer thickness measurement, t = 0.20 mm

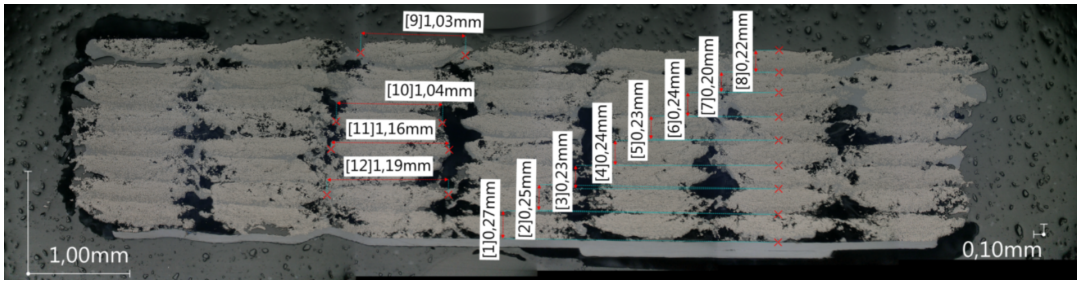

Figure G.2.3: Layer thickness measurement, t = 0.25 mm

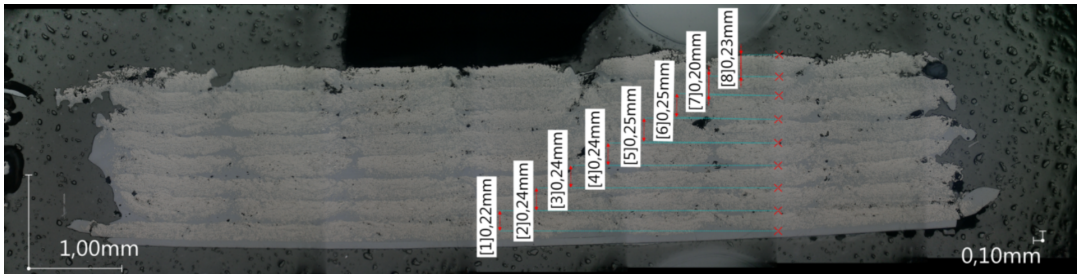

Figure G.2.4: Layer thickness measurement 2, t = 0.25 mm

The images below provide the results from the microscopic inspection.

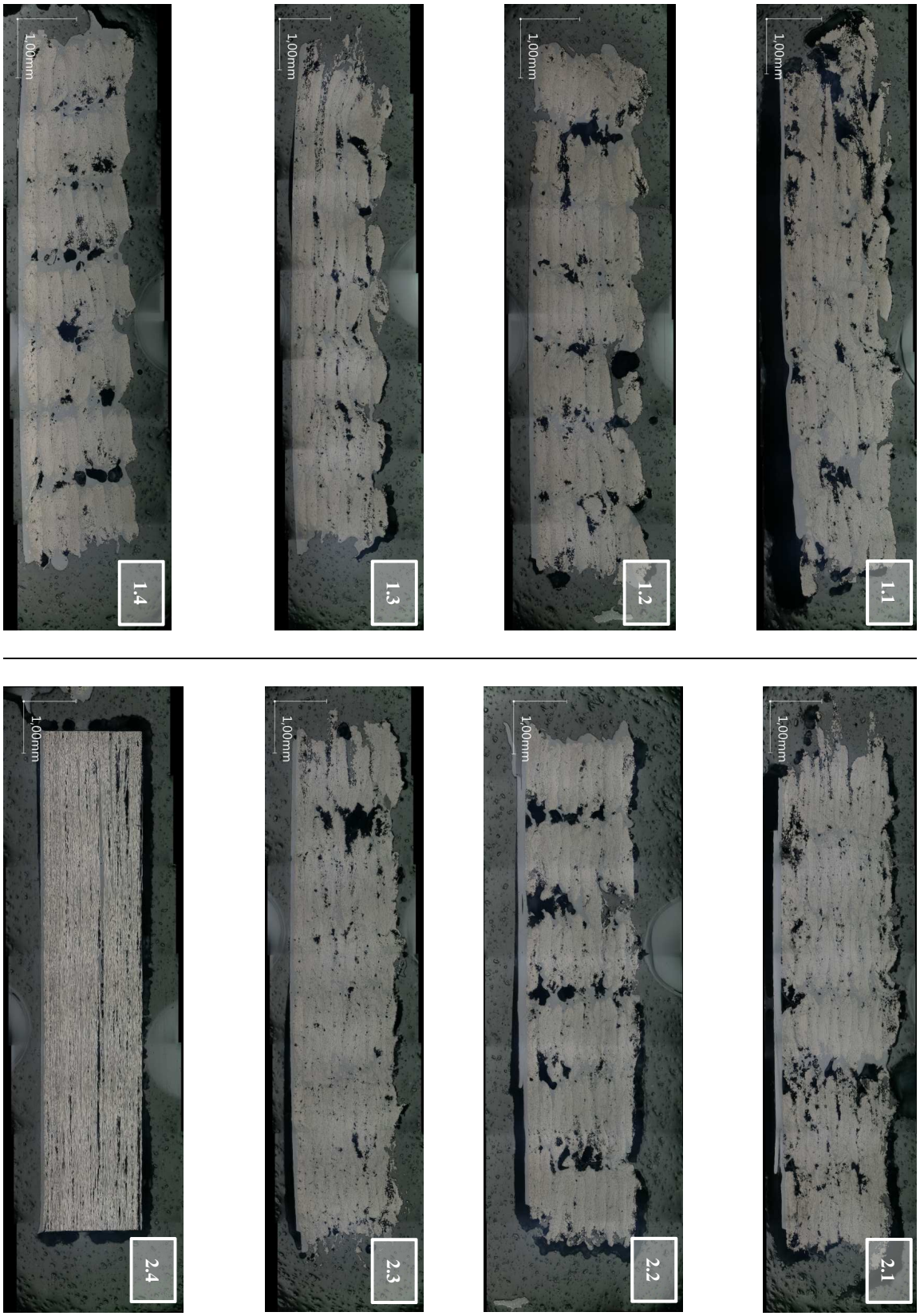
1.00mm
1.1
1.00mm
1.2
1.00mm
1.3
1.00mm
1.4
1.00mm
2.1
1.00mm
2.2
1.00mm
2.3
1.00mm
2.4

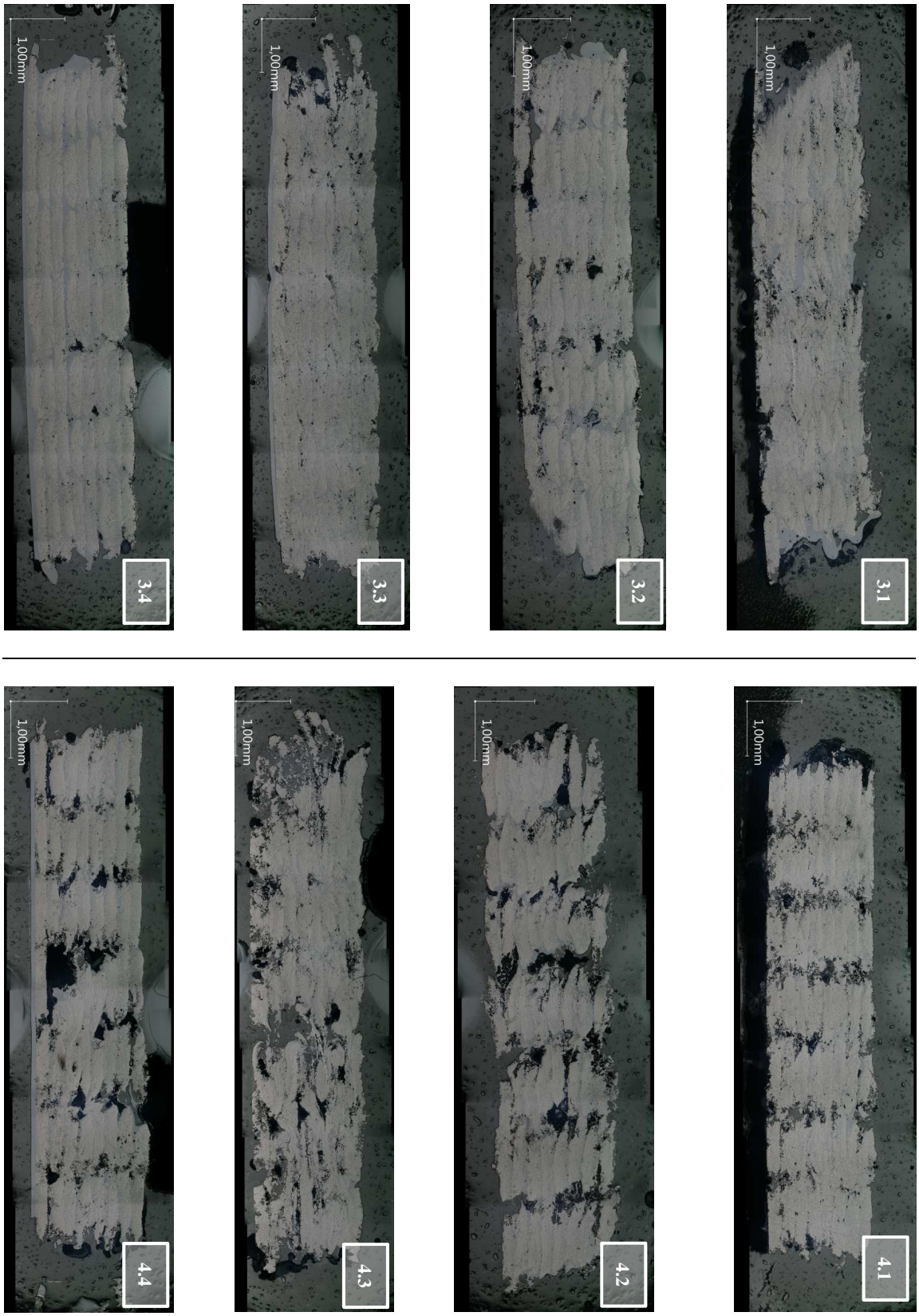
3.1
1,00mm
3.2
1,00mm
3.3
1,00mm
3.4
1,00mm
4.1
1,00mm
4.2
1,00mm
4.3
1,00mm
4.4
1,00mm

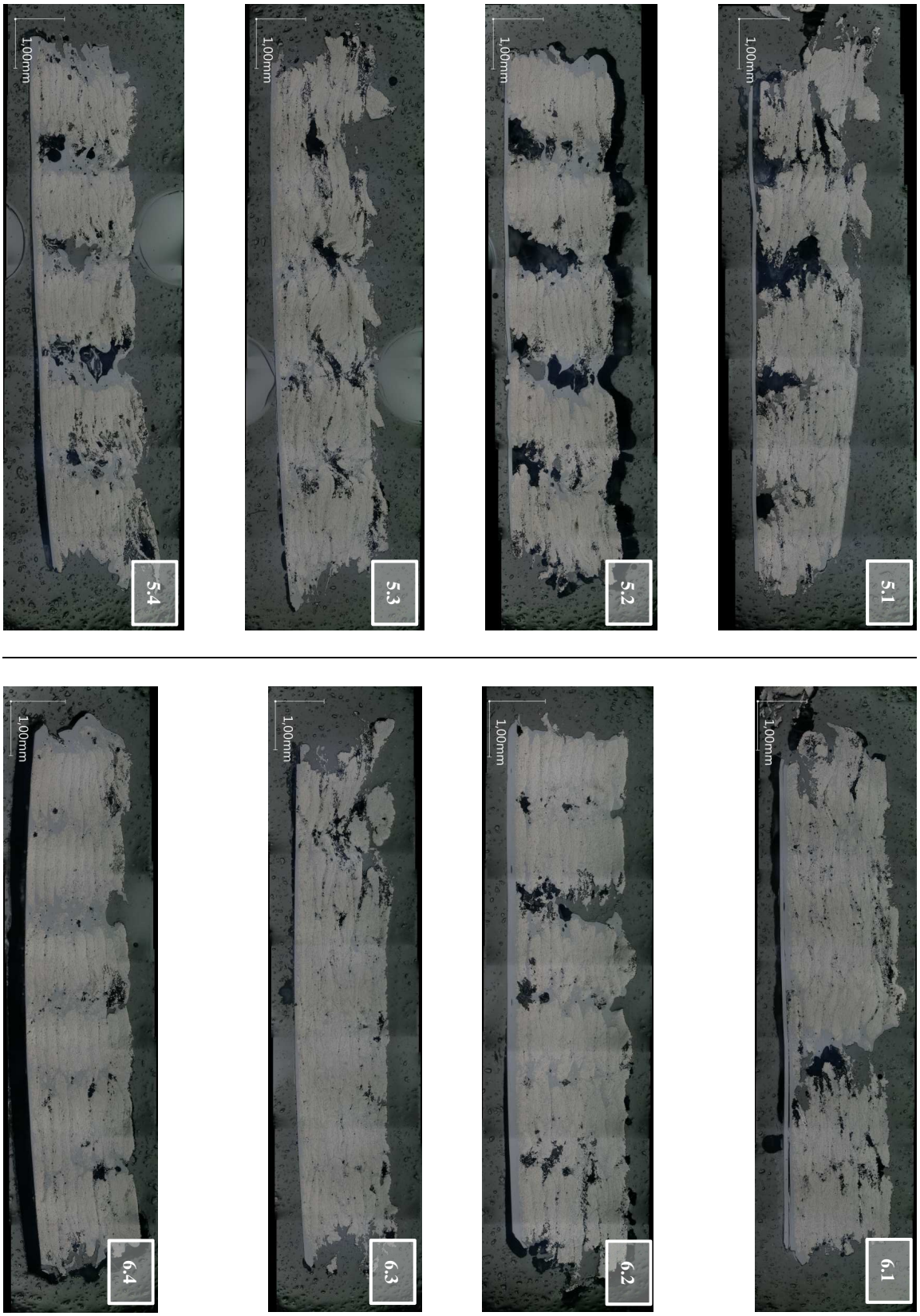
1,00mm
5.1
1,00mm
5.2
1,00mm
5.3
1,00mm
5.4
1,00mm
6.1
1,00mm
6.2
1,00mm
6.3
1,00mm
6.4

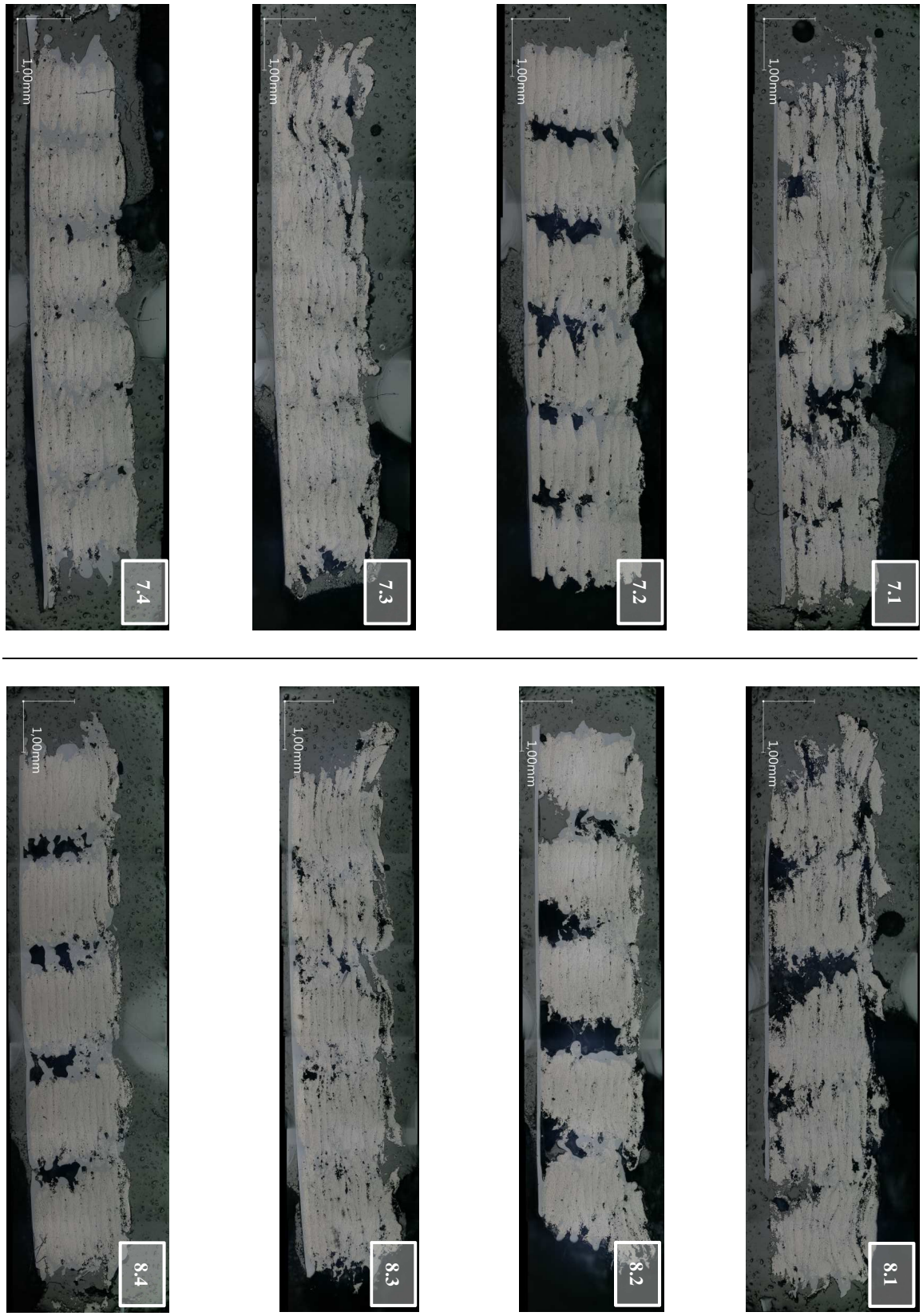
1,00mm
7.1
1,00mm
7.2
1,00mm
7.3
1,00mm
7.4
1,00mm
8.1
1,00mm
8.2
1,00mm
8.3
1,00mm
8.4

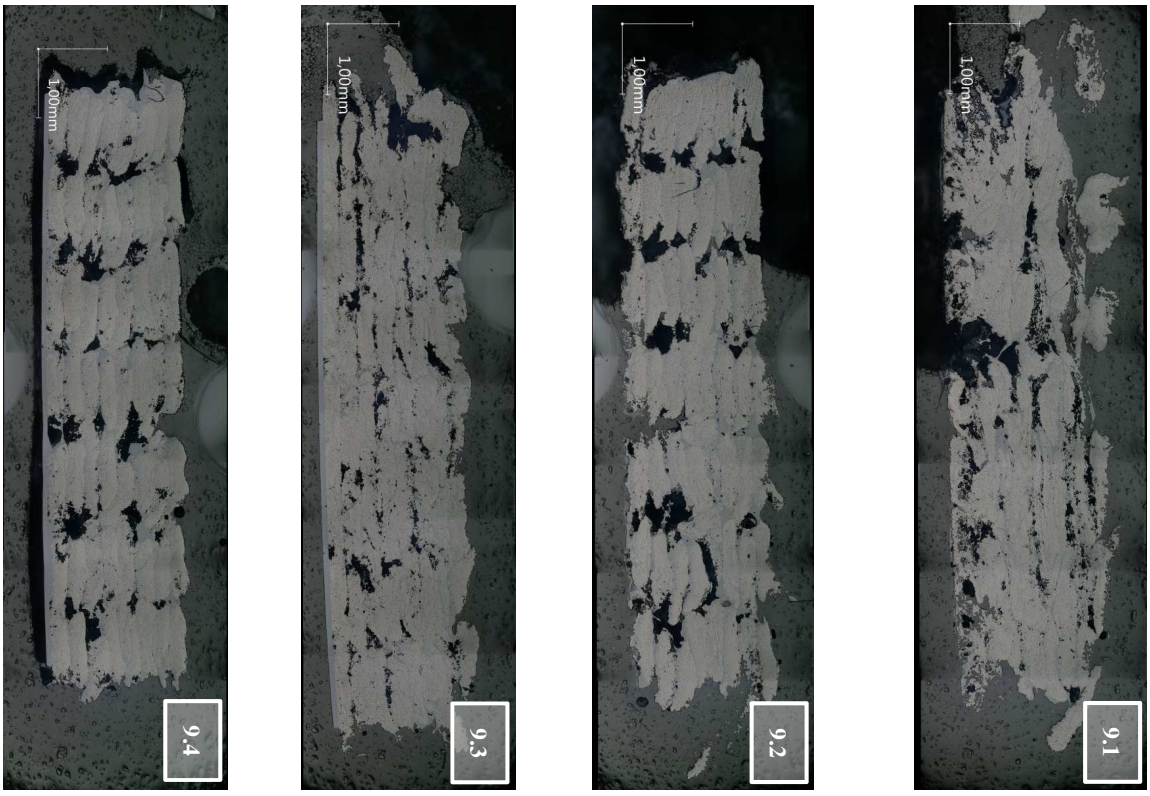
9.1
1.00mm
9.2
1.00mm
9.3
1.00mm
9.4
1.00mm

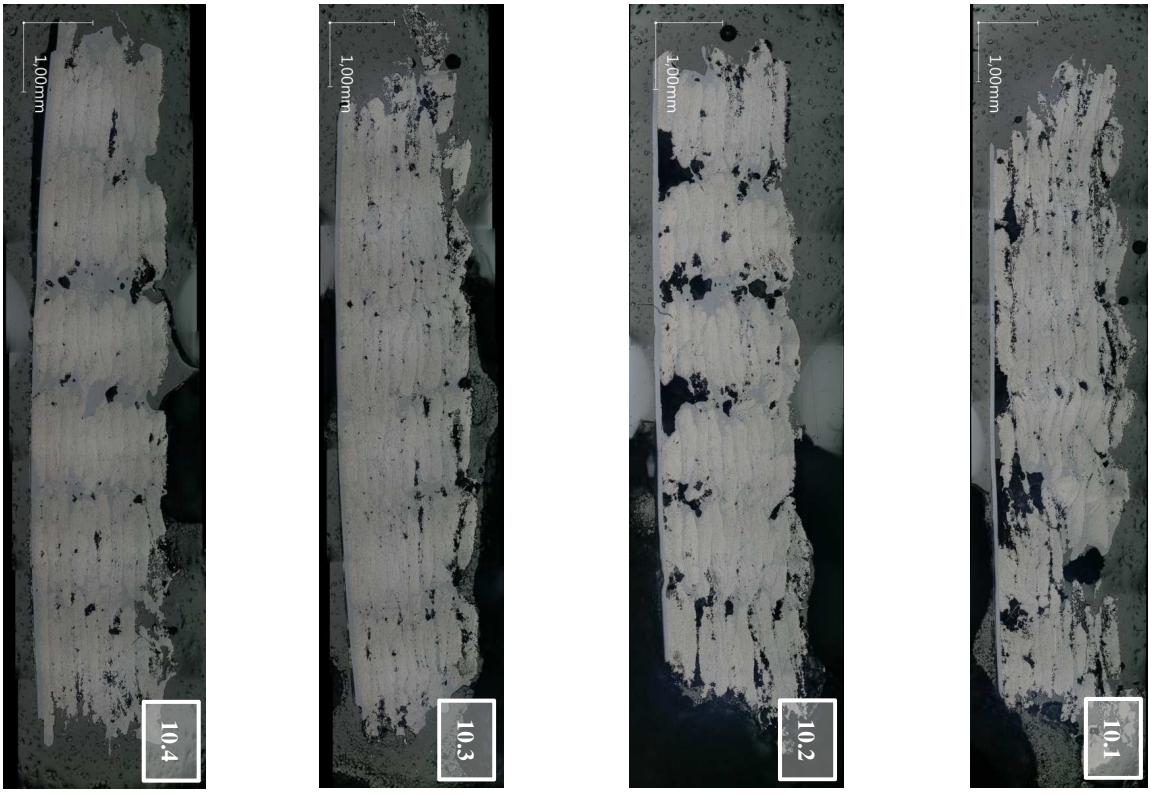
10.1
1.00mm
10.2
1.00mm
10.3
1.00mm
10.4
1.00mm

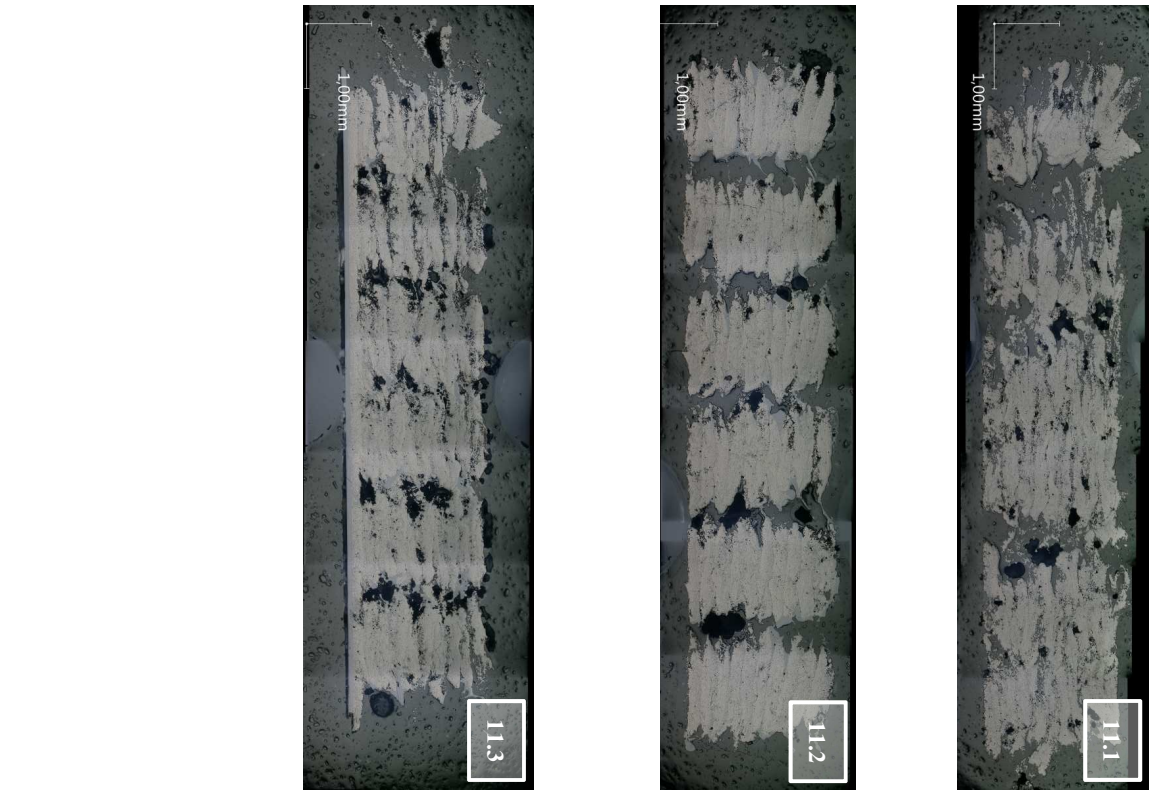
1,00mm
11.1
1,00mm
11.2
1,00mm
11.3

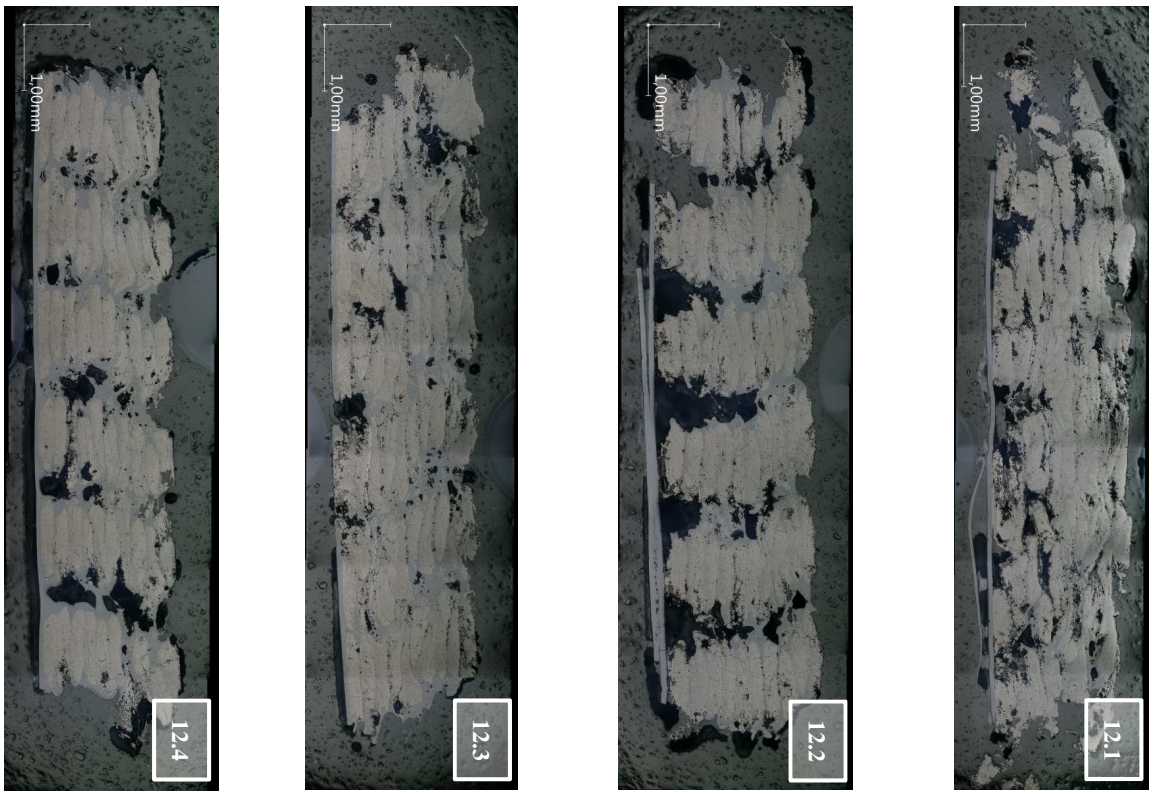
1,00mm
12.1
1,00mm
12.2
1,00mm
12.3
1,00mm
12.4

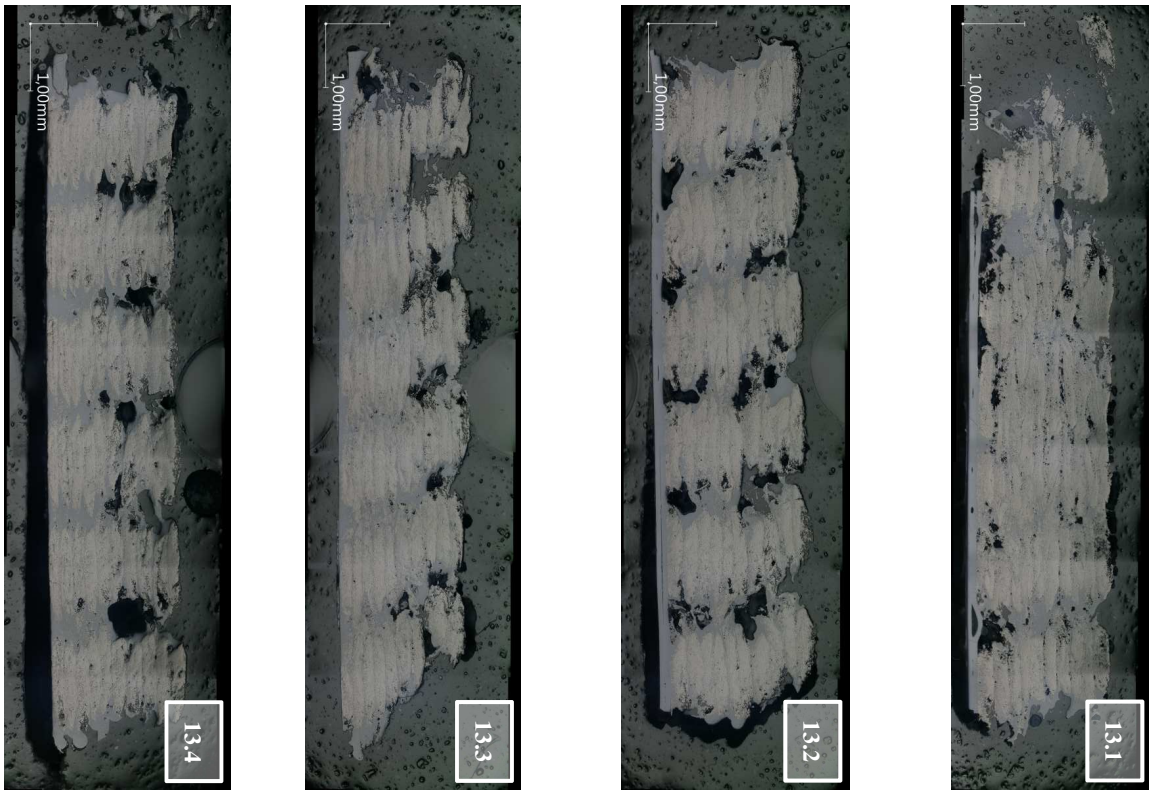
1,00mm
13.1
1,00mm
13.2
1,00mm
13.3
1,00mm
13.4

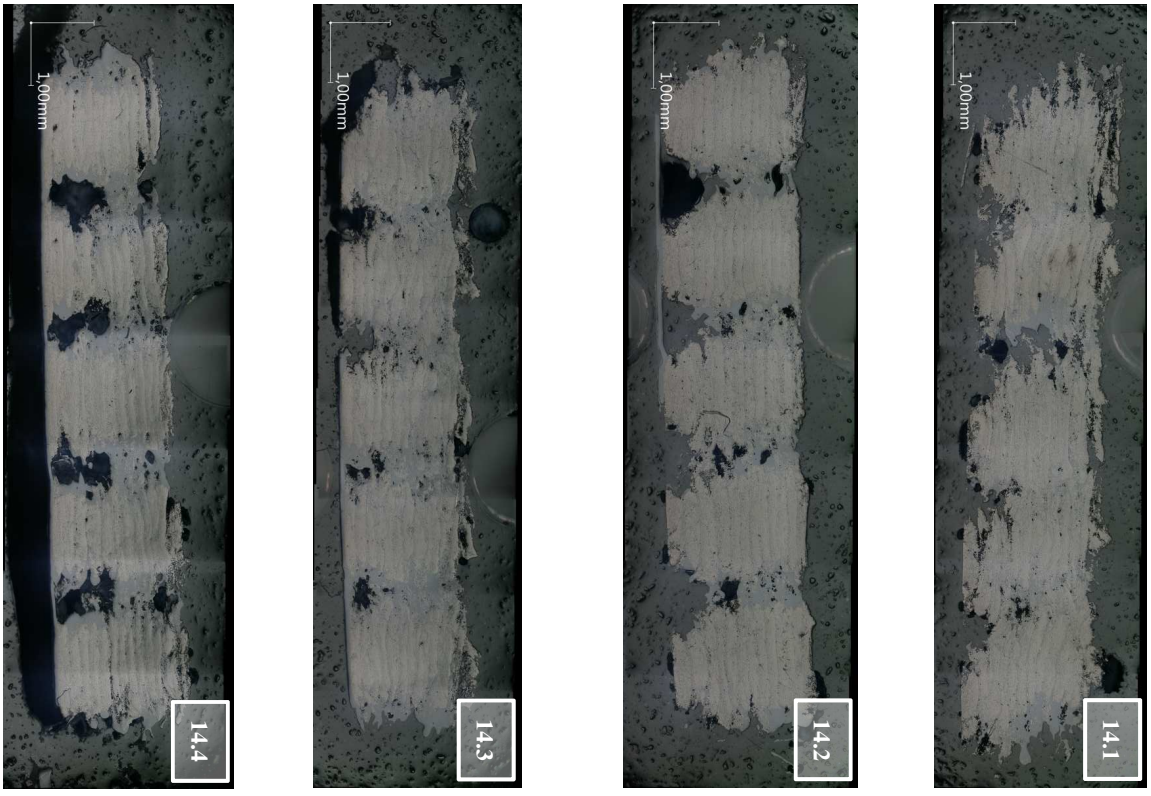
1,00mm
14.1
1,00mm
14.2
1,00mm
14.3
1,00mm
14.4

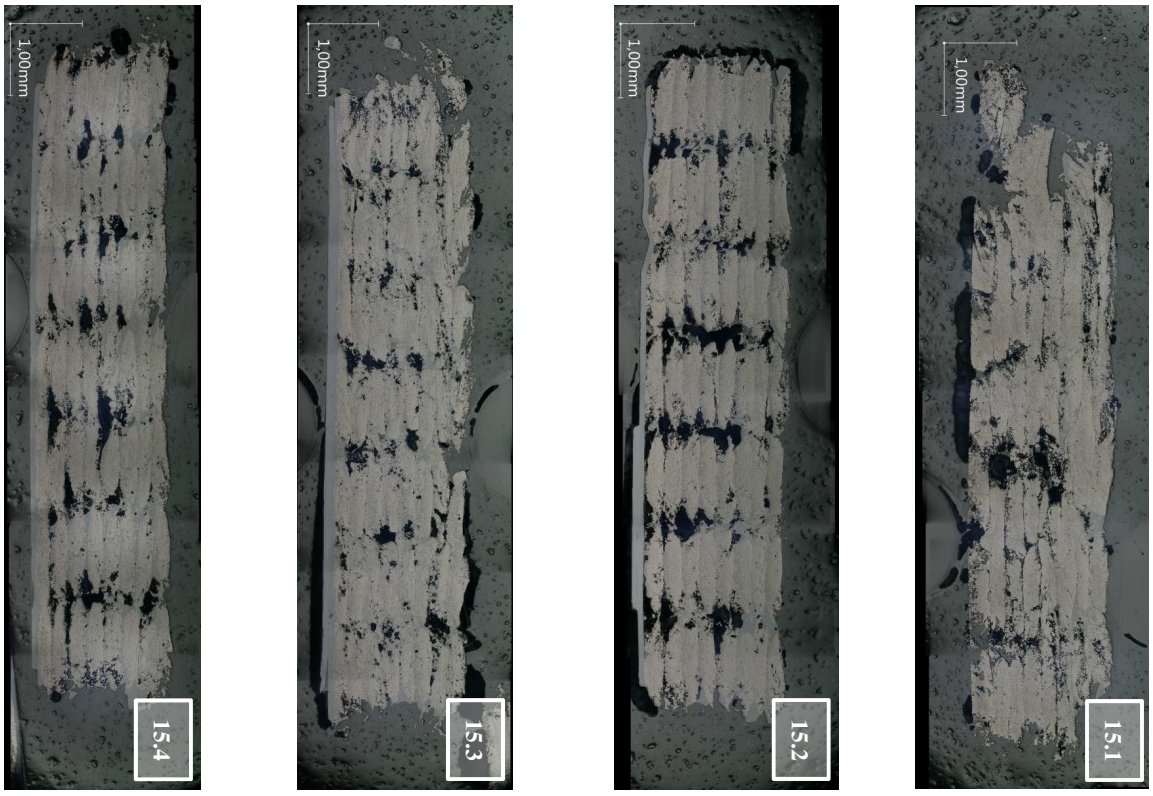
1,00mm
15.1
1,00mm
15.2
1,00mm
15.3
1,00mm
15.4

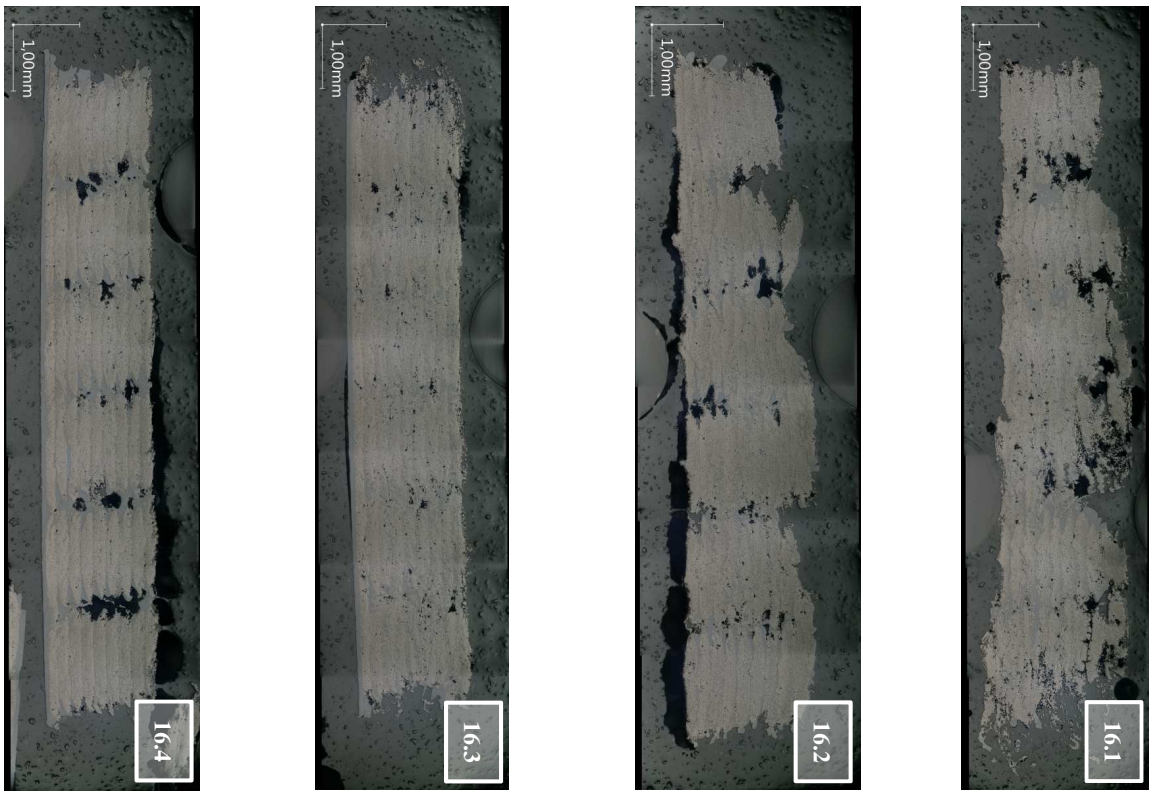
1,00mm
16.1
1,00mm
16.2
1,00mm
16.3
1,00mm
16.4

H

Minitab Response Optimisation

In this Appendix, the model summary and code coefficients for the stress at break and void content response are shown. In addition the residual plots are given from which the validity of the model is being retrieved.

Model Summary

S	R-sq	R-sq(adj)	R-sq(pred)
1.79001	93.25%	88.42%	64.65%

Coded Coefficients

Term	Coef	SE Coef	T-Value	P-Value	VIF
Constant	34.150	0.801	42.66	0.000	
Layer Height	-0.389	0.693	-0.56	0.592	1.15
Print Speed	-1.901	0.693	-2.74	0.029	1.15
Nozzle Temperature	4.578	0.661	6.93	0.000	1.09
Print Speed*Print Speed	-3.36	1.06	-3.17	0.016	1.08
Layer Height*Nozzle Temperature	2.211	0.763	2.90	0.023	1.09

Regression Equation in Uncoded Units

Stress at break = 102.9 - 804 Layer Height + 5.77 Print Speed - 0.213 Nozzle Temperature
- 0.840 Print Speed*Print Speed + 2.211 Layer Height*Nozzle Temperature

Figure H.0.1: Final model summary and coded coefficients for the stress at break response

Model Summary

S	R-sq	R-sq(adj)	R-sq(pred)
0.612076	94.31%	88.63%	61.01%

Coded Coefficients

Term	Coef	SE Coef	T-Value	P-Value	VIF
Constant	5.028	0.274	18.37	0.000	
Layer Height	0.716	0.237	3.02	0.023	1.15
Print Speed	-1.087	0.237	-4.58	0.004	1.15
Nozzle Temperature	-0.365	0.250	-1.46	0.194	1.33
Print Speed*Print Speed	1.440	0.362	3.98	0.007	1.08
Layer Height*Nozzle Temperature	0.753	0.293	2.57	0.042	1.38
Print Speed*Nozzle Temperature	1.820	0.293	6.21	0.001	1.38

Regression Equation in Uncoded Units

Void content = 136.4 - 257 Layer Height - 19.81 Print Speed - 0.3508 Nozzle Temperature
+ 0.3601 Print Speed*Print Speed + 0.753 Layer Height*Nozzle Temperature
+ 0.04551 Print Speed*Nozzle Temperature

Figure H.0.2: Final model summary and coded coefficients for the void content response

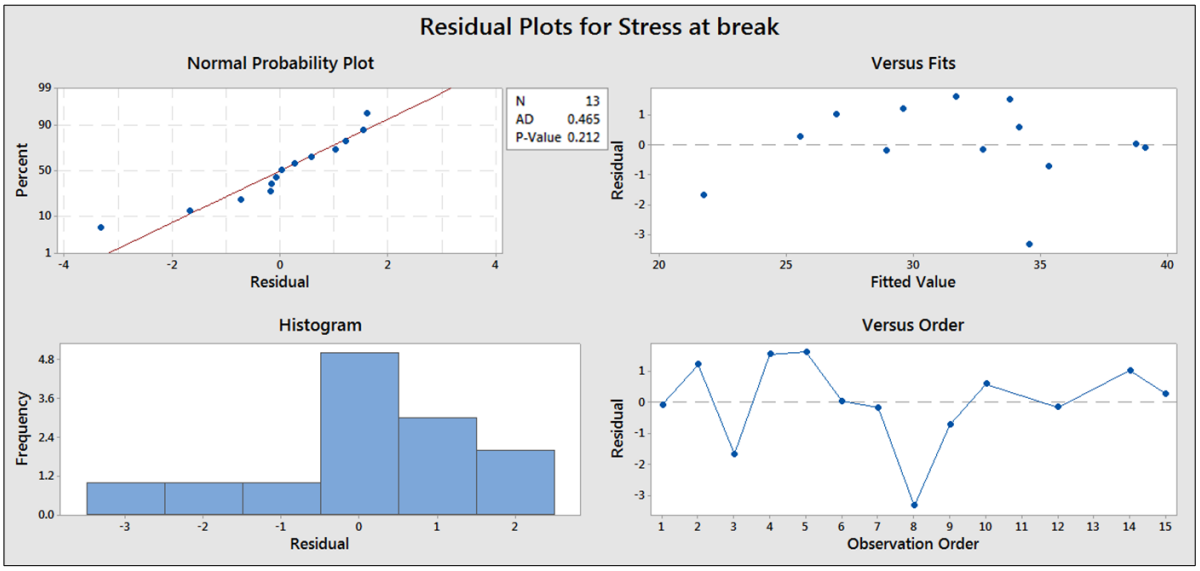

Figure H.0.3: Additional charts used for determining model validity for the stress at break response

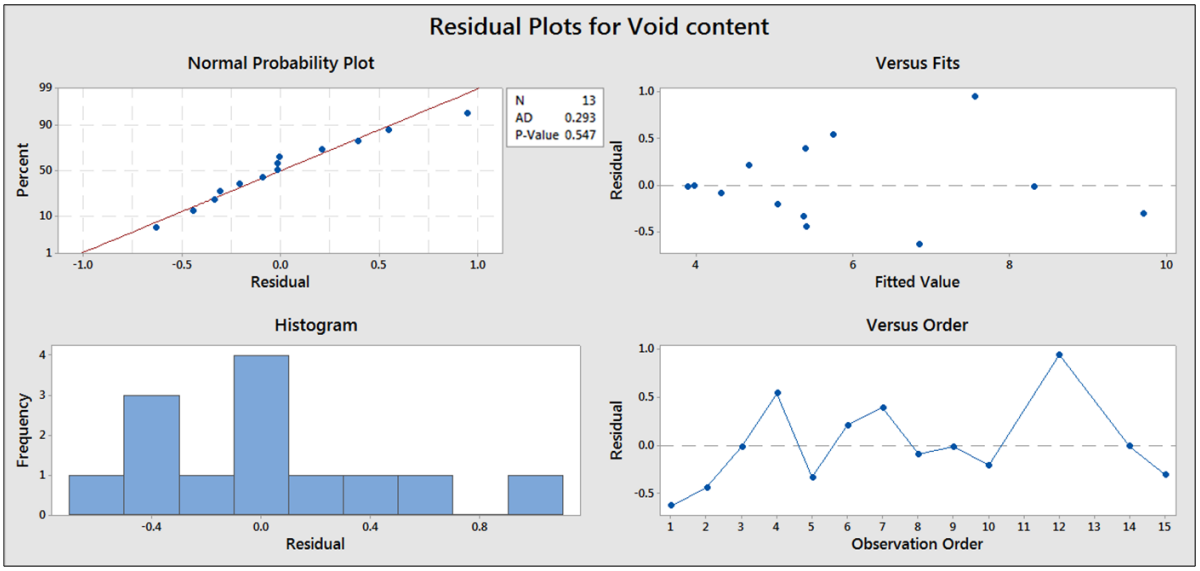

Figure H.0.4: Additional charts used for determining model validity for void content response

Demonstrator

This appendix explains how the support material is being chosen. In addition, the print sequence with the final result of the demonstrator part are given with pictures of every step in the manufacturing process. Finally, the data obtained to assess the maturity of this research is provided.

I.1. Support Study

The most important criteria in the selection of support material is the behaviour once placed within the print process. Due to the heat of the environment and the nozzle, the material can warp or even melt. This behaviour is not wanted and therefore a support study is being performed to select the most ideal support material. Table I.1.1 shows the result of this trade-off with the visualisation in Figure I.1.1 to I.1.6.

Table I.1.1: Trade-off support material

	Neat PPS	**High-T Lay**	**SABIC AMS31F**	**Antero SUP8000B**	**SR-30**	**ABS**
Adhesion	+	+	+	+	+	+
Warpage	-	0	+	+	0	-
Melting Behaviour	+	-	+	+	-	-
	+	**0**	**+++**	**+++**	**0**	**-**

The grading criteria are identified as the adhesion between extruded prepreg filament and support, warpage of the support material and melting behaviour. As can be seen in I.1.1 to I.1.6 and the above table, SABIC AMS31F and Antero SUP8000B are identified as the most feasible materials. The SABIC AMS31F is printed using a Prusa i3 MK3. The dimensional accuracy and robustness of printing the support material is considerably less than the Antero SUP8000B material, which is printed using a Fortus 450mc. Therefore the Antero SUP8000B is used for the demonstrator part manufacturing.

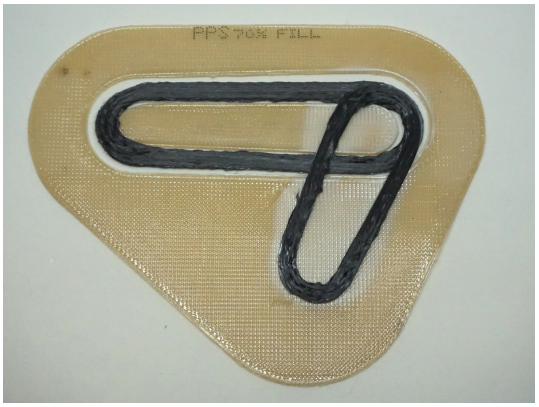

Figure I.1.1: Neat PPS support

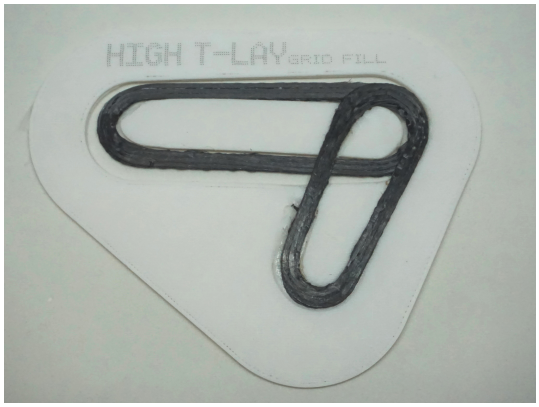

Figure I.1.2: High-T Lay support

Figure I.1.3: Sabic AMS31F support

Figure I.1.4: SUP8000B support

Figure I.1.5: SR30 support

Figure I.1.6: ABS support

I.2. Printing Sequence

Below, pictures are shown of every step in the manufacturing process of the demonstrator part.

Figure I.2.1: Step 1, print the first layer

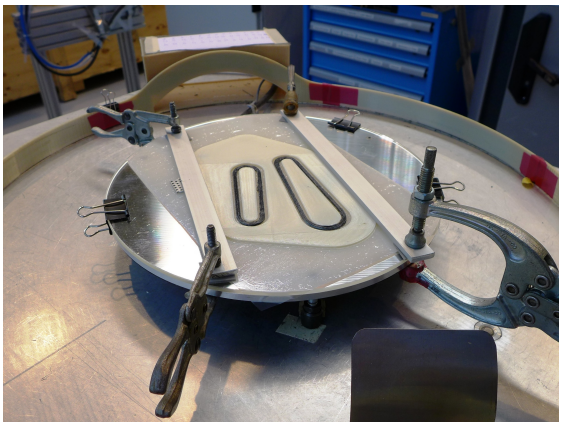

Figure I.2.2: step 2, add support

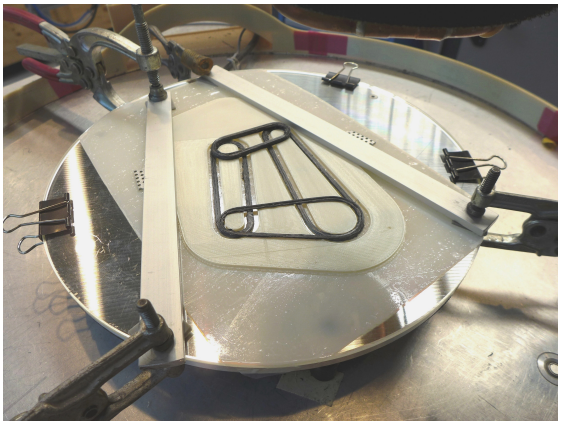

Figure I.2.3: Step 3, print the second layer

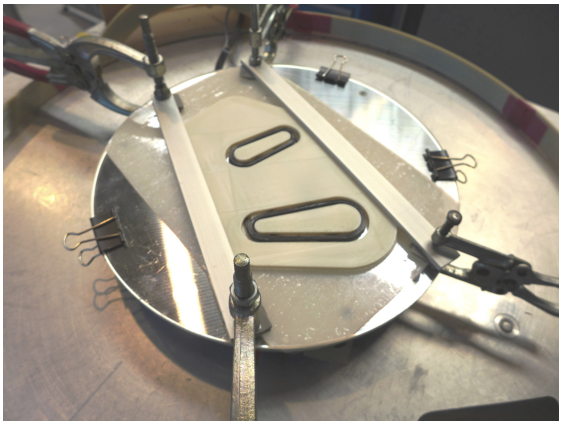

Figure I.2.4: step 4, add support

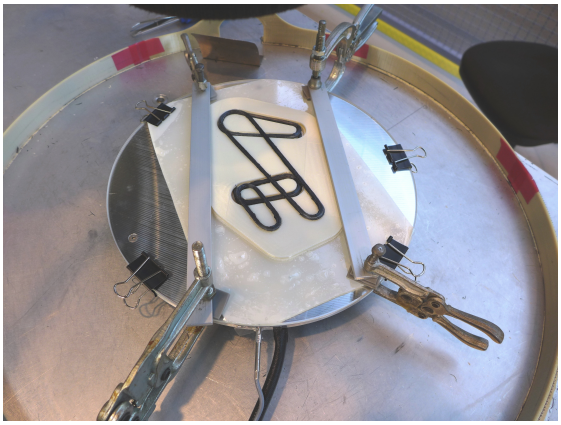

Figure I.2.5: Step 5, print the third layer

Figure I.2.6: step 6, add support

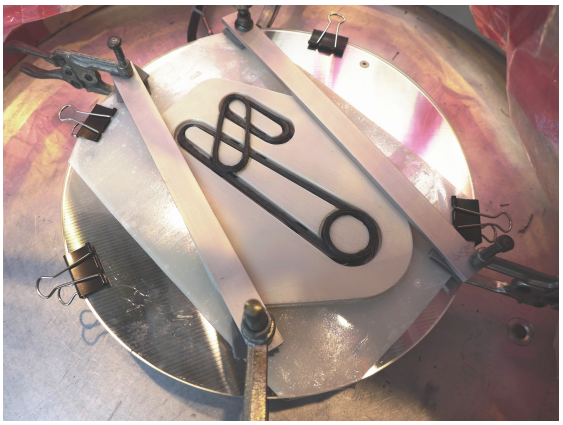

Figure I.2.7: Step 7, print the fourth layer

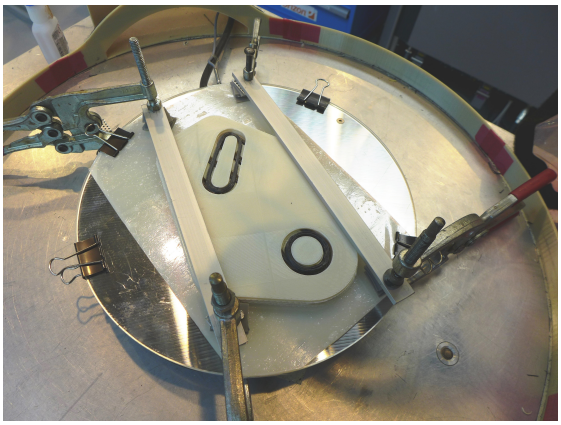

Figure I.2.8: step 8, add support

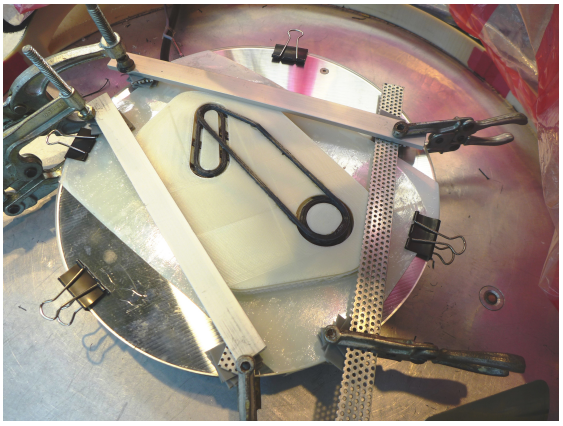

Figure I.2.9: Step 9, print the fifth layer

Figure I.2.10: step 10, anneal the complete part at 80 $^{\circ}C$ for 2 hours

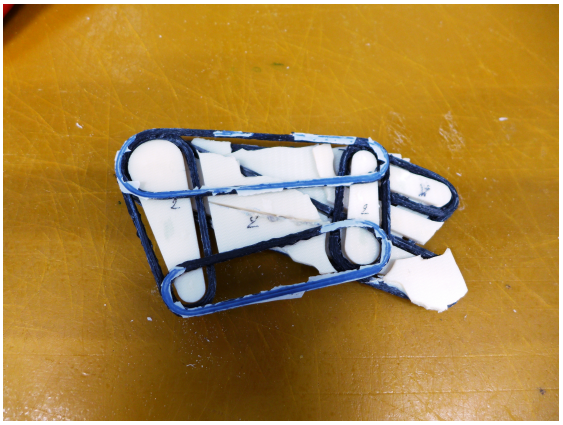

Figure I.2.11: Step 11, remove the support material

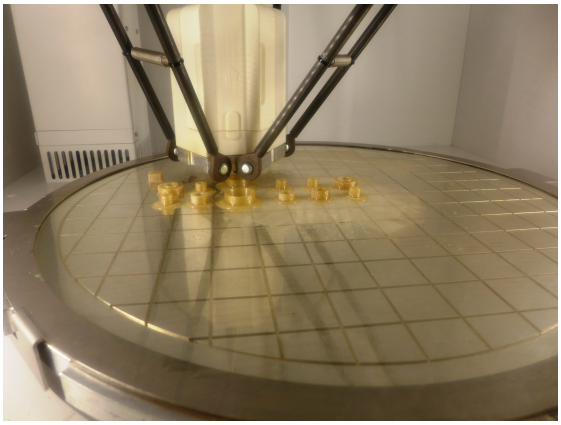

Figure I.2.12: step 12, print neat PPS inserts

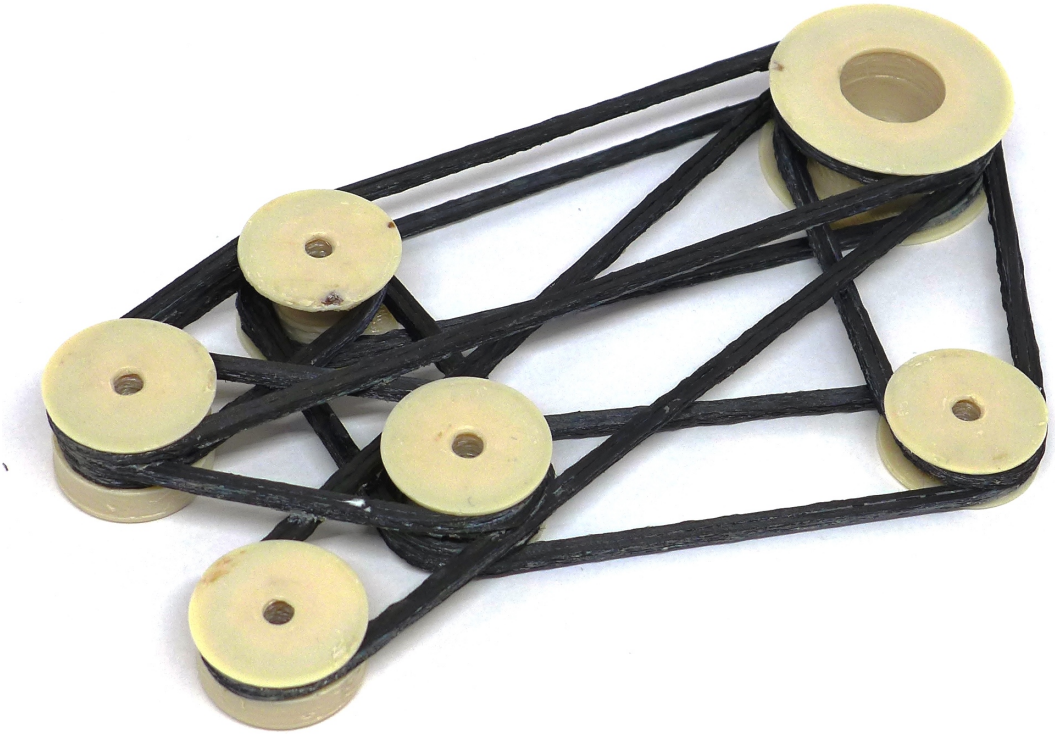

Figure I.2.13: Step 13, assemble and demonstrate

I.3. Assessment on Maturity

The overview of the grading and results are provided in the tables below.

Table I.3.1: Overview of the grading [8]

	Patent Claims	Layup rate	Quality	Polymer performance	Material cost potential	part complexity and size	Control of the build chamber	End-to-end software capability	data base available
Anisoprint Composer A4	0	0.5	0.5	0.5	0	0.3333	0.5	0.5	High
MarkForged Mark2	0	0.5	0.5	0.5	0	0.3333	0.5	0.3333	High
Arevo Labs	0	0.5	1	1	0	0.9444	0	0.6667	Mid
MantisComposites	0.3	0.5	0.5	1	0.5	0.4444	0.5	0	Mid
TIGHITCO	0.3	0.5	0.5	1	0	1	0	0.3333	Mid
9T-labs	0.8	0.5	1	0.5	0	0.3333	0.5	0.3333	Low
CEAD	0.8	1	0.5	1	0	0.6667	0.5	0	Low
FLATISA	1	0.5	0.5	1	1	0.8333	1	1	High

Table I.3.2: Results for the corresponding maturity [8]

Weight criteria	0.1424	0.0676	0.2728	0.1323	0.0532	0.1162	0.1032	0.1122	
	Patent Claims	Layup rate	Quality	Polymer performance	Material cost potential	Part complexity and size	Control of the build chamber	End-to-end software capability	**Overall Score**
Anisoprint Composer A4	0	0.0338	0.1364	0.0662	0	0.0387	0.0516	0.0561	**0.3828**
MarkForged Mark2	0	0.0338	0.1364	0.0662	0	0.0387	0.0516	0.0374	**0.3641**
Arevo Labs	0.0000	0.0338	0.2728	0.1323	0	0.1097	0	0.0748	**0.6235**
MantisComposites	0.0427	0.0338	0.1364	0.1323	0.0266	0.0516	0.0516	0	**0.4751**
TIGHITCO	0.0427	0.0338	0.1364	0.1323	0	0.1162	0	0.0374	**0.4988**
9T-labs	0.1140	0.0338	0.2728	0.0662	0	0.0387	0.0516	0.0374	**0.6145**
CEAD	0.1140	0.0676	0.1364	0.1323	0	0.0774	0.0516	0	**0.5793**
FLATISA	0.1424	0.0338	0.1364	0.1323	0	0.0968	0.1032	0	**0.8105**

Patent claim:	1:	Airbus patent
	0.8:	Open technology
	0.5:	External granted and workaround possible
	0.3:	External patent application without workaround possible
	0:	External limiting patent
Layup rate	1:	High - large nozzle systems
	0.5:	Low - small nozzle systems
Quality	1:	High - less than 1% void content with good mechanical properties
	0.5:	Mid - void content ($1\% < VC < 10\%$) with good mechanical properties
	0:	Low - high void content with low mechanical properties
Polymer performance	1:	High performance thermoplastic
	0.5:	Engineering thermoplastic
	0:	Standard thermoplastic
Material cost potential	1:	Free material choice
	0.5:	modifications possible
	0:	Limited to manufacturers material
Part complexity and size	1:	- 3D printing capability, 6-axis movement possible, large scale (1x1x1m)
	0.5:	Lattice structure printing capability, 5-axis movement possible
	0:	2.5D printing capability, 3-axis movement possible, small scale
	total =	$\frac{1}{3}$ (printing capability + axis movement + scale)
Control build chamber	1:	Fully conditioned
	0.5:	Closed but not conditioned
	0:	Fully open
End-to-end software capability	1:	Use of own solution
	0.5:	Use of existing solution
	0:	No solution
	total =	$\frac{1}{3}$ (optimization + manufacturing engineering + Process simulation)